UNIVERSITY
OF HULL

Self-Assembly of Colloidal Particles at Fluid Interfaces into Complex 2D Structures

being a thesis submitted in fulfilment of the
requirements for the degree of
Doctor of

Physics

in the University of Hull

by

Jack Leighton Eatson M. Phys. (Hons.)
April 2025

Dedication

Dedicated to my late father,
who believed I could excel,
but never got a chance to see it.

Acknowledgements

I would like to thank my supervisor Dr. D. Martin A. Buzza for his outstanding guidance, compassionate support, and invaluable knowledge. Without his support and encouragement, I would not be in the position I am today. I would also like to thank Dr. Tommy S. Horozov, Dr. Ali M. Adawi, and Dr. Jean-Sebastien G. Bouillard for their feedback and encouragement throughout my PhD. Additionally, I would like to thank my colleagues Jacob Gordon, Alina Muravitskaya, Scott Morgan, Niki Vogel, Johannes Menath, Marcel Rey, and all the members of the EU POSEIDON project for their stimulated discussions. I acknowledge the Viper High Performance Computing facility of the University of Hull and its support team. Finally, I would like to thank my partner Bea, my family, and friends for their support.

Publications and Conferences

The work presented in this thesis has produced the following publications and patents.

Publications

1. Eatson, J. L., Gordon, J. R., Cegielski, P., Giesecke, A. L., Suckow, S., Rao, A., Silvestre, O. F., Liz-Marzán, L. M., Horozov, T. S. & Buzza, D. M. A. Capillary Assembly of Anisotropic Particles at Cylindrical Fluid-Fluid Interfaces. *Langmuir* **39**, 6006–6017 (2023). (Chapter 4)
2. Eatson, J. L., Stephenson, B. T., Gordon, J, R., Horozov, T. S., Buzza, D. M. A. Capillary assembly of anisotropic nanoparticles at cylindrical fluid interfaces in the immersion regime. *Acta Mechanica*. As part of the special issue "Interfacial interactions in multiphase systems" (2005). (Chapter 5)
3. Menath, J., Eatson, J. L., Brilmayer, R., Andrieu-Brunsen, A., Buzza, D. M. A. & Vogel, N. Defined core–shell particles as the key to complex interfacial self-assembly. *Proc. Natl. Acad. Sci.* **118**, 1–10 (2021). (Chapter 6)
4. Eatson, J. L., Bauernfeind, S., Midtvedt, B., Ciarlo, A., Menath, J., Pesce, G., Schofield, A. B., Volpe, G., Clegg, P. S., Vogel, N., Buzza, D. M. A., Rey, M. Self-Assembly of defined core-shell ellipsoidal particles at liquid interfaces. *Journal of Colloid and Interface Science* **683**, 435-446 (2025). (Chapter 7)
5. Eatson, J. L., Morgan, S. O., Horozov, T. S. & Buzza, D. M. A. Programmable 2D materials through shape-controlled capillary forces. *Proc. Natl. Acad. Sci.* **121**, (2024). (Chapter 8)

Additionally, some of the work in this thesis has also been presented in both oral and poster format as follows:

Oral Presentations

1. "**Capillary Assembly of Anisotropic Particles at Cylindrical Fluid Interfaces"** UK Colloids 2023, Liverpool, UK, July 2023.

2. "**Defined core–shell particles as the key to complex interfacial self-assembly**", Particle-Based Materials Symposium 2023, Technische Universität Braunschweig, Braunschweig, Germany, October 2023.

Poster Presentations

1. **"Capillary Assembly of rod-Shaped Particles at Curved Liquid Interfaces"**, Designed Assembly of Colloids at Interfaces – fundamentals to Applications, Institute of Physics, Online, June 2021.

2. "**Capillary Assembly of Anisotropic Particles at Cylindrical Fluid Interfaces**", 36th European Colloid & Interface Society Conference, Minoa Palace, Chania, Crete, Greece, September 2022.

Abstract

Colloidal particles are used to stabilise multiphase liquids by adsorbing to liquid interfaces, but they also serve as model systems for studying self-assembly in two-dimensions. The rich variety of interactions at liquid interfaces, e.g., electrostatic, Van der Waals, and capillary, provide powerful handles for designing self-assembly. In this thesis, we exploit the interplay between particle interactions and particle anisotropy to create complex two-dimensional structures. Specifically, we use finite element simulations and Monte Carlo simulations to study the self-assembly of isotropic and anisotropic colloidal particles at flat and curved interfaces.

Firstly, we study the orientation and localisation of single rod-like particles, and the self-assembly of two rods on a cylindrical sessile drop, in both the flotation regime and immersion regime. We show we can control the orientation and self-assembly configuration through the hight of the drop, particle surface chemistry, and particle geometry.

Secondly, we study the self-assembly of core-shell spherical particles adsorbed at a flat liquid interface. This system is experimentally found to form complex phases when the system is compressed. Our simulations reproduce all the key features of the experimental phase behaviour and allows us to estimate the underlying soft shell interaction potential.

Thirdly, we study the self-assembly of core-shell ellipsoidal particles in the absence of external compression. Experimentally, this system forms chains of side-to-side particles or interconnected triangular lattice structures depending on the particles aspect ratio and shell thickness. Our simulations reproduce experimentally observed self-assembled structures as well as the trend of how these structures evolve with aspect ratio and shell thickness.

Finally, we study the self-assembly of polygonal plates with undulating edges, where capillary interactions are controlled purely by the shape of the particles. By using different combinations of polygon shapes and edge undulations, we show that self-assembly can be programmed into the particles through particle shape alone.

Contents

Dedication i

Acknowledgements ii

Publications and Conferences iii

Abstract iv

PhD Funding viii

Chapter 1 Introduction 1

Chapter 2 Background and Literature Survey 4

- 2.1 Spherical Particles at flat Fluid Interfaces 4
- 2.2 Rod-Like Particles at Flat Interfaces 9
- 2.3 More Complex Anisotropic Particles 13
- 2.4 General Theory for Capillary Interactions Between Particles at Flat Liquid Interfaces 18
- 2.5 Particles at Curved Interfaces 24

Chapter 3 Simulation Techniques 30

- 3.1 Surface Evolver 30
- 3.2 Monte Carlo Simulation 39

Chapter 4 Capillary Assembly of Anisotropic Particles at Cylindrical Fluid Interfaces – Floatation Regime 47

- 4.1 Introduction 47
- 4.2 Theoretical Methods 48
- 4.3 Results and Discussion 51
  - 4.3.1 Single Rods at a Flat Interface 51
  - 4.3.2 Single Rods at a Cylindrical Interface – Particle Orientation 52
  - 4.3.3 Single Rods at a Cylindrical Interface – Spatial Confinement 58
  - 4.3.4 Capillary interaction and self-assembly of rods at a cylindrical interface 61
  - 4.3.5 Triblock Patchy Rods 66
- 4.4 Conclusions 68

Chapter 5 Capillary Assembly of Anisotropic Particles at Cylindrical Fluid Interfaces – Immersion Regime 70

5.1 Introduction 70

5.2 Theoretical Methods 71

5.3 Results and Discussion 76

5.3.1 Orientational Transition of Single Rods 76

5.3.2 Orientation and Spatial Confinement of Single Rods 83

5.3.3 Capillary Interaction and Self-Assembly for Two Rods 86

5.4 Conclusions 92

Chapter 6 Self-Assembly of Spherical Core-Shell Particles at Flat Fluid Interfaces 93

6.1 Introduction 93

6.2 Theoretical Methods 96

6.2.1 Jagla Potential 96

6.2.2 Minimum Energy Calculations 96

6.2.3 Monte Carlo Simulation – Slow Cool Simulations 99

6.2.4 Monte Carlo Simulations – Compression Simulations 100

6.2.5 Cluster Analysis 101

6.3 Results and Discussion 102

6.3.1 Summary of Experimental Data 102

6.3.2 Monte Carlo Simulations 107

6.3.3 Minimum Energy Calculations 114

6.3.4 Determination of the Soft-Shell Interaction Potential 115

6.4 Conclusions 119

Chapter 7 Self-Assembly of Ellipsoidal Core-Shell Particles at Flat Fluid Interfaces 120

7.1 Introduction 120

7.2 Theoretical Methods 121

7.2.1 Surface Evolver 121

7.2.2 Monte Carlo Simulation 122

7.2.3 Statistical Analysis of Clusters 125

7.3 Results and Discussion 126

7.3.1 Summary of Experimental Data 126

7.3.2 Monte Carlo Simulations 131

7.3.3 Minimum Energy Calculations 135

7.4 Conclusions 137

Chapter 8 Capillary Assembly of Polygonal Plates with Undulating Edges at Flat Fluid Interfaces 139

8.1 Introduction 139

8.2 Theoretical Methods 141

8.2.1 Particle Geometry 141

8.2.2 Surface Evolver 144

8.2.3 Monte Carlo Simulations 145

8.2.4 Structural Analysis of Quasicrystals 150

8.3 Results and Discussion 151

8.3.1 Hexagons – Isolated Particles 151

8.3.2 Hexagons – Many Particles 153

8.3.3 Truncated Triangles 161

8.3.4 Binary Mixtures of Squares and Triangles 166

8.4 Conclusions 170

Chapter 9 Conclusions and Future Work 172

Reference list / Bibliography 176

Appendix 1: Sphere at a Flat Interface Surface Evolver Script I

Appendix 2: Volume Overlap Between Two Core-Shell Particles V

Appendix 3: Estimation of $\boldsymbol{\varepsilon}$ for experimental Core-Shell System VII

PhD Funding

This thesis has received funding from the European Union’s Horizon 2020 research and innovation programme under grant agreement No 861950, project POSEIDON.

This thesis has also received an additional 3-month stipend courtesy of the University of Hull

Chapter 1 Introduction

Colloids are small solid particles in the size range 1nm - 10μm dispersed in a liquid medium. Unknowingly, we interact with colloids daily in the form of milk,[1] paints,[2] lotions,[3] and many others. Colloidal particles can also be used to stabilise multiphase fluids e.g., emulsions[4–6], foams[7], and bijels[8,9] by adsorbing to liquid interfaces. Utilising this phenomenon is of particular interest to the medical community, where encapsulation of drugs for targeted drug delivery is a new and upcoming treatment method, with hopes to revolutionise difficult to treat conditions like cancer.[10]

However, colloidal particles at liquid interfaces are also an ideal model system for studying self-assembly. For particles with a diameter greater than 10nm, the energy required to detach the particles from the interface is much greater than background thermal noise, leading to irreversible adsorption.[11] For example, a spherical particle with diameter 10nm has a detachment energy of $\sim 10^3 k_B T$ at an air-water interface, meaning typical fluctuations in the thermal background noise will not be strong enough to cause detachment. This provides the perfect system for studying self-assembly in two-dimensions (2D). Colloidal particles at liquid interfaces also exhibit a wide variety of interactions, e.g., electrostatic, Van der Waals, and steric, which are qualitatively different compared to the bulk equivalent,[12,13] and additionally capillary interactions, which have no analogue in the bulk.[14] These interactions can be exploited to serve as powerful handles to control self-assembly.

In addition, modern advances in techniques mean that it is now possible to create complex colloidal building blocks, including non-spherical colloidal particles such as ellipsoids,[15,16] cylinders,[17,18] cubes,[19,20] dumbbells,[21–23] core-shell particles,[24–26] and patchy particles with inhomogeneous surface chemistry.[21,27–29] Even more recently, the emergence of three-dimensional (3D) printing[30,31] and two-photon polymerisation[32,33] techniques allow us to create colloidal particles with complex 3D shapes on the micron scale. These advances provide colloid scientists with more possibilities than ever before to engineer the self-assembly of colloids.

The aim of this thesis is to explore how we can use the interplay between interfacial forces and particle anisotropy and morphology to control the self-assembly of colloids at liquid interfaces to create a rich variety of complex 2D structures. These 2D materials have potential applications in many fields including photonics,[34,35] phononics,[36,37] plasmonics,[38,39] and auxetic materials.[40]

The rest of the Thesis is organised as follows: In Chapter 2 we cover the background and literature surrounding the topics covered in this Thesis. We start by looking at spherical particles and non-spherical particles at flat liquid interfaces, then a generalised theory for capillary interactions, before finally looking at the behaviour of colloidal particles at a curved interface.

In Chapter 3 we cover the simulation techniques used within this research, which includes the finite element software Surface Evolver which is used to perform static interfacial energy calculations, and the Monte Carlo Metropolis method which we used to study the 2D self-assembly of many particles.

In the remaining chapters I cover the results of my work over the course of my PhD. Starting with studying the self-assembly of rod-like particles on a cylindrical interface using the finite element method Surface Evolver. Specifically, in Chapter 4 we study the orientation and localisation of single rods, and the self-assembly of two rods in the floatation regime where the height of the drop is much larger than the width of the particles. This means that the hard steric interactions with the substrate the cylindrical drop sits on does not play any significant role determining particle behaviour, and assembly is driven purely through the interaction of the particle’s meniscus deformation with the curvature of the interface.

In Chapter 5, we study a similar problem to Chapter 4 but this time in the immersion regime where the height of the drop is comparable or smaller than the width of the particle. Here the steric interactions from the substrate play a critical role in the self-assembly.

In Chapter 6, we use minimum energy calculations and Monte Carlo simulations to study the self-assembly of core-shell particles (hard impenetrable core and a soft repulsive shell) adsorbed to a liquid interface when the system is compressed. Experimentally, this system is observed to form complex self-assembled phases such as particle clusters and complex chains, depending on area fraction, relative sizes of the shell to core diameter and the shape of the interaction potential. Our simulations reproduce all the key features of the experimental phase behaviour and allows us to estimate the underlying soft shell interaction potential.

In Chapter 7, we use minimum energy calculations and Monte Carlo simulations to study the self-assembly of core-shell elliptical particles in the absence of external compression. Experimentally, this system is observed to form either chains of side-to-side particles or interconnected triangular lattice structures depending on the aspect ratio and shell thickness of the particles. Our simulations and theoretical calculations reproduce experimentally observed self-assembled structures as well as the trend of how these structures evolve with aspect ratio and shell thickness.

In Chapter 8 we use both Surface Evolver and Monte Carlo simulations to study the self-assembly of polygonal plates with undulating edges interacting through capillary forces. Here the capillary interactions are not controlled by surface chemistry but purely by the shape of the particles. By using different combinations of polygon shapes and edge undulations, we are able to obtain a rich variety of 2D structures, including hexagonal close packed, honeycombs, Kagome and quasicrystal lattices.

Finally, in Chapter 9, we summarise the key conclusions from the thesis and discuss potential future work.

Chapter 2 Background and Literature Survey

In this Chapter we will review the background theory and literature for the thermodynamics of single particles and the assembly of multiple particles adsorbed at liquid interfaces, where the selection of the material is based on what is most relevant to the rest of the thesis. We initially look at spherical and anisotropic rod-like particles at a flat interface then look at more complex particle shapes, such as polygons and cubes. Once we have an intuition about the behaviour of particles at a flat liquid interface, we revisit the problem by studying the system in a more mathematical way. Finally, we expand our discussion to include the assembly of particles at curved liquid interfaces.

2.1 Spherical Particles at flat Fluid Interfaces

We start by looking at the simplest example, a single spherical particle adsorbed to a flat interface between two immiscible fluids, for now we will neglect the effect of gravity and discuss that later in this section. For convenience in the thesis, unless otherwise stated, we will call the top fluid phase oil and the bottom phase water, though our discussion in fact applies to interfaces between any two immiscible fluids. Particles adsorb to the oil-water interface to minimise unfavourable contact between the two immiscible fluids. This creates two new, more favourable interfaces, the particle-oil, and particle-water interfaces. The addition of the new interfaces now means that there is a line around the particle where all three phases (particle, water, and oil) meet, referred to as the three-phase contact line.

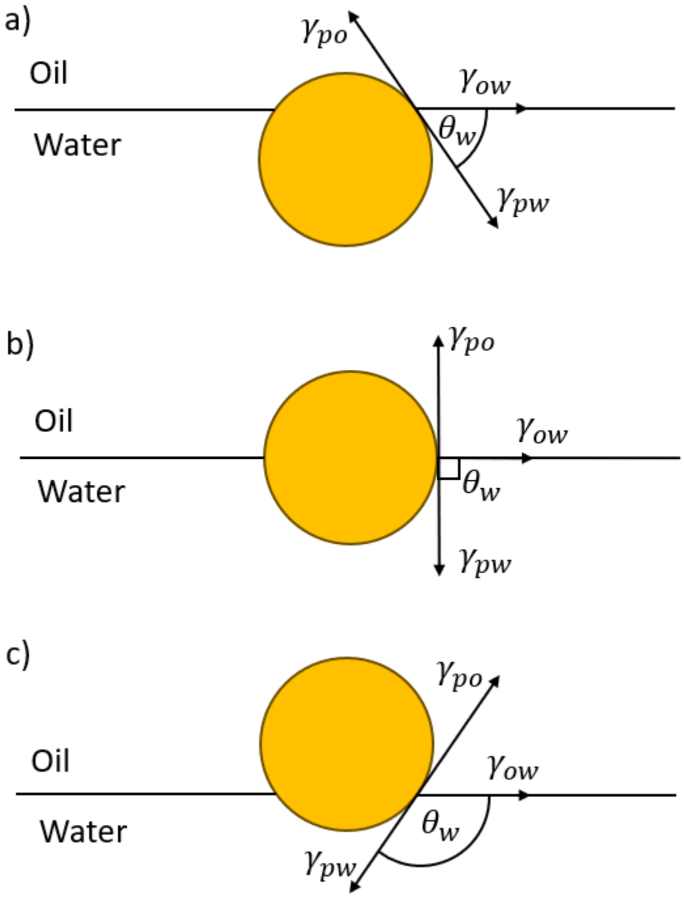

Figure 2.1: A spherical particle adsorbed to an oil-water interface with different surface chemistries. (a) A hydrophilic particle with contact angle $\theta_w < 90°$, (b) a neutrally wetted particle with contact angle $\theta_w = 90°$, (c) a hydrophobic particle with contact angle $\theta_w > 90°$.

The three-phase contact line's position on the particle is controlled by the balance of all surface tension forces from each of the three interfaces. Depending on the surface chemistry of the particle, the particle may prefer to be more in the water (hydrophilic) or more in the oil (hydrophobic). In Figure 2.1 we show examples of particles with different surface chemistries at an oil-water interface. At the three-phase contact line the oil-water surface tension γ_{ow} pulls along the interface, and the particle-oil and particle-water surface tension γ_{po} and γ_{pw} respectively, pulls tangentially to the surface of the particle at the contact point. The balance of these surface tension forces along the tangential plane to the particle at the three-phase contact line can be rearranged and written as

$$\cos\theta_w = \frac{\gamma_{po} - \gamma_{pw}}{\gamma_{ow}} \tag{2.1}$$

where θ_w is the angle between the oil-water interface and the tangential plane to the particle measured towards the more polar bulk fluid (i.e., water in this case), referred to as the contact angle. Equation (2.1) is known as Young's equation, and importantly highlights that around the contact line, there must be a constant contact angle θ_w.[13] For spherical particles, the constant contact angle θ_w can be satisfied by changing the height of the particle relative to the interface. If $\theta_w < 90°$ the spherical particle is more submerged in the water phase and therefore referred to as hydrophilic (Figure 2.1a). If $\theta_w = 90°$ the spherical particle is equally submerged in the water and oil phases and therefore referred to as neutral or neutrally wetted (Figure 2.1b). If $\theta_w > 90°$ the spherical particle is more submerged in the oil phase and therefore referred to as hydrophobic (Figure 2.1c).

The change in the particle's centre of mass relative to the interface causes a change in interfacial area between the three phases, which changes the interfacial energy. The interfacial energy of the system E_{int} can be calculated with these areas using

$$E_{int} = A_{ow}\gamma_{ow} + A_{pw}\gamma_{pw} + A_{po}\gamma_{po} \tag{2.2}$$

where A_{ow}, A_{pw} and A_{po} are the areas of the oil/water, particle/water, and particle/oil interfaces respectively. Equation (2.2) can be recast to eliminate one surface tension between the particle using equation (2.1) resulting in

$$\begin{aligned} E_{int} &= A_{ow}\gamma_{ow} + A_{pw}\gamma_{pw} + A_{po}(\gamma_{ow}\cos\theta_w + \gamma_{pw}) \\ &= \gamma_{ow}\left(A_{ow} + A_{po}\cos\theta_w\right) + \gamma_{pw}(A_{pw} + A_{po}) \end{aligned} \tag{2.3}$$

Additionally, we can eliminate one interfacial area using $A = A_{po} + A_{pw}$, where A is the total surface area of the particle leading to

$$E_{int} = \gamma_{ow}\left(A_{ow} + A_{po}\cos\theta_w\right) + A\gamma_{pw} \tag{2.4}$$

In order to understand the thermodynamic behaviour of the system, we need to minimise equation (2.4). However, the term $A\gamma_{pw}$ on the right-hand side is a constant of the system and will therefore not play a role in the thermodynamic behaviour. For this reason, the term is dropped, and the behaviour is instead effectively given by

$$E_{int} = \gamma_{ow}\left(A_{ow} + A_{po}\cos\theta_w\right) \tag{2.5}$$

For equations (2.2) to (2.5), line tension contributions have been neglected as they are only relevant for nanosized particles and this thesis focuses on particles in the micron and submicron range.[41,42]

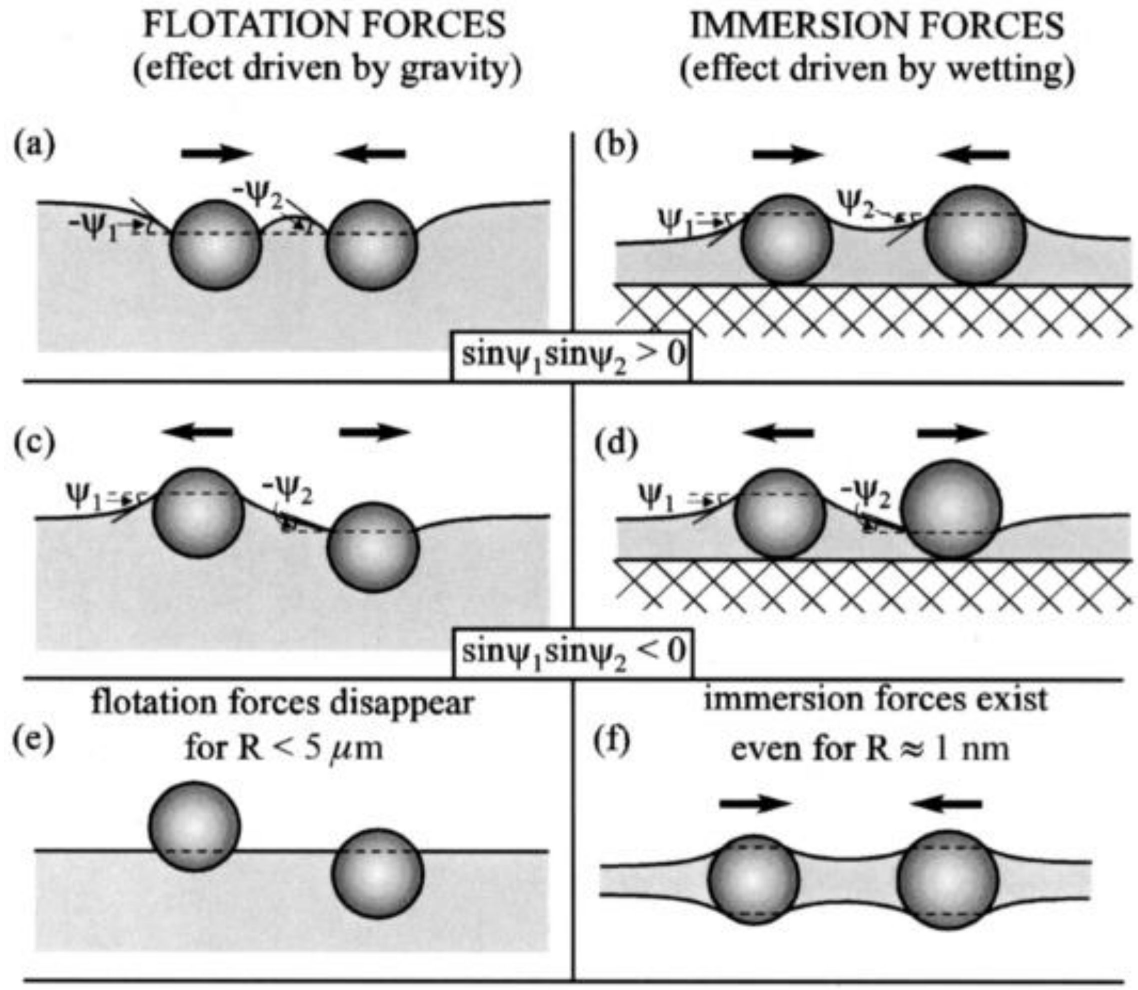

Figure 2.2: Examples of flotation forces (a, c, e) and immersion forces (b, d, e) for attractive (a, b), repulsive (c, d) configurations, as well as for small particles (radius $R < 10\mu$m) (e, f). Ψ_1 and Ψ_2 are the angles of the interface at contact with the particle relative to the horizon and α_1 and α_2 are the contact angles.[14]

When the particle is floating at the interface like in Figure 2.1, i.e., where the height of both fluid phases is much larger than the particle size, the particle is said to be in the flotation regime. In the flotation regime, if the particle has large enough mass, it is susceptible to gravitational forces. The effect of gravity on a particle at the oil-water interface is measured by a quantity called the Bond number Bo. Which can be calculated by

$$Bo = \frac{(\rho_p - \rho_f)gL^2}{\gamma_{ow}} \tag{2.6}$$

where ρ_p and ρ_f are the density of the particle and the density of the bulk fluid (which we assume have similar densities), g is the acceleration due to gravity, and L is the characteristic particle size, e.g., the radius.[43] For large bond numbers $Bo \geq 1$, the interface deforms isotopically, causing an increase to interfacial area (and interfacial energy), and therefore a restoring force from the interface to oppose gravity. We refer to this type of isotropic distortion as a monopolar deformation to the interface. If there are multiple particles at the interface, the system can minimise deformation and therefore energy by aggregating particles together (Figure 2.2a). This can be observed in breakfast cereals floating in milk, where the cereal would aggregate with each other or stick to the walls of the bowl, which led this phenomena often being called the 'Cheerios effect'.[44]

The Bond number Bo doesn't only apply to particles that are denser than the surrounding fluid, but also apply to 'particles' that are buoyant, e.g., bubbles. In this case the force of gravity drives the interface to deform in the opposite direction, with the surface tension again opposing the buoyancy force. We refer to these types of monopolar deformations as either negative if the deformation is negative (i.e., towards the bottom subphase), or positive if the deformation is positive (i.e., towards the top subphase). When two like deformations (positive-positive or negative-negative) overlap, the particles are attracted to each other to minimise interfacial energy. When two opposite deformations (negative-positive or positive-negative) overlap, the interfacial area increases, and the particles are repelled. Describing the deformations as positive or negative has led to the capillary monopole often being called a 'capillary charge' or 'capillary pole' because of the similarity to electrostatic interactions. However, one important difference between electric charges and capillary charges is that for capillary charges, like charges (Figure 2.2a) attract, and unlike charges (Figure 2.2c) repel. The concept of 'capillary charge' and interactions between interfacial deformations is made more rigorous in Section 2.4.

Flotation forces are only important for spherical particles with sizes above 10μm,[6] below this the Bond number $Bo \ll 1$ and gravitational induced deformations are negligible. Interfacial deformations can still be present for spherical particles smaller than 10μm when in the immersion regime. In the immersion regime, the height of one of the bulk fluid phases is smaller than the size of the particle, for example when the particle is in contact with a solid substrate like in Figure 2.2b, d.[45,46] The contact of the particle with the solid substrate causes the particle to protrude from the interface and the interface must to deform to satisfy the constant contact angle condition imposed by Young's equation, leading to monopolar deformation. Immersion forces can also be induced without the use of a solid substrate, by using a thin film of liquid (Figure 2.2f), e.g., a soap bubble.[47] On a the thin film the particle protrudes equally from both sides of the interface and the necessity to satisfy the constant contact angle condition causes both top and bottom interfaces to produce monopolar deformation, like that seen in Figure 2.2f. Unlike in the flotation regime, in the immersion regime the monopolar immersion forces can be relevant even down to the nanoscale.[48] In

Chapter 4 and Chapter 5 of this thesis, we will discuss the behaviour of single and multiple rod like particles at a cylindrical interface in both the flotation and immersion regime.

2.2 Rod-Like Particles at Flat Interfaces

Capillary interactions, however, can still exist between sub-micron sized particles in flotation regime if the particle is anisotropic. In this section we consider rod-like particles, e.g., ellipsoids and cylinders, at a flat interface. The anisotropy of these rod-like particles means that, from the perspective of the interface, the sides and tips of the particles have different slopes. In other words, for a flat interface, if the interface doesn't deform, we will have a different contact angle for the sides and the tips.

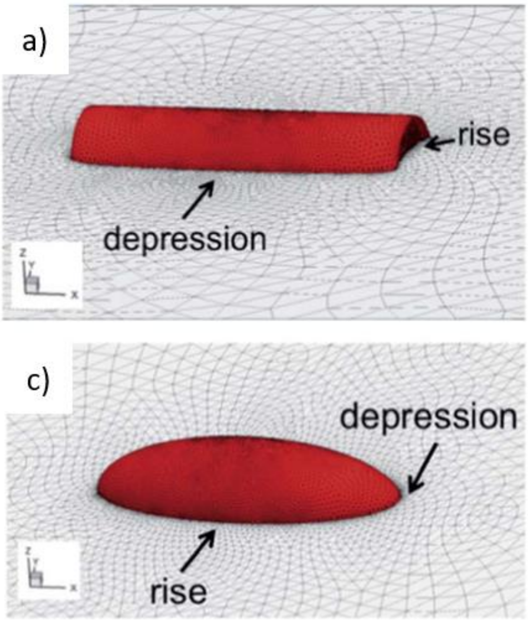

Figure 2.3: Simulations of hydrophilic cylinders (a) and ellipsoids (c) with $\theta_w = 80°$ (red) at a liquid interface (grey), with labelled positive (rise) and negative (depression) deformations. Contact line profile for the cylinder (b) and ellipsoid (d), z-axis scaled for clarity.[49]

Take for example a hydrophilic ($\theta_w < 90°$) cylinder. Because the cylinder is hydrophilic it can reduce its interfacial energy by moving more into the water phase for the same reasons as presented in Section 2.1. However, if the interface remained flat, the contact angle at the flat tips of the cylinders would be $90°$ and at the curved sides would be $< 90°$. To ensure a constant contact angle around the contact line, we therefore need to have negative interfacial deformation at the sides (to increase contact angle) and positive interfacial deformation at the tips (to decrease contact angle). This leads to the interface having a quadrupolar deformation (Figure 2.3a) and the contact line being undulated around the particle (Figure 2.3b). In the case of hydrophilic cylinders, we see that the quadrupolar interfacial deformation has the rise at the tips of the cylinders and a depression at the sides. If we instead look at hydrophobic cylinders ($\theta_w > 90°$) we can use the same procedure to see that they have a rise at the sides, and a depression at the tips. In other words, the contact line undulations are inverted for hydrophilic and hydrophobic homogeneous particles.[50]

For a hydrophilic ($\theta_w < 90°$) ellipsoid, the curvature at the tips is greater than the curvature at the sides, so when the particle is immersed more in the water phase, if the interface remained flat, the slopes and therefore the contact angle at the tips θ_{Tips} and sides θ_{Sides} would be $< 90°$, but $\theta_{Tips} < \theta_{Sides}$. To ensure a constant contact angle around the contact line, we therefore need to have negative interfacial deformation at the tips (to increase contact angle) and positive interfacial deformation at the sides (to decrease contact angle). This again leads to a quadrupolar interfacial deformation (Figure 2.3c) and an undulated contact line (Figure 2.3d). Again, we can apply the same procedure to hydrophobic ellipsoids and see that they have a quadrupolar deformation with a rise at the tips and a depression at the side, again inverse from its hydrophilic counterpart.[51] However, it is important to note that the contact line for ellipsoids are inverted compared to cylinders (hydrophilic ellipsoids have the rise at the sides and hydrophilic cylinders have the rise at the tips). This means that the direction of the contact line undulations can be controlled not only through contact angle, but also by particle shape.

In the special case where either the cylinder or ellipsoid is neutrally wetted ($\theta_w = 90°$), the constant contact angle condition can be satisfied without deforming the interface. Interestingly, a spherocylinder, which is a shape with cylindrical sides but with hemispherical caps at the tips, does not induce any interfacial deformation, regardless of contact angle.[21] For spherocylinders the curvature at the sides of the particle and at the tips of the particle are equal, i.e., they both have circular curvature. This means the constant contact angle condition can always be satisfied regardless of the contact angle by a flat interface by changing the height of the interface relative to the particle, just like a sphere.

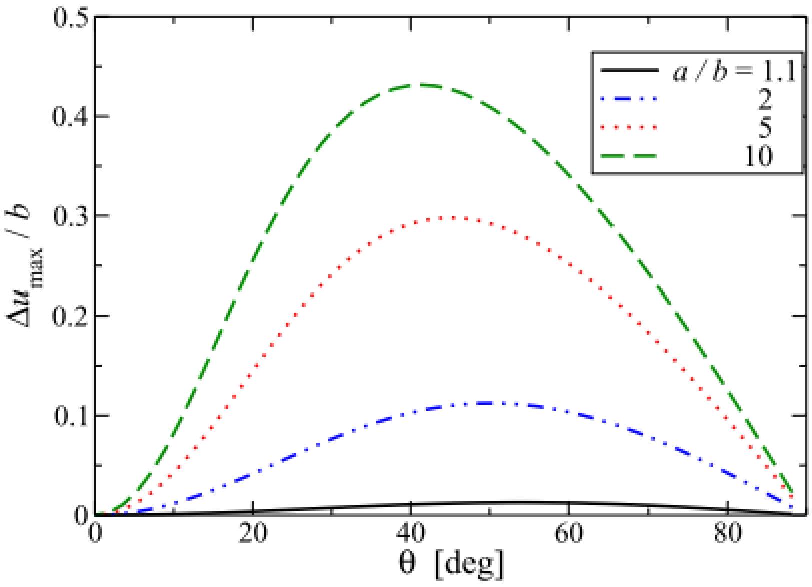

Figure 2.4: Maximum difference in interfacial height Δu_{max} between the positive and negative deformations as a function of contact angle θ for ellipsoidal particles of varying aspect ratio $\Lambda = a/b$.[52]

The undulations at the sides and tips of the rod-like particles leads to a quadrupolar deformation of the liquid interface. This generates anisotropic capillary interactions which cause the particles to spontaneously assemble into either a tip-to-tip or side-to-side configuration because like capillary charges attract. The strength of the interaction between two particles is dependent on the height of the undulations,[50] and they themselves depend on both contact angle θ_w, and aspect ratio Λ.[52] The particle aspect ratio $\Lambda = a/b$ is a measure of how anisotropic the rods are, and is simply the ratio of the length of the semi-major axis a (longest radius) and the semi-minor axis b (shortest radius). Reducing the contact angle from 90° causes the difference between positive and negative deformation to increase, but only to a point, as once the contact angle reaches 0° the particle is detached from the interface. The maximum in interfacial height difference Δu_{max} between positive and negative undulations occurs for contact angles somewhere between 30° and 60° for hydrophilic particles. However, the maxima itself also varies with particle aspect ratio Λ (Figure 2.4), which influences the height of the interface by changing the profile along the three-phase contact line.[52] Increasing Λ for an ellipsoidal particle leads to sharper tips and therefore the contact angle changes even more rapidly at the tips with interfacial height compared to the sides.

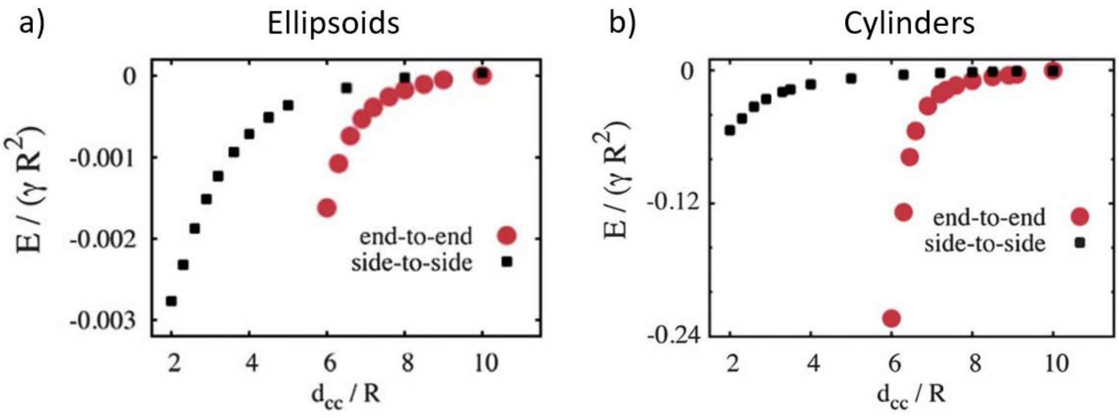

Figure 2.5: Tip-to-tip (end-to-end) and side-to-side capillary interaction energy as a function of centre-to-centre distance d_{cc} for ellipsoids (a), and cylinders (b), with contact angle $\theta_w = 80°$ and aspect ratio $\Lambda = 3$.[49]

Ultimately, energy minimisation is what drives assembly into either tip-to-tip or side-to-side configuration. In Figure 2.5a,b we show the capillary interaction energy as a function of centre-centre separation for ellipsoids and cylinders respectively for both for the tip-to-tip and side-to-side configurations simulated by Botto et al.[49] We can see from Figure 2.5a that the minimum energy state for two ellipsoids is the side-to-side orientation; this fact is not surprising since the capillary attraction between the particles is to a first approximation an inverse power law (i.e., the interaction drops off rapidly with increasing separation (see Section 2.4)) and the particles can achieve the smallest centre-to-centre separation in the side-to-side configuration. However, interestingly for any fixed separation greater than the length of the particle, the tip-to-tip configuration is preferred as this configuration has a lower potential energy compared to the side-to-side configuration. These observations provide an important insight into how a pair of ellipsoids at an interface will assemble. The ellipsoids initially approach each other tip-to-tip until they are in contact with each other. At this point the ellipsoids hinge around the contact point and roll over into the side-to-side configuration whilst always remaining in contact.[49]

For cylinders, as seen from Figure 2.5b, the minimum energy state is the tip-to-tip configuration in both the near field (i.e., small separation) and the far field (i.e., large separation). This is surprising since the minimum energy state for two rods interacting via quadrupolar interactions is the side-to-side configuration. However, cylinders have a much larger contact line undulation at the tips than at the sides as shown in in Figure 2.3, making tip-to-tip assembly more favourable energetically compared to side-to-side assembly. In addition, cylinders have sharp edges which results in a large capillary torque that opposes the rollover of the cylindrical particles into the side-to-side configuration.[49] We will consider the capillary interaction and self-assembly of ellipsoids, cylinders and spherocylinders at a cylindrical interface in Chapter 4 and Chapter 5. Whilst in Chapter 7 we will consider the capillary interaction and self-assembly of core-shell ellipsoids at a flat interface.

2.3 More Complex Anisotropic Particles

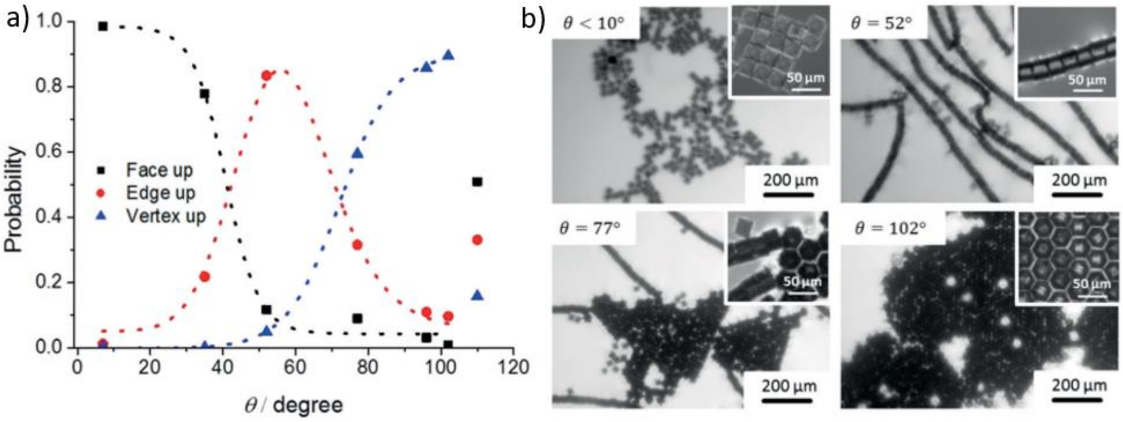

Figure 2.6: (a) Probability of 30μm cube orientation as a function of contact angle θat an air-water interface. Dotted lines serve as predictions for the statistics at non-experimentally tested contact angles, and shapes represent experimentally measured probabilities with greater than 1000 particles. (b) Assemblies of cubes at different contact angles.[19]

With advances in fabrication techniques a whole host of other anisotropic particle shapes have been studied, for example, the cube. Rod-like particles (with large enough aspect ratio)[53,54] only absorb to the interface in one orientation – with their long axis parallel to the plane of the interface. However, cubes can adsorb in three distinct orientations: face-up, edge-up, or vertex-up. Song et al[19,20] found experimentally using 30μm edge length cubes that the orientation at which they adsorb to the interface can be controlled by the cubes contact angle θ_w, face-up ($\theta_w < 20°$), edge-up ($50° < \theta_w < 60°$), and vertex-up ($\theta_w > 90°$), with phase co-existence for cubes with contact angles between these ranges (Figure 2.6a). They found that face-up cubes assemble into a square phase, edge-up cubes assemble into chains, and vertex-up cubes assemble into hexagonal lattices (Figure 2.6b).

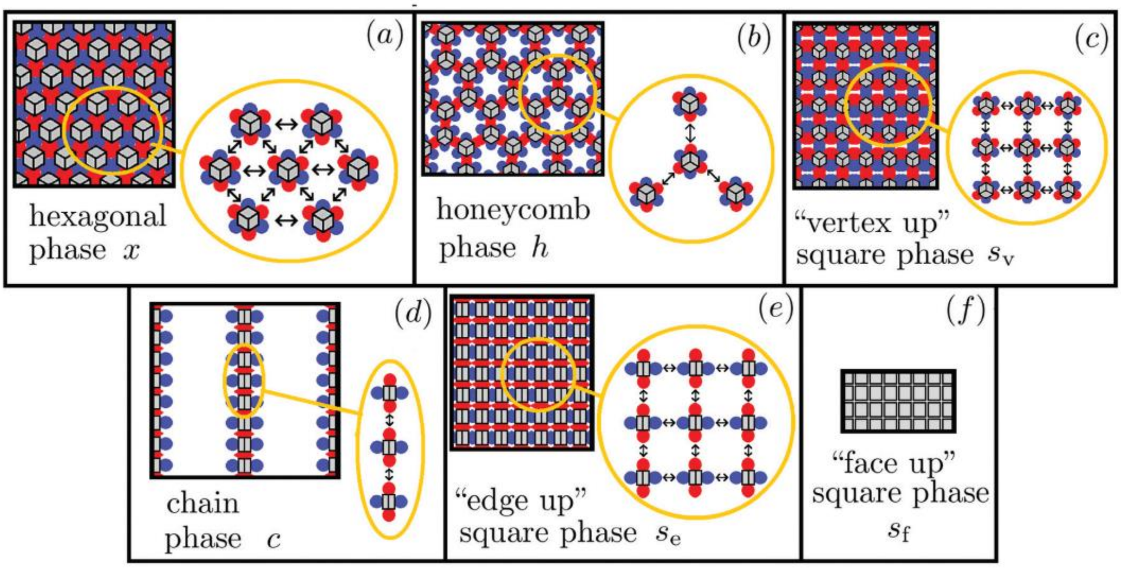

Figure 2.7: Phases formed by 2D assemblies of vertex-up (a-c), edge-up (d,e), and face-up (f) cubes. In the schematics the positive and negative undulations are represented as red and blue lobes around the cubes respectively.[55]

Complementing the experimental studies above, Anzivino et al studied the orientation and self-assembly theoretically using finite element simulations.[55] For micron-sized cubes such as those studied by Song et al,[19,20] the contribution from entropy to the free energy of the self-assembly is negligible, and the equilibrium structures are therefore structures that minimises the energy. For face-up cubes they found that there is no interfacial deformation and therefore there should not be capillary driven assembly in this system, therefore any assembly found in experiments must come from non-capillary interactions.

For edge-up cubes, the projection of the contact line is a rectangle, and they found that the capillary poles coincide with the sides of the projection. This leads to quadrupolar interfacial deformation where it was found that the overlapping of the positive poles from the flat face of the cube at the interface was much stronger than overlapping of the negative poles from the angled faces at the interface. This leads to a strong tendency for particles to assemble into chain-like structures (Figure 2.7d) with positive poles overlapping, or square-like structures (Figure 2.7e).

For vertex-up cubes, the projection of the contact line is a hexagon, and they found that the capillary poles coincide with the vertices of the hexagonal projection. This leads to hexapolar interfacial deformation where the minimum energy state is hexagonal close packed (Figure 2.7a) rather than honeycomb (Figure 2.7b). This is because there is a smaller centre-to-centre distance at side-to-side contact, i.e., dipole-dipole interactions rather than the corner-to-corner contact, i.e., tripole-to-tripole interactions. The importance of the location of the undulations relative to the contact line projection will be discussed further and in more detail in Chapter 8.

Whilst the entropy is negligible in calculations for micro-scale particles like those used by Song et al,[19,20] it does however play a significant role for nano-scale particles. Soligno et al found that when they included entropy in their calculations, it was possible to stabilise the honeycomb structure (Figure 2.7b) for nanoscale vertex-up cubes at finite temperature.[56] Furthermore, Soligno et al,[57] studied cubes with truncated edges where their theoretical calculations were in good agreement with experimental observations of truncated nano cubes.[58,59]

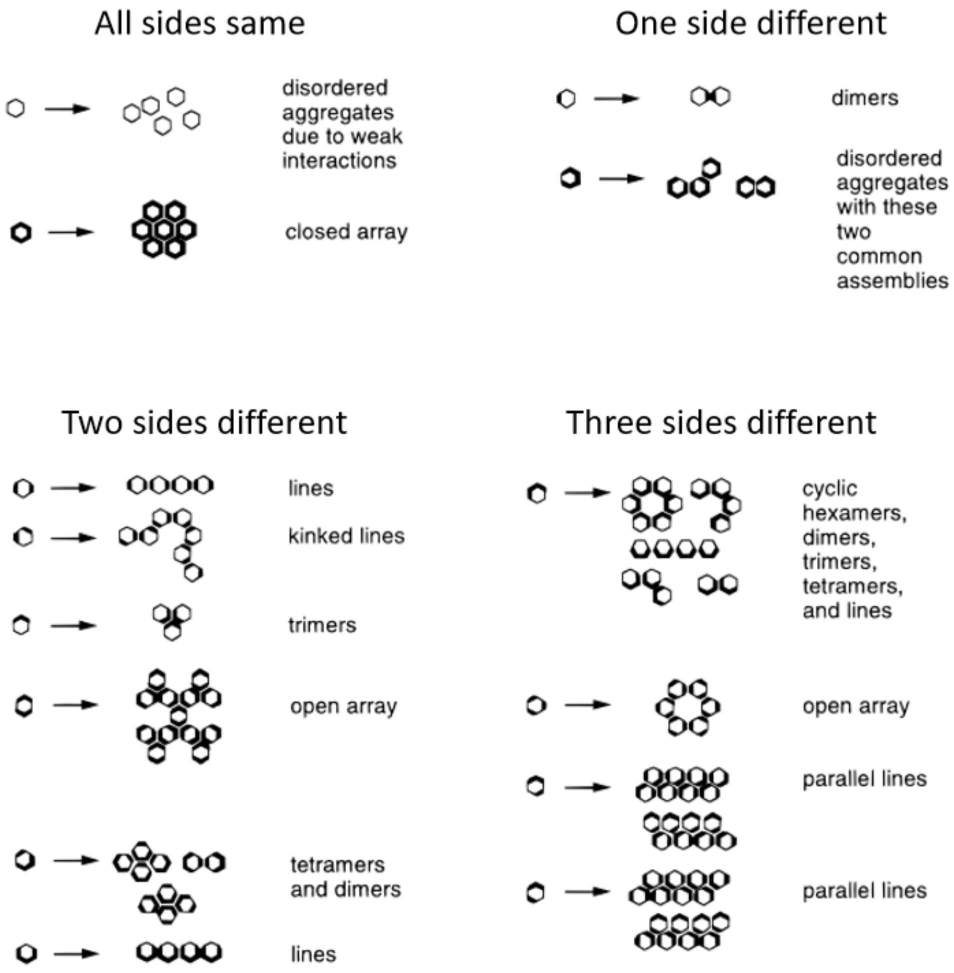

Figure 2.8: Patterned hexagons experimentally tested by Whitesides and co-workers and their self-assembled structures at a perfluorodecalin-water interface (water is the top subphase). Hexagons are categorised by number of sides that have different surface chemistries than the majority. Thick black lines represent hydrophobic faces. Notation for each different arrangement of hydrophilic/hydrophobic faces are as follows: Hydrophobic faces are labelled in square brackets, and the number which are contained within the bracket represents the number of the face which has been hydrophobized (starting with face 1) in a counterclockwise fashion. For example, a [1] hexagon only has one face that is

hydrophobic, a [1,2,3,4] hexagon has four adjacent faces that are hydrophobic, and a [1,3,5] hexagon has alternating hydrophobic and hydrophilic faces.[60]

Fabrication advancements not only allow the creation of interesting microscale shapes, but also open the door for selective surface functionalisation to create particles with patchy surface chemistry. For example, Whitesides and co-workers created flat hexagonal plates with either hydrophobic or hydrophilic sides and deposited these particles at a water-oil interface; they used a high-density oil, so water is the top phase. Since hydrophobic and hydrophilic edges induce positive and negative interfacial deformations respectively at a water-oil interface, by using different combinations of hydrophobic and hydrophilic edges, Whitesides and co-workers were able to create different multipolar edge undulations around the hexagons, leading to the formation of different self-assembled structures (Figure 2.8).

The hexagons used to create these structures are on the mm scale, so to reduce gravitational flotation forces, Whitesides and co-workers density matched the water phase with the polymer used for the hexagons by adding salt. This allows the [0] hexagons (no hydrophobic faces) to produce small monopolar deformations which interact very weakly with each other, forming disordered aggregates. However, by making all faces hydrophobic ([1,2,3,4,5,6] hexagons) strong monopolar deformation occurs and particles aggregate into a compact hexagonal array.

This asymmetry in contact angles also causes similarly configurated particles to behave differently, for example the two configurations that have one face different from the majority. Both the [1] and [1,2,3,4,5] hexagons have a non-centrosymmetric distribution of hydrophilic faces leading to the particles tilting at the interface, which cause complex interfacial deformations making selective faces stickier, leading to dimers or disordered aggregates for the [1] and [1,2,3,4,5] hexagons respectively.

Other noteworthy configurations include, [1,4] and [1,3,5] hexagons. The [1,4] hexagons produce quadrupolar interfacial deformation which coincide with the edges of the particles, this then promotes the formation of chain structures where the particles assemble edge-to-edge to minimise interfacial deformation. The [1,3,5] hexagons produce hexapolar interfacial deformations where the undulations coincide with the edges of the particles this causes them to assemble into honeycomb lattices. Note that this honeycomb lattice is not an incomplete close packed hexagonal phase, as the hole in the honeycomb lattice are surrounded by poles of the same sign, making it energetically unfavourable to insert an additional [1,3,5] hexagon in to fill these holes.

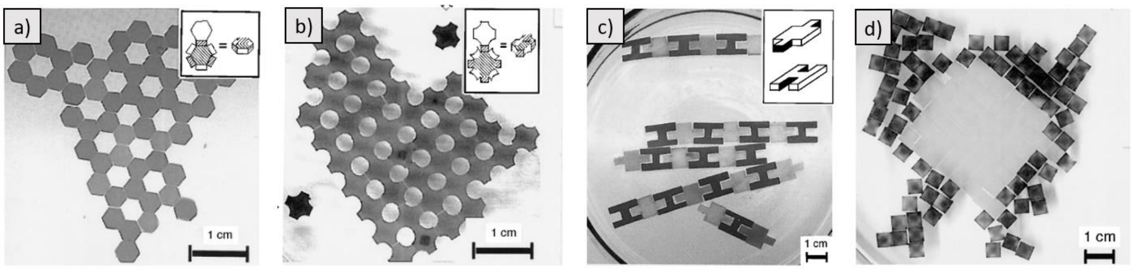

Figure 2.9: (a) Self-assembled hexagonal plates into honeycomb arrays, created by hydrophobising alternating faces. (b) Self-assembled crosses into square arrays, created by hydrophobising only the ‘tips’ of the crosses. (c) Self-assembly of a binary ‘lock and key’ system into chains, created by selectively hydrophobising the inner and outer surfaces of the ‘lock and key’ respectively. (d) Binary system of hydrophobic cubes, light grey cubes have a larger height than those of the dark cubes. Dark surfaces in the insets represent hydrophobic surfaces and white faces indicate hydrophilic faces.[61]

Control over the interfacial deformation is not the only important factor for assembly configuration, as the steric forces from the particles themselves become important in the near field. For hexagons, the shape of the particles cause assembly with 2,3,6 fold symmetry like the honeycomb array (Figure 2.9a), but lattices with 4 fold symmetry (square lattices) are absent from the assembled structures in Figure 2.8. Whitesides and co-workers then further used their patterning technique on other polygonal plates like crosses with hydrophobic ‘tips’ in Figure 2.9b to form open square lattices. They also used a binary system consisting of ‘lock and key’ shaped particles (Figure 2.9c), and selectively hydrophobized surfaces such that cross species interaction is more favourable than same species interaction. In Figure 2.9d Whitesides and co-workers also show hierarchical self-assembly with cubes with identical surface chemistries, but different physical heights. This causes a hierarchy of particle-particle interactions with the largest interaction strength coming from large particles interacting with each other, followed by cross species interaction, and finally short particles interacting with each other.[61]

Whitesides and co-workers have clearly showed that this is a versatile system that allows us to programme self-assembly through combinations of shape, selective surface chemistry, and height. However, for this system, particles are on the mm scale, hence the necessity for density matching of the particle material. Scaling down of this process, could eliminate the need for careful material selection, opening the door to designing metamaterials. However, the main weakness with Whitesides and co-workers approach is that the patchy edge geometry makes it very difficult to scale down the particle synthesis below the mm scale.[62] In Chapter 8, we propose a method to circumvent the fabrication issues by using particle shape alone to control the interfacial deformation and capillary interactions. This enables the possibility to scale down particle synthesis to much smaller sizes using readily available synthesis techniques.

2.4 General Theory for Capillary Interactions Between Particles at Flat Liquid Interfaces

In previous sections, we have discussed the physical origins of interfacial deformations and how systems minimise energy and form self-assembled structures. In this section we approach this problem in a more formal fashion. Starting from first principles, we describe the interfacial deformation for one particle adsorbed at a flat interface in polar coordinates, then consider the far-field energy for two interacting capillary multipoles of arbitrary order, before looking at the energy between two interacting elliptical quadrupoles.

The presence of an interfacial tension between the two immiscible fluids implies that for curvatures in the interface, a Laplace pressure difference occurs between the two fluid phases. This pressure difference can be written as

$$\Delta P = \gamma\left(\frac{1}{r_1} + \frac{1}{r_2}\right) \tag{2.7}$$

where r_1 and r_2 are the principal radii of curvature at a given point on the surface, which will be discussed further in Section 2.5. If we parameterise the height of the interface as a scalar field $h(x, y)$, where x, y are Cartesian coordinates within the interfacial plane, calculation of the principal radii of curvatures and hence Laplace pressure, becomes a non-linear second order partial derivative. However, because the induced curvatures from the presence of the particles are small, we can approximate the curvatures by neglecting higher order gradient terms, i.e., we can take the limit of small slopes.[63] In this limit, equation (2.7) can be rewritten as

$$\Delta P = \gamma \nabla^2 h(x, y) \tag{2.8}$$

where ∇^2 is the 2D scalar Laplace operator $\left(\frac{\partial^2}{\partial x^2} + \frac{\partial^2}{\partial y^2}\right)$. Far from the particle, the interface is flat, and hence $\Delta P = 0$, and because the system is in equilibrium, the pressure difference across any part of the interface must also be zero,[63] so we can write.

$$\nabla^2 h(x, y) = 0 \tag{2.9}$$

Note that equation (2.7) does not imply that the interface is flat everywhere, but rather when the surface is curved the principal radii of curvature are equal, but opposite.

To solve equation (2.9), it is advantageous to use coordinate systems which match the symmetry of the problem, for example polar coordinates for particles with near circular symmetry. By representing the height of the interface in terms of polar coordinates $h(r, \theta)$

and representing this as a product of two functions $R(r)$, $\Phi(\theta)$ (which only depend on one of the scalar parameters respectively) equation (2.9) can be split into two equations and solved independently for $R(r)$ and $\Phi(\theta)$. Since equation (2.9) is a linear equation, from linear superposition a general solution for $h(r,\theta)$ can be written as

$$h(r,\theta) = A_0 \ln(r) + A_1 r^{-1} \cos(\theta + \alpha_1) + A_2 r^{-2} \cos(2\theta + \alpha_2) + \dots \tag{2.10}$$

Here, each of the terms $A_0 \ln(r)$, $A_1 r^{-1} \cos(\theta + \alpha_1)$, and $A_2 r^{-2} \cos(2\theta + \alpha_2)$ etc, represent deformation with monopolar, dipolar, and quadrupolar, etc, symmetry. The coefficients A_i and α_i represent the amplitude and phase (with respect to θ) of the mode and can be solved based upon boundary conditions. In the absence of external forces, the amplitude for the monopolar mode $A_0 = 0$, otherwise there would be a restoring force from surface tension. In the absence of an external torque, the amplitude for the dipolar mode A_1 is also 0, otherwise there would be a restoring torque due to surface tension at the contact line. This means that the leading order term without an external force or torque is quadrupolar.[64]

In equation (2.10) the influence of each mode m decays with respect to r^{-m}. With quadrupolar being the slowest decaying mode, in the far field higher order modes will have minimal influence, and the quadrupolar mode will be the dominating mode effecting the height of the interface. For this reason, particles with rough surfaces or “patchy” wetting conditions lead to quadrupolar deformation.[65] In this case, the height of the interface due to a polar quadrupole is given by

$$h(r,\theta) = H_c \left(\frac{r_c}{r}\right)^2 \cos(2\theta) \tag{2.11}$$

Here the amplitude of the mode (A_2 in equation (2.10)) has been rewritten in terms of H_c and r_c which refers to the amplitude of the height of the interface at the contact line and radius of the contact line respectively. In equation (2.11) we have also removed the phase angle α_2 by orienting the definition of $\theta = 0°$ to coincide with one of the quadrupolar rise axes. For spherical particles with contact angles close to $90°$ the contact radius r_c is very close to that of the radius of the particle.[64] For non-spherical particles like ellipsoids, we can still approximate the interfacial deformation using a circular multipole by choosing an intermediate radius for r_c, e.g. the mean of the semi-major and semi-minor axes. We can then calculate H_c by performing an interfacial simulation and taking a Fourier transform of the height of the interface along a circular contour surrounding the particle and extracting the coefficient for the relevant mode.[65] Then, because we know the interfacial height contribution from each mode at the circular contour, and that the height decays according to equation (2.10), we can calculate H_c at r_c for each mode.

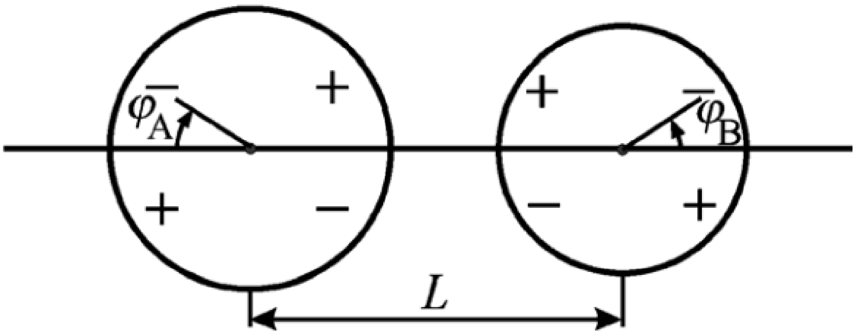

Figure 2.10: Two capillary quadrupoles, A and B at separation L. The "+" and "-" represent positive and negative interfacial deformations and angles ϕ_A and ϕ_B represent the rotation of the negative antinode of the contact line with respect to the line that joins the particles centres. Note that in this definition the ϕ_A rotates clockwise, and ϕ_B rotates counterclockwise.[66]

By using equation (2.11) Stamou et al were able to calculate the "self-energy", i.e., the increase in energy due to the undulated surface, for an individual particle. Furthermore, Stamou et al then went on to calculate the interaction energy between two identical polar quadrupoles. They did this by subtracting the "self-energy" of each of the particles from the increase in energy of the two-particle system at separation L. In the two-particle system the height of the deformed interface is given by the superposition approximation, i.e, $h = h_A + h_B$. Ultimately for this system this calculation involves evaluating the deformation field of particle A at the contact line of particle B using a Taylor approximation, and then doubling the potential (because both particles are identical polar quadrupoles) to find

$$V(L) \approx -12\pi\gamma H_c^2 \cos(2(\phi_A - \phi_B)) \left(\frac{r_c^4}{L^4}\right) \tag{2.12}$$

where ϕ_A and ϕ_B are angles of rotation defined in Figure 2.10.

Danov et al[66] generalised the work of Stamou et al[64] by calculating the capillary interaction between capillary multipoles of arbitrary order. To do this, they used a bi-polar co-ordinate system (which corresponds to the geometry of the system) to calculate the interfacial deformation h from the joint system and then calculated the interaction potential $\mathrm{V}(L)$. For particles at large distances the interaction energy can be approximated to

$$V(L) \approx -\pi\gamma G_0 H_A H_B \cos(m_A\phi_A - m_B\phi_B) \left(\frac{r_A^{m_A} r_B^{m_B}}{L^{m_A+m_B}}\right) \tag{2.13}$$

where m_A, r_A and m_B, r_B are the mode and average contact line radius of particle A and B respectively, and G_0 is given by

$$G_0 = \sum_{n=1}^{\min(m_A, m_B)} \frac{2(-1)^{m_A+m_B} m_A!\, m_B!}{(m_A - n)!\,(m_B - n)!\, n!\,(n-1)!} \tag{2.14}$$

For two identical interacting quadrupoles equation (2.13) reduces to the interaction potential found by Stamou at al in equation (2.12) and for hexapoles ($m_A = m_B = 3$) the interaction potential is given by

$$V(L) \approx -\pi\gamma 60 H_c^2 \cos(3(\phi_A - \phi_B)) \left(\frac{r_c^6}{L^6}\right) \tag{2.15}$$

Equation (2.13) not only allows us to calculate the interaction potential between particles that have a single capillary mode but also allows us to calculate the interaction potential between particles that have multiple modes by performing a sum of each of the separate interacting modes. However, it is important to note that this is a far-field formula which is accurate for $L \geq 3r_c$, but may not capture the near-field behaviour.[66]

So far, we have only described the particle induced deformation in terms of polar multipoles. Whilst this is an accurate description in the far field or for particles whose projection of the contact line is close to circular, it does not capture the near-field behaviour of rod-like particles like ellipsoids and cylinders.[65] For example, in section 2.2 we discussed the interaction potential between two identical ellipsoids and cylinders where, for a fixed separation greater than the length of the particle, the tip-to-tip orientation is preferred compared to the side-to-side. In contrast, if we represent the ellipsoid as a polar quadrupole, we see that the interaction potential is minimised when $\cos(2(\phi_A - \phi_B)) = 1$, i.e., when $\phi_A = \phi_B$. These angles represent mirror symmetric orientations of the particles so that both tip-to-tip and side-to-side configurations have the same energy for two polar quadrupoles. To capture the elongated quadrupolar deformation caused by rod-like particles more accurately, Lewandowski et al calculated the quadrupolar deformation around rod-like particles using elliptical coordinates.[50]

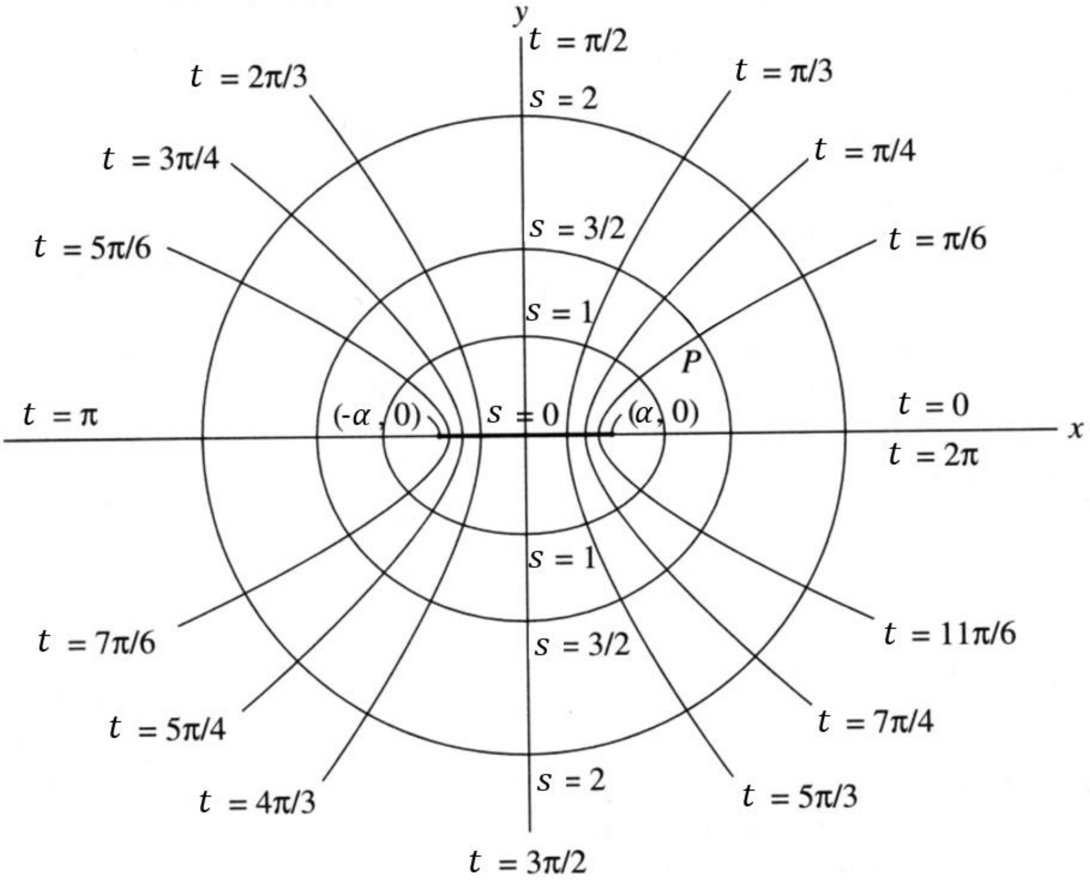

Figure 2.11: Elliptic coordinate system (s, t) plotted on a cartesian plane (x, y). Lines of constant s represent concentric ellipses with focal points $(-\alpha, 0)$ and $(\alpha, 0)$, whilst lines of constant t represent hyperbolae.[67]

To calculate the interaction potential between two rod-like particles, first we represent the height of the interface around each particle in terms of elliptical coordinates. The elliptical coordinates (s, t) are related to cartesian coordinates (x, y) in the interfacial plane by the coordinate transformation

$$x = \alpha \cosh(s) \cos(t)$$

$$y = \alpha \sinh(s) \sin(t) \tag{2.16}$$

where lines of constant s form concentric ellipsoids with focal points $(-\alpha, 0)$ and $(\alpha, 0)$, whilst lines of constant t represent hyperbolae. A diagram of the elliptic coordinate system is show in Figure 2.11. We can calculate α utilizing that the sum of the distances between the focal points and a point on the ellipse is a constant. By taking two points on the ellipse in cartesian coordinates $P_1 = (a, 0)$ and $P_2 = (0, b)$ we can equate both distances and rearrange to find that $\alpha = b\sqrt{\Lambda^2 - 1}$ where $\Lambda = a/b$. We can also define an elliptical distance $s = s_0$ which represents the contour of an ellipsoid of aspect ratio Λ by substituting P_1 and P_2 into Equation (2.16, dividing the results an rearranging to find that $s_0 = \coth^{-1} \Lambda$. For contact angles close to

90° the contact line only deviates slightly from an ellipse defined by s_0 and therefore in these cases, a close approximation to the contact line.[52] By solving equation (2.9) in this coordinate system we obtain an expression for the interfacial height as a function of s and t, where for the quadrupolar mode, the interfacial deformation given by

$$h(s,t) = H_e \exp\left(-2(s - s_0)\right) \cos(2t). \tag{2.17}$$

Here H_e is the amplitude of the quadrupolar interfacial deformation at an ellipse defined by s_0. By using two elliptical coordinate systems, each centred around one of the identical ellipses, the interaction energy can be calculated using the linear superposition approximation, in the same way that Stamou et al[64] performed their calculations in the polar coordinate system.

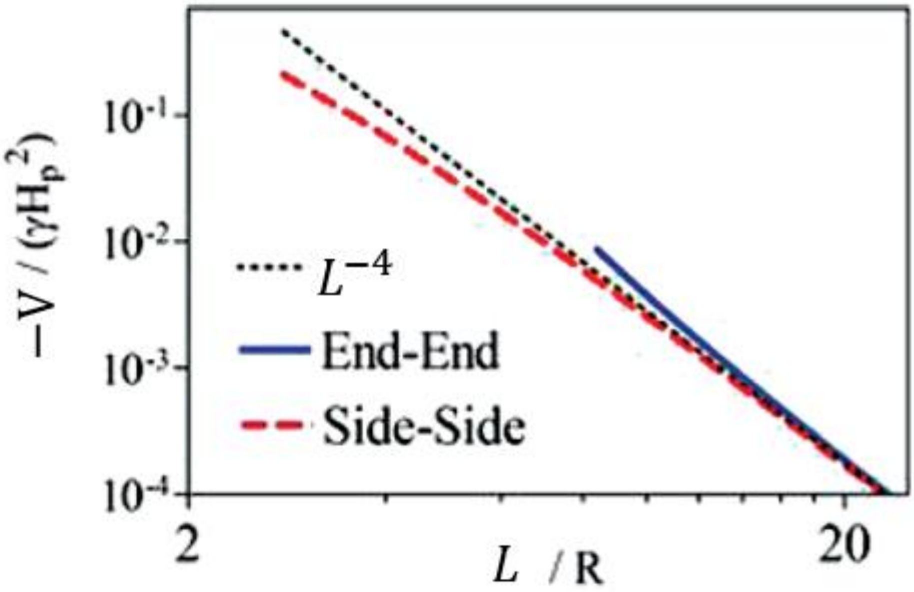

Figure 2.12: Interaction potential as a function of separation L between elliptical quadrupoles with $\Lambda = 3$. The blue line represents and end-to-end or tip-to-tip configuration (i.e., $\phi_A = \phi_B = 0°$), and the red dashed line represents a side-to-side configuration (i.e., $\phi_A = \phi_B = 90°$). The dashed black line represents a power law decaying as L^{-4} which in the far field, both configurations approach.[50]

The calculation for the interaction between two elliptical quadrupoles can be found later in Chapter 7 where we look at the assembly of a system of core-shell ellipsoids. In Figure 2.12 we show the interaction potential for two elliptical quadrupoles with $\Lambda = 3$ for both the tip-to-tip ($\phi_A = \phi_B = 0°$) and side-to-side ($\phi_A = \phi_B = 90°$) configurations. We see that now for a fixed separation greater than the length of the particle the minimum energy orientation is now indeed tip-to-tip. However, the two-particle system can minimise its energy further by assembling side-to-side in the near field which agrees with the work presented in Section 2.2.

2.5 Particles at Curved Interfaces

So far, we have considered the interaction of particles at flat liquid interfaces. In this section we look at the assembly and dynamics of particles at curved liquid interfaces like those formed by droplets. To start our discussion on this topic, we first quantify the geometry of the interface.

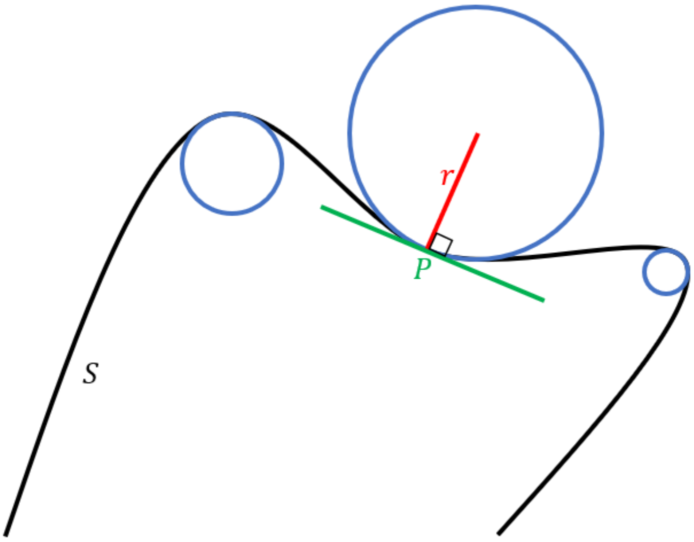

Figure 2.13: Examples of osculating circles (blue) of a curve S (black). For the large osculating circle, additional labels of the osculating circles radius r (red) and tangent line at point P (green).

For any point P on a surface S, we can define a surface normal unit vector $\hat{n}$ which is perpendicular to the tangent plane at P, and define a normal plane which is any plane that contains $\hat{n}$. There are infinitely many normal planes, and each one will intersect with S producing curves called normal sections. These curves will in general have different curvatures at point P and can be parameterised using the radius of the osculating circle, which is a circle that is tangent to, and has the same curvature as, the curve at point P. In Figure 2.13 we illustrate this using one of the normal sections, where we see that small circles are used for sharp curves, and large ones for gentle curves. Whilst there are infinitely many normal sections, and therefore infinitely many osculating circles at point P, only two of these are of interest, that is the osculating circles with the largest, and smallest radius at point P. The two radii of the osculating circles r_1 and r_2 corresponding to either the maxima or minima normal sections are referred to the principal radii of curvature. At point P if $r_1 = r_2$ we refer to this as an umbilic point and every normal section can be considered as containing the principal radii of curvature. However, if $r_1 \neq r_2$ there are distinct normal planes which contain the normal sections with curvature r_1 or r_2 at point P and the normal planes are always orthogonal to each other.[68]

Defining the principal curvatures as $\kappa_1 = \frac{1}{r_1}$ and $\kappa_2 = \frac{1}{r_2}$ where κ_1, κ_2 correspond to the maximum and minimum curvatures respectively, we can define the Gaussian curvature, mean curvature and deviatoric curvature at point P. The Gaussian curvature is simply the product of the principal curvatures $K = \kappa_1\kappa_2$ and contains information about whether the point is dome like (if $K > 0$), plane like (if $K = 0$), or saddle like (if $K < 0$). The Gaussian curvature of a surface also does not change upon bending (without stretching), and therefore the Gaussian curvature is an intrinsic invariant of a surface.[69] The principal curvatures also allow us to define the mean curvature as

$$H = \frac{1}{2}(\kappa_1 + \kappa_2) \tag{2.18}$$

which allows us to write Equation (2.7) as $\Delta P = \gamma 2H$. For a deformable surface in equilibrium and with no external forces, the pressure must be uniform and therefore $H = const.$[70] A special subset of these constant mean curvature surfaces are minimal surfaces where $H = 0$,[71] e.g., a planar interface. A counterpart to the mean curvature H is the deviatoric curvature D given by

$$D = \frac{1}{2}(\kappa_1 - \kappa_2) \tag{2.19}$$

Note that unlike H, the deviatoric curvature D (which is always positive) is not necessarily constant over the equilibrium surface.[72] As we will see later in this section, the deviatoric curvature is very important in regards to self-assembly of particles on curved surface, as particles migrate to regions of high deviatoric curvature.[17]

Whilst previously in Section 2.1 we looked at a spherical particle on a flat interface and found that the three-phase contact line could be satisfied without deforming the interface, at a curved interface generally this is no longer possible. For example, consider the simple curved surface of a cylinder. Here the two principal curvatures are $\kappa_1 = +const$ and $\kappa_2 = 0$, which lie perpendicular and parallel with the long axis of the cylindrical interface respectively. The cylindrical interface therefore has a Gaussian curvature $K = 0$ just like a plane but has a constant mean curvature of $H = \frac{\kappa_1}{2}$. When a spherical particle is adsorbed to the interface, the height and angle of which the unperturbed interface contacts the particle is different along both principal curvature directions. This means that to satisfy the constant contact angle condition, the interface must deform. Just like in our previous discussions in Sections 2.2 and 2.4, the leading order deformation is quadrupolar, with its positive and negative deformation axes aligned with the axes of principal curvature.[70] Note however, that this only applies to interfaces with distinct axes of principal curvature. If an interface has equal curvatures ($\kappa_1 = \kappa_2$), firstly, the axes of principal curvature are undefined. Secondly, the angle at which the unperturbed interface meets the spherical particle is the same from any direction, allowing the constant contact angle condition to be satisfied without deforming the host interface.

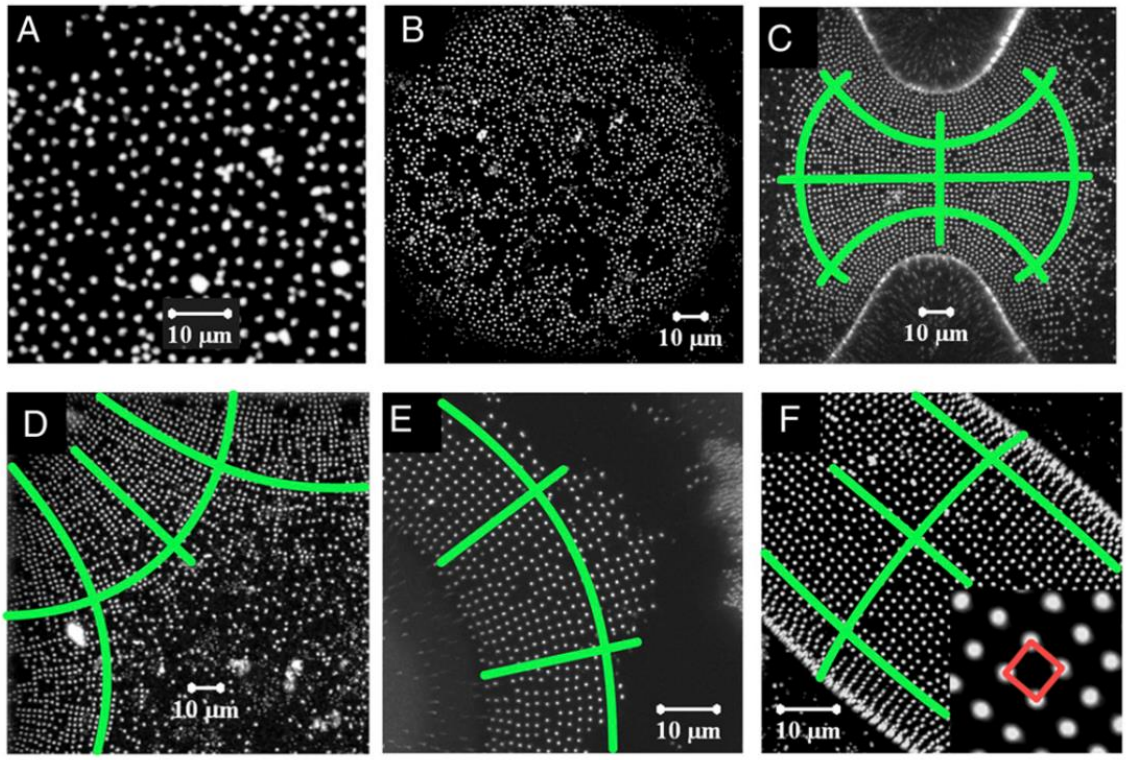

Figure 2.14: Particle assemblies achieved with spherical particles by Ershov et al on oil/water interfaces of different shapes. (A) flat interface, (B) spherical interface, (C) dumbbell-shaped droplet, (D) droplet pinned to a square patch (only one corner is shown), (E) toroid-shaped droplet, and (F) a prolate ellipsoid. Inset in (F) shows square lattice organization. Green lines in C–F indicate the directions of principal curvature.[72]

The quadrupolar deformations caused by the curvature of the interface provide a way for spheres to assemble via capillary interactions. In Figure 2.14 we show the assemblies of spherical particles at various constant mean curvature surfaces used by Ershov et al.[72] To create these curved surfaces they hydrophobized different shaped patches on a glass substrates, added oil to the patches and then covered these with water. The shape and curvature of the drops is then defined by only the shape of the patch and the volume of oil added. In Figure 2.14A they show that at a flat interface there is no attraction between the spherical microparticles, and therefore the particles have no intrinsic deformation. In Figure 2.14B they show that on a hemispherical drop, (i.e., no distinct axes of curvature) the spherical particles still do not assemble. However, in Figure 2.14C-F they absorb the microspheres on surfaces with distinct axes of principal curvatures, and the microspheres assemble into a “square” lattice formation. More specifically, the particles assemble into lattices that follow the axes of principal curvature, which are marked by green lines in Figure 2.14C-F.

We can also see that particles migrate to specific regions in Figure 2.14C-E, which can’t be regions of high or low mean curvature H, because these are all surfaces with constant mean curvature. Nor can it be high or low Gaussian curvature K because in Figure 2.14C and Figure 2.14F we see particles assemble at either. Instead, the particles migrate to regions of high deviatoric curvature D which is also an intrinsic invariant of the surface.[72]

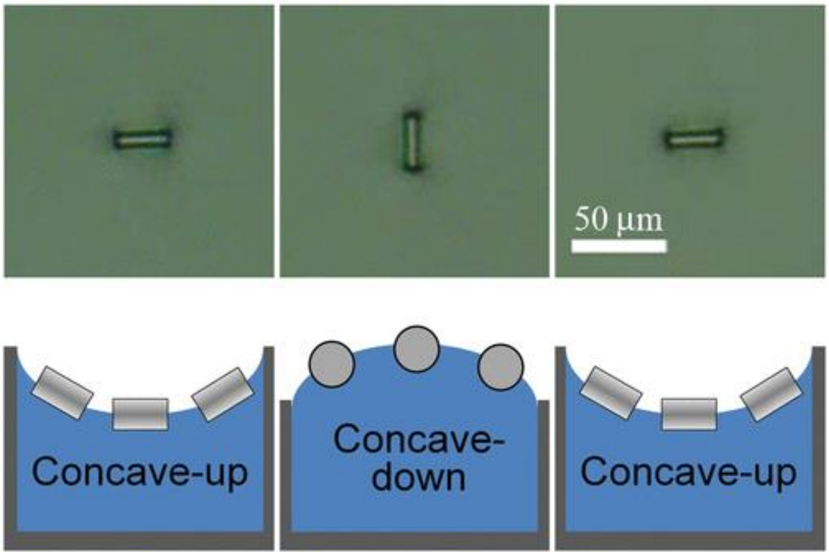

Figure 2.15: Cylinders rotate to align their positive rise axis with the interfaces, whose curvature is changed dynamically from concave-up to concave-down and back. (Top) Images of experimental cylinders aligned in stable states and (bottom) corresponding schematic of a cross section of the plane parabolic interface, showing the interface shape and the particle alignment (not to scale).

The next step is to look at how anisotropic particles assemble at curved interfaces. In Figure 2.15, we show experimental work performed by Lewandowski et al that showed that by controlling the concavity of a plane-parabolic curved interface ($\kappa_1 = 0, \kappa_2 < 0$), cylindrical particles (length 25μm, radius 7μm) would rotate so that their intrinsic quadrupolar rise axis (the axis along the particle which is responsible for the positive deformation) would align with the principal rise axis of the interface.[73] They showed that not only can they control the orientation of the cylinders with respect to the interface, but they could also supress the tip-to-tip assembly typically seen between cylindrical particles (at a flat interface), in favour of side to side-to-side assembly. Later in Chapter 4, we theoretically study a similar system, where instead we use a cylindrical sessile drop to supress the typical side-to-side assembly of ellipsoids (at a flat interface) and other rod-like particles, in favour of tip-to-tip assembly.

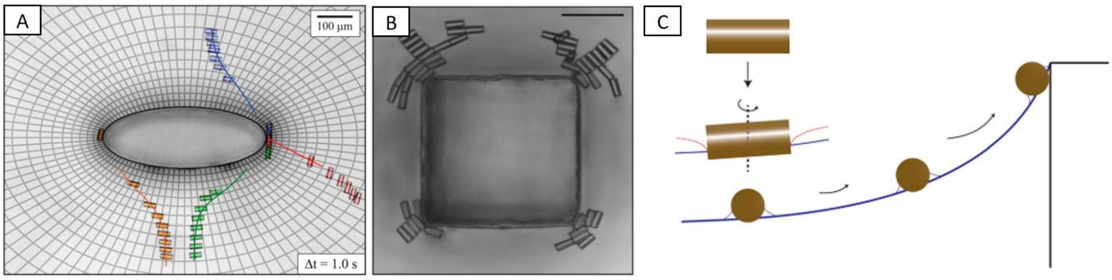

Figure 2.16: (A) Top view of particle migration near an elliptical micropost. Contours of constant s (ellipses) and t (hyperbolae) indicate the principal axes at each location. The trajectory of four particles (red, green, blue, and orange), are tracked as they assemble at the micropost. Along each trajectory, particles align with their major axes tangent to contours of constant s. (B) Particle assembly near a square micropost where complex structures form near the corners of the micropost. (C) Schematic illustrating particle rotation and migration. Left to right, the particle rotates to orient its saddle-like contact line on the saddle-like host interface. Thereafter, the particle migrates to minimise the difference between the curvature of the particle-induced deformation and that of the host interface.[17]

Cavallaro et al, also exploited the nature of curved interfaces to act as external fields orientating and directing the self-assembly of cylindrical particles. In Figure 2.16, Cavallaro et al assemble cylindrical particles at curved interfaces created by using microposts with elliptical (Figure 2.16A) and square (Figure 2.16B) profiles by pinning the interface to the top of the micropost. They found that the cylindrical particles would first orientate themselves so that the rise axis aligned with the interfaces principal rise axis with positive curvature and then migrate along curvature gradients to regions of high deviatoric curvature (Figure 2.16C). In both examples in Figure 2.16 we see that the cylinders migrate to the tips or corners of the microposts and assemble into a tip-to-tip configuration. More specifically in Figure 2.16B we see that the cylinders assemble into tip-to-tip configurations whilst following the curvature of the interface, creating curved assemblies of cylinders. As more cylinders are added, some assemble in a side-to-side orientation based upon their starting position and availability of space in the regions of high deviatoric curvature.

Cavallaro et al, additionally derived an expression for the energy of a capillary quadrupole on a curved interface given by

$$E(\boldsymbol{X}, \phi_p) \cong -\pi \gamma H_c r_c^2 D(\boldsymbol{X}) \cos(2[\phi_p - \phi(\boldsymbol{X})]) \tag{2.20}$$

where $D(\boldsymbol{X})$ is the deviatoric curvature tensor at the position vector of the particle $\boldsymbol{X}$, ϕ_p defines the orientation of the principal rise axes of the particle with respect to the lab-frame x-axis, and $\phi(\boldsymbol{X})$ defines the orientation of the principal axis of the interface with positive curvature at position $\boldsymbol{X}$ with respect to the lab frame x-axis. The energy in Equation (2.20) is minimised at regions of high deviatoric curvature, where the particles rise axis ϕ_p aligns with the interface rise axis $\phi(\boldsymbol{X})$. Therefore, the curved interface not only provides a capillary force driving particles to regions of high deviatoric curvature, but also a capillary torque aligning the particles rise axis with the interface's positive principal axis. In fact, for the work produced by Cavallaro et al, the interfaces are minimal surface or near minimal surfaces ($\kappa_1 \cong -\kappa_2$) and therefore equation (2.20) can be written in terms of just one curvature $\kappa(\boldsymbol{X})$ as

$$E(\boldsymbol{X}, \phi_p) \cong -\pi\gamma\kappa(\boldsymbol{X})H_c r_c^2 \cos(2[\phi_p - \phi(\boldsymbol{X})]) \tag{2.21}$$

Furthermore, Cavallaro et al used equation (2.21) to calculate the trajectories in Figure 2.16, as in this regime, the particles have negligible inertia, and therefore the particles translational and rotational velocities are proportional to the gradient of energy with respect to $\boldsymbol{X}$ and ϕ respectively. In Chapter 4 and Chapter 5 we consider the orientation and position of anisotropic particles absorbed at a curved cylindrical interface, i.e., where $\kappa(\boldsymbol{X}) = const$.

Chapter 3 Simulation Techniques

In this chapter we outline the simulation methods in which we use throughout the thesis to generate our results. For static energy calculations, we utilise an open-source software called Surface Evolver, this interactive program specialises in modelling liquid surfaces subject to various forces and constraints. For self-assembly simulations of many particles, we use Monte Carlo simulations to allow the system to explore phase space with a weighting dictated by the rules of statistical physics.

3.1 Surface Evolver

Surface Evolver is a finite element method which minimises the area (and therefore energy) of a deformable interface subject to forces and constraints. The interface is modeled as a mesh of triangles to approximate the geometry of the interface, and the denser the mesh, the more accurate the approximation. At each of the mesh's vertices on a free surface, Surface Evolver displaces the point in 3D space using the steepest decent method to reduce the energy, ultimately approaching the surface with minimum energy.

In the case of a simple interface the energy is proportional to the area and is calculated using

$$E = \gamma \sum_{F=0}^{F=f} \frac{1}{2} |(\boldsymbol{F}_B - \boldsymbol{F}_A) \times (\boldsymbol{F}_C - \boldsymbol{F}_A)| \tag{3.1}$$

where $\boldsymbol{F}_A, \boldsymbol{F}_B, \boldsymbol{F}_C$ are the three position vectors for the vertices that define a triangular facet F and therefore the total energy contribution is the sum over all these facets. To reach the minimum energy surface, the vertices of the mesh must be moved to reduce the overall area of the surface. To achieve this Surface Evolver evolves the surface using a gradient decent algorithm similar to

$$\boldsymbol{V}_{n+1} = \boldsymbol{V}_n - R\boldsymbol{\nabla}E(\boldsymbol{V}_n) \tag{3.2}$$

where $\boldsymbol{V}_{n+1}$, $\boldsymbol{V}_n$ are the new, and current positions of all the vertices that make up the mesh respectively, $\boldsymbol{\nabla}E(\boldsymbol{V}_n)$ is the gradient of the energy as a function of all the vertices, and R is the learning rate, a parameter that defines how far to move in configurational energy space. The choice of R is critical in obtaining effective simulations that reach energy minima, as if R is too large the system will jump over global and local minima and struggle to converge. On the other hand, if R is too small, convergence takes a long time and is susceptible to getting trapped in local minima, rather than the global minima. Surface Evolver calculates a learning rate R for each gradient decent step by halving or doubling the current R until an energy minimum is bracketed, at which point quadratic interpolation is used to calculate the best learning rate.[74]

A Surface Evolver script can be broken down into two sections, at the top of the file we give information about the geometry and constraints of the system, and in the bottom of the file (referred to as the read section) we define a protocol for energy minimisation. Additionally, in the read section we may tweak parameters to evolve the model and perform external commands such as writing data to another file. We will discuss both these sections in turn with an example script (given in Appendix 1) for a spherical particle adsorbed at a flat liquid interface.

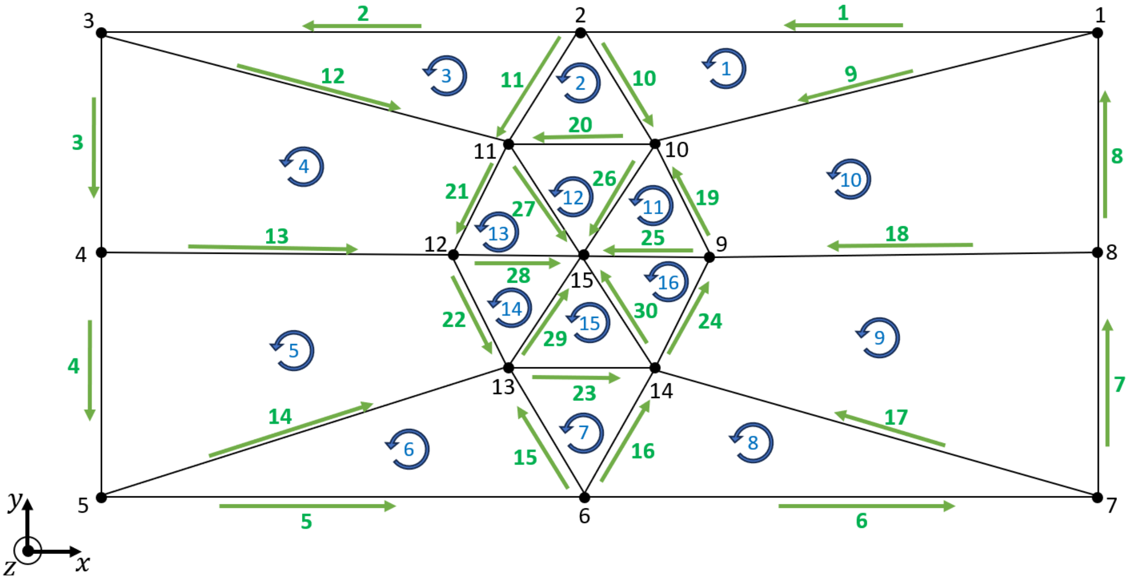

Figure 3.1: Top-down view of initial geometry for the Surface Evolver script given in Appendix 1. Black dots and corresponding black numbers represent the vertices, green arrows (representing direction) and corresponding numbers are the edges, and blue looped arrows (right hand rule definition) and corresponding numbers represent the faces.

To start a Surface Evolver script, we must first define the geometry of the interface or interfaces. We do this by creating vertices (black dots in Figure 3.1) in 3D space by specifying the x, y, z co-ordinates. These vertices are then joined by edges (green lines in Figure 3.1) by specifying a start and end vertex, which gives these edges an inherent direction. We then specify the facets of the interface (blue circular arrows in Figure 3.1) making sure that the surface normal (as given by the right hand rule) points out of the interface by following three or more edges (it is important to make sure that the tip of one arrow meets the tail of the next). We can then define a body, which is a collection of facets and allows control over forces or conserved quantities associated with volume.

Once we have created our geometry, we need to allow Surface Evolver to distinguish between the deformable interface and the rigid body for the particle. We do this by applying a constraint to the vertices, edges and faces corresponding to the particle, requiring all these points to lie on the surface of the sphere, i.e.,

$$f(x, y, z) = x^2 + y^2 + z^2 = r^2 \tag{3.3}$$

where r is the radius of the sphere defined as rad in the script in Appendix 1 using the parameter declaration. There are two ways to declare variables in Surface Evolver, either as a 'parameter' or using the '#define' prompt. Parameters are fixed throughout the simulation but can be manually changed at run time, but the '#define' declarator updates throughout the simulation but cannot be manually changed at run time.

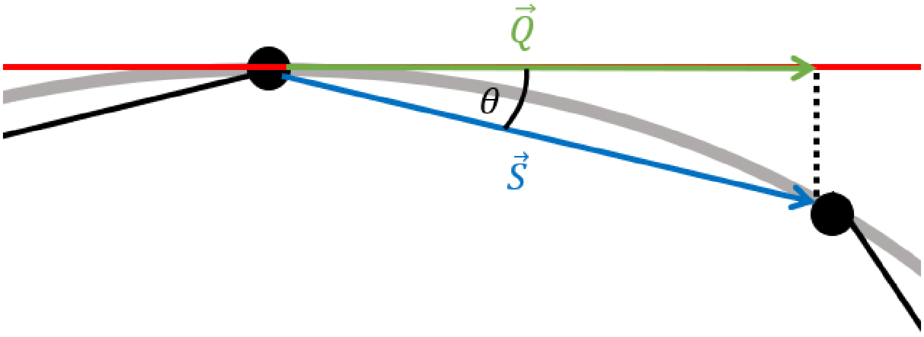

Figure 3.2: Schematic depicting the components of the gap energy, including the constraint (grey), the edge vector $\vec{S}$ (blue), the tangent plane to the constraint of the vertex at the tail of $\vec{S}$ (red), and the projection of $\vec{S}$ to the tangent plane $\vec{Q}$(green).

Additional arguments can be added to constraints for example in Appendix 1 we declare the Sphere constraint as being convex. This adds an associated energy called the gap energy with associated user defined gap constant 'k'. The gap energy E_{Gap} is defined as

$$E_{Gap} = \frac{k|\vec{S} \times \vec{Q}|}{6} \tag{3.4}$$

where $\vec{S}$ is the edge vector and $\vec{Q}$ is the projection of $\vec{S}$ onto the tangent plane of constraint (equation (3.3)) at the tail vertex of $\vec{S}$, see Figure 3.2. Without the gap energy, during minimisation Surface Evolver is incentivised to move vertices closer together as this minimises area but increases the distance between edges and the constraint, which ultimately leads to a worse approximation of the constraint.[74] The grouping of vertices in this way increases the angle between, and magnitude of $\vec{S}$ and $\vec{Q}$ causing a large gap energy; therefore by adding the gap energy this promotes an even distribution of vertices.

We now have a deformable interface with a solid spherical particle adsorbed to it. However, if the simulation is used as it currently is, the edges of the simulation would collapse towards the centre to minimise interfacial energy. To avoid this, we apply other constraints to those vertices and edges that lie on the interface parameter. This constraint requires us to fix the x or y, co-ordinates of each edge of the simulation (depending on which edge we are pinning). Importantly we do not fix the z position as we need to allow the interface to change its equilibrium height to minimise the interfacial energy; this is equivalent to allowing the particle to adjust its height relative to the liquid interface.

We can also add additional properties to the particle that contribute to the interfacial energy of the system, such as contact angle θ_w. The contact angle for the system given by the Young's equation, equation (2.1) and Surface Evolver will return the correct contact angle provided we apply the correct interfacial tensions in the system. However, in equation (2.1), the contact angle is determined by three different interfacial tensions which creates some redundancy, i.e., we can achieve the same contact angle using different combinations of interfacial tensions. For our system, we choose to only simulate one of the particle-fluid interfaces, in this case the particle-oil interface (top), and neglect interfacial energy arising from the particle-water interface (i.e., $\gamma_{pw} = 0$). We can also work in reduced units for the surface tensions, i.e., $\gamma_{ow} = 1$, which allows us to rewrite Young's equation (equation (2.1)) as $\cos\theta_w = \frac{\gamma_{po}-0}{1}$ therefore $\gamma_{po} = \cos\theta_w$. By default, interfaces in Surface Evolver are already set to have an interfacial tension of 1, so all we need to do is make sure that every vertex, edge and face that is either on (or on the boundary) of the particle is set to have interfacial tension of $\cos\theta_w$.

The interface at the boundaries of the simulation by default have an effective contact angle of $90°$ with the simulation box wall. This does not however, imply that the edges of the interface have identical z values, but instead the simulation is reflected across the boundary. This can be very useful when looking at interactions between particles in mirror symmetric configurations, as we are only required to simulate one half of the interaction. We utilise these reflecting boundary conditions extensively throughout this thesis in Chapter 4, Chapter 5 and Chapter 7, as it allows the simulation domain to be halved, leading to much lower computational requirements. It's also possible to instead represent the boundaries of the simulation as periodic boundaries which we will cover more in Chapter 8, where we use periodic boundaries to calculate the interfacial energy of a lattice cell containing one or two particles.

Up to now, we have covered the top section of the datafile responsible for the definitions of geometry and quantities. The bottom section of the datafile or read section is responsible for evolving the simulation through interfacial refinement and gradient decent through the energy landscape.

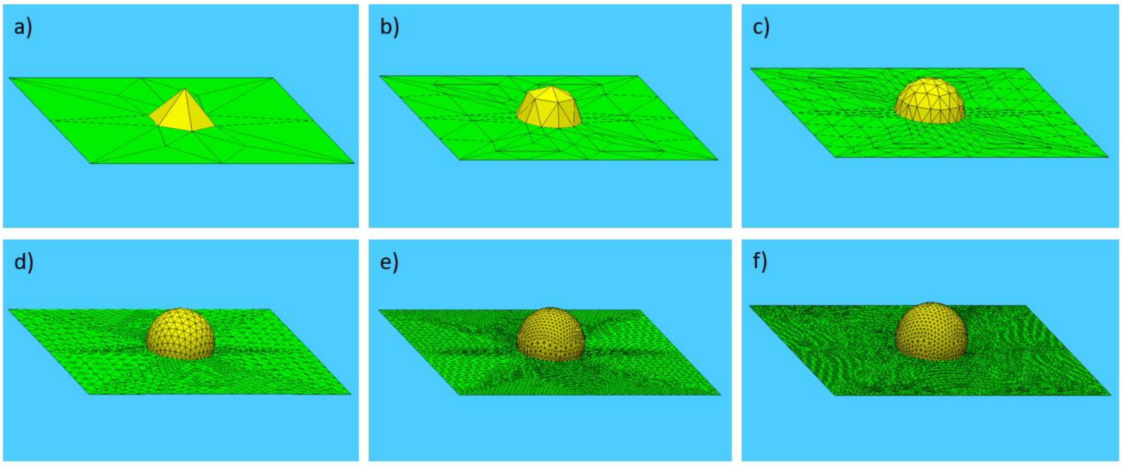

Figure 3.3: System evolution for a rigid spherical particle (yellow) with $\theta_w = 70°$ at a flat deformable interface (green). (a) Initial starting geometry as specified by the Surface Evolver script. (b-d) Refinement of the mesh at different stages. (e) Part way through the energy minimisation. (f) Final result.

The geometry we have defined in the top section of the datafile is typically a very coarse representation of our surface with very minimal features (Figure 3.3a). To more accurately capture the geometry of our surface we can refine it (main command r). Refining bisects each edge by placing a vertex in the centre and connecting the new vertices to each other by new edges, an example of this can be seen in Figure 3.3a,b. Upon refinement we see that the interface now more closely resembles the surface we are attempting to model (sphere at a flat interface), and as we continue to refine the simulation, the particle becomes more spherical. However, because our initial geometry has triangular tessellations of varying size, as we continue to refine the mesh (Figure 3.3c) we find that there become regions that are made up of very thin or small area triangles. To help even out the mesh we can additionally apply an "equiangulation" step (main command 'u'), which attempts to make neighbouring facets have triangles of equal angles. This step checks to see if an edge (which is joining two facets), which is treated as the diagonal of the quadrilateral made up by two adjacent faces produces more equiangular triangles if the triangular mesh was instead created using the other diagonal of the quadrilateral. Additionally, we can also apply a vertex averaging step (main command 'V'), which moves vertices to a new position based upon area-weighted average of the centre of mass of adjacent faces. In the example script given in Appendix 1 we package all these steps, along with a minimum length for refinement (to stop the mesh getting too small) into a function called 'groom' and use this to refine the surface.

Refining the surface alone, however, does not take into consideration any energy contributions, and therefore will not reach equilibrium. To traverse the energy landscape, we perform a step down the energy gradient (main command ‘g’), which calculates the gradient of total energy at each vertex and moves them one step in the opposite direction.[74] Typically, a Surface Evolver simulation requires hundreds if not thousands of these gradient decent steps, but performing all of these at once can lead to surface instabilities as the triangular mesh can get stretched if our initial geometry is far away from equilibrium. In practice this means defining a minimisation procedure (user defined ‘run’ in Appendix 1) in the bottom section of the datafile to be used at runtime.

However, using gradient decent alone to evolve the surface down the energy gradient can take a long time, especially when there are many vertices. To speed up this process we can apply a Newton-Raphson method to the gradient to get the surface to converge quickly (main command ‘Hessian_seek’). This uses a second order Taylor expansion to model the energy of the surface at a new position based upon a small perturbation and then solves for the direction of perturbation that makes the energy gradient zero and then performs a line search along this direction to find the minimum. Essentially this is like the gradient decent, except this uses the second order derivatives (Hessian) rather than the first order derivatives.[74] The downside to using this, however, is that for a surface far away from a minimum the second order approximation is not valid, and the direction of the move may not be towards a minimum, so we must use this technique in combination with the gradient decent in order to achieve quick convergence. Note: in the script in Appendix 1 before we perform a ‘Hessian_seek’ we set the gap constant ‘k’ to 0 as this energy does not have a Hessian calculation.

There is no one size fits all when it comes to the energy minimisation procedure, and in general different geometries require their own energy minimisation procedure to balance the speed and effectiveness of the minimisation. The Surface Evolver simulations are deterministic and therefore running two identical simulations will produce the same results, for this reason it is important when drawing comparisons between simulations to use the same minimisation procedure where possible.

We now look to use our simulation to study some equilibrium properties of the system, for example the change in the height of the spherical particle relative to the interface as a function of contact angle, or equivalently and more conveniently, the height of the interface relative to the spherical particle. We know that based upon topic discussed in Chapter 2.1, the interface should remain flat, but to satisfy the constant contact angle condition, the height at which the sphere intersects the interface changes. In our simulation the particle position is fixed, but the interface can move to satisfy the condition imposed by constant contact angle, specifically the interface should move by $-r\cos\theta_w$ where in the simulation we choose to use $r = 1$.

θ_w (degrees)	Δh_I (Surface Evolver)	$-\cos\theta_w$	%deviation
70	-0.3408	-0.3420	-0.35%
80	-0.1723	-0.1736	-0.75%
90	0.0018	0	-
100	0.1757	0.1736	1.21%
110	0.3447	0.3420	0.79%

Table 3.1: Change in interfacial height of the liquid interface at the contact line (Δh_I) calculated using Surface Evolver and theoretical change in interfacial height $-\cos\theta_w$ as a function of contact angle θ_w, and %deviation from the theoretical value.

In Table 3.1 we show the average z value of vertices on the contact line of the simulation Δh_I compared to the predicted value and the percentage deviation. We see that the percentage deviation is around 1% using this minimisation scheme, these deviations arise partly because even though in our minimisation procedure we switch to using quadratic approximations for our edges (main command M 2) it is still only an approximation for a sphere, and partly because the minimisation procedure doesn't quite reach the minimum energy state. It is also interesting to note that the Surface Evolver simulations underpredict the change in height for contact angles less than $90°$, and overpredicts the change in height for contact angles greater than $90°$. This is likely due to our choice of particle surface we model (i.e., the top surface), as for contact angles less than $90°$ the interface moves down and we simulate most of the particle's surface, whereas for greater than $90°$ we simulate the minority surface.

The simulation we have discussed above is centred around the particle reference frame which can be useful for many applications. However, it is often more intuitive to work in the lab frame, e.g., when rotating an asymmetric particle or working at curved interfaces. To change our reference frame, we first need to fix the edges of our interface to lie at z = 0, which can be done by adding an additional constraint to the edges of the simulation boundary.

Now the interface is constrained to z = 0, but currently the particle is also in a fixed position. For the simulation to reach a physical equilibrium, we need to allow the height of the particle to be minimised during the minimisation procedure. To do this we create a new parameter which represents the height of the particles centre of mass and declare this parameter as an optimising parameter by unfixing the parameter as part of our minimisation procedure. Optimising parameters are parameters that will also be subject to our minimisation procedure, i.e., an additional dimension in parameter space to perform the gradient decent upon. Whilst we can declare the optimising parameter at the start of the simulation, it is often better to allow the surface to refine and evolve a little bit first. Additionally, we can also control how much the parameter is optimised with respect to the rest of the surface as a form of impedance matching with the optional pscale value.

We now must attach the particle centre of mass parameter with the constraint that governs the ridged particle body. In general, we do this by defining a particle reference frame and calculating the particle centred co-ordinates using reference frame transformations (which we will cover in more detail in Chapter 4) and using these co-ordinates to define the constraint. However, in our case as we only are translating the particle vertically, we can encode this directly into the constraint by subtracting the height of the particles centre of mass from the z values on the surface of the sphere.

θ_w (degrees)	Δh_P (Surface Evolver)	$\cos\theta_w$	%deviation
70	0.3405	0.3420	-0.44%
80	0.1728	0.1736	-0.46%
90	0.0002	0	-
100	-0.1725	-0.1736	-0.63%
110	-0.3411	-0.3420	-0.26%

Table 3.2: Change in particle centre of mass (Δh_P) calculated using Surface Evolver and theoretical change in centre of mass $\cos\theta_w$ as a function of contact angle θ_w, and %deviation from the theoretical value.

We can then perform the same experiment looking instead at the change in particle centre of mass Δh_p with respect to contact angle. In Table 3.2 we show the change in height of the centre of mass of the particle Δh_p compared to the theoretical value $r\cos\theta_w$ where $r = 1$, and the percentage deviation from the theoretical value. We see that we obtain similar results to the fixed particle simulations, except in almost all cases Surface Evolver under predicts the change in height, and the percentage deviation is less than 1%.

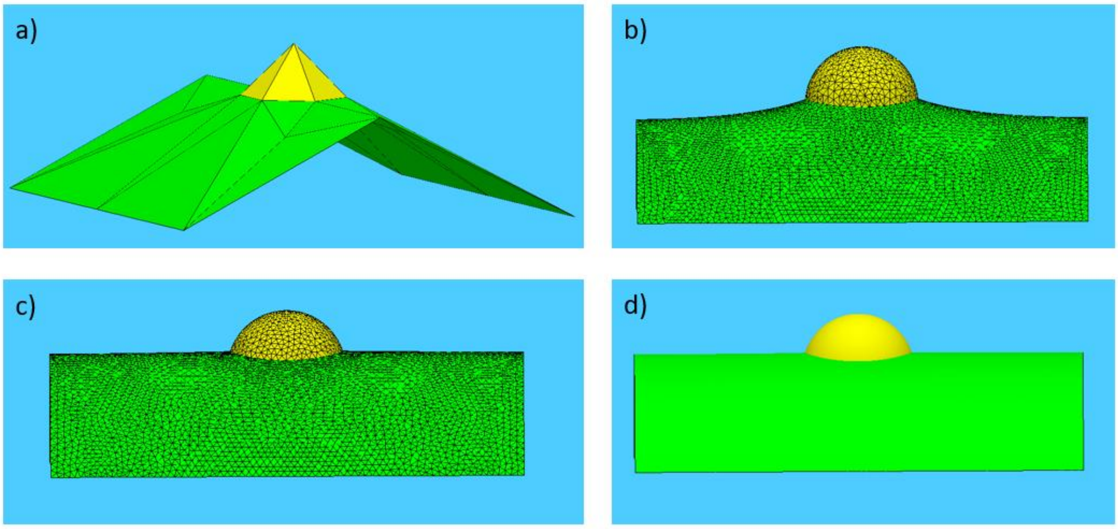

Figure 3.4: Surface Evolver simulations for a spherical particle with contact angle $110°$ at a curved interface of height 2. a) Initial geometry, b) refining and gradient decent before optimisation of the height of the centre of mass of the particle, c) part way through the energy minimisation procedure, d) final surface.

Now we have a model for a fixed interface we can perform simulations where the interface itself is curved, for example a cylindrically curved interface which we will use extensively in Chapter 4 and Chapter 5. Firstly, we should update our geometry so that the initial starting configuration is as close as possible to where we think equilibrium will be. This requires first creating a parameter which controls the height of the cylindrical interface h, and removing the $z = 0$ constraints on the vertices and edges which will represent the curved sides of the cylindrical interface. We should also set those vertices initial z value, as well as the particles vertices and centre of mass optimising parameter to h. This leads to a starting geometry shown in Figure 3.4a that approximates a spherical particle adsorbed to a cylinder.

At this point however, the simulation would just collapse back to a flat interface if it were minimised because there is no force keeping the interface inflated. Recall back to equation (2.7) where we describe the Laplace pressure at a curved interface between two immiscible fluids. We can apply this pressure to the interface by first defining a body which in our case is every face in the simulation and applying a pressure equal to $\frac{1}{r_1} + \frac{1}{r_2}$ where r_1 and r_2 are the principal radii of curvature. For a cylinder (like we discussed in Chapter 2.5) $r_2 = 0$ and $r_1 = R$ which is the radius of a circle related to h by

$$R = \frac{h^2 + \left(\frac{W}{2}\right)^2}{2h} \tag{3.5}$$

where W is the width of the simulation along the direction of the curved edge.

The simulation is now set up with all the necessary forces and constraints to model the interface correctly, and by evolving the surface we see in Figure 3.4b-d that the curved interface is stable because of the applied Laplace pressure. Figure 3.4b shows the evolution of the curved interface simulation before allowing the height of the particle to be an optimising parameter, and Figure 3.4c shows that after the optimising parameter is unfixed, the particle quickly moves to minimise interfacial distortion. Figure 3.4d shows the final state of the simulation.

3.2 Monte Carlo Simulation

Whilst Surface Evolver allows us to study equilibrium properties using a quasi-static approximation, it doesn't allow us to study our system in a dynamic way to so if it is able to reach the minimum energy configurations that Surface Evolver predicts. To do this we study systems of hundreds of particles using a Monte Carlo Metropolis method, which is a way to explore the phase space of a many body system in a way that obeys a probability distribution derived from Statistical Physics (in our case the Boltzmann distribution), i.e., an efficient simulation method for sampling the equilibrium distribution of system configurations.

All our simulations are performed in the canonical ensemble (NVT) where the number of particles N, the total volume V, and the temperature T are fixed. The canonical partition function Q describes the statistical properties of the system in thermodynamic equilibrium which for N identical particles is calculated by

$$Q = c \iint \exp\left(-\frac{H(\boldsymbol{p}^N, \boldsymbol{r}^N)}{k_B T}\right) d\boldsymbol{p}^N d\boldsymbol{r}^N \tag{3.6}$$

where c is a constant of proportionality (which we omit the explicit calculation of in order to simplify our discussion, and as we shall see later is not relevant for this discussion), $\boldsymbol{p}^N$ represents the momentum vector for all N particles, $\boldsymbol{r}^N$ represents the position vector for all N particles, and $H(\boldsymbol{p}^N, \boldsymbol{r}^N)$ represents the Hamiltonian that corresponds to the total energy of the system. The Hamiltonian can be broken down into $H = K + V$ where K is the kinetic energy of the system and V is the potential energy of the system. Under the assumption that the potential energy is not dependent on the momentum of the particles (which is almost always the case), the double integral in equation (3.6) can be separated into

$$Q = c \int \exp\left(-\frac{K(\boldsymbol{p}^N)}{k_B T}\right) d\boldsymbol{p}^N \int \exp\left(-\frac{V(\boldsymbol{r}^N)}{k_B T}\right) d\boldsymbol{r}^N \tag{3.7}$$

Since the kinetic energy is quadratic in the particle momenta, the integration over the momentum can be carried out analytically and absorbed into c, and hence, kinetic information cannot usually be explicitly extracted from Monte Carlo simulations. However, as we shall show later, Monte Carlo simulations can be used to generate kinetic simulations with the addition of three fundamental conditions. The difficult part of evaluating Q is evaluating the configurational integral over all DN particle position variables where D is the number of spatial dimensions.[75,76] We note here that this only applies to isotropic interactions, if the interactions are angularly dependent there will be up to $\frac{D^2(D-1)N}{2}$ variables, for example in Chapter 7 and Chapter 8 we consider a 2D system with angularly dependant interaction potentials, leading to a total of $3N$ variables.

We are not necessarily interested in explicit evaluation of the configurational integral itself, but instead we interested in average properties of the system, for example the average potential $\langle V(\boldsymbol{r}^N)\rangle$, which can be calculated by

$$\langle V(\boldsymbol{r}^N)\rangle = \frac{\int V(\boldsymbol{r}^N)\exp\left(-\frac{V(\boldsymbol{r}^N)}{k_BT}\right)d\boldsymbol{r}^N}{\int \exp\left(-\frac{V(\boldsymbol{r}^N)}{k_BT}\right)d\boldsymbol{r}^N} \tag{3.8}$$

where the constant term c is cancelled. We could now attempt to evaluate this integral but even a coarse integration method over the DN- dimensions would be a massive number of calculations. The key insight that was realised when developing the metropolis algorithm is that many of the configurations contributed very little to the integral, and a better way to approximate the integral is to only generate configurations that make a large contribution.[76] This method of only generating important configurations is also referred to as importance sampling and is the basic premise behind the Monte Carlo Metropolis method. Typically, states with high probability P will contribute greatly to the integral, and therefore, by moving to configurations which make a large contribution, we eventually end up in configurations that have high probability, i.e., low free energy states caused by self-assembly.

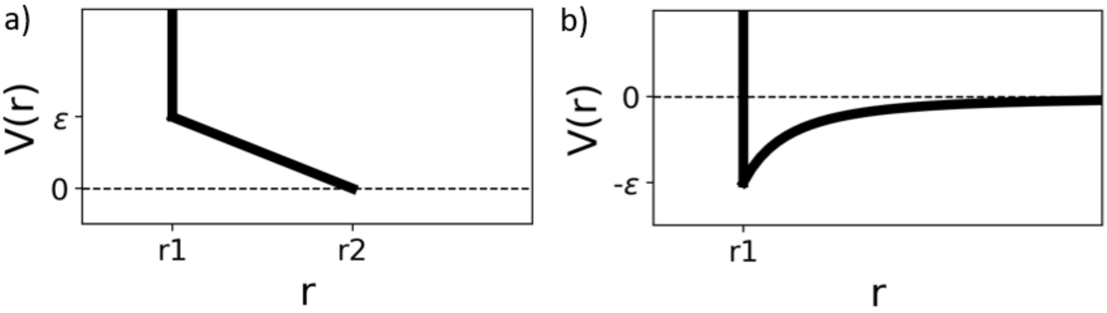

Figure 3.5: Example plots of pair-wise potential $V(r)$ as a function of the interparticle separation r. a) is a repulsive piecewise short-ranged potential where $V(r < r_1) = \infty$ (overlapping particles),

$V(r_1 < r < r_2) = \varepsilon \frac{r - r_2}{r_1 - r_2}$, and $V(r > r_2) = 0$ (short ranged). b) is an attractive long-ranged piecewise potential where $V(r < r_1) = \infty$ (overlapping particles), and $V(r > r_1) = -\varepsilon \left(\frac{r_1}{r}\right)^2$ (long-ranged).

Now that we have discussed why the Monte Carlo Metropolis method is useful for our purposes of obtaining minimum free energy states, let us now discuss the key quantity in equation (3.8), the interaction potential $V(\boldsymbol{r}^N)$. To find the equilibrium states that maximise the integral in equation (3.8), we need to find some way of measuring the potential of the DN position variables. To simplify our task, we assume that the potential is pairwise additive, i.e., the potential for the whole system can be approximated by a sum over all the pair interactions between particles $V(\boldsymbol{r}^N) = \sum_{i \neq j}^{N} V(\boldsymbol{r}_i, \boldsymbol{r}_j)$.

In Figure 3.5 we look at two examples of pair interaction potentials which only depend on the centre-to-centre distance between two isotropic particles (2D circular particles, or 3D spheres). In Figure 3.5a, we show an example of a two length-scale interaction potential which has no interaction between particles that are far apart, and some repulsive distance dependant potential when particles are close to each other. At first sight, this might look like a strange potential for achieving self-assembly as the system actively wants to avoid being close to one and other, but as we shall see later in Chapter 6 the system gives rise to a whole variety of interesting assemblies when compressed. In Figure 3.5b we show an example of an attractive interaction potential that has a finite value for greater than particle contact so is long ranged. The interaction potentials are defined by both their shape (potential profile) and there well depth ε. Comparing the well depth ε with the thermal energy of a system ($k_B T$) can immediately give us insights into the equilibrium structure at that finite temperature. For example, if $k_B T \gg \varepsilon$ then any order induced by the potential will be destroyed by thermal fluctuations, mimicking a ‘hot’ system and leading to disorder. For systems where $k_B T \ll \varepsilon$, the system evolves slowly, causes irreversible assemblies, and is very dependent on its initial starting configuration like a ‘cold’ system. To achieve good mixing, reasonable computation times, and self-assembly, we need to work in a regime that isn’t too ‘hot’ or ‘cold’ but is somewhere in between. To capture the influence of temperature and well depth we define a normalised temperature T^* such that $T^* = \frac{k_B T}{\varepsilon}$, which allows us to couple the potential and the temperature together simplifying our system parameters.

When initialising the simulation, particles need to be placed inside the simulation box without overlapping each other, an easy way to ensure this is to arrange the particles in a regular lattice. In situations where the concentration of particles is low, a square or cubic lattice will suffice. In contrast, when simulating high density systems, it is better to use a hexagonal lattice as this configuration maximises the interparticle distance for a given particle concentration, allowing higher initial concentrations to be simulated. For the 2D colloidal systems studied in this thesis, we measure the concentration of the system in terms of the area fraction η, which is the ratio of particle area (πr^2 for spherical particles) to simulation area ($L_x L_y$ where L_x and L_y are the length of the simulation box in the x and y directions respectively), which with hexagonal packing can go up to $\eta_0 = 0.9069$. For non-spherical particles (e.g., the ellipsoid particles we study in Chapter 7), we use the area the particle sweeps out when performing a full rotation about its centre as a 'pseudo particle area' and ensure that the 'pseudo area fraction' does not exceed η_0 so that the system remains in the dilute regime. After the initialisation of the simulation, the system is disordered to remove any bias from the initial configuration by performing many Monte Carlo moves at high normalised temperature ($T^* \gg 1$).

The basics of the Monte Carlo move starts by selecting a particle at random and performing a trial move which can be translational, rotational, or both. For example, a trial translational move in three dimensions consists of updating the location of the particle according to

$$\begin{aligned} x_n &= x_o + (2X_1 - 1)d_{Max} \\ y_n &= y_o + (2X_2 - 1)d_{Max} \end{aligned} \tag{3.9}$$

where the subscript (n and o) on the position variables x, y represent the new or old position respectively, X is a random number between 0 and 1 ($X \sim U([0,1])$) (the subscript denotes different random numbers), and d_{Max} is the maximum displacement along a cartesian axis. Here the $(2X - 1)$ ensures that both positive and negative displacements are equally likely to ensure the condition of detailed balance is met. Detailed balance requires the attempt probability of going from the old state to the new state ($P(o \to n)$) to be equal to that of going from the new state to the old state ($P(n \to o)$), and obeying detail balance guarantees non-biased simulations.

Once the trial move has been performed, we then calculate the change in potential energy from its previous state. If the energy of the system has decreased, we accept the move, however, if the system energy increases, we accept the move based upon the Boltzmann distribution. Specifically, we accept a move based upon the probability $P = \exp\left(-\frac{\bar{V}(n)-\bar{V}(o)}{T^*}\right)$, where $\bar{V}(o)$ and $\bar{V}(n)$ represent the normalised potential, e.g., $\bar{V}(o) = \frac{V(o)}{\varepsilon}$. To decide within the simulation if on a given move we accept the new position, we check to see if a random number is less than the probability, i.e., $X < P$. We can see here that if the change in energy is very large $P \to 0$, and the move will have a high chance of being rejected, and if the normalised temperature T^* is very high $P \to 1$ and any non-overlapping moves will almost always be accepted (this is why after initialisation we can create a system with a random distribution of particles using a high T^*). This then completes a single move, and typically when we talk about Monte Carlo moves, we refer to an average of one attempted move per particle, i.e., N single Monte Carlo moves attempted.

The choice over parameters d_{Max} and t_{Max} is also important to efficiently reach an equilibrium state. If they are too large, then any attempted move will likely end up in an unfavourable state, increasing the probability of rejecting the move, and if it is too small, the change in energy will be small so the probability the move will be accepted is high, but the system will explore phase space very slowly. Instead, we start with reasonable guesses for the values of these parameters and update their values as the system evolves to achieve a certain target percentage for moves that are accepted. For hard-core interactions, where overlapping of particles leads to rejection of the Monte Carlo move, it is believed that the optimum acceptance percentage for efficient exploration of phase space is closer to 20% though many simulation studies use 50%.[77] In our simulations we use a target acceptance percentage of 30%. To achieve this target, every few hundred Monte Carlo moves we check to see how many attempts were successful and increase the value of the parameters by 5% if the acceptance percentage is too high or reduce the value of the parameters by 5% if they are too low. For simulations of very dilute systems, sometimes d_{Max} can increase to be larger than the simulation box size, so it is useful as a fail-safe to set an upper bound to d_{Max} and t_{Max} to avoid this from happening.

Typically, simulations consist of a few hundred to a few thousand particles due to limitation of computation resources. The number of particles is still very far away from the thermodynamic limit, and we need to consider how particles interact with the boundary of the simulation box to minimise finite size effects to observe bulk behaviour. For example, we could reject any move that places a particle outside of the simulation domain, but a hard wall represents a very strong perturbation to the system so that we must go to a very large number of particles for the simulation to approximate bulk behaviour well. To reduce finite size effects, minimize boundary effects, and reduce the number of particles needed for bulk behaviour, we implement periodic boundary conditions. Periodic boundary conditions handle particles leaving the simulation box by making the particle re-appear on the opposite side (keeping N constant), this is also equivalent to our simulation being effectively a unit cell in a larger scale simulation. For example, a particle leaving the simulation via the right-hand cell wall means a new particle will enter from the left-hand cell wall with an equal y value and an x value calculated by

$$x_{|n|} = x_n - L_x \left\lfloor \frac{x_n}{L_x} \right\rfloor \tag{3.10}$$

where $x_{|n|}$ is the new x coordinate of the particle after it has been translated, and $\lfloor\ \rfloor$ is the floor function (rounding down).

The periodic boundaries also effect interactions across the boundary. For example, if a particle is close to one of the edges after a move, the particles at the opposite side of the simulation box have a 'mirror' particle (one that is in the neighbouring unit cell) that is much closer to the newly moved particle, which dramatically changes the interaction energy. To calculate the smallest distance between two particles (Δx_{Min}) we use the minimum image convention, which for example can be calculated for the x coordinate by

$$\Delta x_{Min} = \frac{\Delta x}{|\Delta x|}\left(\Delta x - L_x \left\lfloor \frac{2|\Delta x|}{L_x} \right\rfloor\right) \tag{3.11}$$

where Δx is the signed distance from the newly moved particle to the interacting particle x_i in the same simulation cell ($x_i - x_{|n|}$). Equation (3.11) ensures that $|\Delta x_{Min}| \leq \frac{L_x}{2}$ and calculates which direction the minimum image particle is in relative to the newly moved particle. For example, if Δx_{Min} is negative, the interacting particle is to the left of the newly moved particle. This is important for particles where their interaction potential is not isotropic, but instead angularly dependant e.g., quadrupolar capillary interactions from ellipsoids adsorbed to a flat liquid interface, which we will cover in Chapter 7.

When dealing with potentials which have a non-zero interaction potential at large Δr_{Min} (minimum image separation in D-dimensional space), i.e., long-range interactions, the computation time of potential energy calculations per particle scales with N, even though the number of nearest neighbours which contribute the most energy stays the same. To reduce computation time, we could consider only interactions with particles within a certain cutoff radius r_c of a given particle. The cutoff radius is only applicable to systems where the interaction potential decays more rapidly than the increasing number of particles. For example, for a 2D system, the number of additional particles increases linearly with increasing r, and therefore even potentials which decrease as r^{-2} can have a non-negligible contribution to the total potential energy for some r_c values. Fortunately, in Chapter 6 we consider a short-range finite potential which has its own natural cutoff length, and in Chapter 7 and Chapter 8 we consider a long-range interaction potential which decays very rapidly with r^{-4} to a first approximation, which allows r_c to be relatively small.

As discussed earlier the kinetic part of the partition function can be analytically computed and therefore when we perform our Monte Carlo simulations, we usually cannot obtain kinetic information. However, it has been shown in the literature that if additional criteria are satisfied, both static and dynamic properties of a system can be obtained using Monte Carlo simulations.[78] These criteria are: (1) a "dynamical hierarchy" of transition probabilities is created which also satisfy the detailed-balance criterion; (2) time increments upon successful events are calculated appropriately; and (3) the effective independence of various events comprising the system can be achieved.[78]

The first criteria require the creation a “dynamic hierarchy”, that is, a list of all possible transitions along with transition probability, ensuring that detail balance is obeyed for all transitions. A transition is then picked according to its probability and the list is then updated with all new transitions and transition probabilities and the process is repeated.[79] As discussed earlier, all Monte Carlo moves in the Metropolis scheme obey detailed balance. In addition, whilst we do not explicitly calculate the transition probability for possible Monte Carlo moves but displace particles at random up to a maximum range, all of our moves are physical, i.e., they involve small spatial or rotational displacements with no cluster or random high temperature moves. In this case, previous studies have shown that in the limit of small displacements, Metropolis Monte Carlo simulations are approximately equivalent to Brownian dynamic simulations which do include kinetic information.[80,81]

The second criteria require us to map a Monte Carlo step to some physical time interval. This mapping is physically related to the average transition rate of local moves in the system, which in turn can be calculated from the dynamic hierarchy discussed above.[79] For our Monte Carlo simulations, we are more interested in studying the kinetic pathways rather than the absolute times for different kinetic processes and therefore do not need to explicitly calculate the time interval for Monte Carlo moves.

Finally, by using a large enough system, the independence of events can be achieved because we consider systems where the range of interactions is small (see Chapters 6 -8) and the small step sizes we use in our simulations.[78] Specifically, the movement of particles only affects the local region around the particle and not Monte Carlo moves that happen elsewhere.

In summary, we believe that our Monte Carlo simulations satisfy all three criteria listed above, and therefore that it is possible to extract kinetic information about the systems we study from our simulations. In the rest this thesis, we will use both Surface Evolver and Monte Carlo simulations to study the self-assembly of both isotropic and anisotropic particles at liquid interfaces.

Chapter 4 Capillary Assembly of Anisotropic Particles at Cylindrical Fluid Interfaces – Floatation Regime

4.1 Introduction

In this Chapter, we study the self-assembly of anisotropic rod-shaped particles at a cylindrical interface formed by a sessile liquid drop. Specifically, using the finite element method Surface Evolver,[74] we study the assembly of single and multiple rods as a function of drop curvature and particle properties such as shape (ellipsoid, cylinder, spherocylinder), contact angle, aspect ratio and chemical heterogeneity (homogeneous and triblock patchy). The simple curved geometry of cylinders (constant finite curvature transverse to the cylinder, zero curvature along the cylinder) allows us to elucidate the interplay between interfacial curvature and particle properties in determining the configuration of single and multiple rods. Surprisingly, we find that, although the lateral dimension of the cylindrical drop is larger than the length of the rods in all cases studied, the curved interface allows us to effectively control the orientation of the rods so that they lie parallel, perpendicular or oblique, with respect to the cylindrical drop. In addition, by tuning particle properties to achieve parallel alignment of the rods, we show that the cylindrical drop geometry favours tip-to-tip assembly for two rods, not just for cylinders, but also for ellipsoids and triblock patchy rods. Finally, although there are no curvature gradients in the host interface that can be used to control particle position, we can still achieve some degree of spatial confinement of the rods transverse to the cylindrical drop by using the capillary repulsion from the pinned contact lines of the sessile drop.[82,83]

In other studies,[84–86] the assembly of $20-50$nm width nanorods into tip-to-tip configurations have been achieved by patterning a substrate with trenches with dimensions so that two rods may not assemble side to side and three rods in a tip-to-tip configuration will not assemble. The nanorods are then assembled into these trenches through the use of the "squeegee" method,[85] which relies on a combination of evaporation of a colloidal drop (which causes accumulation at the three phase contact line) and immersion forces to drive the particles into the trenches.[84,86] However, these methods require using electron beam lithography to pattern the substrates in order to achieve features in the $20-70$nm range, which requires the use of expensive specialist equipment. The method we propose in this Chapter relies on utilising the curvature of a liquid drop that is much larger than the dimensions of the nanorods to obtain tip-to-tip assembly. Not only does our method allow us to assemble rods that are much smaller (10nm width), but it also allows us to use photolithography to create a patterned substrate, providing a low-cost, high throughput method for assembling nanoscale particles.

4.2 Theoretical Methods

In this section, we describe the geometry and thermodynamics of the composite system consisting of rod-like particles adsorbed at a sessile cylindrical liquid drop and the Surface Evolver method used to study this system theoretically.

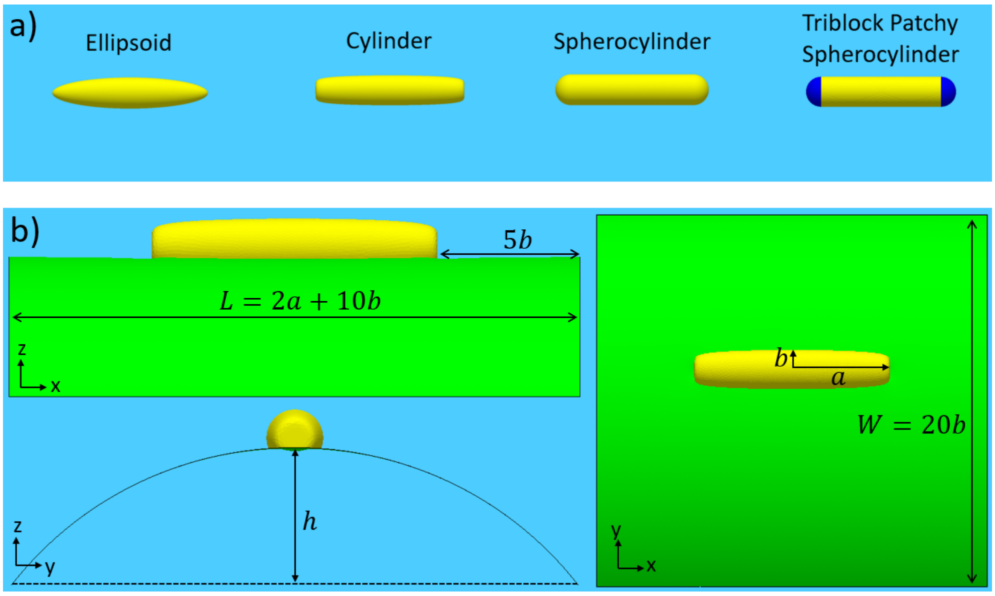

Figure 4.1: (a) Geometry of the simulated rod-like particles; (b) Geometry of a rod-like particle adsorbed at a cylindrical sessile drop.

For rod-like particles, we consider three different particle shapes, namely, ellipsoids, cylinders, and spherocylinders (Figure 4.1). For ellipsoids and cylinders, we use the super-ellipsoid equation[49,83]

$$\left(\frac{x'^{\,2}}{a^2}\right) + \left(\frac{y'^{\,2} + z'^{\,2}}{b^2}\right)^{\eta} = 1 \tag{4.1}$$

to define the particle shape, where x', y', z' are the Cartesian coordinates in the particle reference frame (see below in this section), a, b are the semi-major and semi-minor lengths of the rod, respectively, and η is a sharpness parameter that defines the sharpness of the super-ellipsoid edge. We use $\eta = 1$ for ellipsoids and $\eta = 4$ for cylinders (i.e., we consider cylinders with rounded edges; see Figure 4.1a). For spherocylinders, we use

$$f(x',y',z') = \begin{cases} y'^{\,2} + z'^{\,2} = b^2, & |x'| < a - b \\ \left(x' - \dfrac{x'}{|x'|}(a-b)\right)^2 + y'^2 + z'^2 = b^2, & |x'| \geq a - b \end{cases} \tag{4.2}$$

Note that in all cases, the particle aspect ratio is a/b.

In terms of surface chemistry, we consider ellipsoids, cylinders, and spherocylinders with homogeneous surface chemistry, as well as spherocylinders with triblock patchy surface chemistry (Figure 4.1a).

For the cylindrical sessile drop, we consider a drop with a rectangular base of width $W = 20b$ and length $L = 2a + 10b$. For convenience, we refer to the top and bottom fluid phases as oil and water, respectively (i.e., the fluid making up the drop is water), though our model is in fact general and applies to any fluid−fluid interface. Assuming the origin of the lab frame in Cartesian coordinates to be at the centre of the base with z perpendicular to the base and x, y parallel and perpendicular to the long axis of the cylinder, respectively, we assume that the contact lines of the cylindrical drop at $y = \pm 10b$ are pinned and apply reflecting boundary conditions for the interface at $x = \pm(a + 5b)$ (see Figure 4.1b). Note that the width of the drop is greater than the particle length for all cases studied in this work ($W > 2a$), and we have chosen L to be large enough so that for a particle positioned at the centre of the drop ($x, y = 0$), the effect of the reflecting boundary conditions is small and the particle is effectively isolated. We fix the curvature of the cylindrical drop by applying a Laplace pressure of γ_{ow}/R across the interface, where γ_{ow} is the oil−water interfacial tension and R is the radius of the cylinder in the absence of any adsorbed particles. Although the behaviour of adsorbed rods is controlled by the curvature of the cylindrical drop,[18,73] it is easier to control and measure the height of the drop experimentally. For convenience, we therefore parameterize the curvature of the drop using the drop height in the absence of adsorbed particles, h, which is related to R and W according to $R = h/2 + W^2/8h$. Note that we consider drop heights $h > b$, so that the substrate does not play a critical role in determining particle behaviour, that is, the adsorbed particles are in the flotation rather than the immersion regime.[14,87]

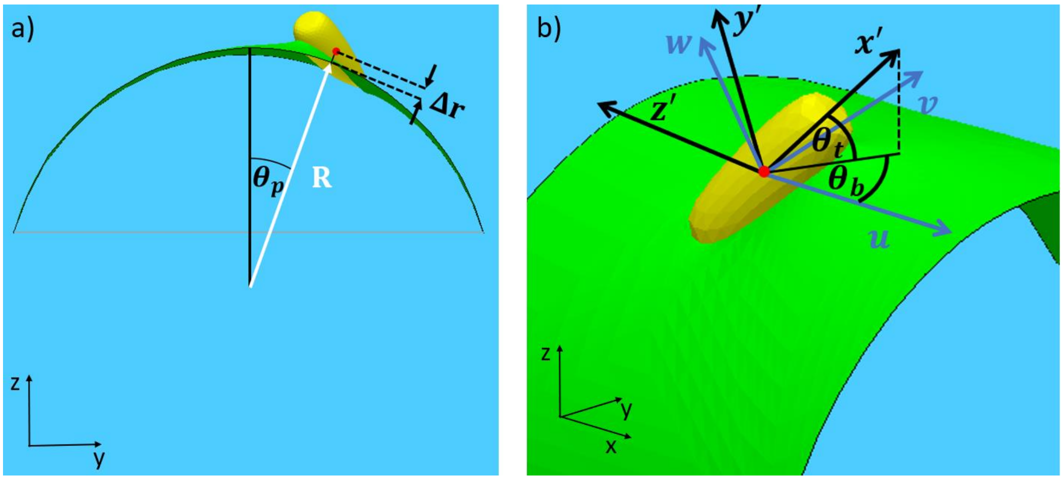

Figure 4.2: Degrees of freedom of a rod adsorbed at the cylindrical interface; the red dot represents the centre of mass of the rod. (a) Cylindrical polar coordinates used to specify the position of the rod; (b)

Bond angle θ_b and tilt angle θ_t (defined with respect to the interfacial frame u, v, w) used to specify the orientation of the rod.

In order to specify the centre-of-mass position of the adsorbed particle, we use cylindrical polar coordinates, where the position transverse to the cylindrical drop is given by the polar angle θ_p, the radial distance from the long axis of the cylindrical drop is given by $r_p = R + \Delta r$, and the position along the long axis is given by x_p (see Figure 4.2a).

In order to specify the orientation of the adsorbed particle, we first define a Cartesian coordinate system in the interfacial frame (u, v, w), with the origin coinciding with the particle centre and u, v, w pointing in the directions of change for the cylindrical coordinates x, θ, r, respectively (see Figure 4.2a); the interfacial frame coordinates are related to the lab frame coordinates (x, y, z) by

$$\begin{pmatrix} u \\ v \\ w \end{pmatrix} = \begin{pmatrix} 1 & 0 & 0 \\ 0 & \cos\theta_p & -\sin\theta_p \\ 0 & \sin\theta_p & \cos\theta_p \end{pmatrix} \begin{pmatrix} x - x_p \\ y - y_p \\ z - z_p \end{pmatrix} \tag{4.3}$$

where $y_p = r_p \sin\theta_p$, $z_p = r_p \cos\theta_p$ are the centre-of-mass coordinates of the particle in the lab frame. Since we are considering axisymmetric rod-like particles, the orientation of the particle can be specified relative to (u, v, w) using two angles that we call the bond angle θ_b and the tilt angle θ_t, as defined in Figure 4.2b.

Finally, we can define a Cartesian coordinate system in the particle frame (x', y', z'), with x' aligned along the semi-major axis of the particle and y', z' aligned along the semi-minor axes of the particle. These coordinates are related to the interfacial frame (u, v, w) coordinates by the following rotational transformations[88]

$$\begin{pmatrix} x' \\ y' \\ z' \end{pmatrix} = \begin{pmatrix} \cos\theta_t & 0 & -\sin\theta_t \\ 0 & 1 & 0 \\ \sin\theta_t & 0 & \cos\theta_t \end{pmatrix} \begin{pmatrix} \cos\theta_b & \sin\theta_b & 0 \\ -\sin\theta_b & \cos\theta_b & 0 \\ 0 & 0 & 1 \end{pmatrix} \begin{pmatrix} u \\ v \\ w \end{pmatrix} \tag{4.4}$$

For micron or sub-micron particles, which is the focus of this Chapter, gravity is negligible, and the energy of the composite system is primarily due to the interfacial energy, which is given by equation (2.2)[53,89] Again, we have neglected line tension contributions in equation (2.2) because these are sub-dominant compared to interfacial tensions for the particles that we are considering, where $a, b > 10$ nm.[41] For a given particle configuration, the energy given by equation (2.5) is calculated using Surface Evolver.[74] We work with length and energy units such that $b = 1$, $\gamma_{ow} = 1$ and we use a variable triangular mesh edge length between $0.02b$ to $0.1b$ and quadratic edges, to capture the shape of the fluid-fluid interface and three-phase contact line more accurately.

In this Chapter, we only consider particles with aspect ratio $a/b \geq 2.5$, where the equilibrium tilt angle at a flat interface is $\theta_t = 0°$, i.e., particles are in the 'side-on' state.[53] For the curved cylindrical interfaces and representative rod-shaped particles we are considering in this Chapter, we have checked that this result remains true, independent of the bond angle θ_b; we have therefore set $\theta_t = 0^{\circ}$ in all simulations. In a typical simulation, we specify the position variables θ_p, x_p, and the bond angle θ_b of the rod-like particles but allow the radial coordinate Δr to equilibrate for a given particle configuration.

4.3 Results and Discussion

4.3.1 Single Rods at a Flat Interface

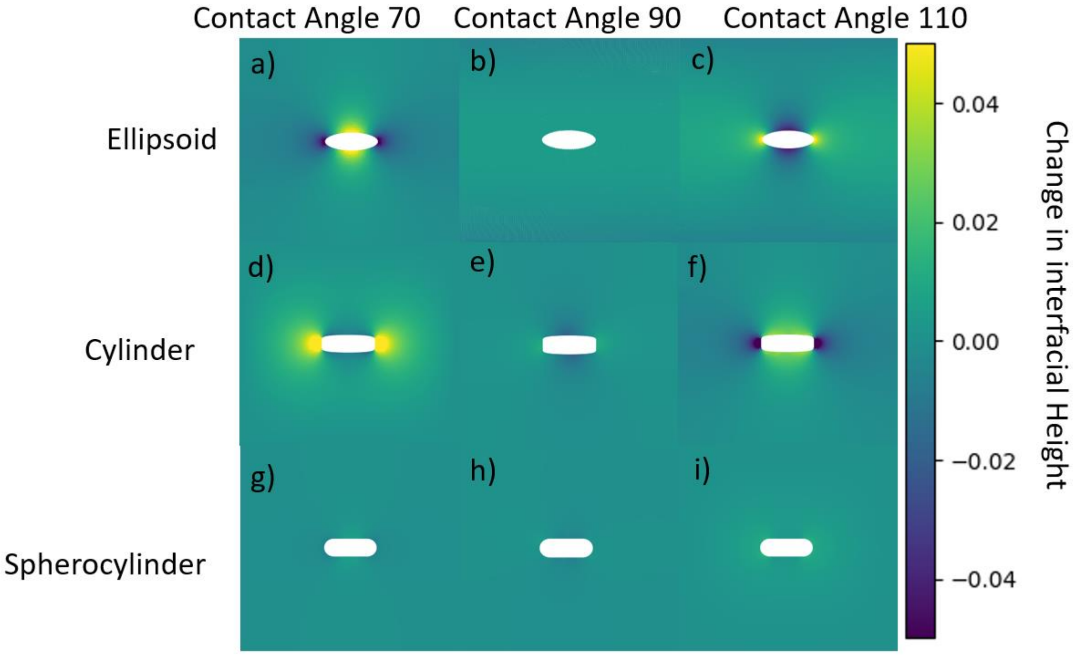

Figure 4.3: Contour plot of meniscus deformation around rod-like particles with aspect ratio 2.5 and homogeneous surface chemistry, adsorbed at a flat fluid-fluid interface for different particle shapes and contact angles.

To establish a baseline for our simulations of particles at cylindrical interfaces, we first analyse the behaviour of single rods with homogenous surface chemistry at a flat interface (we consider the behaviour of patchy rods in Section 4.3.5 below). In Figure 4.3 we show contour plots of the meniscus deformation for particles with aspect ratio $a/b = 2.5$, for different particle shapes (ellipsoids, cylinders and spherocylinders) and contact angles ($\theta_w = 70°, 90°, 110°$). As expected, no meniscus deformations are observed for spherocylinders or neutrally wetting ellipsoids or cylinders ($\theta_w = 90°$). On the other hand, for non-neutrally wetting ellipsoids and cylinders, we see quadrupolar meniscus deformations, in agreement with the literature.[50–52] Good agreement with the literature is also obtained for the direction of the contact line curvature, relative to the long axis of the particle. For ellipsoids, the quadrupolar rise axis lies parallel and perpendicular to the long axis, for hydrophobic ($\theta_w =$

$110°$) and hydrophilic ($\theta_w = 70°$) particles, respectively. In contrast, for cylinders the quadrupolar rise axis lies parallel and perpendicular to the long axis, for hydrophilic and hydrophobic particles respectively. This means that the contact line curvature can be controlled by tuning particle shape and wettability, providing an effective way to control the orientation of rod-like particles at a cylindrical drop.

4.3.2 Single Rods at a Cylindrical Interface – Particle Orientation

Having studied the behaviour of single rods with homogenous surface chemistry at a flat interface, we next analyse their behaviour at a cylindrical interface. Specifically, in this section we study the impact of particle shape, contact angle, aspect ratio and droplet curvature on particle orientation, as specified by the bond angle θ_b. As discussed in Section 4.2, since we are considering particles with aspect ratio ≥ 2.5, we set the tilt angle to $\theta_t = 0^{\circ}$.[53] In addition, since we are interested in the effect of interfacial curvature on the orientation of isolated rods, we set $\theta_p = 0^{\circ}$, $x_p = 0$ (i.e., particle at apex of cylindrical drop, in the centre of simulation box) to minimise the impact of the pinned contact line and reflecting boundary conditions of the cylindrical drop. We then calculate the energy of the system as a function of bond angle from $\theta_b = 0^{\circ}$ to 90° in increments of $1°$, noting that the energy only needs to be calculated within this range due to the symmetry of the energy with respect to θ_b.

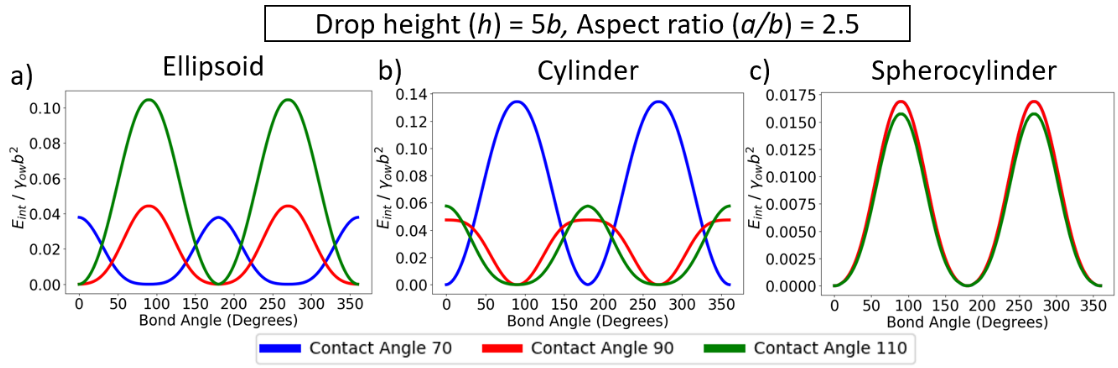

Figure 4.4: Interfacial energy as a function of bond angle for relatively short rods with different contact angles, adsorbed at a cylindrical interface, for: (a) ellipsoids; (b) cylinders; (c) spherocylinders. All rods have $\theta_p = 0°$, $x_p = 0$, $\theta_t = 0°$. Note that in (c), the curve for $\theta_w = 70°$ is not visible as it lies underneath the curve for $\theta_w = 90°$.

We first discuss the effect of contact angle on the orientation of rods with different shapes for relatively short rods (aspect ratio $= 2.5$) and a cylindrical drop height $h = 5b$. In Figure 4.4a, we plot interfacial energy (relative to the minimum energy state) as a function of bond angle θ_b for ellipsoids with contact angles $\theta_w = 70°, 90°, 110°$. The equilibrium orientation of the ellipsoids (i.e., θ_b corresponding to the energy minimum) clearly depends on contact angle: for hydrophilic ellipsoids ($\theta_w = 70°$), the particles are aligned perpendicular to the cylindrical drop, i.e., $\theta_b = 90°$, whereas for hydrophobic ellipsoids ($\theta_w = 110°$) the particles are aligned parallel to the cylindrical drop, i.e., $\theta_b = 0°$. This result can be readily understood from the fact that, when particles with a capillary quadrupole are adsorbed at a curved interface, the particle will rotate to try to align its quadrupolar rise axis to the principal axis of curvature of the host interface (where the interface is concave up) to minimize the distortion to the host interface.[17,73] Since hydrophilic and hydrophobic ellipsoids have their rise axis perpendicular and parallel to the long axis, respectively (see Figure 4.3), but the principal axis of curvature for a cylindrical drop is parallel to its long axis, it is not surprising that hydrophilic ellipsoids align perpendicular to the cylindrical drop whereas hydrophobic ellipsoids align parallel to it.

We additionally found (Figure 4.4a) that neutrally wetting ellipsoids ($\theta_w = 90°$) preferentially align parallel to the cylindrical drop. Since these ellipsoids do not possess an intrinsic capillary quadrupole (see Figure 4.3), the primary driving force for such an alignment is not contact line curvature but shape anisotropy. Specifically, because of the curvature of the cylindrical interface, an anisotropic particle such as an ellipsoid removes a larger area of the energetically unfavourable oil-water interface when it is parallel, rather than perpendicular, to the cylindrical drop and therefore the parallel orientation has a lower energy. Shape anisotropy also has an impact on the orientational energy of the non-neutrally wetting ellipsoids (Figure 4.4a). For hydrophobic ellipsoids, where both contact line curvature and particle anisotropy favour parallel alignment, i.e., where the two effects are synergetic, both the depth and curvature of the energy minima (the latter being proportional to the ‘spring constant’ of the potential confining the rod to its equilibrium orientation) are greater compared to the case of hydrophilic ellipsoids, where contact line curvature favours perpendicular alignment but particle anisotropy favours parallel alignment, i.e., where the two effects are antagonistic.

In Figure 4.4b, we plotted the interfacial energy as a function of bond angle for cylinders with contact angles $\theta_w = 70°, 90°, 110°$. In this case, the dependence of particle orientation on contact angle is opposite to that for ellipsoids, with hydrophilic and hydrophobic cylinders aligning parallel and perpendicular to the cylindrical drop, respectively. This difference is not surprising because the orientation of the quadrupolar rise axis relative to the long axis of the particle is opposite for cylinders compared to ellipsoids for a given contact angle (see Figure 4.3). However, like ellipsoids, the depth and curvature of the energy minima are greater for cylinders in the parallel orientation, compared to those in the perpendicular orientation, due to the synergistic effect of contact line curvature and shape anisotropy. Unexpectedly, we see that neutrally wetting cylinders preferentially align perpendicular to the cylindrical drop. We believe that this counterintuitive result is due to the short cylinders considered here ($a/b = 2.5$) removing a larger area from the oil-water interface in the perpendicular orientation than in the parallel orientation; as discussed in this section below, for longer cylinders, particle anisotropy always favours the parallel orientation. Note that in Figure 4.4, the energy scale for the orientational energy is slightly larger for cylinders compared to ellipsoids and we attribute this difference to the larger amplitude for contact line undulations in cylinders compared to ellipsoids. For example, for the particles shown in Figure 4.3, the difference between maximum and minimum height of the contact line is approximately $0.15b$ for cylinders and $0.11b$ for ellipsoids.

In Figure 4.4c, we plot interfacial energy as a function of bond angle for spherocylinders with contact angles $\theta_w = 70°, 90°, 110°$. For all contact angles, spherocylinders are found to lie parallel to cylindrical drop. This is not surprising since spherocylinders do not possess an intrinsic capillary quadrupole (Figure 4.3) and particle orientation is therefore primarily determined by particle anisotropy, which favours the parallel orientation. We also note that the energy scale of the orientational energy for spherocylinders is almost one order of magnitude smaller than that for ellipsoids and cylinders. This effect is again due to spherocylinders not possessing an intrinsic capillary quadrupole, so that the only interfacial deformations are those induced by the curvature of the host interface, which are much weaker.

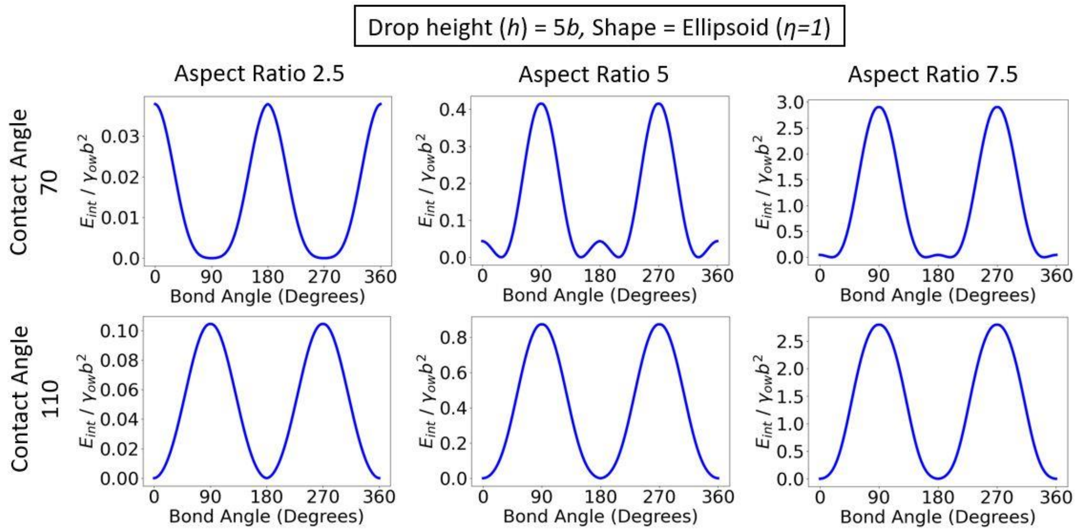

Figure 4.5: Interfacial energy as a function of bond angle for ellipsoids with different aspect ratios and contact angles, adsorbed at a cylindrical interface. All rods have $\theta_p = 0°$, $x_p = 0$, $\theta_t = 0°$.

Next, we study the effect of aspect ratio on the orientation for particles of different shapes and contact angles. In Figure 4.5 we plot the orientational energies for ellipsoids for a cylindrical drop of height $h = 5b$. When the contact line curvature favours parallel alignment ($\theta_w = 110°$), increasing the aspect ratio of the ellipsoids only leads to an increase in the energy scale of the potential well, but does not change the equilibrium orientation. This is as we would expect because the effect of particle anisotropy on particle orientation is synergistic to the effect of contact line curvature in this case.

However, when the contact line curvature favours perpendicular alignment ($\theta_w = 70°$), particle anisotropy is antagonistic to contact line curvature. As the aspect ratio of the ellipsoid is increased from $a/b = 2.5$ to 5 and 7.5, particle anisotropy simultaneously leads to the formation of high energy barriers at $\theta_b = 90°, 270°$ and suppresses the energy barrier due to contact line curvature at $\theta_b = 0°, 180°, 360°$. Intriguingly, the competition between particle anisotropy and contact line curvature means that the ellipsoid does not align either parallel or perpendicular in this case, but instead aligns obliquely to the long axis of the cylindrical drop, where the bond angle of the oblique orientation is determined by the length of the particle relative to the radius of curvature of the drop.

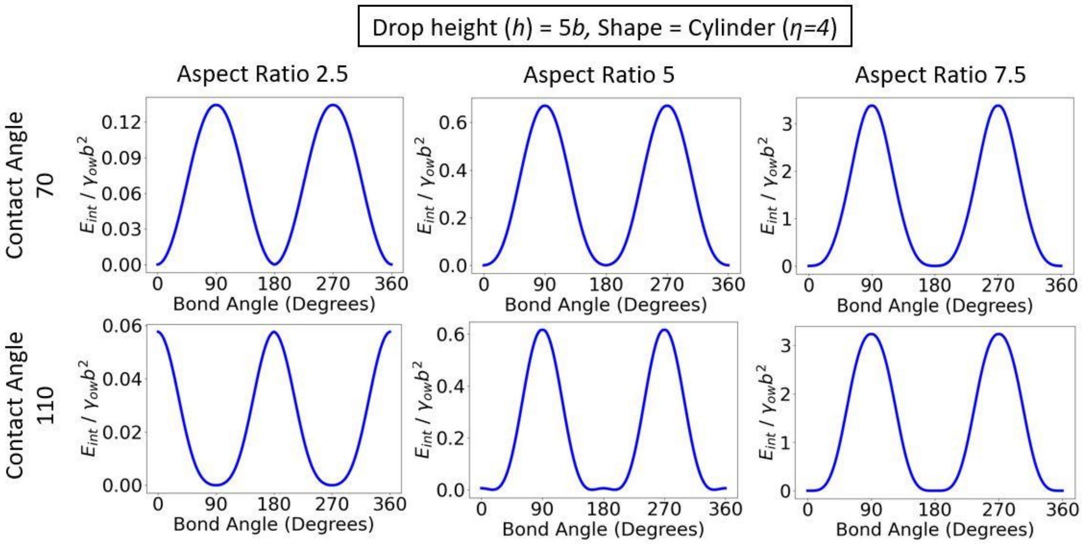

Figure 4.6: Interfacial energy as a function of bond angle for cylinders with different aspect ratios and contact angles, adsorbed at a cylindrical interface. All rods have $\theta_p = 0°$, $x_p = 0$, $\theta_t = 0°$.

For cylindrical particles (Figure 4.6), we see the same trends as those for ellipsoids, except that the parallel orientation is now observed for $\theta_w = 70°$ (where particle anisotropy and contact line curvature are synergistic), whereas the novel oblique orientation is observed for $\theta_w = 110°$ (where particle anisotropy and contact line curvature are antagonistic). Note that the effect of particle anisotropy is stronger for cylinders compared to ellipsoids, so that the energy barrier at $\theta_b = 0°, 180°, 360°$ is strongly suppressed for $a/b = 5$ and essentially disappears for $a/b = 7.5$.

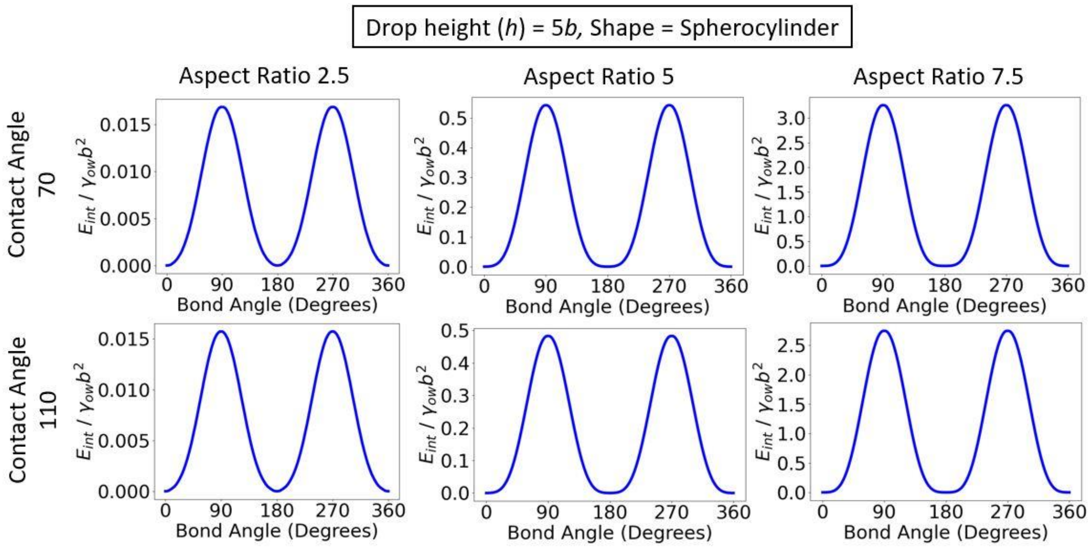

Figure 4.7: Interfacial energy as a function of bond angle for spherocylinders with different aspect ratios and contact angles, adsorbed at a cylindrical interface. All rods have $\theta_p = 0°$, $x_p = 0$, $\theta_t = 0°$.

For spherocylinders (Figure 4.7), which do not have an intrinsic capillary quadrupole so that contact line curvature essentially plays no role in determining particle orientation, we find that the particles are in the parallel orientation for both $\theta_w = 70°$ and $110°$ but the depth of the confining potential well increases with increasing particle aspect ratio.

It should be noted that the oblique orientations seen for ellipsoids and cylinders in Figure 4.5 and Figure 4.6 only arise when the particle is long enough relative to the radius of curvature of the host interface. For example, in Figure 4.5 the oblique orientation is observed for rods with aspect ratios $a/b = 5$ and 7.5, where $2a/R = 0.8, 1.2$, respectively, but not for particles with aspect ratio 2.5, where $2a/R = 0.4$. This explains why the oblique orientation was not observed in previous studies, for example in Lewandowski *et al.*[73] for cylindrical particles adsorbed at a plane-parabolic interface, where $2a/R = 6 \times 10^{-3}$.

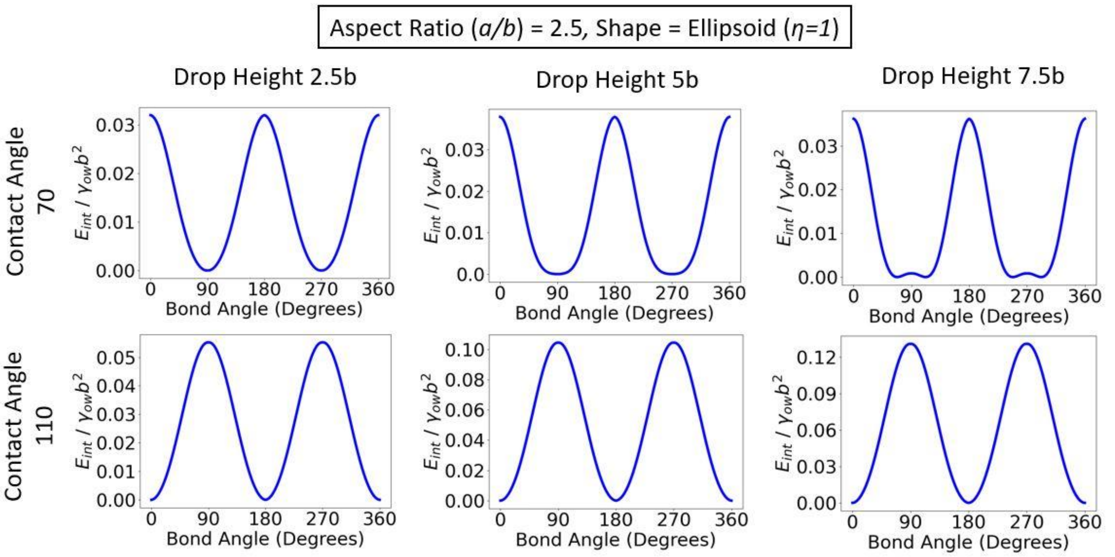

Figure 4.8: Interfacial energy as a function of bond angle for ellipsoids adsorbed at a cylindrical interface with different contact angles and drop heights at fixed W = 20b. All ellipsoids have $\theta_p = 0°$, $x_p = 0$, $\theta_t = 0°$.

Next, we study the effect of changing droplet curvature (parameterised by droplet height at fixed $W = 20b$) on the orientation of rod-shaped particles. For simplicity, we only present results for ellipsoids, but the same trends were observed for cylinders (results not shown). In Figure 4.8, we show the orientational energy for ellipsoids with aspect ratio $a/b = 2.5$ and contact angles $\theta_w = 70°$ (top row) and $\theta_w = 110°$ (bottom row) for cylinder drop heights $h = 2.5b, 5b, 7.5b$. For $\theta_w = 110°$, where parallel alignment of the ellipsoids is favoured (particle anisotropy and contact line curvature are synergistic), increasing interfacial curvature by increasing h leads to an increase in the depth of the potential well, but otherwise does not change the equilibrium orientation of the ellipsoid. On the other hand, for $\theta_w = 70°$, where perpendicular alignment of the ellipsoids is favoured (particle anisotropy and contact line curvature are antagonistic), a similar increase in the interfacial curvature causes an initial flattening of the minima at $\theta_b = 90°, 270°$ (for $h = 5b$), followed by emergence of a small energy barrier (for $h = 7.5b$), resulting in the novel oblique orientation of the ellipsoid that was also observed for hydrophilic ellipsoids in Figure 4.5.

In general we find that increasing drop height (and hence interfacial curvature) at fixed rod length (Figure 4.8) produces the same trend for the orientation of the rods as increasing rod length at a fixed interfacial curvature (Figure 4.5, Figure 4.6, and Figure 4.7). This result can be readily understood by recognising that, the competition between particle anisotropy and contact line curvature depends primarily on the ratio between particle length and interfacial radius of curvature so that increasing particle length is essentially equivalent to decreasing the radius of curvature (i.e., increasing curvature). However, for the parameter ranges explored in this Chapter, we find that changing particle aspect ratio (Figure 4.5) has a much bigger impact on orientational energy compared to changing droplet height (Figure 4.8).

Note that, even though the lateral dimension of the cylindrical drop is larger than the length of the rods in all cases studied above ($W > 2a$), the potential energy well confining the orientation of rods is very large. For example, for a hydrophobic ellipsoid with aspect ratio $a/b = 5$ and cylindrical height $h = 5b$, the potential energy well depth is $\Delta E_{int}/\gamma_{ow} b^2 \approx 0.8$ (Figure 4.5). For an oil-water interface with $\gamma_{ow} = 30$ mN/m, this translates into $\Delta E_{int} \approx 6 \times 10^6 kT$ for a micron-sized rod with $b = 1$ µm, and $\Delta E_{int} \approx 600kT$ for a nanorod with $b = 10$ nm. This result is consistent with what has been found by Lewandowski *et al.* who were able to control the orientation of a cylindrical microparticle using a curved interface which has radius of curvature much greater than the particle length.[73]

4.3.3 Single Rods at a Cylindrical Interface – Spatial Confinement

Having studied particle orientation in the previous section, in this section we study the impact of the cylindrical interface on the spatial confinement of rod-like particles. Although no curvature gradients are present in a cylindrical sessile drop, which could provide control over particle position,[17]spatial confinement of the rods transverse to the cylindrical drop can still be achieved due to steric repulsion from the substrate and capillary repulsion from the pinned contact lines.[82,83] Both effects will be considered in this section. We restrict our analysis to rods in the parallel alignment as this is the most favourable alignment toward achieving the tip-to-tip assembly considered in the next section.

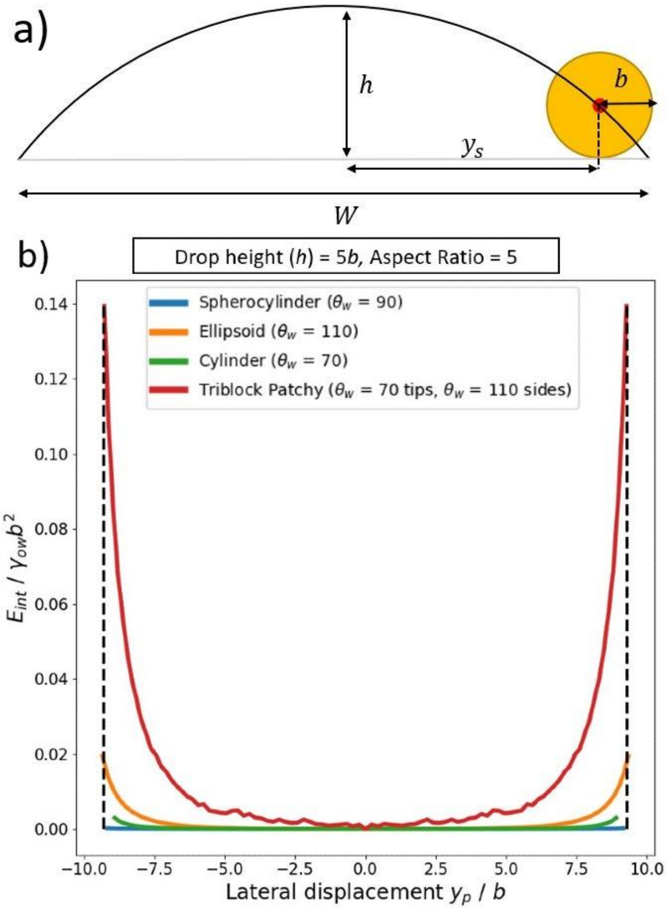

Figure 4.9: (a) Simplified model for calculating the maximum displacement of adsorbed rods lateral to a cylindrical drop, due to steric repulsion from the substrate. (b) Interfacial energy as a function of lateral displacement for adsorbed rods with different shapes and surface chemistry, which are aligned parallel to the cylindrical drop. The dashed black line indicates maximum lateral displacement allowed by steric repulsion with the substrate.

To estimate the spatial confinement due to steric repulsion from the substrate, we make the simplifying assumption that the fluid-fluid interface is the unperturbed cylindrical interface and that this interface goes through the centre of the rod. In this case, from simple geometry, the maximum displacement of the rod from the origin in the y direction, y_s, is given by (see Figure 4.9a)

$$y_s = \sqrt{R^2 - (R - h + b)^2} \tag{4.5}$$

Substituting R in terms of W and h from (3.5) into equation (4.5), we can rewrite equation (4.5) as

$$y_s = \frac{1}{2}\sqrt{(1 - b/h)(W^2 + 4bh)} \tag{4.6}$$

Note that in the limit where the short axis length of the rod $b \to 0$, we recover $y_s = W/2$ as expected. From equation (4.6), we find that y_s decreases as we reduce the drop height h, i.e., the rods become increasingly confined laterally, and indeed $y_s = 0$ for $h = b$. However, for the relatively large drop heights considered here, y_s is close to $W/2$, i.e., the degree of lateral confinement due to steric repulsion from the substrate is insignificant. This point is illustrated in Figure 4.9b for the case $h = 5b$, where $\pm y_s$ is represented by the vertical dashed lines.

Next, we consider the lateral confinement due to capillary repulsion from the pinned contact line of the sessile drop. This repulsion arises because the meniscus around the particle would like to deform because of the particle's contact line undulations, but this deformation is suppressed when the particle approaches the pinned contact line, causing the energy of the system to increase.[82,83] To calculate this effect, we set $\theta_t = 0°$, $x_p = 0$, $\theta_b = 0°$, and calculate the energy of the system as a function of the polar angle, from $\theta_p = 0^{\circ}$ to θ_{max}, in increments of 1°, where θ_{max} is approximately the polar angle corresponding to $y = W/2$. Note that we only need to calculate the energy for positive θ_p because the energy is symmetric about $\theta_p = 0°$.

In Figure 4.9b, we plot the energy of the system (relative to the energy at $\theta_p = 0°$) as a function of $y_p = R \sin \theta_p$, for ellipsoids with $\theta_w = 110°$, cylinders with $\theta_w = 70°$, and spherocylinders with $\theta_w = 90°$, where the contact angles have been chosen to ensure that the rods are in the parallel orientation (triblock patchy rods will be discussed in Section 4.3.5 below). All particles have an aspect ratio of $a/b = 5$ and the drop height is $h = 5b$. We see that all particles are repelled by the pinned contact line at $y = W/2$. The repulsion is strongest for the ellipsoidal particle because this shape has the largest contact line undulation at the sides (see Figure 4.3). The repulsion is smaller for the cylindrical particle because the contact line undulation at the side is smaller, but the repulsion is weakest for spherocylinders which do not have an intrinsic capillary quadrupole (see Figure 4.3).

However, our main conclusion from Figure 4.9b is that, for rod-shaped particles with homogeneous surface chemistry, the potential well around $y_p = 0$ is very flat so that the lateral spatial confinement due to capillary repulsion from the pinned contact lines is weak. For example, for ellipsoids with $b = 10$ nm, the range of y_p values for which $\Delta E_{int} < 3kT$ is $-8.4b \leq y_p \leq 8.4b$ ($3kT$ is a reasonable estimate for the point where the confining potential starts to become significant compared to thermal energy), which corresponds to 91% of $2y_s$, the maximum lateral spatial range available to the ellipsoid due steric repulsion by the substrate (i.e., the range between the dashed vertical lines in Figure 4.9). The spatial confinement for cylinders and spherocylinders with $b = 10$nm is even weaker, with $\Delta E_{int} < 3kT$ at $y_p = \pm y_s$. We therefore conclude that the lateral spatial confinement due to capillary repulsion from the pinned contact lines of the sessile drop is weak for rods with homogeneous surface chemistry.

4.3.4 Capillary interaction and self-assembly of rods at a cylindrical interface

Having considered the orientation and spatial confinement of single rods at a cylindrical interface in previous sections, we now consider the interaction and self-assembly of two rods at a cylindrical interface. We restrict our analysis to rods with parallel alignment and primarily consider the tip-to-tip assembly of such rods. However, we point out that it is also possible to use our method to orient the rods perpendicular to the cylindrical drop, which would favour side-to-side assembly.

For the sake of simplicity, we first consider the case where the long axes of the two parallel rods are aligned to each other, and they are both at the apex of the cylindrical drop, i.e., $\theta_b, \theta_p = 0°$; later in this section, we will consider the case where the rods are not aligned to each other. We also exploit the fact that the energy of one rod approaching the reflecting boundary of the simulation cell is equal to half the energy of a two-particle system where both rods are approaching each other. When calculating the tip-to-tip interaction between two rods, we therefore just need to consider a one-rod simulation where we vary the distance of the rod to the reflecting boundary. Note that when two rods in the tip-to-tip orientation are close to each other, they may induce a capillary dipole in each other so that θ_t is no longer zero. To check the size of this effect, we performed Surface Evolver simulations of two ellipsoids in a mirror symmetric configuration at the smallest surface-to-surface separation we studied and calculated the interfacial energy of the system as a function of the tilt angle of the rods θ_t. We found that the equilibrium tilt angle $\theta_t < 1°$, suggesting that this capillary polarization effect is very small. We therefore set $\theta_t = 0°$ for both interacting rods in our calculations.

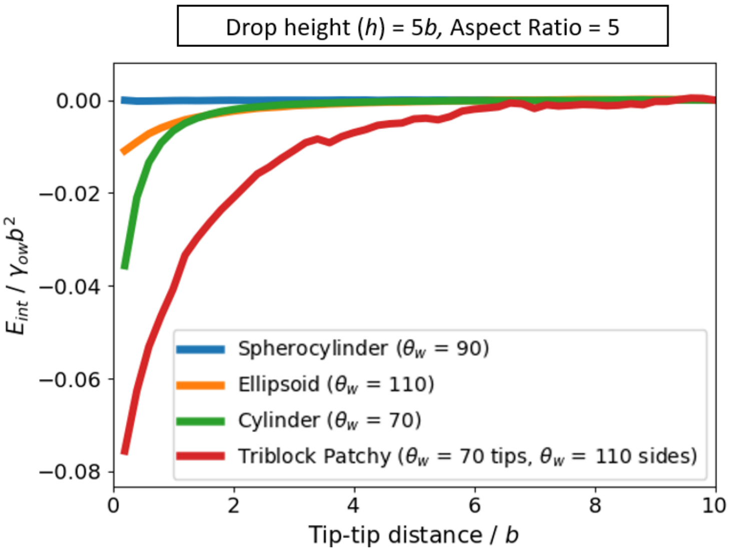

Figure 4.10: Tip-to-tip capillary interaction for adsorbed rods with different shape and surface chemistry, which are aligned parallel to the cylindrical drop.

In Figure 4.10, we plot the tip-to-tip interaction energy between two rods (i.e., energy relative to the energy of the two rods at maximum separation) as a function of the surface-to-surface separation between the two rods, for ellipsoids with $\theta_w = 110°$, cylinders with $\theta_w = 70°$, and spherocylinders with $\theta_w = 90°$ (triblock patchy rods will be discussed in Section 4.3.5 below). The contact angles have been chosen so that all rod shapes are in the parallel alignment since, as explained at the start of this section, we are primarily interested in the tip-to-tip assembly of rods. All particles have an aspect ratio of $a/b = 5$ and the drop height is $h = 5b$. We observe that tip-to-tip attraction is strongest for cylindrical particles and weakest for spherocylinders. These results are like what has been observed at flat interfaces[49] and is due to cylinders having the largest contact line undulation around their tips, compared to ellipsoids and spherocylinders (see Figure 4.3). Specifically, for nanoscale rods with $b = 10$ nm, at an oil-water interface with $\gamma_{ow} = 30 \times 10^{-3}$ N/m, the interaction energy for tip-to-tip contact is $25kT$ for cylinders, $8kT$ for ellipsoids and $0.05kT$ for spherocylinders. The capillary interaction for nanoscale cylinders and ellipsoids is therefore significant, whereas that for spherocylinders is negligible compared to thermal energy.

Note that, at a flat interface, ellipsoids tend to approach each other tip-to-tip initially, then ‘roll-over’ into the side-to-side configuration because of its lower energy (see Section 2.2).[49,52,90] However, for ellipsoids at a cylindrical interface, the reduction in capillary interaction energy when going from the tip-to-tip to the side-to-side configuration is generally much smaller than the increase in orientational energy incurred in making this transition. For example, for ellipsoids with aspect ratio $a/b = 3$, contact angle $\theta_w = 80°$ or $100°$, studied in Botto *et al.*,[49] the reduction in capillary interaction energy is $\approx 0.001\gamma_{ow}b^2$, whereas the increase in the orientational energy for a similar ellipsoid at a cylindrical interface in Figure 4.5

($a/b = 2.5, \theta_w = 110°$) is $\approx 0.1\gamma_{ow}b^2$. Therefore, for two ellipsoids aligned tip-to-tip at a cylindrical interface of high enough curvature, the roll-over into the side-to-side configuration is suppressed and the ellipsoids remain assembled tip-to-tip. A similar phenomenon has also been observed in Lewandowski *et al.*[73] for cylinders where for high enough curvatures of the host interface, the cylinders assemble side-to-side because the reorientation of the cylinders that would allow them to assemble tip-to-tip is suppressed.

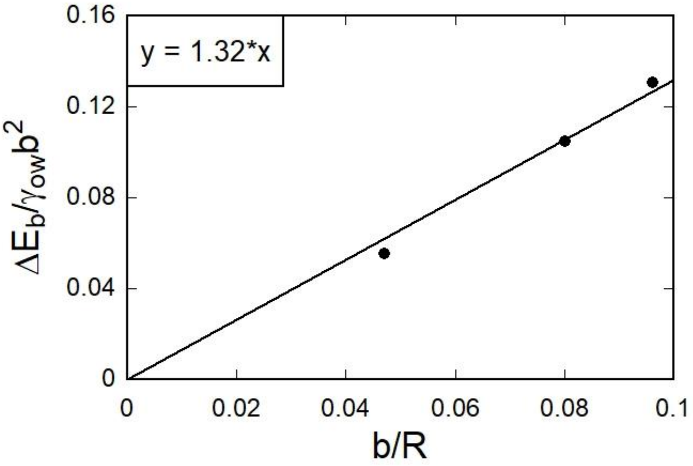

Figure 4.11: Energy barrier for the roll-over transition ΔE_b versus interfacial curvature $1/R$ for ellipsoids with aspect ratio $a/b = 2.5$, contact angle $\theta_w = 110°$ adsorbed at a cylindrical interface. The data points are calculated from the data in Figure S2, along with the limiting case 0,0 (i.e., at a flat interface there is no energy barrier) while the straight line is the best fit of the data to the scaling form $\Delta E_b = A/R$.

We can estimate the minimum cylindrical drop height (and hence interfacial curvature) required to suppress the roll-over transition by equating the energy barrier for the roll-over transition ΔE_b to the reduction in capillary energy achieved by this transition. We illustrate this point by considering ellipsoids with aspect ratio $a/b = 2.5$ and contact angle $\theta_w = 110°$, for the three data sets we have generated based on the rotational energy landscape for different drop heights (Figure S2, bottom row), and the limiting case at a flat interface (0,0). Using the data in Figure 4.8, we can calculate the energy barrier from $\Delta E_b = E_{int}(\theta_b = 90°) - E_{int}(\theta_b = 0°)$ and the radius of curvature of the cylinder from $R = (h^2 + w^2/4)/2h$. From the leading order multipole expansion of the interfacial energy, we expect $\Delta E_b = A/R$, where A is a prefactor that depends on the characteristics of the capillary quadrupole such as contact line radius and the amplitude of the contact line undulation.[17] By fitting this scaling form to the ΔE_b versus $1/R$ data in Figure 4.11, we find $A = 1.32\gamma_{ow}b^3$. As discussed in the previous paragraph, we estimate the reduction in the capillary energy achieved by the roll-over transition for this system to be $\approx 0.001\gamma_{ow}b^2$. By equating ΔE_b from the straight-line fit in Figure 4.11 to $0.001\gamma_{ow}b^2$, we find that the roll-over transition is suppressed for $b/R > 8 \times 10^{-4}$ which corresponds to $h > 0.04b$. Whilst we can obtain a more accurate linear fit by generating intermediate datasets, this condition is easily satisfied in the flotation regime $h > b$ we are considering in this chapter and therefore there is sufficient evidence for us to safely neglect the roll-over transition when studying the self-assembly of rod-like particles at a cylindrical interface.

Up to now, we have considered the capillary interaction between two parallel rods which are already aligned tip-to-tip. However, from our previous discussion we know that rods with homogeneous surface chemistry are only weakly confined transverse to the cylindrical drop. Therefore, the most usual case is in fact where the two interacting rods are not aligned initially. We now consider this more general case. Since the energy scale for rotating the rods away from their preferred parallel alignment is so high, we set $\theta_t,\ \theta_b = 0°$ for both particles. However, even with this restriction on particle configuration, a full analysis of the two-particle problem is very expensive in Surface Evolver as it would require us to calculate the capillary interaction for different lateral positions of one of the rods and different positions of the second rod relative to the first. To make the problem numerically tractable, we therefore fix the position of the first rod and study the trajectory of the second rod at different starting positions relative to the first one. Specifically, to obtain an upper bound estimate for the effect of non-alignment on self-assembly, we fix the position of the first rod to be close to the edge of the cylindrical drop (roughly one rod diameter away, along the interface, from the pinned contact line of the cylindrical drop).

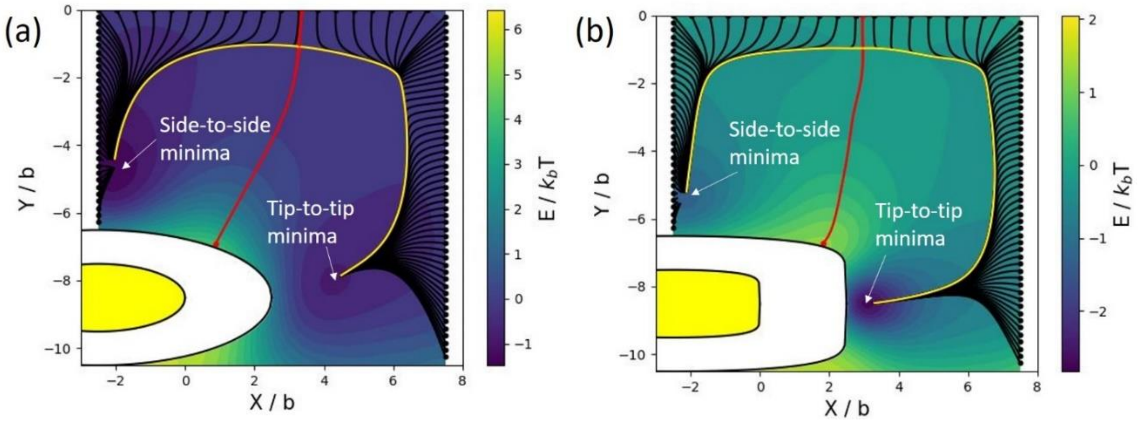

Figure 4.12: Capillary interaction energy of a two-particle system as a function of the position of the second particle relative to the first one, which is positioned at the edge of the cylindrical drop. The black lines are the trajectories of the second particle for different starting positions, the red curve is the separatrix that separates trajectories ending up in the tip-to-tip or side-to-side configurations, and the yellow lines are the dynamical attractors to which the trajectories converge at the later stages of their evolution. The energy landscape and trajectories are shown for: (a) ellipsoids with $a/b = 2.5$, $\theta_w = 110°$; (b) cylinders with $a/b = 2.5, \theta_w = 70°$. The shaded-out white region on the bottom left of each plot represents the region excluded to the second particle due to steric repulsion with the first particle (coloured yellow).

In Figure 4.12, we plot the interaction energy of the two-particle system (i.e., energy relative to the energy of the two rods at maximum separation) as a function of the position of the second particle, expressed in terms of the coordinates $X = x_p, Y = R\theta_p$, for ellipsoids with $a/b = 2.5, \theta_w = 110°$ (Figure 4.12a) and cylinders with $a/b = 2.5, \theta_w = 70°$ (Figure 4.12b) on a cylindrical drop with height $h = 5b$. The shaded-out region on the bottom left of each plot represents the region excluded to the second particle due to steric repulsion with the first one. Note that the energy landscape in Figure 4.12 was obtained by first calculating the energy for X, Y values on an approximately 30 x 30 grid. Since the capillary interaction between the rods is small, the resultant discrete energy landscape was quite noisy. Therefore, to obtain the full energy landscape for any X, Y, we use a radial basis function to interpolate the data with the Python package SciPy. Using the radial basis function allows us to use a smoothing parameter that makes the interpolation smoother by not insisting that it fits each discrete data point exactly. This procedure resulted in a smoother energy landscape, which we could use to calculate the trajectory of the second particle.

Assuming that the trajectory of the second particle follows paths of steepest descent in the interaction energy landscape,[91,92] we plot the trajectories of the second particle for different initial positions on the edge of a rectangular region around the first one (black lines in Figure 4.12). We see that, for initial positions closer to the tip of the first particle, the final state of the system is the tip-to-tip configuration, whereas for initial positions closer to the side of the first particle, the final state of the system is the side-to-side configuration. The red line shown in Figure 4.12 is the 'separatrix' which demarcates the boundary between two different types of trajectories;[92,93] all trajectories originating from points to the left of the separatrix will flow towards the side-to-side configuration but all trajectories originating from points to the right of the separatrix will flow towards the tip-to-tip configuration. Interestingly, trajectories on either side of the separatrix each converge to their own 'dynamical attractor' in the later stages of their evolution (yellow lines), a feature that is commonly seen in many dynamical systems.[91–93] To draw the separatrix we use two trajectories that follow the same path to the dynamical attractor but end up in different configurations. To find these trajectories, we take two points on the outer perimeter, and two points on the inner exclusion region perimeter that end up in opposite configurations. Then by moving the starting trajectories on the perimeters closer together we can effectively bound a small region in which trajectories follow the same path to the dynamical attractor. These two pairs of paths (one from the outer perimeter, and one from the exclusion zone perimeter) are used together to illustrate the separatrix in Figure 4.12.

Since the adsorption of rods onto the cylindrical drop is essentially a random process, the probability that an adsorbed rod will end up in the side-to-side or tip-to-tip configuration relative to a fixed rod at the edge of the cylindrical drop is proportional to the areas of the 'domain of influence' of the fixed rod that are on either side of the separatrix (we define the domain of influence as the region where the capillary interaction energy $\gtrsim kT$). In the far-field, we can approximate the capillary interaction energy between two rods with centre-to-centre separation r using (2.12) or (2.13) as $V_{cap}(r) \approx -\gamma_{ow} H_c^2 (2r_c/r)^4$,[15,50,52] where H_c is the amplitude of the contact line undulation and $r_c \approx (a+b)/2$ is the average radius of the contact line. It is useful to estimate the radius of the rod b where the domain of influence of the fixed rod extends across the entire width of the cylindrical drop, i.e., where $|V_{cap}(W = 20b)| \approx kT$. For a typical rod-like particle, e.g., an ellipsoid with aspect ratio $a/b = 2.5$ and contact angle $\theta_w = 110°$ where $H \approx 0.05b$ (see Figure 4.3), we find this radius to be $b \approx 50$ nm. This means that for rods with $b \gtrsim 50$ nm, the domain of influence of the fixed rod extends beyond the width of the cylindrical drop, and the drop width acts as a cut-off length limiting the area to the left of the separatrix. In contrast, there is essentially no such cut-off along the length of the cylindrical drop and the area to the right of the separatrix therefore increases indefinitely as we increase b. These results show that for rods with $b \gtrsim 50$ nm, the cylindrical drop geometry favours the tip-to-tip assembly of both ellipsoids and cylinders, even when the long axes of the two interacting rods are not lined up initially. Finally, if more than two rods are present at the cylindrical interface, our analysis suggests that capillary interaction will lead to the formation of a long chains of rods that are connected to each other tip-to-tip.

4.3.5 Triblock Patchy Rods

Up to now, we have considered rod-like particles with homogeneous surface chemistry and controlled contact line undulations through particle shape. In this section, we consider the assembly of patchy rods which have heterogeneous surface chemistry. To minimise the effect of particle shape on self-assembly, we consider patchy spherocylinders. As discussed in the introduction, diblock patchy rods (i.e., Janus rods) have hexapolar contact line undulations.[18,28,94] In order to compare the results in this section with those in the previous sections on particles with capillary quadrupoles, we therefore consider spherocylinders with triblock patchy geometry as this is the simplest patchy-particle geometry that possesses a capillary quadrupole; with advances in synthetic chemistry, such patchy particles can now be readily synthesised.[27] In order to achieve parallel alignment of the rods, we consider spherocylinders with hydrophilic hemispherical caps ($\theta_w = 70°$) and hydrophobic cylindrical sides ($\theta_w = 110°$), so that the contact line is concave upwards along the long axis of the particle (Figure 4.1a).

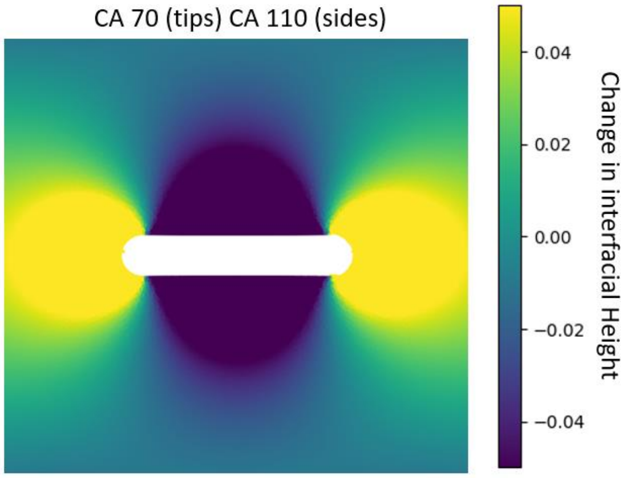

Figure 4.13: Contour plot of meniscus deformation around a triblock patchy particle with aspect ratio 5 adsorbed at a flat fluid-fluid interface.

In Figure 4.13, we show a contour plot of the meniscus deformation around the patchy particles at a flat plane. We can see that despite the spherocylinder shape, the triblock patchy particle has much larger contact line undulations both at the sides and the tips compared to rods with homogeneous surface chemistry (compare the range of interfacial heights in Figure 4.3 and Figure 4.13). We anticipate that these large undulations will lead to much stronger spatial confinement and the tip-to-tip capillary interactions for the patchy rod compared to the non-patchy rods.

In Figure 4.9b, we plot the energy as a function of $y_p = R \sin \theta_p$ for the triblock patchy rods with aspect ratio $a/b = 5$ at a cylindrical drop with height $h = 5b$ compared to the corresponding non-patchy rods. As anticipated, the patchy rod experiences a much stronger spatial confinement lateral to the cylindrical drop. For example, the potential well depth is $\Delta E_{int} \approx 0.14\gamma_{ow}b^2$ for the patchy rod but only $\Delta E_{int} \approx 0.02\gamma_{ow}b^2$ for non-patchy ellipsoids; for $\gamma_{ow} = 30 \times 10^{-3}$ N/m, these well depths correspond to $100kT$ and $15kT$ respectively for nanoscale particles with $b = 10$ nm.

In Figure 4.10, we plot the tip-to-tip interaction energy as a function of separation between two patchy rods with aspect ratio $a/b = 5$ at a cylindrical drop with height $h = 5b$ compared to the corresponding non-patchy rods. Once again, as anticipated, the capillary interaction is much greater for patchy rods compared to the non-patchy rods. For example, the interaction energy at contact is $-0.08\gamma_{ow}b^2$ for the patchy spherocylinder but only $-0.04\gamma_{ow}b^2$ for non-patchy cylinders; for $\gamma_{ow} = 30 \times 10^{-3}$ N/m, these contact energies correspond to $-50kT$ and $-25kT$ respectively for nanoscale particles with $b = 10$ nm. In addition, the range of the interactions is much greater for the patchy rod ($\approx 6b$) compared to the non-patchy rods ($\approx 2b$ for the non-patchy cylinder). Since both lateral spatial confinement and tip-to-tip attraction are much greater for patchy rods, we conclude that tip-to-tip assembly at a cylindrical interface is much more likely for triblock patchy rods compared to non-patchy rods.

4.4 Conclusions

We have used the finite element method Surface Evolver to study the capillary assembly of rod-shaped particles adsorbed at a sessile liquid drop with cylindrical geometry. We considered the flotation regime where the drop height is greater than the diameter of the rods and studied the assembly of rods as a function of interfacial curvature, particle shape (ellipsoid, cylinder, spherocylinder), contact angle, aspect ratio and chemical heterogeneity (homogeneous and triblock patchy).

For rods with homogeneous surface chemistry, we can achieve very strong localisation of particle orientation using cylindrical drops with a lateral width much greater than the length of the rods. By changing particle shape, contact angle and aspect ratio, we can tune the interplay between interfacial curvature, particle contact line curvature and particle anisotropy, and control the rod not only to align parallel or perpendicular to the long axis of the cylindrical drop, but also to align in novel oblique orientations. In contrast, we can only achieve weak spatial confinement of the rods transverse to the cylindrical drop because of the weak repulsion between the capillary quadrupole of the particle and the pinned contact lines of the sessile drop.

For ellipsoids and cylinders oriented parallel to the cylindrical drop, the capillary interaction is strong when the rods are oriented tip-to-tip, even at the nanoscale. In contrast, the capillary interaction between spherocylinders in the parallel orientation is extremely weak because these particles do not possess an intrinsic capillary quadrupole. Since in the confined geometry of the cylindrical drop rods in the parallel orientation are more likely to approach each other in a tip-to-tip orientation, whereas interfacial curvature suppresses the transition from the tip-to-tip to the side-to-side configuration, the cylindrical drop favours the tip-to-tip assembly of rod in the parallel orientation, not only for cylinders but also for ellipsoids.

Finally, for triblock patchy rods which possess much larger contact line undulations compared to non-patchy rods, the stronger capillary quadrupole leads to stronger lateral spatial confinement and tip-to-tip capillary attraction, resulting in an even stronger tendency for patchy rods in the parallel orientation at a cylindrical interface to assemble tip-to-tip compared to non-patchy rods.

The proposed capillary assembly mechanism allows us to manipulate the configuration of single and multiple rod-like particles and therefore offers a facile strategy for organising such particles into useful functional materials.

Chapter 5 Capillary Assembly of Anisotropic Particles at Cylindrical Fluid Interfaces – Immersion Regime

5.1 Introduction

In the previous Chapter, we explored the self-assembly of anisotropic rod-like particles at a curved interface formed by a cylindrical sessile drop, where the width of the drop was much larger than the length of the rods, and the height of the drop was much greater than the radius of the rods so that we are in the flotation regime. The advantage of using a cylindrical drop is that the geometry of the curved interface is very simple (constant finite curvature transverse to the cylinder, zero curvature along the cylinder), allowing us to elucidate the interplay between interfacial curvature and particle properties in determining the behaviour of single and multiple rods. Using this curved geometry, we showed that it was possible to control the rods to align parallel, perpendicular or obliquely with respect to the long axis of the sessile drop by tuning the contact angle and particle shape. We also showed that the orientational confinement of the rods in the flotation regime was strong (e.g., orientational confining potential of 100s of $k_B T$ for nanoscale rods). However, we also found that the spatial confinement of the rods transverse to the long axis of the cylindrical drop and the capillary interaction between rods was much weaker compared to the orientational confinement (e.g., spatial confining potential and capillary interaction of 10s of $k_B T$ for nanoscale rods), limiting the degree to which we can control particle self-assembly in this regime.

To overcome these limitations, in this Chapter we study the self-assembly of rod-shaped particles at a cylindrical sessile drop in the immersion regime, i.e., where the height of the drop is comparable to or smaller than the radius of the rods. Specifically, we use the finite element method Surface Evolver[74] to study the self-assembly of single and multiple rods as a function of drop height, particle shape (ellipsoid, cylinder, spherocylinder) and particle contact angle. As we will see later in the Chapter, although working in the immersion regime leads to slightly weaker orientational confinement of the rods due to a decrease in the curvature of the cylindrical interface, we can still achieve strong orientational confinement even for rods on the nanoscale. More importantly, we show that it is now possible to achieve very strong spatial confinement of the rods lateral to the cylindrical drop because the confining potential is a strong function of drop height in the immersion regime and drop height varies with lateral position. We also show that the capillary interactions between the rods in the immersion regime are much stronger and longer ranged because they are monopolar rather than quadrupolar in nature. Working in the immersion regime thus gives us good control over the orientation, position and self-assembly of rod-like particles adsorbed on a cylindrical drop, providing a facile method for creating to functional nanoclusters.

The rest of this Chapter is organised as follows. In Section 5.2, we describe the geometry and thermodynamics of the system as well as the finite element method (Surface Evolver) we use to study the system. In Section 5.3, we present and discuss results for the orientation and spatial confinement of single rods and the self-assembly of two rods at a cylindrical liquid drop as a function of drop height, particle shape and contact angle. Finally in Section 5.4, we present our conclusions.

5.2 Theoretical Methods

In this section, we discuss the geometry and thermodynamics of the system, which consists of rod-like particles adsorbed at a sessile cylindrical drop, as well as the Surface Evolver method we use to study this system theoretically.

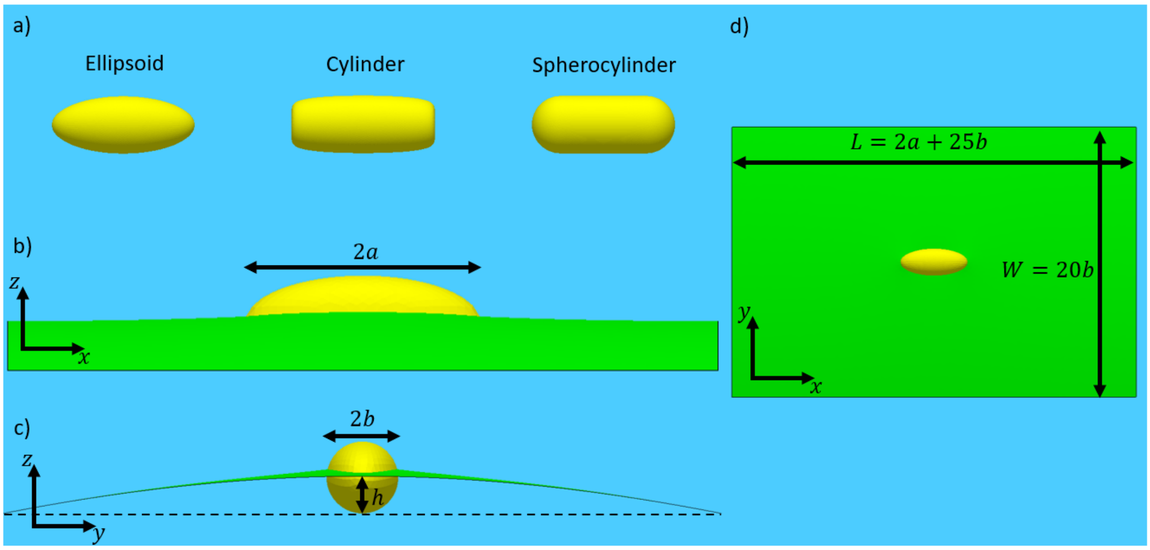

Figure 5.1: (a) Geometry of the rod like particles studied in our simulations. All particles have aspect ratio $a/b = 2.5$. (b-d) Geometry of an ellipsoidal particle adsorbed to the simulation interface with views from the (b) side, (c) end, and (d) top.

For the rod-like particles, we consider the same homogeneous particles described in Chapter 4, i.e., ellipsoids, cylinders and spherocylinders (Figure 5.1a). However, in this Chapter we only consider rods with aspect ratio $a/b = 2.5$.

For the cylindrical sessile drop, we consider a drop with a rectangular base with identical width $W = 20b$ (i.e., 4 times the length of the rods) as in Chapter 4, but increased length $L = 2a + 25b$ (i.e., 6 times the length of the rods). Again, for convenience, we refer to the top and bottom fluid phases as oil and water, respectively (i.e., the fluid making up the drop is water), though our model is in fact general and applies to any fluid-fluid interface.

Assuming the origin of the lab frame in Cartesian coordinates to be at the centre of the base with z perpendicular to the base and x, y parallel and perpendicular to the long axis of the cylinder, respectively, we assume that the contact lines of the cylindrical drop are pinned at $y = \pm W/2$ and apply reflecting boundary conditions at the ends of the cylindrical drop at $x = \pm L/2$ (Figure 5.1b,d). We chose L to be as large as possible to minimise finite size effects due to the reflecting boundaries at the cylindrical drop ends while still being computationally feasible. When dealing with large monopolar deformations which arise in the immersion regime, it is important to quantify and minimise finite size effects (within the constraints of computation time and memory) since monopolar deformations are very long range and can lead to significant finite size effects.

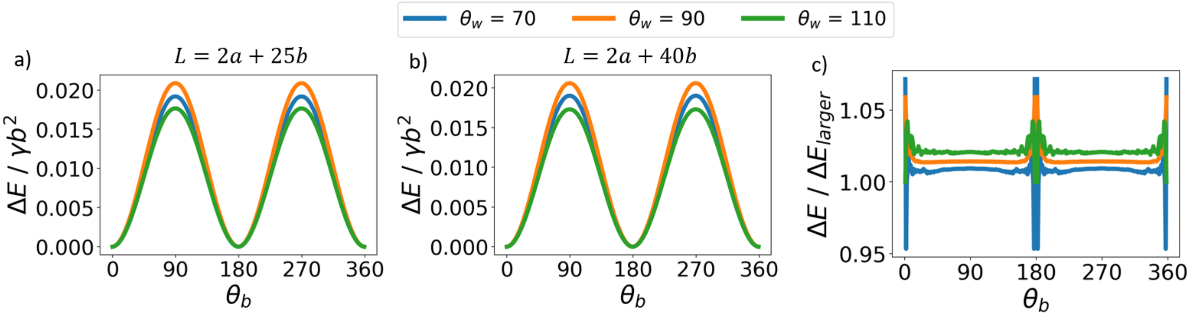

Figure 5.2: Interfacial energy (relative to energy minimum) as a function of bond angle for an ellipsoidal particle with contact angles $\theta_w = 70°, 90°, 110°$at a drop height of $0.5h_t$ for: (a) a simulation box with width $W = 20b$ and length $L = 2a + 25b$, and (d) larger simulation box with length $L = 2a + 40b$ (b) and comparison between the two systems (c).

In Figure 5.2 we plot the interfacial energy (relative to the energy minimum) as a function of bond angle θ_b (see later in this section) for ellipsoidal particles in the centre of the cylindrical drop with contact angles $\theta_w = 70°, 90°, 110°$ for a drop height of $0.5h_t$, which is deep within the immersion regime, where h_t is the transition height between the flotation and immersion regimes (see later in this section). To quantify the finite size effects for this system, we calculate the interfacial energy curves using a simulation box with width $W = 20b$ and length $L = 2a + 25b$ (Figure 5.2a), and a larger box with the same width but 50% larger length $L = 2a + 40b$ (Figure 5.2b). We see that both simulations have similar energy curves visually for all the contact angles considered. To compare the two simulations more quantitatively, we plot in Figure 5.2c the ratio of change in energies between both systems as a function of bond angle θ_b. We see that the differences between the two simulations are relatively large (around 5%) at $\theta_b = 0°, 180°, 360°$ where the interfacial energy is close to zero. These relatively large differences are to be expected since the signal-to-noise ratio is very small when the interfacial energy is small. A more representative assessment of the impact of system size comes from comparing the peaks in energy at $\theta_b = 90°, 270°$ between the two simulations. In the case, the smaller box size leads to an increase in the peak energy of $1.5\%, 2\%, 2.5\%$ compared to the larger box size for contact angles $\theta_w = 70°, 90°, 110°$ respectively. We therefore conclude that the systematic error due to finite size effects is <3% for the simulation box size we use in this Chapter. In Section 5.3.3, we consider much lower drop heights down to values of $0.1h_t$ where finite size effects will be even more severe. However, in this case, the closer reflecting boundary is used to essentially double our system size and the finite size error comes only from the farther reflecting boundary, which because it is twice as far away compared to the simulations in Figure 5.2a, at least partially mitigates for the more severe finite size effects.

We control the curvature of the sessile drop by applying a Laplace pressure of γ_{ow}/R across the interface in our simulations, where R is the radius of curvature of the cylindrical interface in absence of any adsorbed particles, and γ_{ow} is the oil-water interfacial tension. Although the behaviour of adsorbed rods is controlled by the curvature of the cylindrical drop, it is easier to control and measure the height of the drop experimentally. For convenience, we therefore parameterise the curvature of the drop using the drop height in the absence of adsorbed particles, h (Figure 5.1c), which is related to R and W according to $R = h/2 + W^2/8h$ as described in Section 4.3.3.

Contact angle / Shape	Ellipsoid	Cylinder	Spherocylinder
70°	1.1b	1.2b	1.2b
90°	1.0b	1.0b	1.0b
110°	0.75b	0.7b	0.7b

Table 5.1: Values for h_t, the flotation to immersion transition height, for the particle shapes and contact angles studied in this Chapter.

In this Chapter, we focus on the immersion regime, and it is therefore important to calculate h_t, the value of h where an adsorbed rod in its equilibrium configuration just touches the solid substrate, since h_t demarcates the boundary between the immersion and flotation regimes. To calculate the transition height between the flotation and immersion regimes h_t, we perform simulations for each shape and contact angle at various cylindrical drop heights h, with the particle fixed at the centre of the cylindrical drop but allowing the height of the particle centre above h (i.e., Δr as discussed in Chapter 4) to find its equilibrium value in the absence of a solid substrate. As the cylindrical interface is curved, particles orientated parallel to the long axis of the cylindrical drop (i.e., bond angle $\theta_b = 0°$) need not have the same equilibrium height as particles orientated perpendicular ($\theta_b = 90°$). For this reason, we perform simulations for particles in both orientations for all values of the drop height h.

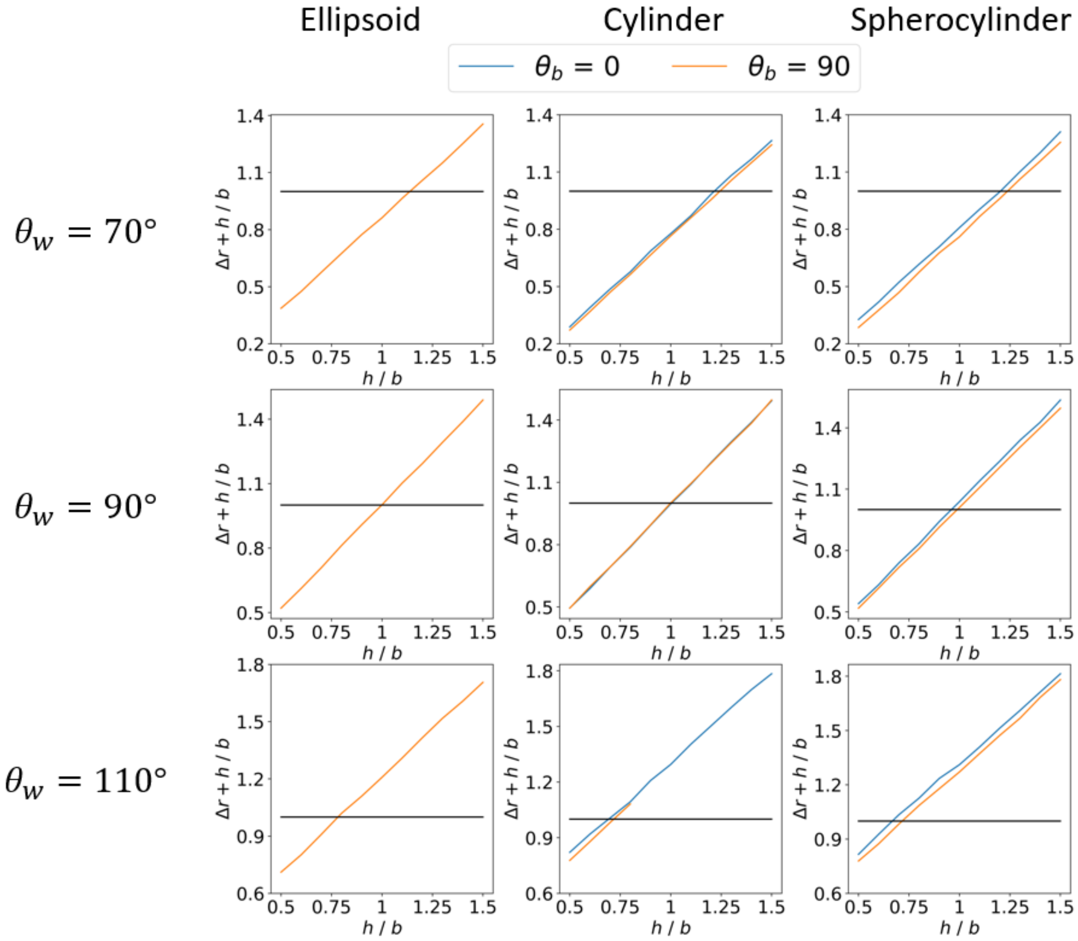

Figure 5.3: Simulations to determine h_t for each shape and contact angle combination. Each graph includes simulations for particles parallel (blue) and perpendicular (orange) to the long axis of the cylindrical drop. The black line represents the point at which the particle is just touching the substrate.

In Figure 5.3 we plot $(\Delta r + h)$, the height of the particle above $z = 0$, i.e., the position of the substrate if it were present, for particles with parallel (blue) and perpendicular (orange) orientation against h for all the particle shapes and contact angles we study. The transition height h_t is the value of h where the bottom of the adsorbed rod is at $z = 0$, i.e., the value of h that satisfies the condition $h + \Delta r = b$. In Figure 5.3, h_t for each case is therefore the value of h where the blue or orange curves intersect the horizontal black line which represents the height b. We note that in some cases, it was only possible to obtain the $\Delta r + h$ vs. h curves for one particle orientation as simulations for the other orientation were not numerically stable (e.g., for ellipsoids). However, in cases where results for both orientations are available, we see that h_t values obtained from both particle orientations are quite close, and we can therefore obtain a reasonable estimate of h_t even if we only have simulation data for one of the orientations. We therefore define h_t to be the average value obtained from data for both rod orientations (where both are available) or from one of the orientations (where data only exists for that orientation), and these are the values listed in Table 5.1. Note that as expected, the value of h_t for any given particle shape decreases as we go from hydrophilic to neutral to hydrophobic particles. The immersion regime is defined as the case where $h < h_t$.

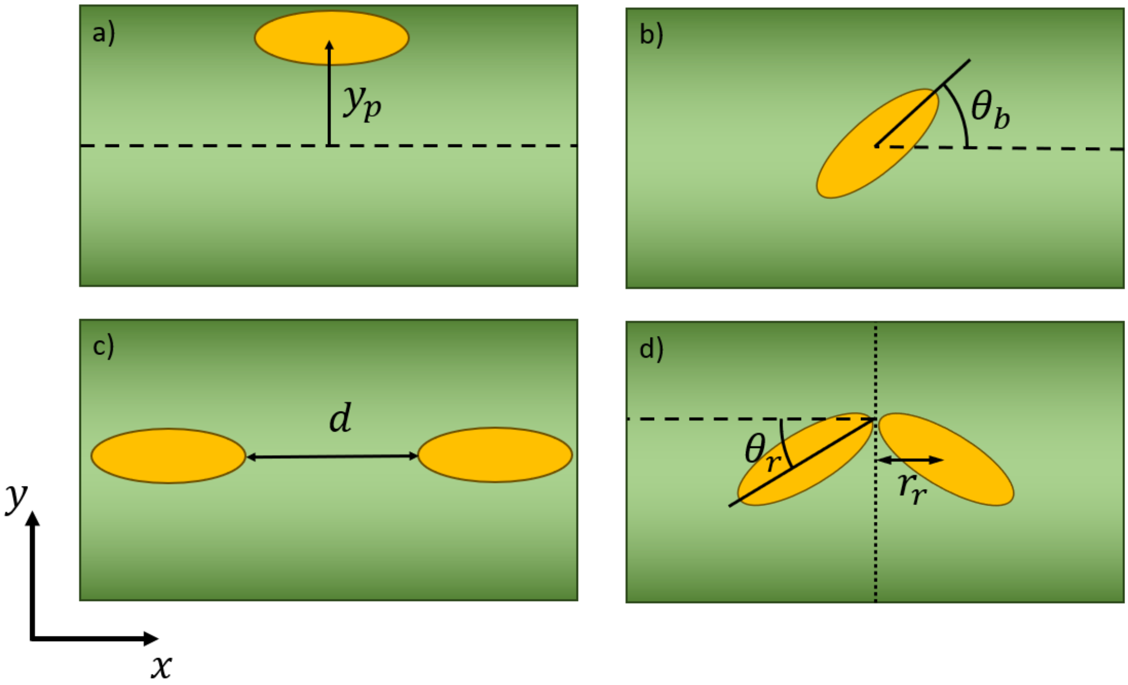

Figure 5.4: Coordinates characterising single and two particle configurations: (a) lateral displacement, (b) bond angle, (c) tip-to-tip separation, (d) roll-over angle.

For rod-like particles in the immersion regime, the rods sit on the solid substrate with their long axis parallel to the solid substrate and their centre heights fixed to be $z_p = b$. To specify the position of the rods on the substrate, we use the position of the rod centre parallel and perpendicular to the long axis of the cylindrical drop which we denote as x_p and y_p respectively (Figure 5.4a, x_p not shown). To specify the orientation of the adsorbed rods, we use the angle of their long axis to the long axis of the cylindrical drop which we denote as the bond angle θ_b (Figure 5.4b). Note that we only need one angle to specify orientation since all the rod shapes we consider in this Chapter are axisymmetric. Later, we also compare the immersion regime to some simulations for particles in the flotation regime ($h > h_t$), where we also allow the height of the particle relative to the interface to be equilibrated for a given particle configuration. We define the particle reference frame (x', y', z') such that its origin coincides with the centre of the rod, x' lies along the semi-major axis of the rod while y' and z' lie along the semi-minor axes of the rod with z' parallel to substrate normal. The particle frame coordinates (x', y', z') are readily related to the lab frame coordinates (x, y, z) using equation (4.3).

When studying the capillary interaction and self-assembly of two rods later, we will primarily focus on rods in the tip-to-tip configuration (with $y_p = 0$) and we specify the separation of the two rods in this case by their surface-to-surface separation d (Figure 5.4c). As we shall see later in Section 5.3.3, in some regions of system parameter space, the immersion capillary forces are so strong that they drive two rods in the tip-to-tip configuration to first come into tip-to-tip contact, then 'roll-over' into side-to-side contact.[18,22] To study this roll-over transition, we define the roll-over angle θ_r, which is the angle that two mirror-symmetric rods make to the long axis of the cylindrical drop as shown in Figure 5.4d. Note that the two particles are in contact with $y_p = 0$ throughout the transition.

The energy of the adsorbed rod system is primarily due to the interfacial energy and is given by equation (2.2)[53,95] Again, we have neglected line tension contributions in equation (2.2) because these are sub-dominant compared to interfacial tensions for the particle sizes we are considering where $a, b \geq 10$ nm.[41] For a given particle configuration, the interfacial energy of the system given by equation (2.5) is calculated using Surface Evolver.[74] In the simulations, we work with length and energy units such that $b = 1, \gamma = 1$ (we use γ to denote the oil-water surface tension for simplicity) and use a variable triangular mesh edge length between $0.02b$ to $0.1b$ and quadratic edges to capture the shape of the liquid interface and three-phase contact line more accurately.

5.3 Results and Discussion

5.3.1 Orientational Transition of Single Rods

In this section, we consider the impact of particle shape, contact angle and cylindrical drop height on the orientation of single adsorbed rods in the immersion regime, as specified by the bond angle θ_b (Figure 5.4b). As we shall see later in Section 5.3.2, adsorbed rods are strongly confined to lie along the centre line of the cylindrical drop in the immersion regime and we therefore set $y_p = 0$ in our simulations. In addition, since we are interested in studying the behaviour of isolated adsorbed rods in this section, we set $x_p = 0$, i.e., the particles are situated at the centre of simulation box to minimise the impact of the reflecting boundary conditions at the cylindrical drop ends. We then calculate the energy of the system as a function of bond angle from $\theta_b = 0°$ to $90°$ in increments of $1°$, noting that the energy only needs to be calculated for this range due to the symmetry of the energy with respect to θ_b.

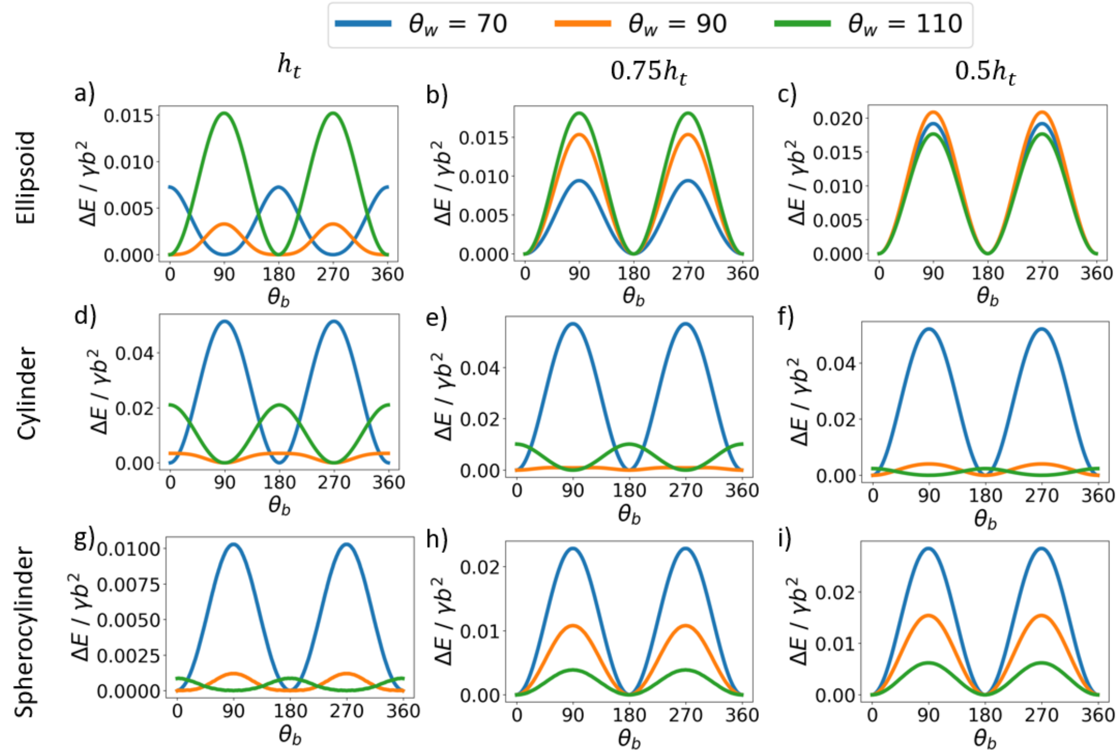

Figure 5.5: Interfacial energy (relative to the minimum energy state) as a function of bond angle θ_b for different particle shapes, drop heights and contact angle θ_w.

In Figure 5.5 we plot the orientational energy curves, i.e., interfacial energy (relative to the minimum energy state) as a function of bond angle θ_b, for ellipsoids, cylinders and spherocylinders (first, second and third row respectively), drop heights $h = h_t, 0.75h_t, 0.5h_t$ (first, second and third column respectively), and contact angles $\theta_w = 70°, 90°, 110°$ (i.e., hydrophilic, neutral and hydrophobic rods respectively), with the value of h_t for the different cases given in Table 5.1.

We first consider the orientation of the rods at the transition height $h = h_t$, i.e., first column of Figure 5.5. We see that in this case, the equilibrium orientation of the different rod shapes (i.e., θ_b corresponding to the energy minimum) can be engineered to lie either parallel ($\theta_b = 0°$) or perpendicular ($\theta_b = 90°$) to the long axis of the cylindrical drop by tuning the contact angle. In particular, we see that hydrophilic ellipsoids lie perpendicular, while neutral and hydrophobic ellipsoids lie parallel to the cylindrical drop (Figure 3a); on the other hand, hydrophilic cylinders lie parallel, while neutral and hydrophobic cylinders lie perpendicular to the cylindrical drop (Figure 5.5b). These results are similar to those covered in Chapter 4.3.2 for ellipsoids and cylinders in the flotation regime ($h > h_t$). This fact is not surprising since for $h = h_t$, we expect the monopolar deformation of the liquid meniscus due to the protrusion of the rod above the cylindrical drop to be relatively weak so that the orientational behaviour of the rods is determined by the quadrupolar deformation of the liquid meniscus, similar to the flotation case (see Chapter 4 and later in Figure 5.6). Specifically, the capillary quadrupole will align its rise axis with the principle axis of curvature of the cylindrical interface (where the interface is concave up) in order to minimize the distortion to the host interface.[17,73,96] This is why hydrophilic ellipsoids align perpendicular since they have a rise axis at their sides, while hydrophobic ellipsoids align parallel since they have their rise axis at their tips. The trend is reversed for cylinders since the curvature of their capillary quadrupole is opposite to that of ellipsoids for a given contact angle as seen in Chapter 4.

Interestingly, the dependence of particle orientation on contact angle for spherocylinders is different at $h = h_t$ (Figure 5.5c) compared to the behaviour in the flotation regime. Specifically, spherocylinders are always aligned parallel regardless of contact angle in the flotation regime while at $h = h_t$, hydrophilic and neutral spherocylinders are aligned parallel while hydrophobic spherocylinders are aligned perpendicular. This difference is not surprising since spherocylinders do not possess an intrinsic capillary quadrupole, so the dependence of particle orientation on contact angle is more subtle and harder to predict *a priori*. The absence of an intrinsic capillary quadrupole in spherocylinders is also evidenced by the fact that the energy scales in the orientational energy curves for spherocylinders (Figure 5.5g) are significantly smaller than that for ellipsoids and cylinders (Figure 5.5a,d).

In addition to the curvature of the capillary quadrupole, another important factor determining the orientation of rods at a cylindrical interface is particle anisotropy. For $h \geq h_t$, the effect of particle anisotropy arises from the fact that, because of the curvature of the cylindrical interface, a rod-like particle removes a larger area of the energetically unfavourable oil-water interface when it is parallel rather than perpendicular to the cylindrical drop. Particle anisotropy therefore favours the parallel orientation compared to the perpendicular orientation. This effect explains why for non-neutrally wetting rods in Figure 5.5a,d,g, the potential energy well depth for the parallel orientation is significantly greater than for the perpendicular orientation. Specifically, for non-neutrally wetting rods in the parallel orientation, both contact line curvature and particle anisotropy favour parallel alignment, i.e., the two effects are synergetic. On the other hand, for non-neutrally wetting rods in the perpendicular orientation, contact line curvature favours perpendicular alignment, but particle anisotropy favours parallel alignment, i.e., the two effects are antagonistic.

We next consider the effect of decreasing cylindrical drop height below h_t on the orientation of the rods, starting with the case of ellipsoids and spherocylinders (first and third row in Figure 5.5). We see that as we decrease drop height to $h = 0.75h_t$ and $0.5h_t$, ellipsoids and spherocylinders align parallel to the cylindrical drop regardless of contact angle. The parallel alignment of these rods comes from the fact that as we decrease h, there is now significant monopolar deformation of the liquid meniscus so that the orientation of the rods is now controlled by monopolar deformations rather than by the capillary quadrupole of the rods. Specifically, the shape anisotropy of the rods means that they create larger monopolar deformations when they are in the perpendicular orientation compared to the parallel orientation since their ends protrude above the cylindrical interface more in the perpendicular orientation, making the parallel orientation more energetically favourable. Not surprisingly, this effect becomes stronger as we decrease h, as can be seen from the fact that the potential energy well depth for the parallel orientation increases for both ellipsoids and spherocylinders as we go from $h = 0.75h_t$ to $h = 0.5h_t$.

While particle anisotropy plays the dominant role in determining particle orientation in the immersion regime, the effect of contact line curvature is still significant. This can be seen from the fact that for $h = 0.75h_t, 0.5h_t$, the potential energy well depth for parallel orientation is largest for hydrophobic ellipsoids and hydrophilic spherocylinders, i.e., where contact line curvature and particle anisotropy both favour the parallel orientation so that the two effects are synergetic. On the other hand, the potential energy well depth is smallest for hydrophilic ellipsoids and hydrophobic spherocylinders, i.e., where contact line curvature favours the perpendicular orientation, but particle anisotropy favours the parallel orientation so that the two effects are antagonistic.

We next consider the case of cylinders (second row in Figure 5.5). As we decrease the drop height to $h = 0.75h_t$ and $0.5h_t$, we see that particle anisotropy again drives the rods towards the parallel orientation, so that both hydrophilic and neutral cylinders now have parallel orientation, while the potential energy well depth for perpendicular orientation for hydrophobic cylinders is significantly reduced. However, hydrophobic cylinders are still in the perpendicular orientation even at $h = 0.5h_t$, and we have to decrease h below $0.4h_t$ before this system transitions to the parallel orientation (see later in Figure 5.9). We believe that the much lower values of h required to drive hydrophobic cylinders into the parallel orientation arises from the fact that for cylinders are in the perpendicular orientation, their flat ends allow them to accommodate different interfacial heights more readily compared to particles with rounded ends such as ellipsoids and spherocylinders. This means that we need to go to much lower values of h before the system can generate large enough monopolar deformations to drive cylinders into the parallel orientation.

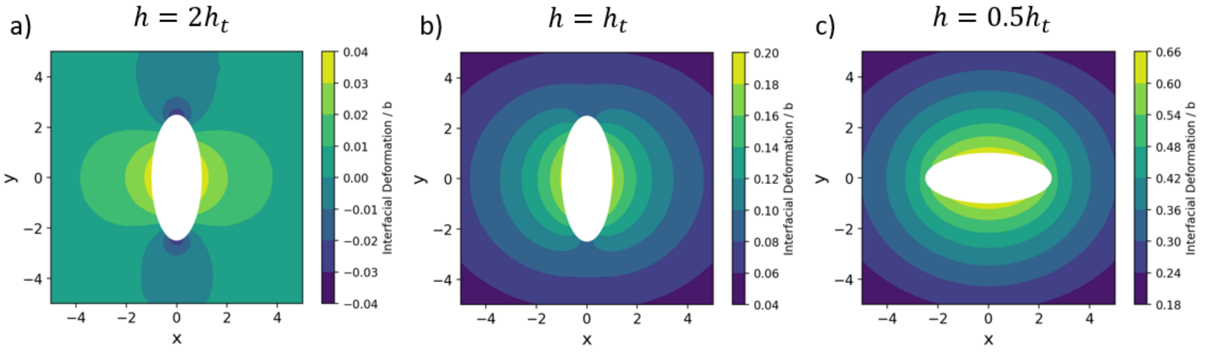

Figure 5.6: (a) Meniscus deformation around an ellipsoidal particle with contact angle $\theta_w = 70°$ adsorbed at a cylindrical drop for drop heights of (a) $2h_t$ (flotation regime), (b) h_t (transition height), (c) $0.5h_t$ (immersion regime). The long axis of the cylindrical drop is in the x direction and the ellipsoid is in its equilibrium orientation at each height.

In the preceding discussion, we have assumed that the orientation of the adsorbed rods is primarily determined by quadrupole deformations of the liquid meniscus for $h = h_t$ and by monopolar deformations of the liquid meniscus for $h < h_t$. To confirm that this is indeed the case, we analyse in more detail how the multipolar character of the liquid meniscus changes as we change the drop height across h_t. In Figure 5.6a,b,c, we plot the deformation of the liquid interface (relative to the unperturbed cylindrical interface) around an adsorbed hydrophilic ellipsoid (contact angle $\theta_w = 90°$) for $h = 2h_t, h_t, 0.5h_t$ respectively; note that this ellipsoid has a perpendicular orientation for $h = 2h_t, h_t$ and a parallel orientation for $h = 0.5h_t$ (see Figure 5.5). From Figure 5.6, we see that the interfacial deformation is quadrupolar for $h = 2h_t$ (Figure 5.6a), monopolar for $h = 0.5h_t$ (Figure 5.6c) and a combination between the two for $h = h_t$, specifically quadrupolar in the near-field but monopolar in the far-field (Figure 5.6b). These results confirm that quadrupolar deformations are only significant for $h \geq h_t$, while monopolar deformations become dominant for $h < h_t$.

In Figure 5.5, we saw that as we decrease h, rods that were initially in the perpendicular orientation at $h = h_t$ undergo a transition to the parallel orientation due to monopolar interfacial deformations becoming increasingly dominant over quadrupolar deformations. We now study this transition in more detail. However, the energy scales of orientational energy curves become quite small close to an orientational transition and the energy curves can therefore be quite noisy due to the reduced signal-to-noise ratio. To obtain smooth energy curves so that we can identify minima and maxima accurately, we therefore use a filter to reduce the noise from the simulations. Specifically, we use the Savitzky-Golay filter which is a convolution method which fits a subset of N datapoints with a low-level polynomial of order M using a least-squares algorithm.[97] We chose this method because of its availability in the Python package SciPy, its ability to maintain the original data trends and its simplicity. For the filtered data, we found that to ensure that the filtered curve captures the key features in the original data, it is best to use the full data as the subset, essentially fitting the whole dataset with a low order polynomial of order M.

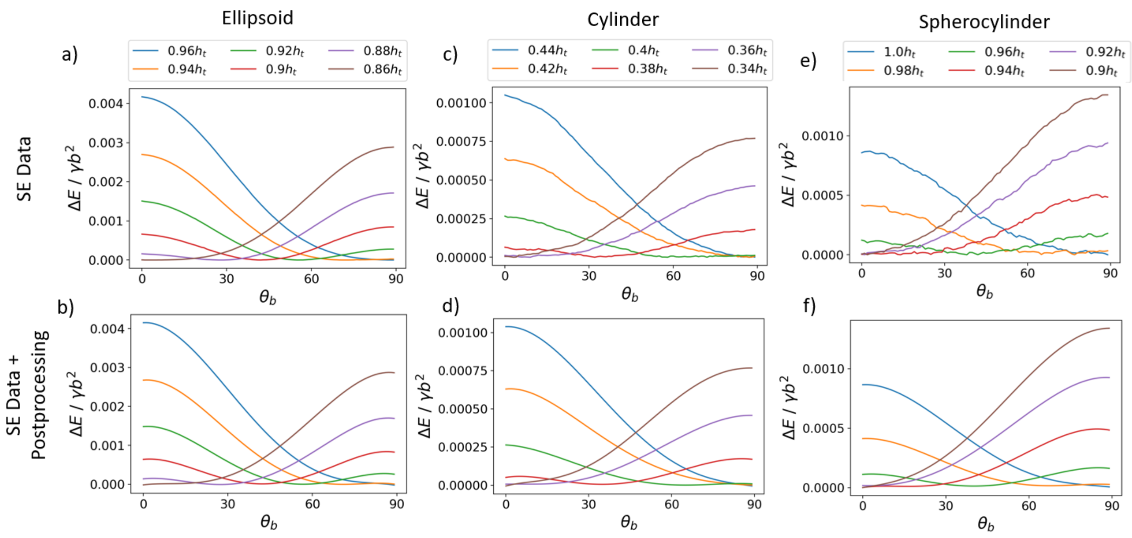

Figure 5.7: Orientational energy curves for ellipsoids, cylinders, and spherocylinders with $\theta_w = 70°, 110°, 110°$respectivly for different drop heights around the orientational transition: (a,c,e) before and (b,d,f) after post processing with the Savitzky-Golay filter with polynomial order $M = 5$.

In Figure 5.7 we plot the orientational energy curves (relative to the minimum energy state) for ellipsoids, cylinders, and spherocylinders with $\theta_w = 70°, 110°, 110°$ respectively (i.e., shape and contact angle conditions that favour perpendicular alignment at $h = h_t$) for h values around the orientational transition. We present both the raw Surface Evolver data (Figure 5.7a,c,e) and the postprocessed data using the Savitzky-Golay filter with polynomial order $\mathrm{M} = 5$ (Figure 5.7b,d,f). We see that the filtering process we use allows us to capture the key features of the raw data faithfully and allows us to numerically identify key features such as the minima.

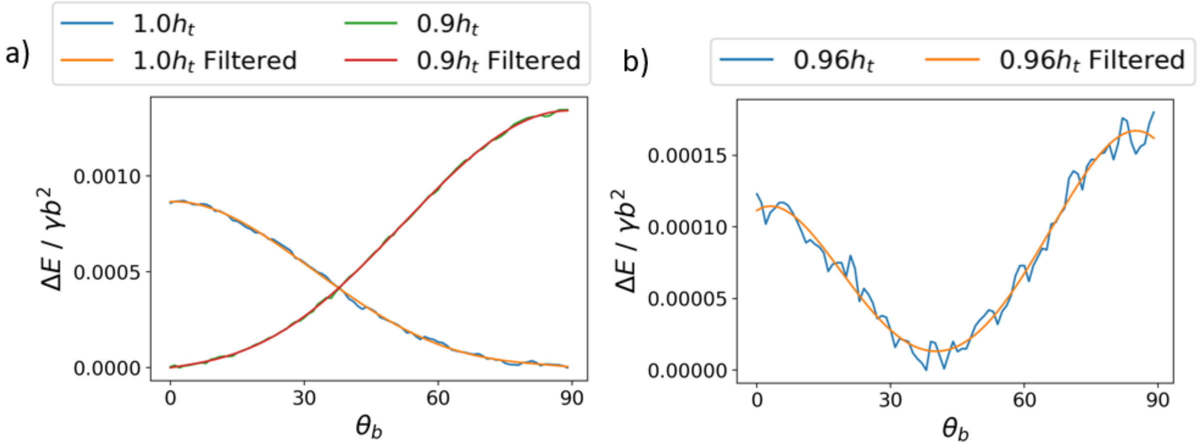

Figure 5.8: Comparison between the raw Surface Evolver data and filtered data for orientational energy curves for a spherocylinder with contact angle $\theta_w = 110°$ for: (a) $h = h_t$, $0.9h_t$ and (b) $h = 0.96h_t$ where the signal to noise ratio is low particularly low. The filtering is achieved using a Savitzky-Golay filter with polynomial order $M = 5$.

As a more direct comparison, in Figure 5.8 we plot the interfacial energy (relative to the minimum energy state) as a function of bond angle θ_b for a spherocylinder with contact angle $\theta_w = 110°$ (as it has the lowest signal to noise ratio) at for different values of h around the orientational transition of the rod from the perpendicular to the parallel orientation. Specifically, Figure 5.8a shows the comparison between the raw Surface Evolver data and filtered data for drop heights at either end of the transition, i.e., $h = h_t$, where the rod has parallel orientation, and $h = 0.9h_t$, where the rod has perpendicular orientation. For the filtered data, we found that a polynomial order $M = 5$ was sufficient to capture the key features of the raw data faithfully. In Figure 5.8b we again compare the raw Surface Evolver data with the filtered data, but this time for $h = 0.96h_t$ which is the raw data set with the lowest signal to noise ratio. We can see that even in this case the Savitzky-Golay filter still performs well in capturing the key features of the raw data faithfully.

From Figure 5.7 we see that each orientational energy curve only has one minimum and the position of this minimum decreases continuously from $\theta_b = 90°$ (perpendicular orientation) to $\theta_b = 0°$ (parallel orientation) as h is decreased. We therefore conclude that the orientational transition for ellipsoids, cylinders and spherocylinders are a second order (or continuous) transition.

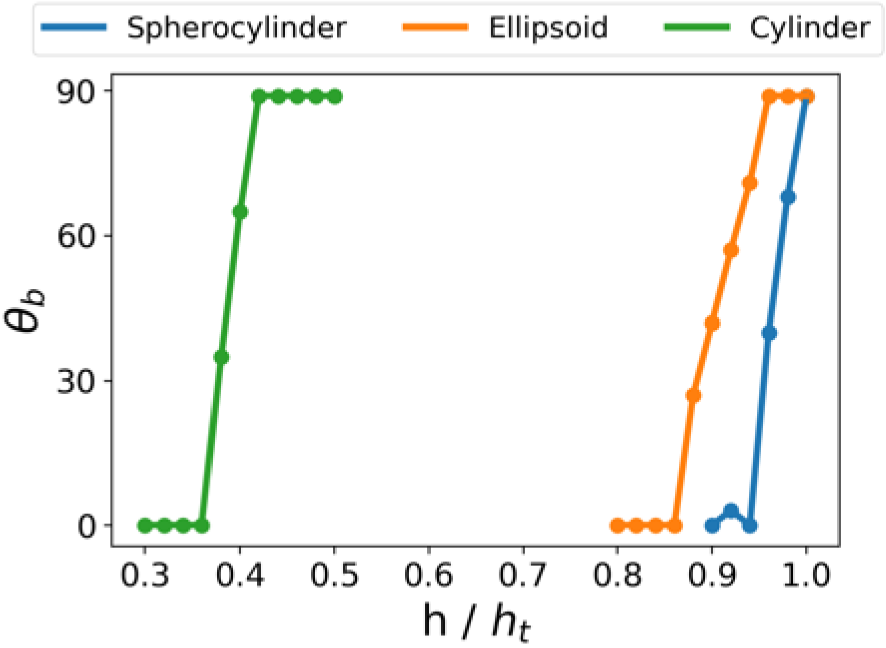

Figure 5.9: Equilibrium bond angle as a function of cylindrical drop height for ellipsoids with $\theta_w = 70°$, cylinders with $\theta_w = 110°$ and spherocylinders with $\theta_w = 110°$.

The results for all three orientational transitions are summarised in Figure 5.9 where we plot the equilibrium bond angle as a function of cylindrical drop height for each of the three rods. As expected, as we decrease h, the equilibrium bond angle decreases continuously from the perpendicular orientation to the parallel orientation for all three rods. Interestingly, the transition for cylinders occurs at significantly lower drop heights compared to ellipsoids or spherocylinders. As discussed earlier, we believe that this difference is due to the fact that when the rods are in the perpendicular orientation, the flat ends of the cylinder allow it to accommodate different interfacial heights more readily compared to particles with rounded ends such as ellipsoids and spherocylinders. This means that we need to go to much lower values of h before the energy penalty from the monopolar deformations are large enough to drive cylinders into the parallel orientation.

The results in Figure 5.5 and Figure 5.9 show that for low enough cylindrical drop heights, all adsorbed rods will orientate themselves parallel to the long axis of the cylindrical drop, regardless of the shape or contact angle of the rods. Working with adsorbed rods in the immersion regime thus provides a robust method for preparing rods in the parallel orientation.

5.3.2 Orientation and Spatial Confinement of Single Rods

In the previous section, we studied how we can control the orientation of adsorbed rods in the immersion regime by changing particle shape, contact angle and cylindrical drop height. In this section, we study how the strength of the orientational confinement and spatial confinement of the adsorbed rods changes as we go from the flotation regime ($h > h_t$) to the immersion regime ($h < h_t$). To simplify our discussion, we focus on the case where the adsorbed rods are aligned parallel to the cylindrical drop as this is the most favourable alignment for achieving the tip-to-tip assembly considered in the next section. Specifically, we consider the behaviour of ellipsoids with $\theta_w = 110°$, cylinders with $\theta_w = 70°$, and spherocylinders with $\theta_w = 70°$ in this section.

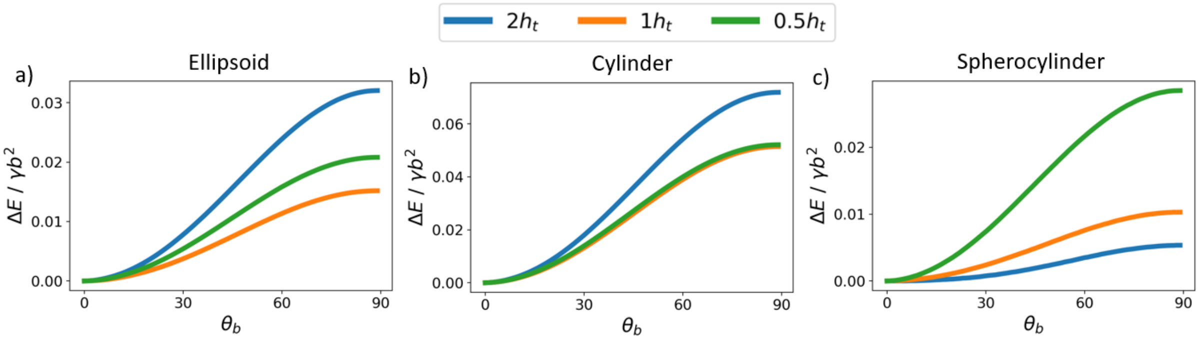

Figure 5.10: Interfacial energy (relative to energy at $\theta_b = 0°$) as a function of bond angle θ_b for different cylindrical drop heights for: (a) ellipsoids with $\theta_w = 110°$, (b) cylinders with $\theta_w = 70°$, (c) spherocylinders with $\theta_w = 70°$.

In Figure 5.10a,b,c we plot the orientational energy curves from $\theta_b = 0°$ to $90°$ for hydrophobic ellipsoids, hydrophilic cylinders and hydrophilic spherocylinders respectively, for drop heights of $h = 2h_t, h_t$ and $0.5h_t$. Note that for the results in Figure 5.10, we set $x_p, y_p = 0$ as in the previous section, and the equilibrium orientation is the parallel orientation $\theta_b = 0°$ in all cases. For ellipsoids and cylinders (Figure 5.10a,b), we see that the well depth for the orientational energy curves is greater for $h = 2h_t$ compared to $h = 0.5h_t$, i.e., the orientational confinement of the rods is stronger in the flotation regime compared to in the immersion regime. This is not surprising since the confining potential due to interfacial curvature is proportional to the product of the deviatoric curvature of the host interface and the capillary quadrupole of the adsorbed particle (refer to Chapter 2.5) and the deviatoric curvature of the cylindrical drop decreases as we reduce h.

From Figure 5.10a,b, we note that there is a slight increase in the orientational confinement of ellipsoids and cylinders when we reduce the drop height from $h = h_t$ to $h = 0.5h_t$. As discussed in the previous section, this increase comes from the fact that in the immersion regime, particle orientation is determined not only by interfacial curvature, but also by monopolar deformations of the interface. Specifically, since larger monopolar deformations are generated in the perpendicular orientation compared to in the parallel orientation, monopolar forces drive the rods into the parallel orientation, and this effect becomes stronger as we reduce h. Once again, the increase in the confining potential is smaller for cylinders compared to ellipsoids because the flat ends of the cylinder allow it to accommodate different interfacial heights more readily when it is in the perpendicular orientation compared to ellipsoids, thus reducing the monopolar driving force for the parallel orientation.

Interestingly, from Figure 5.10c, we see that for hydrophilic spherocylinders, the orientational confinement is stronger for $h = 0.5h_t$ (immersion regime) compared to for $h = 2h_t$ (flotation regime). This result can be understood from the fact that spherocylinders do not have an intrinsic capillary quadrupole so that the orientational confinement due to interfacial curvature is weak, as evidenced by the fact that the confining potential at $h = 2h_t$ is significantly smaller for spherocylinders compared to ellipsoids and cylinders. This means that the dominant contribution to orientational confinement for spherocylinders comes from monopolar immersion forces, which increase as we decrease h.

It is important to emphasise that although the orientational confinement of the rods is weaker in the immersion regime for some rod shapes, the confinement is still significant for all the rods studied above. Specifically, the well depth of the confining potential at $h = 0.5h_t$ is $\approx 0.02\gamma b^2$ for the ellipsoid, $\approx 0.05\gamma b^2$ for the cylinder and $\approx 0.03\gamma b^2$ for the spherocylinder. For nanoscale rods with $b = 10$ nm adsorbed at an oil-water interface with $\gamma = 30 \times 10^{-3}$ N/m, this translates to well depths of $\approx 15k_BT$, $\approx 40k_BT$ and $\approx 20k_BT$ respectively. This means that the orientational confinement is significant in the immersion regime even for nanorods.

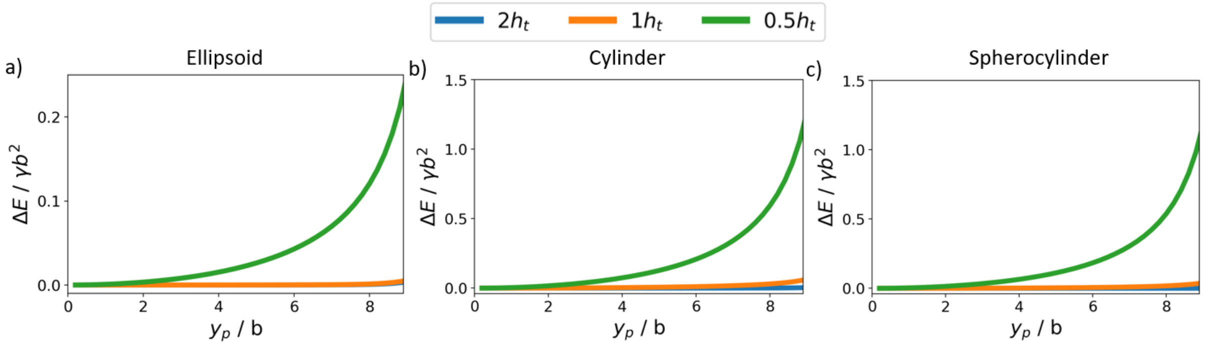

Figure 5.11: Interfacial energy (relative to value at $y_p = 0$) as a function of lateral displacement y_p for different cylindrical drop heights for (a) ellipsoids with $\theta_w = 110°$, (b) cylinders with $\theta_w = 70°$, (c) spherocylinders with $\theta_w = 70°$. Note that the $h = 2h_t$ line in (a) cannot be seen as it lies underneath the $h = h_t$ line.

In order to study the spatial confinement of the rods lateral to the cylindrical drop, in Figure 5.11 we plot interfacial energy (relative to the value at $y_p = 0$) as a function of lateral displacement y_p for hydrophobic ellipsoids, hydrophilic cylinders and hydrophilic spherocylinders respectively, for drop heights of $h = 2h_t, h_t$ and $0.5h_t$. For the results in Figure 5.11, we set $\theta_b = 0°$ since all rods have a parallel equilibrium orientation, and we set $x_p = 0$ to minimise the impact of the reflecting boundary conditions at the cylindrical drop ends in our simulations. We see that for all the rods, the spatial confinement of the adsorbed rods to the centre line of the cylindrical drop ($y_p = 0$) in the flotation regime (i.e., for $h = 2h_t, h_t$) is very weak compared to in the immersion regime (i.e., for $h = 0.5h_t$). As discussed in 0, the very weak spatial confinement in the flotation regime is due to the fact that cylindrical drops have no curvature gradients which we can use to control particle position, and the spatial confinement comes only from the capillary repulsion between the capillary quadrupole of the rods and the pinned contact lines of the sessile drop which is weak and short ranged.[82,83] In contrast, the spatial confinement is very strong in the immersion regime because the confinement is due to monopolar deformations of the liquid interface that come from the mismatch in the height of the rod three-phase contact line compared to the local height of the cylindrical drop, and this mismatch becomes greater for larger lateral displacements of the rod.

Interestingly, from Figure 5.11 we see that confining potential for both cylinders and spherocylinders (Figure 5.11b,c) is significantly greater compared to ellipsoids (Figure 5.11a). We believe that this difference is due to the tips of the ellipsoid being much more rounded compared to cylinders and spherocylinders. This means that for ellipsoids, the monopolar deformations of interface only occur along the middle portion of the rod as the bottom surface of the tips lie above the cylindrical interface, while for cylinders and spherocylinders, the monopolar deformations essentially occur along the whole length of the rod. Notwithstanding this difference, the spatial confinement for all the different rod shapes in Figure 5.11 is very strong in the immersion regime. Specifically, for $h = 0.5h_t$ the well depth of the spatial confining potential (i.e., the potential at $y_p = 9b$, the largest value of y_p that we could access numerically, compared to at $y_p = 0$) is $0.25\ \gamma b^2$, $1.3\ \gamma b^2$ and $1.2\ \gamma b^2$ respectively for the ellipsoids, cylinders and spherocylinders, which translates to $180\ k_B T$, $920\ k_B T$ and $860\ k_B T$ for $b = 10$nm and $\gamma \approx 30 \times 10^{-3}$N/m. In summary, by working in the immersion regime, we can achieve strong orientational and spatial confinement of the adsorbed rods, even in the case of nanorods.

5.3.3 Capillary Interaction and Self-Assembly for Two Rods

Having considered both the orientational and lateral confinement of single particles at a cylindrical interface in the previous section, in this section we consider the interaction and self-assembly of two rods at the cylindrical interface in the immersion regime. To simplify our discussion, we focus on the tip-to-tip interaction and assembly of adsorbed rods and therefore we restrict our analysis to rods with parallel alignment, specifically ellipsoids with $\theta_w = 110°$, cylinders with $\theta_w = 70°$ and spherocylinders with $\theta_w = 70°$. Since our focus is on two-particle configurations that are mirror symmetric (see Figure 5.4c,d), we can simplify our calculations by exploiting the fact that the energy of the two-particle system where both rods are approaching each other is equal to twice the energy of one rod approaching the reflecting boundary of cylindrical drop end. We therefore calculate the energy of the two-rod system by considering a one-rod simulation where we vary the distance of the rod from the reflecting boundary like we covered in Chapter 3.1. Since, as we saw in the previous section, the adsorbed rods are strongly confined to the centreline of the cylindrical drop in the immersion regime, we set $y_p = 0$ in our simulations.

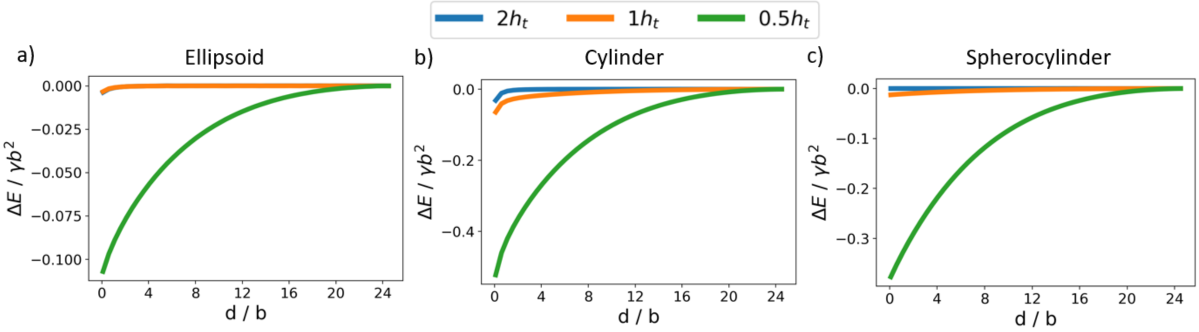

Figure 5.12: Capillary interaction energy between two particles in the tip-to-tip configuration as a function of surface-to-surface separation d for different drop heights for: (a) ellipsoids with $\theta_w = 110°$, (b) cylinders with $\theta_w = 70°$, (c) spherocylinders with $\theta_w = 70°$. Note that the curve for $h = 2h_t$ in (a) cannot be seen as it lies beneath the curve for $h = h_t$.

We first consider the capillary interactions between two rods in the tip-to-tip configuration (see Figure 5.4c), i.e., we set $\theta_b = 0°$ in our simulations. In Figure 5.12a,b,c, we plot the tip-to-tip capillary interaction energy (i.e., energy relative to the energy of the two rods at maximum separation) as a function of the surface-to-surface separation between the rods d for the ellipsoid, cylinder and spherocylinder respectively for $h = 2h_t$, h_t and $0.5h_t$. We see that in all cases, the strength and range of the capillary interaction increases dramatically as we go from $h = 2h_t$ (flotation regime) to $h = 0.5h_t$ (immersion regime). This is not surprising since particle interactions in the flotation regime covered in Chapter 4 are quadrupolar and therefore weak and short ranged (negligible beyond one rod length away), while those in the immersion regime are monopolar and therefore strong and long ranged (significant up to 4 – 5 rod lengths away).[14,48]

Interestingly, we see from Figure 5.12 that the strength of the capillary interactions in the immersion regime decreases as we go from cylinders to spherocylinders to ellipsoids. We believe that this trend is due to the increasingly rounded nature of the particle tips for this sequence of particle shapes which means that the monopolar deformations near the tips occur over a smaller and smaller effective cross-sectional area. Notwithstanding this fact, the capillary bond energy at contact is very large for all the particles in the immersion regime. Specifically, for $h = 0.5h_t$, the capillary bond energy is $0.11\,\gamma b^2$, $0.52\,\gamma b^2$ and $0.38\,\gamma b^2$

respectively for the ellipsoids, cylinders and spherocylinders, which translates to $78\ k_BT$, $380\ k_BT$ and $270\ k_BT$ for $b = 10$nm and $\gamma \approx 30 \times 10^{-3}$N/m.

For parallel rods in the immersion regime, the strong spatial confinement transverse to the cylindrical drop and tip-to-tip capillary interactions between the rods provide a strong driving force for them to form tip-to-tip clusters. However, from the preceding discussion, we see that as we decrease the cylindrical drop height h in the immersion regime, the capillary interaction increases dramatically (Figure 5.12) but the orientational confinement does change significantly (Figure 5.10). We therefore anticipate that if we decrease h too much, we may destabilise the tip-to-tip clusters that are formed since the system can lower its energy by undergoing a roll-over transition to the side-to-side configuration which has a smaller centre-to-centre separation between the rods at contact; note that this transition is also seen for ellipsoids at a flat interface.[49,52] In what follows, we consider the mechanical stability of tip-to-tip clusters in our system against the roll-over transition as we change h in the immersion regime.

We note that the roll-over transition occurs when the two rods in the cluster pivot about their contacting tips in a mirror-symmetric configuration as shown in Figure 5.4d, where the configuration of the cluster during the transition is characterised by the roll-over angle θ_r. Our first task is therefore to calculate the perpendicular distance of each rod centre from the mirror plane r_r as a function of θ_r. For spherocylinders, r_r can be calculated from simple geometry to be $r_r = (a - b)\cos\theta_r + b$. For superellipsoids given by equation (4.1) r_r can be calculated as follows. We first set $z' = 0$ in equation (4.1) since the contact point lies in the $z' = 0$ plane. We next note that the surface normal vector for the rod is given by $\boldsymbol{\nabla} f$, where $f(x', y', z')$ is given by equation (4.1) and $\boldsymbol{\nabla}$ is the 3D grad vector in the lab frame. Since the surface normal vector points in the x direction at the contact point by symmetry, the contact point coordinate satisfies $\partial f/\partial y = 0$. This equation, together with equation (4.1) give us two simultaneous equations which we can solve to find the contact point coordinate (x_c, y_c) and r_r is then given by $r_r = x_c - x_p$. In the case of ellipsoids ($\eta = 1$), we can obtain an analytical expression for r_r as a function of θ_r using this procedure.[88] In the case of cylinders ($\eta = 4$), we can calculate r_r as a function of θ_r numerically using this procedure. Having found r_r for the different rod shapes, we fix x_p such that the rod centre is a distance $r_r + \Delta$ away from the reflecting boundary, where we include a thin exclusion zone of thickness $\Delta = 0.05b$ around each rod to avoid the numerical issues that occur when the rod is in contact with the reflecting boundary.

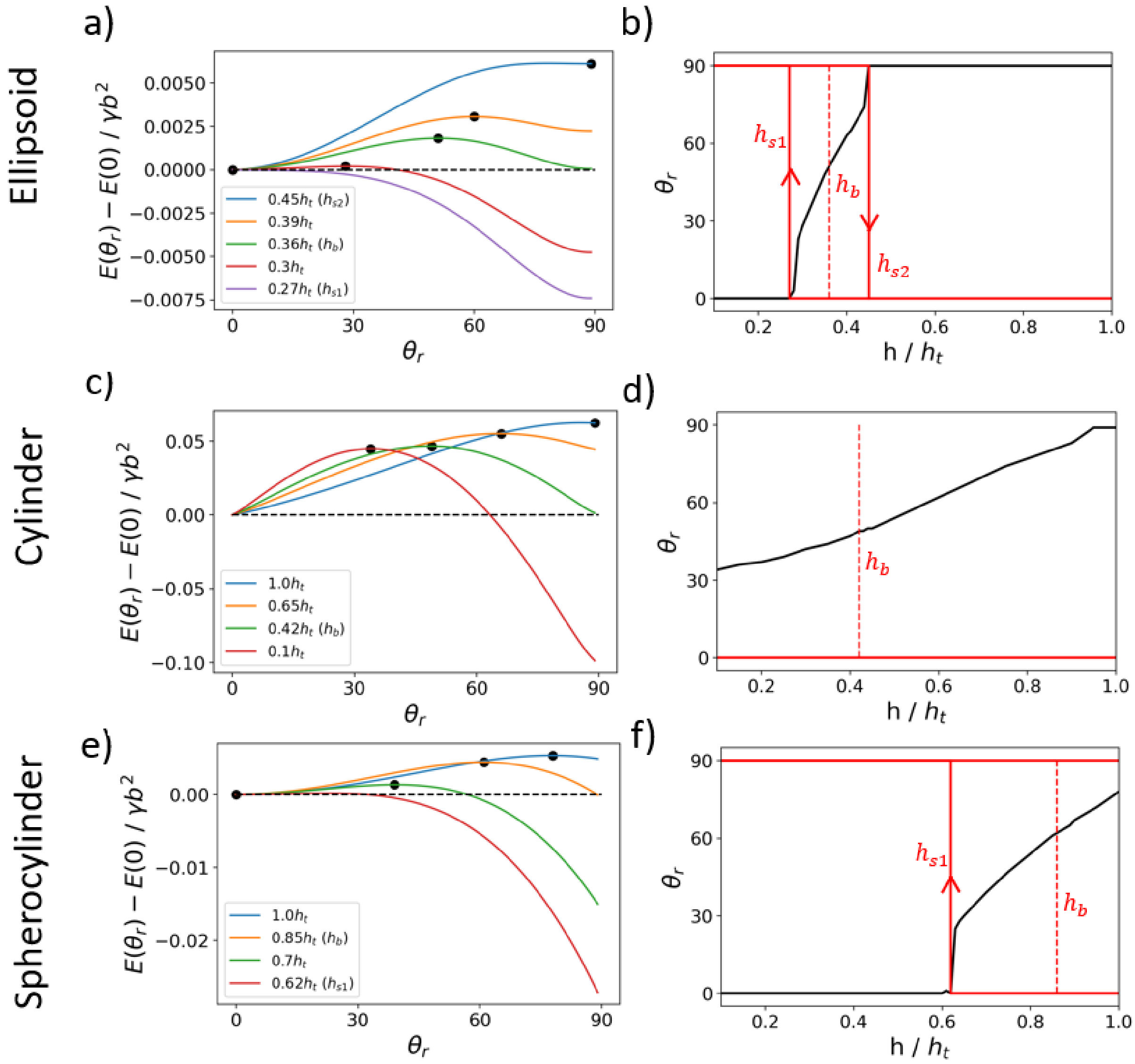

Figure 5.13: (a,c,e) Interfacial energy curves for two particles in contact as a function of the roll-over angle θ_r (relative to the energy at $\theta_r = 0°$) for different drop heights around the roll-over transition for (a) ellipsoids with $\theta_w = 110°$, (c) cylinders with $\theta_w = 70°$, (e) spherocylinders with $\theta_w = 70°$. The filled black circles represent the maxima for each curve. (b,d,f) Locally stable values of θ_r as a function of h (red curve) and the value of θ_r corresponding to the energy barrier maxima as a function of h (black curve) for (b) ellipsoids with $\theta_w = 110°$, (d) cylinders with $\theta_w = 70°$, (f) spherocylinders with $\theta_w = 70°$. The vertical dashed curve denote the thermodynamic roll-over transition at the binodal point $h = h_b$, while the vertical arrows pointing up or down denote the actual roll-over transitions that occur at the spinodal points $h = h_{s1}, h_{s2}$.

In Figure 5.13a, we plot the interfacial energy (relative to the value at $\theta_r = 0°$) as a function of θ_r for hydrophilic ellipsoids for different drop heights h around the roll-over transition. The Savitzky-Golay filter used in Section 5.3.1 is also use in Figure 5.13 in order to smooth out the data and allow us to numerically access information such as the minima or maxima. In this case, the energy scales (and therefore signal-to-noise ratio) is an order of magnitude larger and therefore we opt for a larger order polynomial $M = 10$ for the filter. The higher order polynomial allows the postprocessed data to fit the smoother raw energy curves better and therefore allows us to identify the local minima and maxima more accurately. From

Figure 5.13a, we see that at large h (e.g., the blue curve), there is a single minimum at $\theta_r = 0°$ corresponding to the tip-to-tip configuration, but as we decrease h below a critical value, the energy curve develops a local minimum at $\theta_r = 90°$ corresponding to the side-to-side configuration, which is separated from the primary minimum at $\theta_r = 0°$ by an energy barrier. As h is decreased further to $h_b = 0.36b$ (green curve), the energy of the side-to-side configuration becomes equal to that of the tip-to-tip configuration. At this point, the primary minimum switches from $\theta_r = 0°$ to $\theta_r = 90°$, and the system in principle undergoes a first order (i.e., discontinuous) transition from the tip-to-tip state to the side-to-side state. The height h_b therefore corresponds to the binodal point of the roll-over transition. However, in practice, because the energy barrier between the two minima is typically much larger that $k_B T$, even for rods on the nanoscale, there is significant hysteresis in the roll-over transition. Specifically, for decreasing h, the system only undergoes an irreversible transition from the tip-to-tip state to the side-to-side state when $h = h_{s1} = 0.27b$ (purple curve), where the maxima of the energy barrier shifts to $\theta_r = 0°$ and the local minimum at $\theta_r = 0°$ disappears. On the other hand, for increasing h, the system only undergoes an irreversible transition from the side-to-side state to the tip-to-tip state when $h = h_{s2} = 0.45b$ (blue curve), where the maxima of the energy barrier shifts to $\theta_r = 90°$ and the local minimum at $\theta_r = 90°$ disappears. The heights h_{s1}, h_{s2} therefore correspond to the spinodal points of the roll-over transition.

The key features of the roll-over transition for hydrophobic ellipsoids are summarised in Figure 5.13b where we plot the locally stable values of θ_r as a function of h (red curve) and the value of θ_r corresponding to the energy barrier maxima as a function of h (black curve). We see that at large h, the system is initially in the tip-to-tip state $\theta_r = 0°$. As we decrease h to the binodal point h_b, thermodynamically the system will undergo a first order transition from the tip-to-tip state to the side-to-side state (dashed vertical line). However, as discussed earlier, in practice, it is only when we decrease h to the spinodal point h_{s1} that the system undergoes an irreversible transition from the tip-to-tip state to the side-to-side state (solid vertical line pointing up). Similarly, when the system is initially in the side-to-side state $\theta_r = 90°$ at low values of h, it is only when we increase h to the spinodal point h_{s2} that the system undergoes an irreversible transition from the side-to-side state to the tip-to-tip state (solid vertical line pointing down). Note that the spinodal points h_{s1} and h_{s2} are the values of h where the energy maxima curve (black curve) first meets $\theta_r = 0°$ and $\theta_r = 90°$ respectively. Note also that points to the right of the binodal point on the bottom branch of the red curve and to the left of the binodal point on the top branch of the red curve are equilibrium states while all other points on the red curve are metastable states.

In Figure 5.13c, we plot the interfacial energy (relative to the value at $\theta_r = 0°$) as a function of θ_r for hydrophilic cylinders for different drop heights h. Once again, we see that at large h (e.g., the blue curve), there is a single minimum corresponding to the tip-to-tip configuration, but as we decrease h, the energy curve develops a local minimum at $\theta_r = 90°$ which is separated from the primary minimum at $\theta_r = 0°$ by an energy barrier. As h is decreased further to the binodal point $h_b = 0.42b$ (green curve), the energy of the side-to-side configuration becomes equal to that of the tip-to-tip configuration and thermodynamically, the system should undergo a first order transition from the tip-to-tip state to the side-to-side state at this point. However, this transition does not occur in practice because the energy barrier between the two minima is generally too large. Interestingly, for cylinders, the local minima at $\theta_r = 0°$ does not disappear, or equivalently the maximum of the energy barrier does not shift to $\theta_r = 0°$, even at the lowest drop height we studied at $h = 0.1h_t$ (red curve). This means that cylinders effectively do not have a lower spinodal point h_{s1} so that they do not undergo a roll-over transition from the tip-to-tip state to the side-to-side state even for small h. Interestingly, cylinders adsorbed at flat interfaces also do not undergo a roll-over transition because they are prevented from doing so by the capillary ‘hinges’ between contacting cylinders created by the sharp edges of the cylinders.[49] The significant and persistent energy barrier we see in Figure 5.13c is presumably due to the same effect. The key features of the roll-over transition for hydrophilic cylinders discussed above are summarised in Figure 5.13d where all the lines have the same meaning as in Figure 5.13b.

Finally, in Figure 5.13e we plot the interfacial energy (relative to the value at $\theta_r = 0°$) as a function of θ_r for hydrophilic spherocylinders for different drop heights h. Interestingly, we see that even at $h = h_t$ (blue curve), while the primary minimum is at $\theta_r = 0°$, there is already a local minimum at $\theta_r = 90°$, suggesting that spherocylinders do not have an upper spinodal point h_{s2}. As h is decreased to the binodal point $h_b = 0.85b$ (orange curve), the energy of the side-to-side configuration becomes equal to that of the tip-to-tip configuration. Thermodynamically, the system undergoes a first order transition from the tip-to-tip state to the side-to-side state at this point, but in practice this transition only occurs when we decrease h further to the lower spinodal point $h_{s1} = 0.62b$, where the maxima of the energy barrier shifts to $\theta_r = 0°$ and the local minimum at $\theta_r = 0°$ disappears. The key features of the roll-over transition for hydrophilic spherocylinders discussed above are summarised in Figure 5.13f where all lines have the same meaning as in Figure 5.13b.

We note that the effective roll-over transition height h_{s1} is significantly greater for spherocylinders ($h_{s1} \approx 0.62h_t$) compared to ellipsoids ($h_{s1} \approx 0.27h_t$) and cylinders ($h_{s1} \approx 0$). Since the strong lateral spatial confinement needed to align the rods into the tip-to-tip configuration requires us to work in the immersion regime $h < h_t$, this means that it is easier to use our capillary assembly method to prepare tip-to-tip assemblies of ellipsoids and cylinders compared to spherocylinders because the drop height window over which we can prepare tip-to-tip assemblies ($h_{s1} < h < h_t$) is much wider for the former compared to the latter. Finally, we note that the results in this section provide insights into how the structure of clusters of rods adsorbed at cylindrical drops evolve during the drying of the droplet.

5.4 Conclusions

We have used the finite element method Surface Evolver to study the capillary assembly of rod-shaped particles adsorbed at a sessile liquid drop with cylindrical geometry. Specifically, we considered the immersion regime where the drop height is less than the radius of the rods and the lateral width of the cylindrical drop is much greater than the length of the rods, and we studied the configuration of single and multiple rods as a function of drop height, particle shape (ellipsoid, cylinder, spherocylinder) and contact angle.

We found that for low enough drop heights, regardless of the shape or contact angle of the rods, all rods orientate themselves parallel to the long axis of the cylindrical drop and are strongly confined laterally to be at the centre line of the cylindrical drop. We also found that the rods experience strong and long-range immersion capillary forces which assemble the rods tip-to-tip at larger drop heights and, in the case of ellipsoids and spherocylinders, side-to-side when we reduce the drop height, for example through drying. We note that the capillary forces discussed above are very strong, allowing us to order rods even on the nanoscale.

The fact that we can control the self-assembly of rods using cylindrical drops whose lateral dimensions are much greater than the length of the rods allows us, for example, to control the configuration of nanorods using near micron-scale droplets, greatly simplifying the task of fabricating the liquid templates required to realise this assembly method. Our capillary assembly method therefore provides a facile method for organising micro- and nanoscale objects into complex cluster structures and we hope that our study will stimulate future experiments in this direction.

Chapter 6 Self-Assembly of Spherical Core-Shell Particles at Flat Fluid Interfaces

6.1 Introduction

In the previous two chapters, we considered the self-assembly of non-spherical particles at a liquid interface. In this chapter, we will consider the self-assembly of spherical particles. The structural motifs accessible to 2D colloidal assembly are typically determined by the shape of the particles via their most efficient packing. In particular, the general propensity of spherical particles to assemble into hexagonal lattices limits the versatility of using spherical building blocks to create complex structures. However, an elegant solution to directly decouple particle shape from the resulting self-assembled phases has been theoretically proposed decades ago. In 1998, Jagla showed that a simple addition of a soft repulsive shell surrounding a hard sphere introduces a second length scale in the interaction potential, which allows for the creation of nonhexagonal minimum energy configurations (MECs) such as chains, squares, and rhombic phases.[98] The formation of such counterintuitive phases results from the competition between the two length scales in the interaction: when the core–shell particles are compressed such that their shells begin to touch, the system can minimize its energy by fully overlapping neighbouring shells in some directions to prevent the overlap of shells in other directions.[99–101] Jagla further showed that through the use of a 'generic' potential (see Section 6.2.1), controlled by a single parameter g (where $g = 1$ produces a linear potential profile (as seen in Figure 3.5a), $g < 1$ results in a concave down potential (similar to Figure 3.5b), and $g > 1$ results in a concave up potential), that he could tune the resultant self-assembly behaviour. In particular, the minimum energy phase in such core–shell systems is determined by three parameters: the ratio of the shell-to-core diameter (r_1/r_0), the shape of the soft repulsive potential, and the area fraction of the system η, which determines the total amount of shell overlap.[98,102] Since this initial discovery, many theoretical reports have shown that dozens of different structures can originate from simple spherical particles interacting via such Jagla-like 'generic' potentials, including honeycombs, or quasicrystals of various symmetries for relative small shell-to-core ratios ($r_1/r_0 \lesssim 2$),[101–104] as well as defined particle clusters and complex chains phases at higher shell-to-core ratios ($r_1/r_0 \gtrsim 2$).[99,105–108]

In contrast to this theoretical understanding, the experimental progress of such systems has remained largely elusive. The fundamental bottleneck that has impeded the experimental realization of such complex assembly phases is the difficulty of engineering suitable interaction potentials. For a system to form Jagla phases, two stringent requirements need to be met. First, the particle interaction potential requires two distinct length scales as described earlier and, in particular, a soft repulsive shell with a concave down shape,[98,100,101] meaning that the repulsion should have at least a linear ramp profile ($g \lesssim 1$). Second, the interaction potentials need to be strictly pairwise additive (i.e., many-body effects where the interaction between two core–shell particles is influenced by the presence of other neighbouring particles need to be avoided).

In principle, interaction potentials satisfying the two length scale criteria can be implemented experimentally using core–shell particles consisting of a solid, incompressible core and a compressible shell. Microgels[109] are ideally suited as shell material because of their soft nature and their ability to deform under the influence of surface tension.[110–113] In particular, when adsorbed at a liquid interface, microgels with and without a solid core exhibit a pronounced, very thin corona at the periphery, which is formed by the interfacial spreading of dangling chains.[114–118] This corona acts as a compressible spacer between the cores, effectively introducing a repulsive shoulder to the interaction potential.

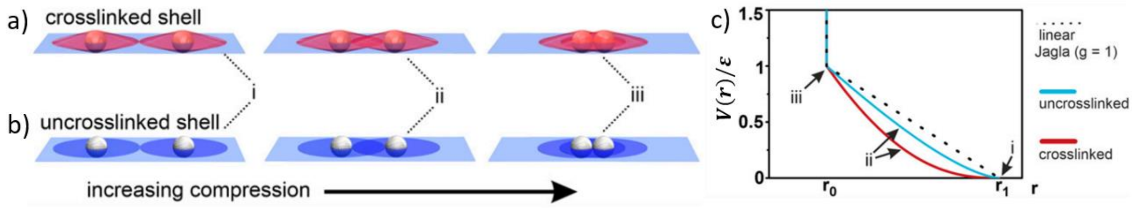

Figure 6.1: a) 3D representation of crosslinked core-microgel particle at the air water interface during i) shell-to-shell contact, ii) during shell overlap, and iii) at core-to-core contact. b) 3D representation of the uncrosslinked core-microgel particles studied in this Chapter at the air water interface during i) shell-to-shell contact, ii) during shell overlap, and iii) at core-to-core contact. c) potential profile of core-shell particles with a linear potential profile as one of the examples proposed by Jagla ($g = 1$) and potential profiles for the crosslinked and uncrosslinked core-microgel particles assuming that the potential is proportional to the area/volume of overlap.

However, despite their interfacial core–corona morphology, for pure microgels[25,119] and typical core–microgel shell systems,[26,120,121] only an isostructural hexagonal non–close packed to hexagonal close-packed transition is observed. This behaviour has been rationalized by the quasi–three-dimensional shape that these particle systems retain despite their deformation at the interface (Figure 6.1a). Due to their crosslinked nature, the shell protrudes significantly into the water subphase.[111] This interfacial morphology causes a rapid increase in shell overlap upon compression. If the energy penalty associated with the compression of the polymer shell scales with the overlap volume, this interfacial morphology therefore can be assumed to form a concave down shape for the interaction potential (See Appendix 2, Figure 6.1c).

This results in a potential profile similar to a Jagla potential with a g parameter much less than 1, which is not sufficient for observing complex assembly phases.[100–102] In contrast, the only reports of anisotropic chain phases to date were observed in interfacial systems with extremely flat coronae, formed by binary mixtures of polystyrene microspheres and very small microgels,[100] and core–shell particles with a pronounced crosslinker gradient.[122] These examples indicate that the ideal interfacial morphology to achieve Jagla-type interaction potentials with sufficiently large g-parameters is a core–shell system with an effectively 2D shell, where the overlap volume increases nearly linearly with compression. Again, assuming that the overlap volume is proportional to the resultant energy penalty, this results in a near-linear ramp potential (i.e., $g \approx 1$) (see Appendix 2, Figure 6.1b,c).

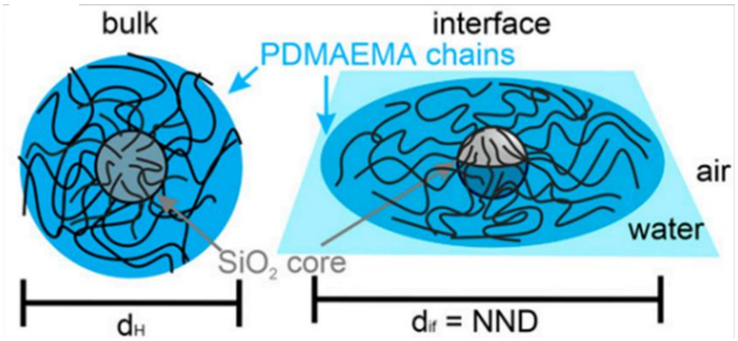

Figure 6.2: Cartoons of uncrosslinked microgel core-shell particles in the bulk, and at the interface where the chains spread to form a 2D corona.

The interconnected nature of a crosslinked microgel shell not only limits the interfacial spreading but also forces the polymer chains in the corona to react in a concomitant manner. Specifically, upon compression, cross-linked shells are forced to distribute stress across the entire shell. Consequently, a collapse of the shell with one neighbouring particle also facilitates the collapse of the same shell with other neighbouring contacts. It has been shown that such many-body interactions destabilize the formation of anisotropic Jagla phases and bias the system toward the conventionally observed isostructural phase transitions.[122]

To circumvent the problems associated with conventional core–shell, in this Chapter, we consider core-shell particles consisting of an inorganic silica core functionalized with individual, noncrosslinked, and surface-active polymer chains (Figure 6.2). As we will see, at a liquid interface, the polymer chains in these hairy particles spread very efficiently and form an effectively 2D corona, which as we argued earlier translates into a near-linear repulsive potential. By completely avoiding any crosslinking in the shell, we also ensure that mechanical stress, arising from a local shell collapse upon compression, is not translated throughout the entire microgel shell. This, in turn, facilitates the partial and anisotropic collapse of a single shell in the vicinity of a neighbouring particle. In the Jagla terminology, this behaviour reflects a pairwise-additive character of the interaction potential. The experimental particle system thus fulfils both the stringent conditions required for the formation of Jagla phases. As we will see later, upon compression, these particles indeed form a series of complex 2D phases. In this chapter, we will study the self-assembly of such core-shell hairy particles at a liquid interface using minimum energy calculations and Monte Carlo simulations.

6.2 Theoretical Methods

6.2.1 Jagla Potential

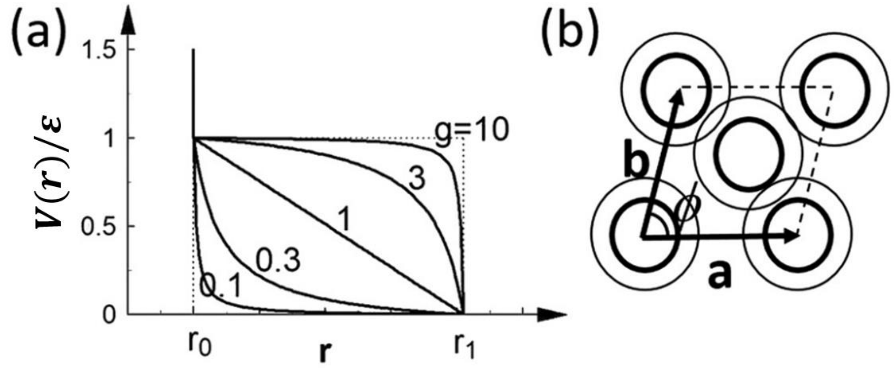

Figure 6.3: (a) Jagla potential for different values of g. The dotted lines on the Left and the Right correspond to $g = 0$ (no shoulder) and $g = \infty$ (square shoulder), respectively. (b) Two-particle unit cell used in the minimum energy calculations, where $\boldsymbol{a}, \boldsymbol{b}$ are the lattice vectors, ϕ is the unit cell angle, and the thick and thin circles represent the particle core and shell, respectively.

As mentioned in the introduction Jagla proposed a 'generic' two length scale potential which is given by the piecewise function

$$V(r) = \begin{cases} \infty & , r < r_0 \\ \varepsilon \dfrac{g + \left(\left(\dfrac{r/r_0 - 1}{r_1/r_0 - 1} \right) (g - g^{-1}) - g \right)^{-1}}{g - g^{-1}} & , r_0 \leq r \leq r_1 \\ 0 & , r > r_1 \end{cases} \tag{6.1}$$

where r is the separation between the interacting particles, r_0, r_1 are the range of the hard-core and soft-shell repulsion, respectively, ε is the height of the soft-shell potential, and the parameter g controls the profile of the soft-shell interactions. Specifically, $g > 1$ leads to concave up potentials, $g < 1$ leads to concave down potentials and $g = 1$ leads to linear ramp potentials (see Figure 6.3a).

6.2.2 Minimum Energy Calculations

In order to determine the equilibrium structures formed by core-shell particles when they are compressed in two dimensions, we calculate the minimum energy configurations (MECs) of the system, i.e., the equilibrium structure at zero temperature. The zero-temperature regime is relevant so long as the energy scale of the soft-shell repulsion is much greater than the thermal energy, i.e. $T^* \ll 1$ (Appendix 3). As we shall see later in Section

6.3.3, we perform a comprehensive exploration of all two-dimensional structures containing (up to) two particles per unit cell for core-shell particles with $r_1/r_0 = 4$. Specifically, we can define the unit cell as a parallelogram spanned by two lattice vectors $\boldsymbol{a} = a(1,0)$, $\boldsymbol{b} = a\gamma(\cos\phi\,,\sin\phi)$, where ϕ is the angle between the lattice vectors, $\gamma = b/a$ is the aspect ratio of the unit cell and a, b are the lattice constants (see Figure 6.3b). Within this unit cell, the first particle is at $(0,0)$ (without loss of generality) while the second particle is at $\boldsymbol{r} = \alpha\boldsymbol{a} + \beta\boldsymbol{b}$, where $\alpha, \beta \in (0, 1)$ are the coordinates of the second particle in the lattice basis set.

When calculating the zero-temperature phase diagram, it is convenient to work in the NPT ensemble where the area per particle is variable. This is because the system exists as a single phase in the NPT ensemble except at the coexistence pressure between two or more phases. Specifically, parameterising the area per particle as $\sqrt{3}\ell^2/2$, where ℓ is the lattice constant of the system in the hexagonal phase, and noting that the area per unit cell is $a^2\gamma\sin\phi$, for two particles per unit cell, the lattice constant a is fixed by the condition $(a^2\gamma\sin\phi)/2 = \sqrt{3}\ell^2/2$. We can therefore express a as a function of ℓ, γ and ϕ as $a = \ell\left(\frac{\sqrt{3}}{\gamma\sin\phi}\right)^{\frac{1}{2}}$. Note that the number density of core-shell particles (i.e., number of particles per unit area) is given in terms of the parameter ℓ by $\rho = 2/(\sqrt{3}\ell^2)$ while the core area fraction is given by $\eta = \pi r_0^2/(2\sqrt{3}\ell^2)$.

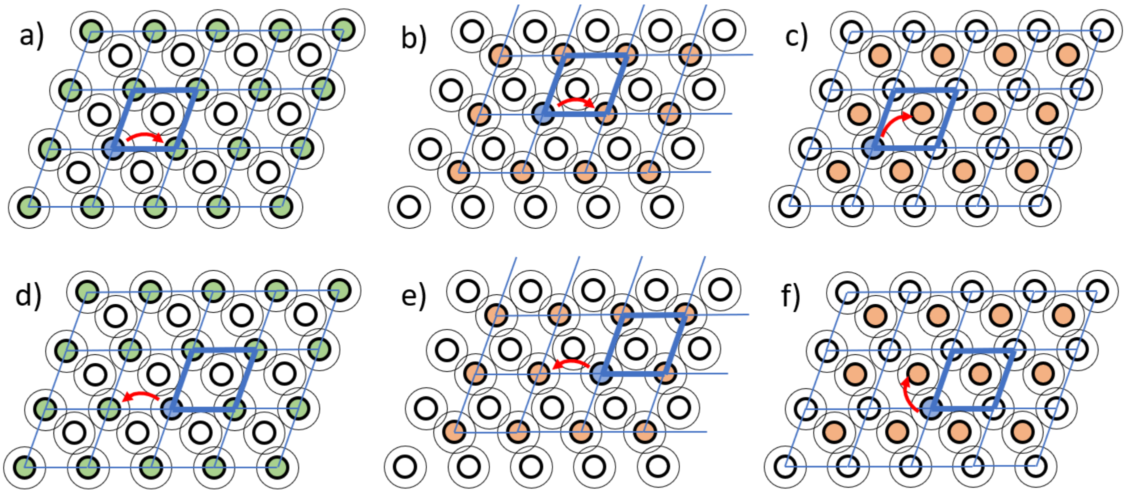

Figure 6.4: Schematics for lattice sum calculations. In a,d) particle 1-particle1 interactions, b,e) particle 2-particle 2 interactions, and c,f) particle 1-particle 2 interactions. The two rows (a-c and d-f) correspond to using a different unit cell to form the basis of our lattice sum. The parallelograms bounded by blue lines represent the unit cells in the crystal and the parallelogram bounded by thicker blue lines represents the specific unit cell we are using as the 'starting' unit cell when performing the lattice sum calculation (see main text). The green, orange and blue particles represent particle 1, particle 2 and the origin particle in the highlighted unit cell respectively. The red arrow represents an interaction of the origin particle with a neighbour.

In the NPT ensemble, the equilibrium state is found by minimising the Gibbs free energy, or more specifically by minimising the enthalpy when we are at zero temperature. To simplify the calculation of the N bodied system it is convenient for us to derive an expression in terms of total enthalpy per particle. To calculate this, we first look at the interaction energy per unit cell between all identical particles, i.e., particle 1–particle 1 and particle 2-particle 2. The interaction energy per unit cell for particle 1 within the unit cell interacting with all other particle 1's (see Figure 6.4a) is

$$E_{11} = \sum_{h,k \neq 0,0} V(|h\boldsymbol{a} + k\boldsymbol{b}|) \tag{6.2}$$

The particle 2-particle 2 interactions can be calculated in a similar way, in fact, if we move our origin to be the centre of particle 2, we can see that Equation (6.2) also describes the particle 2-particle 2 interactions (see Figure 6.4a,b). Therefore, the interaction per unit cell between like particles is just double that of equation (6.2). In addition, to calculate the total energy of the system from interactions between like particles, we need to sum the interaction energy above over all m unit cells in the system, so equation (6.2) becomes

$$E_{like}^{tot} = \sum_{m\ unit\ cells} \sum_{h,k \neq 0,0} 2\, V(|h\boldsymbol{a} + k\boldsymbol{b}|) \tag{6.3}$$

However, as can be seen from Figure 6.4a,d and Figure 6.4b,e when calculating the interactions starting from different unit cells, we double count each pair interaction. By including a factor of $1/2$ to remove double counting and summing and recognising that the interaction per unit cell is the same regardless of which unit cell we start from, we have

$$E_{like}^{tot} = m \sum_{h,k \neq 0,0} V(|h\boldsymbol{a} + k\boldsymbol{b}|) \tag{6.4}$$

Next, we calculate the interaction energy per unit cell between all unlike particles, i.e., particle 1-particle 2 interactions (Figure 6.4c) which is calculated by

$$E_{unlike} = \sum_{h,k} V(|h\boldsymbol{a} + k\boldsymbol{b} + \alpha\boldsymbol{a} + \beta\boldsymbol{b}|) \tag{6.5}$$

To obtain the total interaction energy from unlike particles, we once again need to consider the interactions starting from different unit cells. However, as can be seen in Figure 6.4c,f, when calculating the interactions from other unit cells, there is no double counting of the interactions in this case. This means that the total energy of the system from the interaction of unlike particles is

$$E_{unlike}^{tot} = m \sum_{h,k} V(|h\boldsymbol{a} + k\boldsymbol{b} + \alpha\boldsymbol{a} + \beta\boldsymbol{b}|) \tag{6.6}$$

The sum of equation (6.4) and (6.6) give the total interaction energy due to all particle interactions. In order to find the interaction energy per particle in this system we need to divide by $2m$ (as there are two particles per m unit cells) making the total interaction energy per particle

$$E = \frac{1}{2}\left[\sum_{h,k\neq 0,0} V(|h\boldsymbol{a} + k\boldsymbol{b}|) + \sum_{h,k} V(|h\boldsymbol{a} + k\boldsymbol{b} + \alpha\boldsymbol{a} + \beta\boldsymbol{b}|)\right] \tag{6.7}$$

Finally, to calculate the enthalpy per particle ($H = E + PV$) for crystals containing two particles per unit cell we add the product of the surface pressure P and area per particle as discussed earlier to obtain

$$H = \frac{1}{2}\left[\sum_{h,k\neq 0,0} V(|h\boldsymbol{a} + k\boldsymbol{b}|) + \sum_{h,k} V(|h\boldsymbol{a} + k\boldsymbol{b} + \alpha\boldsymbol{a} + \beta\boldsymbol{b}|)\right] + \frac{\sqrt{3}}{2} P\ell^2 \tag{6.8}$$

Both summations run over all integer values of h, k satisfying $|h\boldsymbol{a} + k\boldsymbol{b}| \leq r_c$ (except for $h, k = 0,0$ in the first sum), where r_c is the cut-off radius for interactions. Since we are considering interactions with a finite range of r_1, we are able to use a short cut-off length of $r_c/r_0 = r_1/r_0 + 1$.

In order to calculate the zero-temperature phase diagram, we determined the MECs of the system as a function of g and P (the parameter ε is irrelevant at zero temperature) by minimising H given in equation (6.8) with respect to the lattice parameters ϕ, γ, ℓ, α and β. Since this is a relatively high dimensional minimisation, the minimisation proceeded via several stages. We first minimised H over a relatively wide range of values for the lattice parameters to obtain an initial estimate for their equilibrium values. We then further minimised H over a much smaller range around these initial estimates to obtain more refined estimates for the equilibrium lattice parameters.

6.2.3 Monte Carlo Simulation – Slow Cool Simulations

In this Chapter we use Monte Carlo simulations as covered in Section 3.2 to study the self-assembly of core-shell particles as a function of area fraction η. Specifically, for the slow cool MC simulations used to scan phases formed at different g values, we used 1,024 core–

shell particles interacting via the Jagla potential (equation (6.1)) in a fixed rectangular simulation box with aspect ratio of $2:\sqrt{3}$ starting with particles in a hexagonal lattice at the desired area fraction. The particles were first disordered at the reduced temperature of $T^* = 100$, then brought to the final temperature $T^* = 0.005$ through a slow cool process by successively quenching to $T^* = 0.5, 0.3, 0.2, 0.1, 0.08, 0.06, 0.04, 0.03, 0.02, 0.01$, and 0.005. We use this slow cooling procedure to reduce computation time, whilst still allowing the simulation to be ergodic. For example, at $T^* = 0.5$ the system will still move into more energetically favourable states, but this is easily reversible, whereas at $T^* = 0.005$ the system evolves very slowly, and the system will almost always only move to more energetically favourable states. Note that even though T^* is changing as the system evolves, we are still in the NVT ensemble as we are effectively simulating at fixed T^* where the starting particle distribution is the final evolution from the previous T^*. The system was equilibrated for 10^5 attempted moves per particle at each temperature.

6.2.4 Monte Carlo Simulations – Compression Simulations

As we shall see later in this Chapter, in the experiments, the different area fractions of the core-shell system were accessed by subjecting the system to a uniaxial compression in a Langmuir trough. In order to match the experimental system more accurately and capture the kinetic history of the system, in addition to the slow cool simulations described above, we also perform compression MC simulations. Specifically, we use an elongated rectangular simulation box with aspect ratio $8:\sqrt{3}$ was used instead. The particles were initially set out in a low density (no shell overlaps) hexagonal lattice at an area fraction of $\eta = \pi r_0^2/(2\sqrt{3}r_1^2)$ through the slow cool protocol described in the Results section. Higher area fractions were then accessed by slowly reducing the length of the simulation box along its long dimension by steps of $r_0/5$ and affinely displacing all particles at each compression step. The system was equilibrated by 3×10^4 attempted moves per particle between each compression. A reduced temperature of $T^* = 0.005$ was used throughout these simulations, as this represents a good compromise between satisfying the experimental condition that $\varepsilon \gg k_B T$ (see Appendix 3) while still being computationally accessible in terms of system equilibration times. A higher temperature of $T^* = 0.02$ was used for the thin shell case $r_1/r_0 = 2.5$ to account for the fact that in the experimental system, attractive capillary forces cannot be ignored in the thin shell regime, and these lead to a softening of the thin shell repulsion. Multiple compression runs (around 10) were carried out to increase the effective sample size from which to identify the different defined phases. To remove any core overlaps arising from the affine displacement of the particles, the hard-core region $r < r_0$ of the potential in equation (6.1) was replaced with a very high inverse power law potential $\varepsilon(r/r_0)^{-30}$, which led to a very efficient removal of core overlaps when the Metropolis acceptance criteria was applied. Note that the compression MC simulations produced severe finite size effects at high compressions as the uniaxial compression from low-density results in very small dimensions of the simulation box along the compression axes.

6.2.5 Cluster Analysis

In order to categorise particle aggregates for colouring and statistics we use a clustering algorithm. In both experiments and simulations, particle cores which according to visual inspection are in contact generally have particle separations greater than r_0. To correctly capture particle aggregates from the snapshots, we therefore define a threshold separation below which cores are considered to be in contact. For our MC simulations, we define this threshold separation to be $1.4r_0$ for the particles with thicker shells ($r_1/r_0 = 4.0,\ 5.0$) and $1.25r_0$ for the particles with thinner shells ($r_1/r_0 = 2.5$). For the experimental data, we define this threshold separation to be $1.4r_0$ for particles with thin shells (20-min irradiation). For particles with thicker shells (i.e., 80- and 320-min irradiation), a fixed threshold separation did not accurately capture clusters since with increased area fraction, there is a greater proportion of collapsed polymer chains between contacting cores leading to a larger core–core separation. To account for this effect, we define the threshold separation to be $(1.4 + 2\eta)r_0$ for the thicker shell experimental systems. Having defined the threshold separation, we define an aggregate as a group of particles where each particle is in contact with at least one other particle in the group. For aggregates containing five or more particles, we differentiate between chains and clusters by calculating the gyration tensor of the aggregate

$$\boldsymbol{S}_{mn} = \frac{1}{2N_a^2}\sum_{i=1}^{N_a}\sum_{j=1}^{N_a}(\boldsymbol{r}_m^{(i)} - \boldsymbol{r}_m^{(j)})(\boldsymbol{r}_n^{(i)} - \boldsymbol{r}_n^{(j)}) \tag{6.9}$$

where N_a is the number of particles in the aggregate, and $r_n^{(i)}$ is the x or y coordinate of the i^{th} particle in the aggregate ($n = x, y$). The eigen values of the symmetric 2 × 2 gyration tensor give the mean squared separation of particle pairs in the aggregate along the long and short axes of the aggregate (i.e., along the eigen vectors). We define an aggregate to be a chain if the ratio of the eigen values exceeds 10 (i.e., long axis/short axis $\geq \sqrt{10}$). For the compression MC simulations, this scheme for classifying chains and clusters breaks down at high compressions when the length of chains become comparable to the shortest dimension of the simulation box and periodic boundary conditions start to interfere with the calculation of the gyration tensor. To get around this problem, we classify any aggregate containing more than 100 particles to be a chain, as we observe from our MC simulations that there are no clusters containing more than 100 particles. The resulting particle categorization is used for statistical analysis of the phases and for the creation of colorized monolayer representations, where the cores are represented by circles with a radius of $r_0/2$ in simulation and 85 nm in experiment.

6.3 Results and Discussion

6.3.1 Summary of Experimental Data

The computational work in this chapter was motivated and guided by experimental results generated by our colleagues at the Friedrich-Alexander University in Germany. To provide context for our theoretical study, in this Section, we report the key experimental data produced by our experimental colleagues as this is the data that we will seek to model in this Chapter. Further details about the experiments can be found in Menath, J. *et al.* Defined core–shell particles as the key to complex interfacial self-assembly. *Proc. Natl. Acad. Sci.* **118**, 1–10 (2021).

To fabricate the particles, silica core particles ($d = 170$ nm) were functionalized with the iniferter using silane chemistry (56, 57).[123,124] Subsequently, they graft poly(2-dimethylaminoethyl) methacrylate (PDMAEMA) polymer chains from these cores in an ultraviolet (UV) light ($\lambda = 365$nm) using initiated controlled radical polymerization. The key advantage of this reaction is that it allows a convenient yet precise control of the shell thickness via the exposure time. This is important as the length of the polymer chains controls the interfacial dimensions of the particles and, therefore, the radius of the repulsive shell (r_1) in the assumed interaction potential.

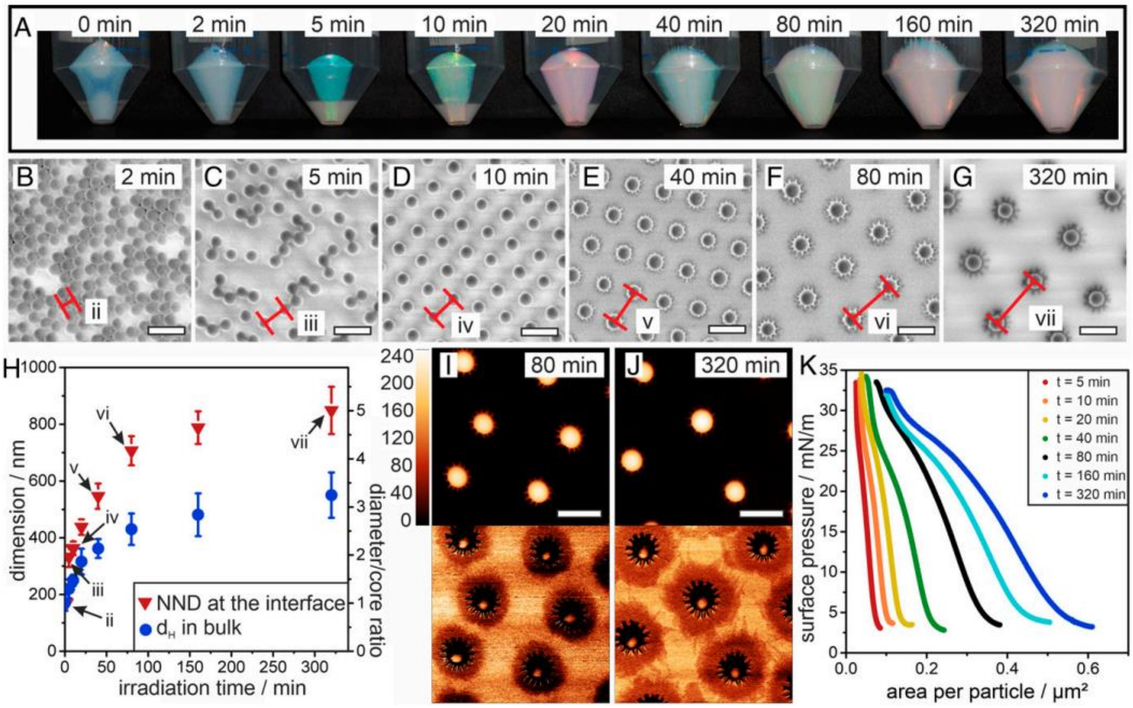

Figure 6.5: Shell growth for PDMAEMA@SiO2 core–shell particles. (A) Photographs of core–shell particles after centrifugation. An increase in mass and particle dimensions can be observed from the colour change with increasing irradiation time. (B–G) SEM images of the core–shell particles transferred to a solid substrate from the air/water interface at a surface pressure of 5 mN/m. The distance between two particles is marked in red. (H) Dimension of the core–shell particles with increasing irradiation time, measured by dynamic light scattering in the bulk (i.e., the hydrodynamic diameter d_H, polydispersity index width as error bars) and by determination of the NND from SEM images (standard deviation σ as error bars). (I and J) AFM height (Top) and phase (Bottom) images of particles irradiated for 80 (I) and 320 (J) min. (K) Surface pressure-area isotherms for the different core–shell particle systems (Scale bar: 500 nm).

Figure 6.5A shows photographs of dispersions of hairy particles after increasing UV exposure time up to 320 min. The increase in shell thickness can be directly observed by the colour change of the colloidal crystal formed upon centrifugation (Figure 6.5A).[125,126] The photonic stop band shifts through the visible spectrum as the spacing of the silica cores in the formed crystal increases. The shell growth can also be seen in the increase in hydrodynamic diameter (d_H measured by dynamic light scattering in Figure 6.5H. The diameter increases from 170 nm at 0 min of irradiation to 550 nm at 320 min of irradiation, corresponding to a shell thickness of 190 nm in bulk.

Subsequently, colloidal monolayers were formed by spreading the particles at an air/water interface and investigate the resulting interfacial morphologies using the simultaneous compression–deposition technique on a Langmuir trough.[127] Stable non-close packed phases with increasing interparticle distance emerge from irradiation times of 10 min or more (Figure 6.5 D–G), indicating that the corona reliably separates the individual cores at the liquid interface. Note that the absence of particles in direct contact indicates that the transferred colloidal monolayer retains its interfacial arrangement as immersion capillary forces upon drying would inherently push particles together, as is the case for shorter irradiation. These findings corroborate previous reports and demonstrate that this ex-situ analysis can yield an accurate picture of their interfacial morphology and phase behaviour.[25,116,117,122] Using image analysis, the experimentalists extract the average nearest-neighbour distance (NND), which they take as a proxy for the interfacial corona dimensions, since the particles can be assumed to be in corona–corona contact at the interface at this surface pressure (Figure 6.5H).[113,118]

Atomic force microscopy (AFM) phase contrast images, shown in Figure 6.5I and Figure 6.5J for core–shell particles from irradiation times of 80 and 320 min, respectively, give direct evidence of the interfacial morphology. The solid core is surrounded by a pronounced, extended 2D corona. The very thin, quasi-2D nature of this corona is obvious from the fact that it is revealed in phase contrast but not visible in the height image. The star-shaped appearance of core–shell particles with longer polymer chains (Figure 6.5F, G, I, and J) indicates a bundling of polymer chains close to the core, presumably by collapse of polymer chains protruding into the water subphase upon drying. The increasing dimensions of the coronae is also reflected in the surface pressure-area isotherms shown in Figure 6.5K, which show a continuous shift to larger areas per particle and an increasing compressibility of the interfacial assembly for samples with increasing exposure times.

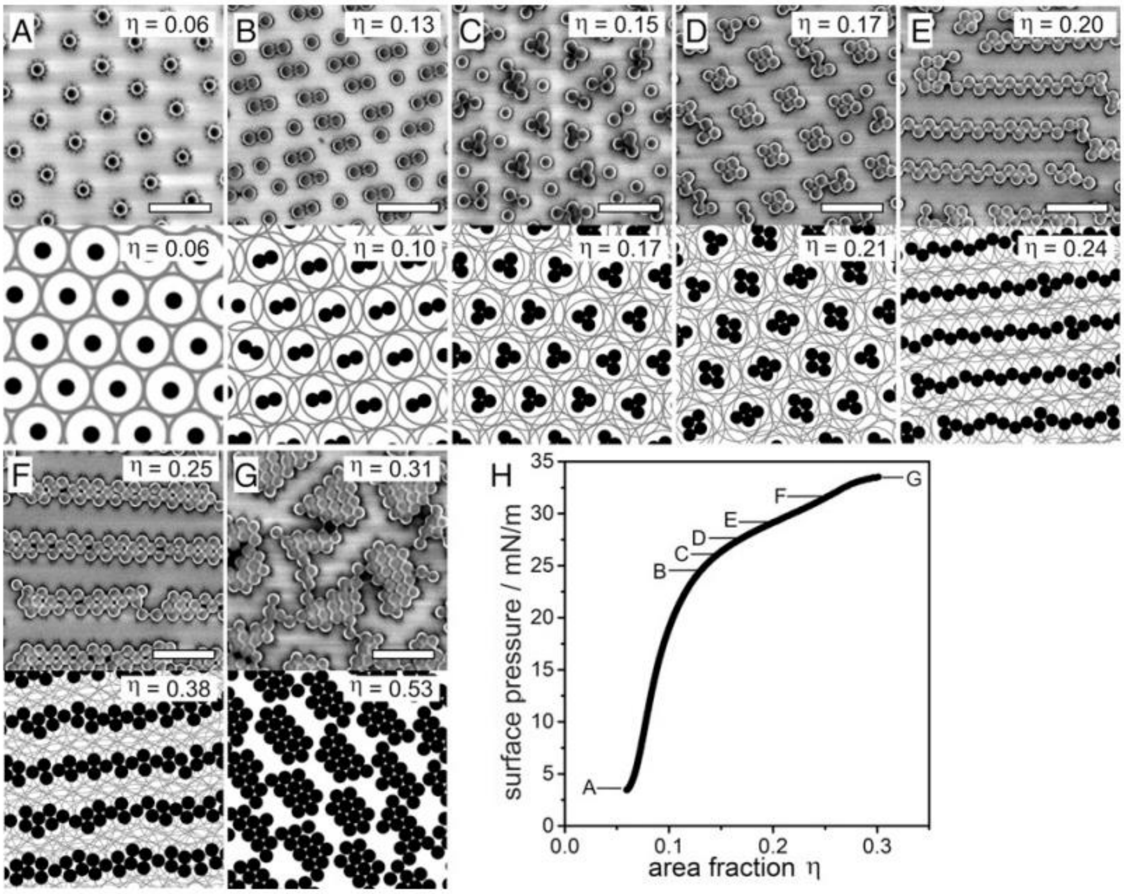

Figure 6.6: Phase behaviour of the core–shell system upon compression in experiment and MC simulations based on particles interacting via a Jagla potential with a linear ramp potential and shell-to-core ratio $r_1/r_0 = 4$. (A–G) Representative SEM image of characteristic phases observed in experiment (Top row) and snapshots of the MC simulations (Bottom) at different area fractions specified in the images. (H) Surface pressure-area fraction isotherm indicating the regions in which the phases are observed (Scale bar: 1 µm).

Next, the interfacial phase behaviour as a function of the particle area fraction was investigated using a Langmuir trough. We will use the example of core–shell particles from 80 min irradiation (Figure 6.5 F and I) as an example. Experimentally, the r_1/r_0 ratio was determined from the NND at the interface (Figure 6.5H) and the core diameter to be $r_1/r_0 = 4.1$. The core–shell particles form a hexagonal non–close packed monolayer at surface pressures below 5mN/m. Upon compression, both surface pressure and the area fraction of the particles (η) increases, as seen in Figure 6.6H. The hexagonal non–close packed phase prevails up to $\eta = 0.11$, and the compression only results in a decreasing lattice constant (Figure 6.6A). Above this area fraction, the system undergoes phase transitions into cluster phases. First, lattices of defined particle dimers are observed (Figure 6.6B), which are increasingly replaced by trimers (Figure 6.6C) and tetramers (Figure 6.6D). At even higher area fractions, the lattices of small clusters collapse into larger clusters and complex chain phases with characteristic morphologies. These morphologies include well-defined zig-zag chains (Figure 6.6E), observed around $\eta = 0.2$, and braided chains (Figure 6.6F) which emerge at $\eta =$

0.25. At $\eta > 0.3$, the chains and clusters merge to form a less defined network of very large clusters at the highest compressions achievable in experiments (Figure 6.6G).

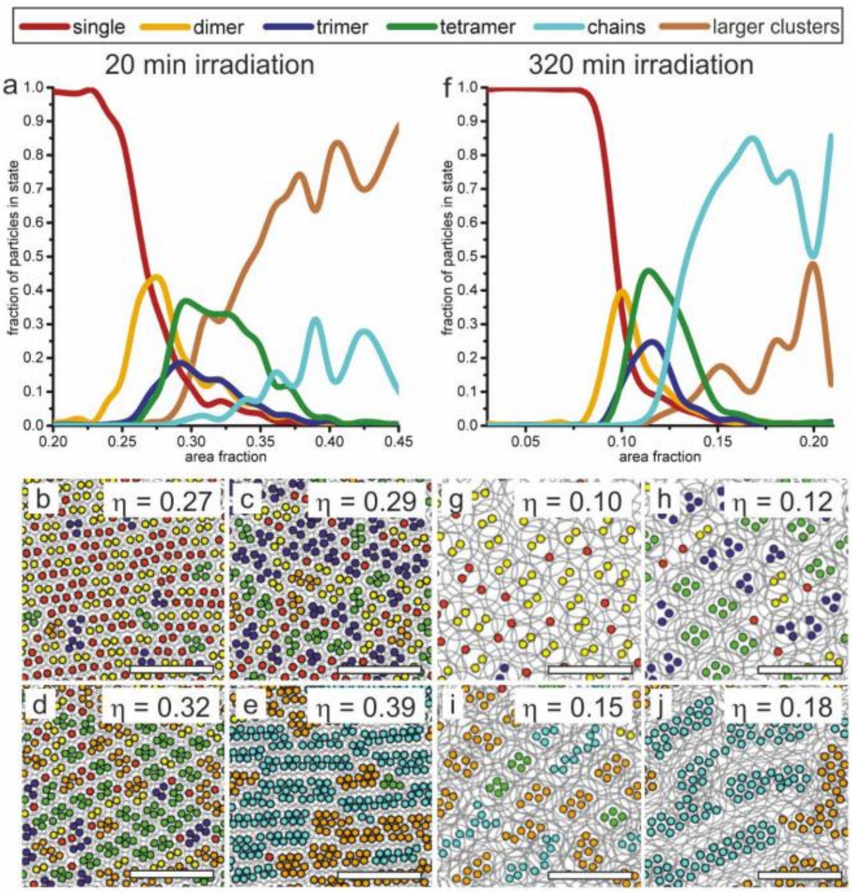

Figure 6.7: a-j) Statistical evaluation of the phase transitions in experiment for 20 min and 320 min irradiation. a) Fraction of particles in different phases as a function of area fraction for 10 min irradiation. b-e) Post-processed SEM images with color-coded cores (d = 170 nm) detected in image analysis for 20 min irradiation (corresponding to $r_1/r_0 = 2.5$). Scale bar: 2µm. f) Fraction of particles in different phases as a function of area fraction for 320 min irradiation. g-j) Post processed SEM images with color-coded cores (d = 170 nm) detected in image analysis for 320 min irradiation (corresponding to $r_1/r_0 = 5$). Scale bar: 2µm.

Finally, a major limitation in existing experimental approaches based on microgel/microsphere mixtures[100] and shells with a pronounced crosslinker gradient[122] is the inability to accurately control the dimensions and structure of the shell. These limitations prevent the formation of more complex Jagla phases and limit the system to the formation of single chains. In contrast, the iniferter-based controlled radical polymerization scheme produces hairy polymer chains with tailored dimensions (Figure 6.5) and affords shells with large dimensions. The ability to engineer the shell dimensions allowed them to also study the impact of varying the shell-to-core ratio on interfacial phase behaviour. In Figure 6.7 key phases are shown for both the 20min irradiated particles ($r_1/r_0 = 2.5$) and the 320min irradiated particles ($r_1/r_0 = 5$), the colour and statistics are generated based upon our cluster analysis (see Section 6.2.5). As expected, the onset of phase transitions is shifted to larger area fractions for smaller r_1/r_0 ratios and to smaller area fractions for larger r_1/r_0 ratios (Figure 6.7).

6.3.2 Monte Carlo Simulations

In order to elucidate the driving force behind these phase transitions, we perform MC simulations of core–shell particles interacting via the Jagla potential (equation (6.1)). The shape of the soft repulsive shoulder and hence the value of g is not known a priori. However, from our arguments in the introduction (Figure 6.1, Appendix 2), we hypothesize that the repulsion for the effectively 2D soft shells in the experimental system should be reasonably approximated by a linear ramp, and we therefore choose $g = 1$. We will discuss the soft-shell interaction profile in more detail in Section 6.3.4 and show that by comparing the self-assembled structure obtained from simulations and minimum energy calculations with experiments, we can narrow the Jagla g-parameter of the system to between 0.9 and 2, which is consistent with our assumption of $g = 1$ here.

Additionally, to more closely mimic the kinetic history of the experimental system, the different area fractions η were accessed through a slow uniaxial compression of the simulation box starting from the hexagonal non–close packed phase at a reduced temperature of $T^* = k_BT/\varepsilon = 0.005$ (see Section 6.2.4). Snapshots of the phase behaviour resulting from the MC simulations are shown in Figure 6.6A–F below their experimental counterparts. The size of the soft shell (r_1) is shown as a grey circle surrounding the black hard cores to help visualize the degree of shell overlap in the different phases. Our compression MC simulations accurately reproduce all the characteristic phases observed in the experiments. There is also excellent agreement between simulation and experiment in the area fractions for the cluster phases but slightly larger discrepancies in the area fractions for the complex chain phases. The close agreement between experiment and simulation provides evidence that the complex self-assembly observed experimentally can indeed be rationalized by Jagla-type interactions. Note that the highest-density simulation data shown in Figure 6.6G was obtained using the slow cool equilibration protocol to avoid finite size effects in the simulation box occurring during the uniaxial compression.

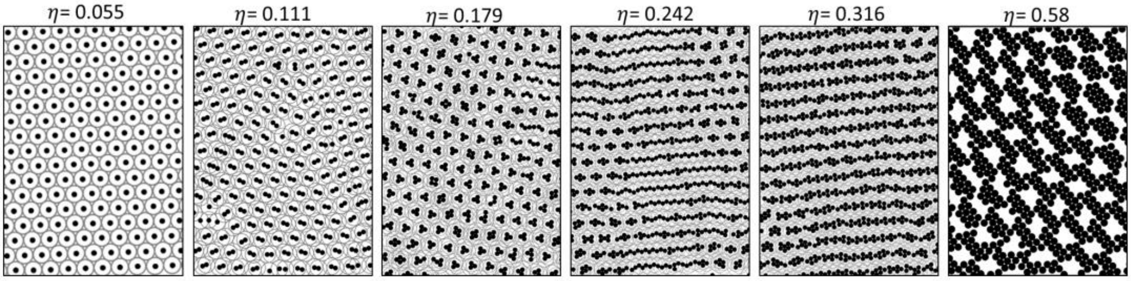

Figure 6.8: Large area snapshots of different phases obtained from compression Monte Carlo simulations of core-shell particles with $r_1/r_0 = 4$, $g = 1$. Note that the snapshot for $\eta = 0.58$ was obtained from slow cool MC simulations as the area fraction was too high to be reached using compression MC simulations.

In the evolution of the experimental interfacial assembly, characteristic phases often coexist, in lower-magnification SEM images, and similarly, larger area simulation snapshots show the presence of multiple phases in the MC simulations (Figure 6.8). This behaviour is expected for area-controlled experiments (i.e., a canonical or NVT ensemble) but also hints at small energetic differences between the different phases. We use image analysis to detect and analyse the characteristic phases as the system evolves with increasing compression.

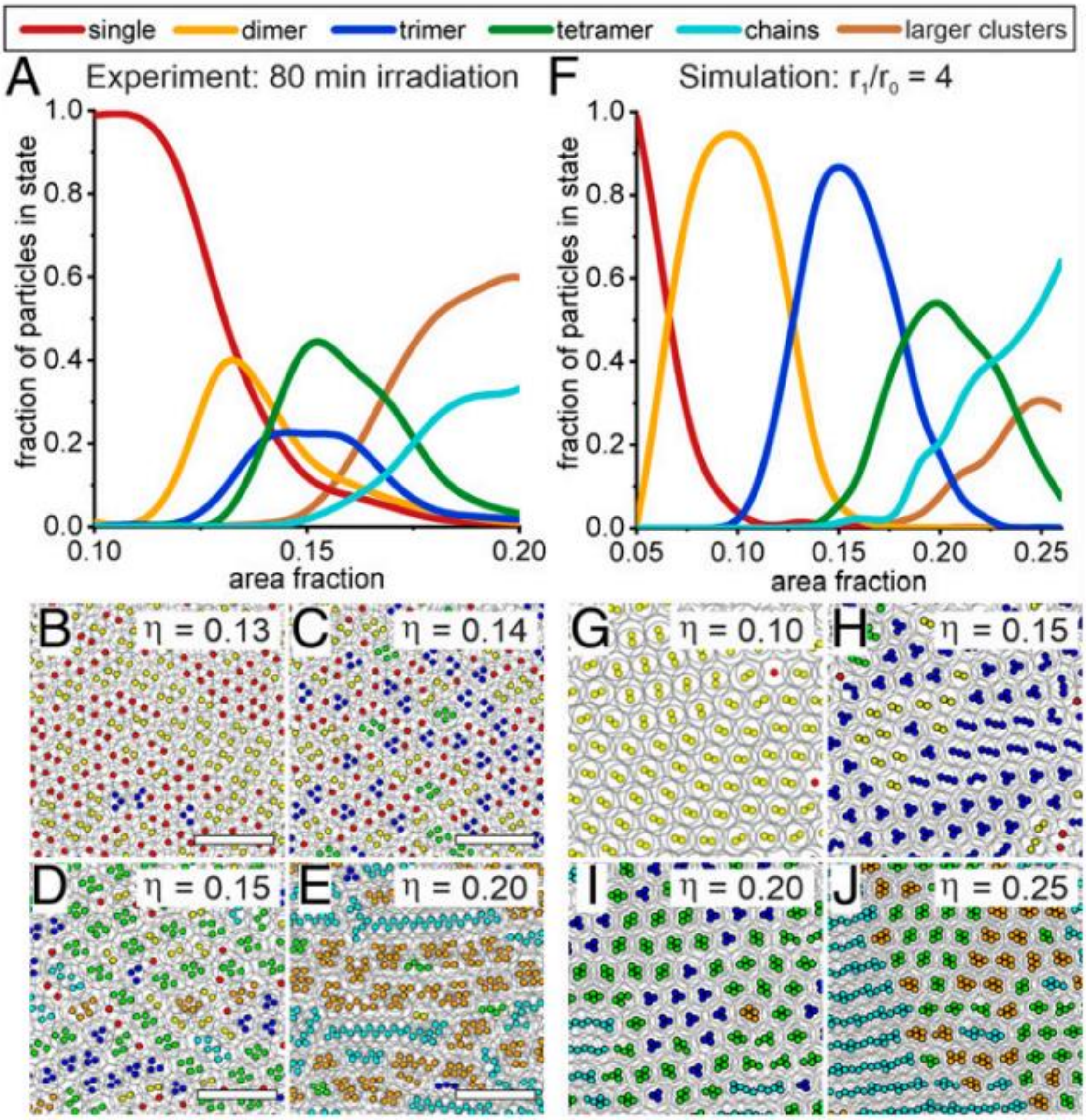

Figure 6.9: Statistical evaluation of the phase transitions in experiment and simulation. (A) Fraction of particles in different phases as a function of area fraction in experiment. (B–E) Postprocessed SEM images with color-coded cores (d = 170 nm, Scale bar: 2 µm). (F) Fraction of particles in different phases as a function of area fraction in compression-type MC simulation. (G–J) Simulation snapshots with color-coded phases detected in image analysis.

Figure 6.9 shows the statistical evaluation of the phase behaviour as well as snapshots of characteristic area fractions where different phases are dominant for both experiment (Figure 6.9 A–E) and simulation (Figure 6.9 F–J) with $r_1/r_0 = 4$. Considering the complexity of the phase behaviour and the experimental system and the simplicity of the theoretical model, the qualitative agreement between the statistical analysis for experiment and simulations is surprising. In particular, the statistical data from both experiment and simulation supports the qualitative picture shown in Figure 6.6 and clearly shows that with increasing compression, the system evolves from a non–close packed hexagonal phase, via defined clusters to chains and large clusters in both experiments and simulation.

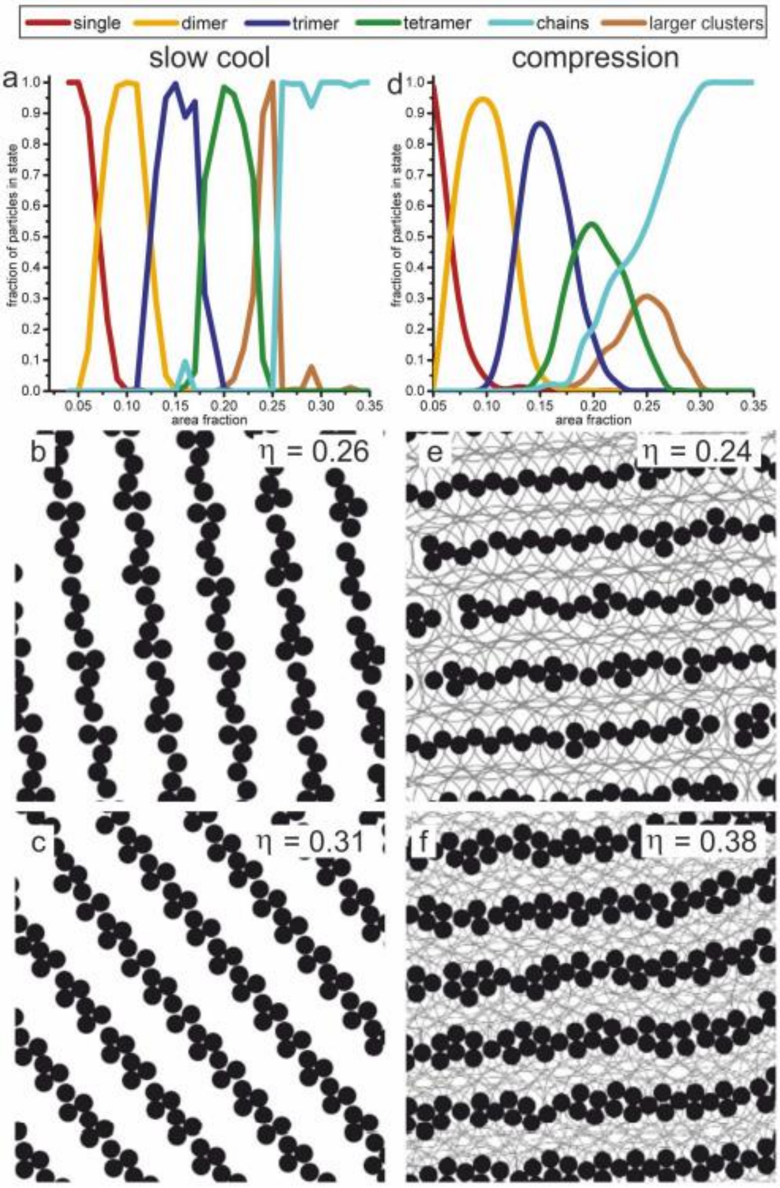

Figure 6.10: Distribution functions for the different phases and representative complex chain structures obtained from slow cool MC simulations (a-c) and compression MC simulations (d-f) of core shell particles with $r_1/r_0 = 4$, $g = 1$. Note that both zig-zag chains and braided chains could only be obtained from the compression MC simulations (right snapshots, e,f) but not the slow cool MC simulations (left snapshots, b,c).

Interestingly, using the slow cool MC simulations reliably reproduces the cluster phases but not the zig-zag chains or braided chains (Figure 6.10b,e and Figure 6.10c,f respectively), suggesting that these complex chain phases are sensitive to the kinetic history of the sample and can only be accessed via specific kinetic pathways. This sensitivity is confirmed by the fact that in both the compression MC simulations and experiments, the complex chains are aligned along the compression axis. We note that the general phase behaviour with chain and cluster formation agrees with literature results using similar potentials,[99,128] with the important exception of the complex zig-zag and braided chains. Additionally using the slow cool protocol instead of the compression protocol in our MC simulations led to much poorer agreement of the distribution of the different phases compared to experiment (Figure 6.10a,d).

The nonergodic nature of the system provides a post-hoc justification for using our compression MC method rather than a MC method that is more efficient at finding the ground state in a rugged energy landscape (e.g., parallel tempering, simulated annealing, etc.)[75] since the former mimics the kinetic history of the experimental system more accurately. Interestingly, we did not find any evidence of a glass transition either in our simulations or experiments, and we therefore conclude that the soft shells in our system are soft enough to allow local rearrangements of the colloidal particles into (at least locally) ordered structures so that they are not trapped in an amorphous, glassy state.

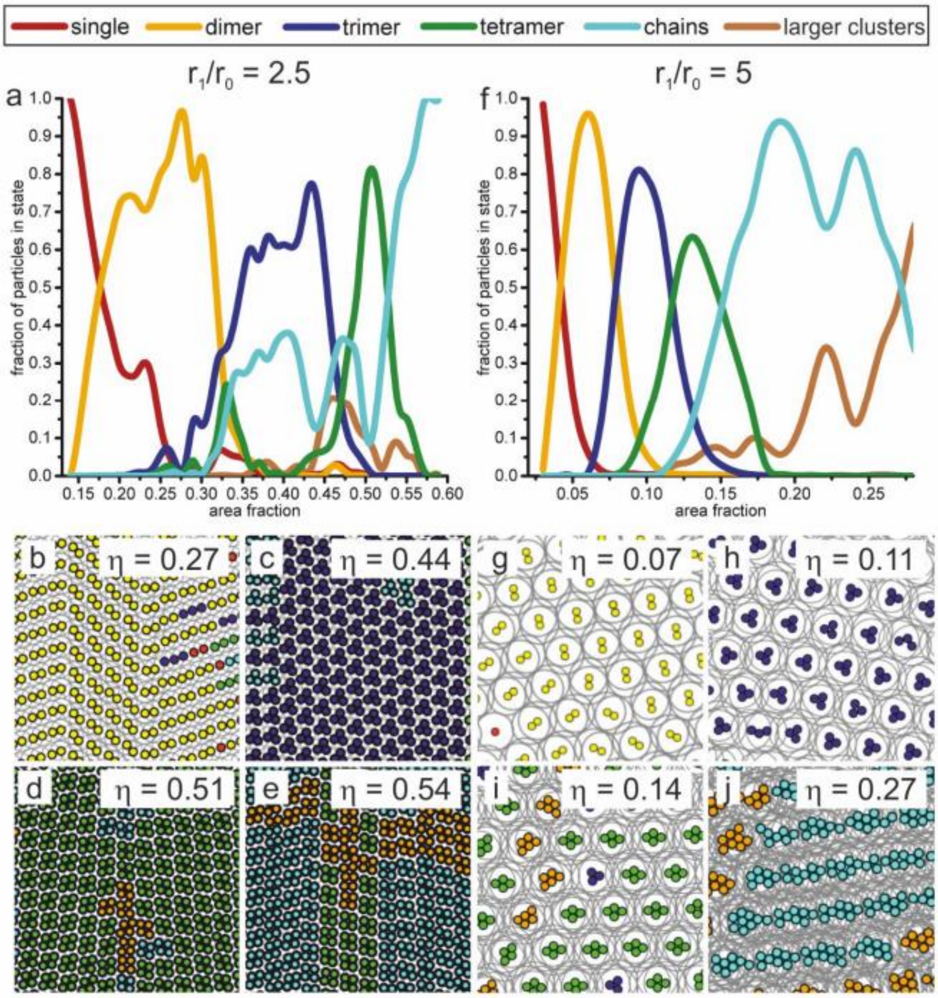

Figure 6.11: a-j) Statistical evaluation of the phase transitions in simulation for r1/r0-ratios of 2 and 5. a) Fraction of particles in different phases as a function of area fraction for $r_1/r_0 = 2.5$. b-e) Simulation snapshots with color-coded phases detected in image analysis for $r_1/r_0 = 2.5$. f) Fraction of particles in different phases as a function of area fraction for $r_1/r_0 = 5$. g-j) Simulation snapshots with color-coded phases detected in image analysis for $r_1/r_0 = 5$.

To match all the experimental data, we also used our Monte Carlo simulations to study core-shell particles with $r_1/r_0 = 2.5,\ 5$. Similar to the $r_1/r_0 = 4.0$ case, the observed phase behaviour agrees between experiment and simulations for $r_1/r_0 = 2.5$ and $r_1/r_0 = 5$ (Figure 6.11). One small discrepancy that occurs for the thin shell case $r_1/r_0 = 2.5$ is that simulations show that chain phases start to appear together with the trimer phase, which is not seen in experiments (Figure 6.11). We hypothesize that this discrepancy is due to the fact that attractive capillary forces cannot be completely ignored in thin shell experimental systems, and these may suppress the emergence of the chain phase until we reach higher area fractions. Indeed, for even thinner shells—or larger core particle dimensions— capillary forces dominate over the soft-shell repulsion and lead to aggregation and the formation of close-packed structures. In contrast, we can safely ignore capillary forces for thicker shells because the cores are separated by much larger distances, leading to increasingly better agreement between experiment and simulation as we increase shell thickness.

While our compression MC simulations capture the key features of the phase distribution, a closer examination of Figure 6.9 A and F reveals subtle differences between experiment and simulations. First, the area fraction range over which the phase transitions take place is larger, and the peaks for the individual phases are better separated in the simulations compared to in the experiments. This difference can be attributed to an underestimation of the experimentally determined area fraction, which is based on the nominal area of the silica cores and ignores the presence of highly compressed polymer chains between cores in contact. Secondly, the peak population of the particles in the different phases is higher in the simulations (dimers 93%, trimers 83%, and tetramers 52%) compared to in the experiments (dimers 43%, trimers 30%, and tetramers 42%). This difference may be attributed to particle polydispersity and the presence of minor amounts of impurities in the experimental system.[129]

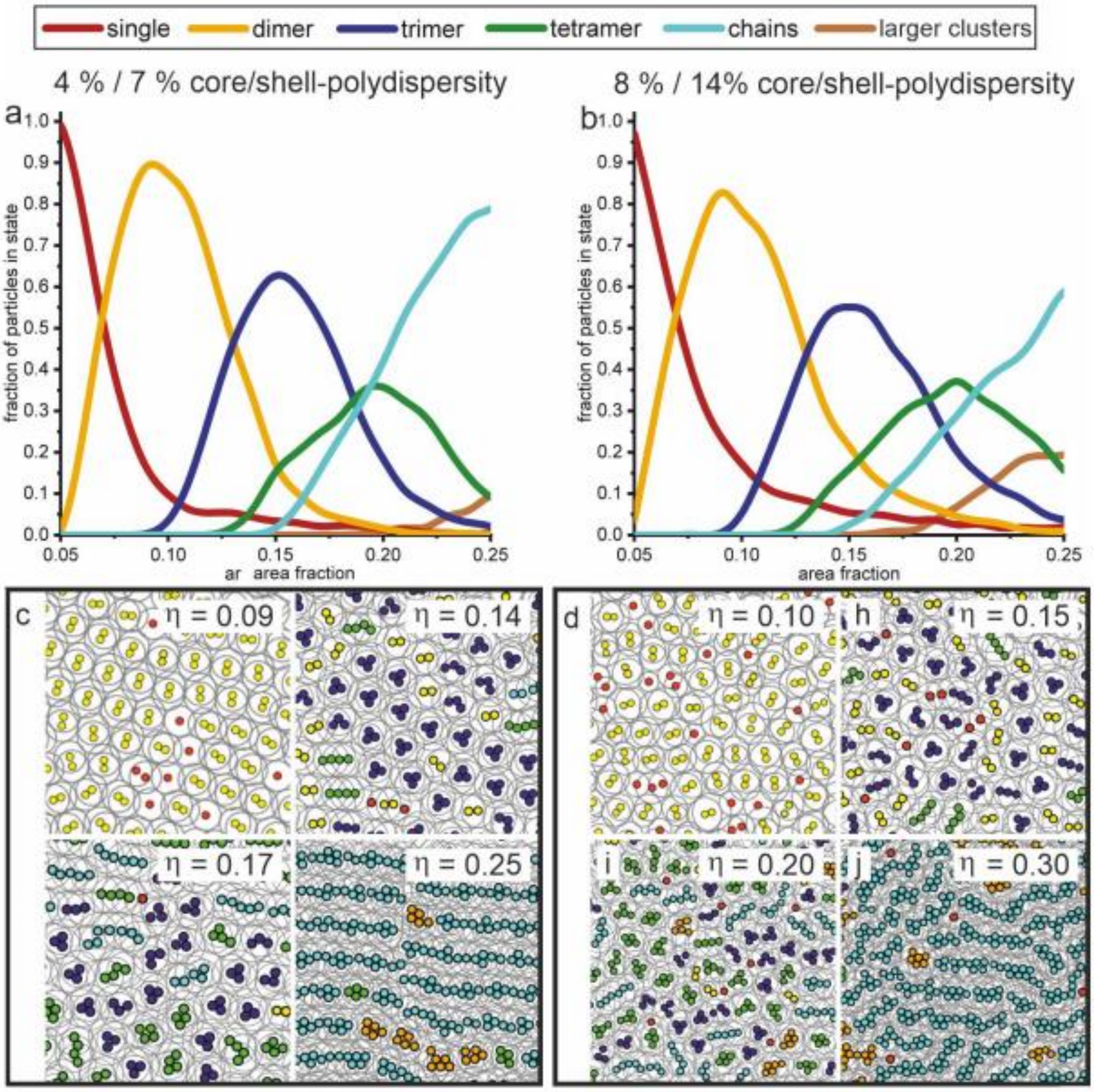

Figure 6.12: Compression MC simulations of core-shell particles with polydispersity, using $r_1/r_0 = 4$, $g = 1$, where r_1, r_0 refer to the average shell and core diameter respectively. We assume that the core and shell diameters of the simulated particles follow a Gaussian distribution, with the standard deviation in the core diameter approximately equal to the uncertainty measured by the experimentalists using the zeta-sizer method and the standard deviation in the shell diameter equal to the uncertainty in the SEM measured nearest neighbour distance (see Figure 6.5h) in the data on the left side. On the right, the same simulations are shown with an increased polydispersity of twice the experimental values. a,b) Distribution functions for the populations of the different phases for 4 % core and 7 % shell polydispersity (a) and 8 % core and 14 % shell polydispersity (b); c,d) Snapshots of representative phases for 4 % core and 7 % shell polydispersity (c) and 8 % core and 14 % shell polydispersity (d).

To assess the effect of polydispersity, we included the experimental polydispersities for both the core and shell diameters in our MC simulations and further increased these values to probe the evolution of the system (Figure 6.12). These simulations reveal that polydispersity does not change the phase behaviour of the system qualitatively, though it suppresses the peak population for clusters. The latter result confirms that the smaller peak populations for the different phases observed in the experiments compared to the simulations of monodisperse particles is at least partially due to polydispersity. Finally, at high area fractions, the dominant phase is observed to be large clusters in the experiments but predicted to be chains in the simulations. The latter is in fact an artifact due to finite size effects in the simulations at high compressions. Specifically, for large area fractions above $\eta \gtrsim 0.25$, the largest chain length in the simulation is equal to the dimension of the simulation box along the compression axis. At higher area fractions, periodic boundary conditions start to connect clusters into chains, artificially driving up the proportion of chains relative to clusters.

6.3.3 Minimum Energy Calculations

In order to gain a deeper understanding of the phase transitions occurring in our system, we calculate the zero-temperature phase diagram and MECs for an ensemble of core–shell particles interacting via the generic core–shell potential proposed by Jagla equation (6.1). Note that although our core–shell system is not globally ergodic as discussed earlier, we are justified in using minimum energy calculations to determine the local structure of the different phases since the experimental system is effectively in the zero-temperature regime ($\varepsilon \gg k_B T$) as demonstrated in Appendix 3.

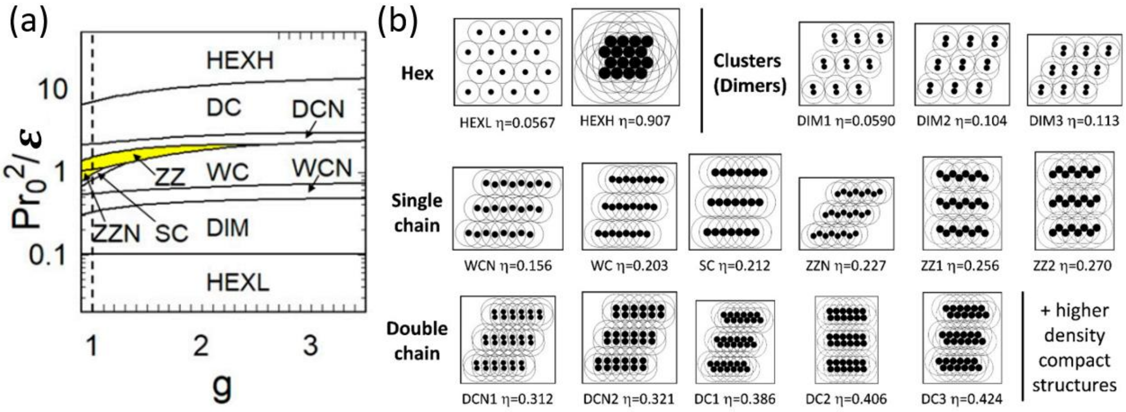

Figure 6.13: Minimum energy calculations for $r_1/r_0 = 4$. (a) Zero-temperature phase diagram for the core–shell particles in the $g - P$ plane, where P is surface pressure. The vertical dashed line represents $g = 1$. The region for zig-zag phases (i.e., ZZN and ZZ) is highlighted in yellow in the phase diagram. (b) Minimum energy configurations (MECs) containing two particles per unit cell and their corresponding area fractions η for $r_1/r_0 = 4$. In order of increasing η these include: low density hexagonal phase (HEXL), dimers (DIM1, DIM2, DIM3), non-close packed and close packed wavy chains (WCN, WC), straight chains (SC), non-close packed and close packed zig-zag chains (ZZN, ZZ1, ZZ2), non-close packed and close packed double chains (DCN1, DCN2, DC1, DC2, DC3), a series of higher density compact structures and finally close-packed hexagonal phase (HEXH).

Following the experiments in Figure 6.6, we fix $r_1/r_0 = 4$. To simplify the discussion, we only consider 2D structures containing up to two particles per unit cell (Figure 6.13B) as this model is simple enough to allow us to perform a comprehensive exploration of the all the MECs but complex enough to generate the representative phases and their approximants seen in the experiments and simulations such as clusters (i.e., dimers) and complex chains (e.g., zig-zag chains and double chains). Working in the NPT (i.e. isobaric-isothermal) ensemble, we calculate the MECs for each value of g and reduced pressure $P^* = r_0^2 P/\varepsilon$ by minimizing the enthalpy per particle H with respect to the lattice parameters.[101] Note that the value of ε is not relevant to the phase behaviour in the low-temperature regime $T^* = k_B T/\varepsilon \ll 1$ that we are considering here.

Figure 6.13a shows the phase diagram in the $g - P$ plane, while Figure 6.13b shows the low area faction MECs together with their area fractions. The dashed line in Figure 6.13a corresponds to $g = 1$ considered in our simulations. With increasing pressure, corresponding to increasing η in the experiments and simulations, the system evolves from a low-density hexagonal phase (HEXL), via defined dimers (DIM) to a series of distinct chain phases, including non–close packed and close-packed wavy chains (WCN, WC), straight chains (SC), non–close packed and close-packed zig-zag chains (ZZN, ZZ), non–close packed and close-packed double chains (DCN, DC), and finally a series of higher-density compact structures culminating in the close-packed hexagonal phase HEXH. Note that within the framework of our two-particle calculation, trimer and tetramer clusters and braided chains cannot be formed and are therefore absent in the MECs. However, if we consider the double-chain phases as approximants for the braided chain phase, the evolution of the minimum energy phases in our simplified model closely mimics the phases observed in the experiments and simulations (Figure 6.6), going from the non–close packed hexagonal phase, to defined clusters, zig-zag chains, and complex double chains. There is also excellent agreement in the area fractions of these phases between theory and simulation.

6.3.4 Determination of the Soft-Shell Interaction Potential

The agreement between experiment, simulation, and theory on the observed phases and their evolution suggests that the developed particle system with its tailored interfacial morphology indeed exhibits an interaction potential that can be described via pairwise-additive Jagla potentials. Unfortunately, the small particle dimensions prevent the direct measurement of the interfacial interaction potential to confirm this conclusion. An alternative method for determining the interaction potential from first principles is to use monomer-resolved simulations,[130,131] but such a calculation is nontrivial and requires a separate and substantial study, which lies outside the scope of this Thesis.

However, while it is not possible to determine the experimental interaction potential directly, it is possible to constrain the effective values of g for these particles by comparing the experimentally observed morphology of the different characteristic phases with those predicted by theory and simulation. Our minimum energy calculations predict that the zig-zag chain phases (ZZN and ZZ) are only stable for $g \leq 2$ (Figure 6.13a, yellow highlighted region).

At first sight, this seems to contradict the minimum energy calculation results of Fornleitner and Kahl, who observed a zig-zag chain phase for core–shell particles with a square shoulder profile $g = \infty$ and $r_1/r_0 = 5$.[108] However, a closer examination of bond angles and density of the phase reveals that the zig-zag chain phase found by Fornleitner is in fact essentially equivalent to what we have called the double-chain phase (DC1) in Figure 6.13b. Therefore, the experimental observation of zig-zag chains therefore puts an upper boundary of $g \approx 2$ for the g parameter. The lower boundary for g is more difficult to access via minimum energy calculations because the complex energy landscape when $g < 1$ makes the calculation of the zero-temperature phase diagram challenging.[101,102] We therefore determine the lower bound for g by performing slow cool MC simulations for g values varying between 0.85 and 1 and comparing the resultant phase behavior to our experimental observations (Figure 6.14).

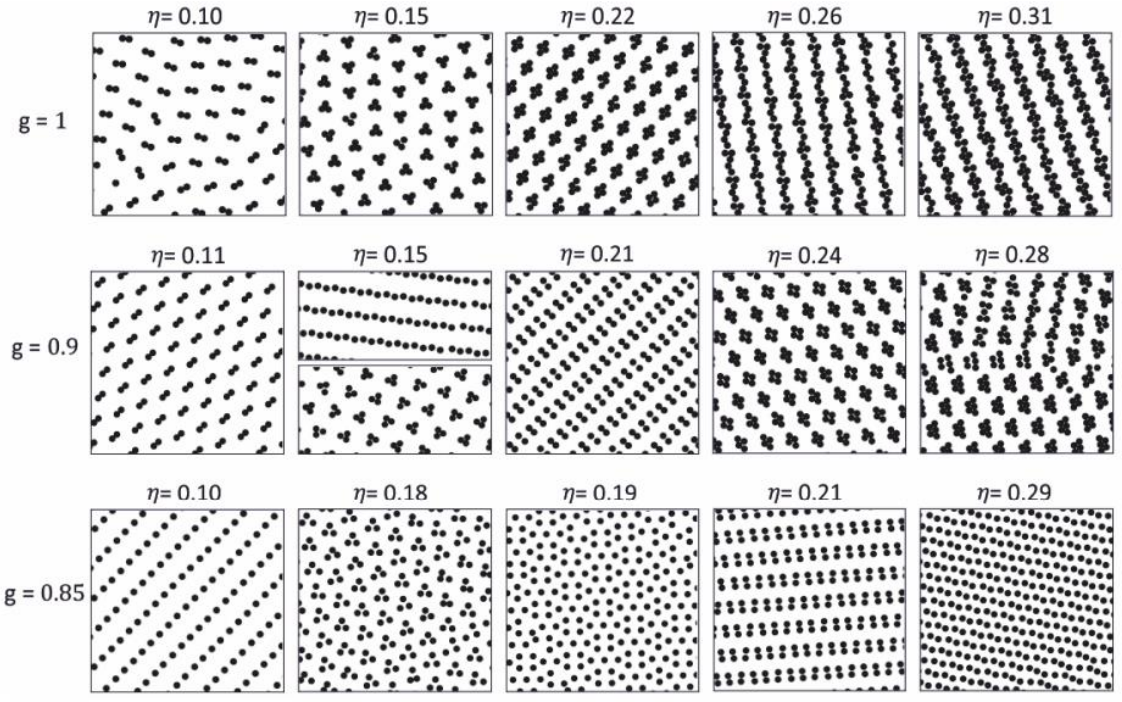

Figure 6.14: Using Monte Carlo (MC) simulations to bracket the value of g in the experimental systems. Successive rows show the evolution of phases with increasing area fraction η obtained from slow cools MC simulations of core-shell particles with $r_1/r_0 = 4$ and $g = 0.85, 0.9, 1.0$.

These simulations reveal that the characteristic dimer phase at low area fractions, which is pronounced in experiments, is absent for $g < 0.9$. Based on these indirect evaluations from theory and simulation, we therefore bracket the effective g parameter for our experimental system to be $0.9 \leq g \lesssim 2$. This range is consistent with our simple model of overlapping 2D shells, which suggests that the soft shoulder repulsion should be reasonably approximated by a linear ramp profile (i.e., $g = 1$ (Figure 6.1)).

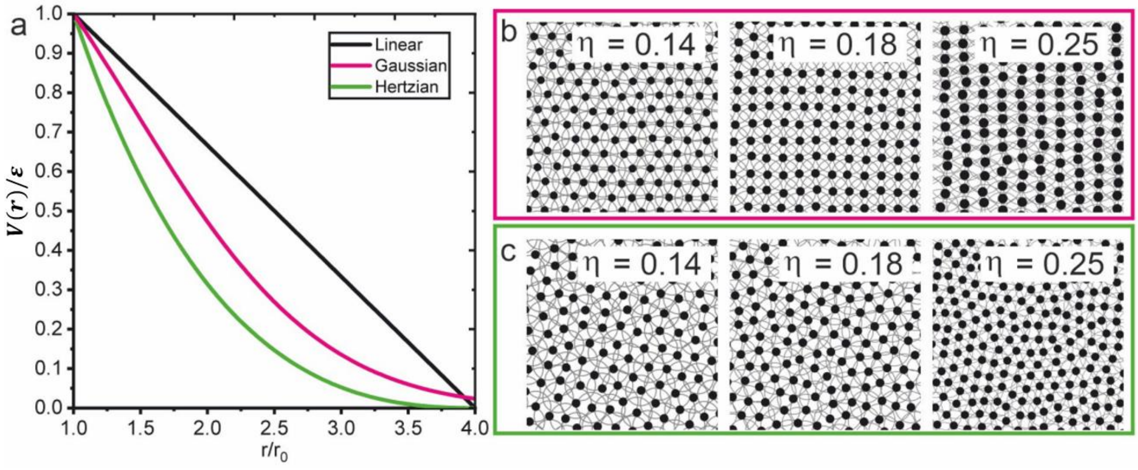

Figure 6.15: Compression Monte Carlo simulations of core-shell particles interacting via potentials derived from previous monomer-resolved simulations on systems similar to our core-shell particles instead of the linear ramp potential. (a) Plot of the Gaussian potential[130] given by $V_g(r) = \varepsilon_g \exp\left(-r/\sigma_g\right)^2$ and the Hertzian potential[131] given by $V_H(r) = \frac{\pi Y \sigma_{eff}^2 \left(1-r/\sigma_{eff}\right)^2}{2\ln\left(\frac{2}{1-r/\sigma_{eff}}\right)}$ compared to the linear ramp Jagla potential. We choose $\sigma_g = r_1/2$, $\sigma_{eff} = r_1$ and $r_1/r_0 = 4$ so that the range of both potentials is approximately the same as the Jagla potential, and we choose ε_g and Y so that the magnitude of both potentials is ε at $r = r_0$. (b,c) Snapshots of characteristic phases for core-shell particles interacting via the Gaussian and Hertzian potentials respectively. None of the characteristic cluster phases are observed for these potentials.

It is important at this point to compare the Jagla potentials we have used in our MC simulations with those derived from previous monomer-resolved simulations on similar systems. For example, Schwenke et al. found the interaction potential between polymer-coated colloids at a liquid interface to be a Gaussian,[130] while Camerin et al. found the interaction potential between microgels at a liquid interface to be a Hertzian.[131] Both these potentials clearly have a concave downward shape (effective $g < 1$) which is qualitatively different from the linear ramp Jagla potential ($g = 1$) we have used in this Chapter (Figure 6.15A). In order to assess whether these concave downward potentials are applicable to our experimental system, we used them in place of the Jagla potential in our MC simulations and compared the resultant phase behaviour with what we find in our experiments (Figure 6.15). We see that neither the Gaussian potential nor the Hertzian potential could reproduce the phase behaviour seen in our experiments, indicating that our experimental system does not interact via these potentials.

We believe the reason why the effective potential for the experimental polymer-coated colloids is different from that studied by Schwenke et al. is because although the two systems appear to be similar, they are in fact in different regimes.[130] Specifically, in the simulations that gave rise to Gaussian interaction potentials, both bulk phases were assumed to act as a good solvents for the grafted polymer chains, so the majority of the polymer chains were stretched out into the bulk and only a small fraction are stretched out along the interface (i.e., those grafted close to the equatorial plane).[130] In addition, the polymer chains along the interface are only stretched out slightly more compared to the chains that are stretched out into the bulk. As a result, the interactions in their system are dominated by the swollen chains in the bulk rather than the interfacial chains, leading to Gaussian interactions, as predicted for dilute polymer solutions in the bulk.[132–134] In contrast, the experimental polymer-coated particles we are studying are at an air–water interface, where all the polymer chains on the air side and presumably a significant fraction of the polymer chains on the water side are adsorbed at the interface. In addition, the polymer chains along the interface are stretched out around 60% more compared to polymer chains in the bulk (Figure 6.5H). As a result, the interactions in the experimental system are dominated by interfacial chains rather than swollen chains in the bulk, which as we have argued earlier, leads to a ramp-like potential (Figure 9.1).

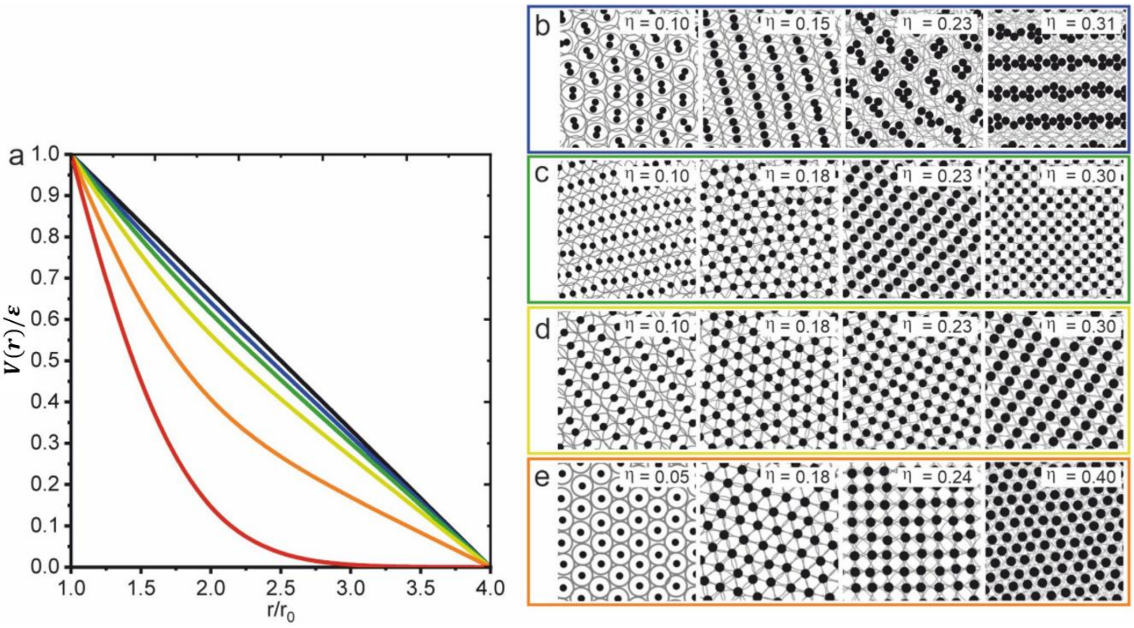

Figure 6.16: Compression Monte Carlo simulations of core-shell particles interacting via a composite potential consisting of a Gaussian potential and a linear ramp potential with different relative contributions. (a) Plot of the composite potential given by $V(r) = wV_g(r) + (1 - w)V_{lin}(r)$ for various values of w, where w is the weighting of the Gaussian potential ($0 \leq w \leq 1$), $V_g(r)$ is the Gaussian potential given the caption for Figure 6.15 and $V_{lin}(r)$ is the Jagla potential given by equation (6.1) with $g = 1$. Note that following the experimental data in Figure 6.5h, we choose $\sigma_g/r_0 = 1.25$ and $r_1/r_0 = 4$ so that the range of the linear ramp potential (i.e., due to polymer chains along the interface) is approximately 1.6 times the range of the Gaussian potential (i.e., due to polymer chains swollen into the bulk). (b-e) Snapshots of characteristic phases for core-shell particles interacting via the composite potential with $w = 0.05, 0.1, 0.2, 0.5$ respectively. Cluster and chain phases are only observed for $w = 0.05$.

In order to gain further insight into the relative contribution of the different terms to the total interaction, we performed MC simulations using a composite potential consisting of a

Gaussian potential (with weighting w, $0 \leq w \leq 1$) and a linear ramp potential (with weighting $1 - w$) (Figure 6.16). We find that cluster formation, which is pronounced in the experimental system, only occurs when $w < 10\%$. This behaviour suggests that the interactions in the experimental system we are studying are dominated by the pronounced and extended corona formed by the interfacially adsorbed polymer chains.

6.4 Conclusions

We use Monte Carlo simulations and minimum energy calculations to study the phase behaviour of core-shell particles at a liquid interface under compression. Assuming a linear ramp potential and that particle interactions are pairwise-additive, the phases produced by the MC simulations and minimum energy calculations agree well with the experimentally observed phases for defined core-shell particles consisting of a hard silica core functionalised with uncross-linked polymer chains. The good agreement between experiment, simulation and theory indicates that control of the interfacial morphology of soft particles can be used to realize Jagla-type phases, provided the experimental particles follow the following criteria:

1. The particles have a two-length scale interaction consisting of a hard core with a soft shell which forms a 2D corona at the interface. The 2D corona allows for interaction potentials with sufficiently large g parameters.

2. The interaction between particles are pair-wise additive, i.e., interactions between two particles do not affect neighbouring interactions, enabling the formation of anisotropic structures.[122] This has been achieved by ensuring the polymer chains that make up the shell are not crosslinked and therefore allow different degrees of shell overlap with neighbouring particles.

3. The interactions are isotropic, requiring the polymer shell to be uniform to produce a regular interfacial structure in all directions.

This demonstration of a single component, spherical system to form a series of defined, anisotropic interfacial assembly phases provides a paradigm to experimentally realize the vast variety of theoretically predicted Jagla phases. The combination of available predictive theoretical models with the ability to use functional core materials and to tailor the chemical nature, chain architecture, density, structure, and dimensions of the polymer shell will spark discoveries in functional, self-assembled materials.

Chapter 7 Self-Assembly of Ellipsoidal Core-Shell Particles at Flat Fluid Interfaces

7.1 Introduction

In the previous Chapter, we modeled the self-assembly of spherical core-shell particles in an experimental system. In this Chapter, we will model the self-assembly of core-shell ellipsoids. As discussed in Section 2.2, for ellipsoidal particles at liquid interfaces, the deformation of the meniscus along the long axis differs from that along the short axes, resulting in capillary forces with quadrupolar symmetry that greatly exceed the thermal energy $k_B T$.[15] The saddle-like distortion field around the ellipses causes them to attract each other either tip-to-tip or side-to-side, while repelling each other in the side-to-tip configuration.[15,51,65]

Both of these configurations have been found experimentally. Sterically stabilized ellipsoids at an air/oil interface assembled into a side-to-side configuration, corroborated by calculations and simulations as the energetically most stable configuration.[49,135] Selectively removing the steric stabilizer from the tip of the ellipsoids changed the self-assembly into tip-to-tip configurations.[136] The self-assembly behaviour of charge-stabilized ellipsoids is less understood. At an air/water interface, side-to-side[137–139] and tip-to-tip[15,139–141] arrangements have been reported. In one study, ellipsoids with low aspect ratios assembled preferentially side-to-side, while a tip-to-tip arrangement was found for higher aspect ratios.[140] Another study reported "flower-like" tip-to-tip arrangements at the air/water interface, whereas the same particles formed a "chain-like" tip-to-tip arrangement at a decane/water interface.[141] This difference was rationalized by the different contact angle of the ellipsoids adsorbed at the air/water and decane/water interface, respectively.[141] Additionally, core-shell ellipsoids consisting of an incompressible core and a hydrogel shell initially self-assembled into a side-to-side assembly, which transitioned over time into a tip-to-tip assembly.[142] Furthermore, the shell thickness of these core-shell ellipsoids was reported to affect their assembly, with thicker shells resulting in a tip-to-tip arrangement, while thinner shells led to a side-to-side assembly.[143] To summarize, both tip-to-tip and side-to-side arrangements for seemingly similar ellipsoids have been observed experimentally. However, the origin of the preference for either structure is not yet fully understood and deterministic control of their self-assembly thus remains challenging.

The synthesis of ellipsoidal particles is more challenging compared to isotropic spheres. A convenient method to produce such anisotropic particles with controlled aspect ratios is the thermo-mechanical stretching technique.[144,145] In this process, spherical polymer particles are embedded in a water-soluble polymer film. This composite film is subsequently heated above the glass transition temperature of the particles and stretched. After cooling, the elongated particles can be released by dissolution of the matrix in water, yielding polymer ellipsoids with an aspect ratio determined by the degree of stretching.

It was recently discovered that the fabrication process and cleaning protocol significantly impact the behaviour of ellipsoidal particles due to residual polymer chains that remain on their surfaces after dissolution of the matrix.[146] These polymer residues impact the behaviour of both the individual particle and the particle dispersion. Contrary to the previous belief that the anisotropic shape of ellipsoidal particles prevents the coffee ring effect, it was found that it is actually the presence of polymeric residues adsorbed on the particle surface that leads to homogeneous drying.[146] When these polymer residues are properly removed using an appropriate solvent,[41] the ellipsoidal particles exhibit the coffee ring effect.[146] They therefore hypothesize that the potential presence of polymer residues, an artifact of the synthesis, fabrication or cleaning process, may similarly affect the interfacial self-assembly and thus explain the variety of different assembly structures reported for ellipsoidal particles.

Here, we work with our experimental colleagues to investigate the interfacial self-assembly behaviour of core-shell ellipsoids, focussing on the role of the shell provided by water-soluble polymer chains adsorbed to the particle surface. By meticulously controlling the fabrication process and cleaning protocol, they synthesize either pure ellipsoids or core-shell ellipsoids with polymeric hairs on their surfaces. These polymers significantly influence the self-assembly behaviour of the ellipsoids. Pure ellipsoids consistently assemble into a side-to-side arrangement, independent of their aspect ratio. In contrast, core-shell ellipsoids exhibit a transition from a tip-to-tip assembly at lower aspect ratios to a side-to-side assembly at higher aspect ratios, with the onset of this transition shifting to higher aspect ratios as the relative shell size (i.e. the ratio of shell to core) increases. We support the experimental observations with theoretical calculations and Monte Carlo simulations, mapping out the phase diagram for core-shell ellipsoids as a function of aspect ratio and shell thickness, which accurately reproduces the experimental results.

7.2 Theoretical Methods

7.2.1 Surface Evolver

As discussed in the introduction, the main driving force behind the assembly of the core-shell ellipsoids are capillary interactions. Whilst in Section 2.4 and indeed later on in Section 7.2.2.2 we discuss a general elliptical quadrupolar interaction, it is useful to verify the analytical interaction (see Section 7.2.2.2) with an exact calculation from Surface Evolver.[74] An adjustable triangular mesh between $0.02b - 0.1b$ with quadratic edge lengths was used to capture the shape of the interface near the contact line more accurately. Since the interactions between the ellipsoids of aspect ratio a/b are essentially quadrupolar and fall off rapidly with separation, a relatively small simulation box with reflecting boundary conditions at $x = \pm 6a$ and $y = \pm 6a$ was used. To calculate the capillary interaction potential between two ellipsoids, the reflecting walls to calculate the interfacial energy of a single ellipsoid interacting with its image at a reflecting wall was exploited, varying the particle surface-to-reflecting wall distance from $0.1b$ to $3a$ and using the ellipsoid at the centre of the simulation box to represent the 'infinite' separation case.

7.2.2 Monte Carlo Simulation

In order to simulate the self-assembly, we use NVT Metropolis simulations on an ensemble of 625 core-shell ellipsoids with periodic boundary conditions using a fixed rectangular box with aspect ratio $2{:}\sqrt{3}$. The particles are initially arranged in a hexagonal array with random azimuthal orientations and a core area fraction $\eta = \pi ab/8(a+h)^2$ to ensure that the system is in the dilute regime. Each MC move consisted of a simultaneous translation and rotation move, with an adjustable maximum translational distance of d_{max} and azimuthal rotation angle of d_{max}/a about the particle centre to ensure an acceptance probability of 30% for the MC moves. The particles were initially randomized at a high temperature of $T^* = 100$ for 10^3 attempted moves per particle, then quenched to $T^* = 0.2$ for a further 10^6 attempted moves per particle. To reduce computation time, particle interactions for separations greater than a cutoff distance of $2a + 10b$ were neglected.

7.2.2.1 Steric Interactions between Core-Shell Ellipsoids

As discussed in the introduction, the steric interactions between core-shell particles in our Monte Carlo (MC) simulations arise from the shell of the particles which we assume are impenetrable and treat the core-shell particles at liquid interfaces as hard ellipses with long and short axis lengths of $a' = a + h$ and $b' = b + h$ respectively, where h is the experimentally measured shell thickness, $a = R_0 \mathrm{AR}^{2/3}$, $b = R_0 \mathrm{AR}^{-1/3}$ are the long and short axis lengths of the ellipsoidal core respectively derived from the conservation of core volume, R_0 is the radius of the original unstretched spherical core and $\mathrm{AR} = a/b$ is the aspect ratio of the final stretched ellipsoidal core. This approach for modelling steric repulsions requires us to know the contact separation σ_c between hard ellipses, which is given in the Berne-Pechukas model[147] by

$$\sigma_c(\hat{\boldsymbol{u}}_1, \hat{\boldsymbol{u}}_2, \hat{\boldsymbol{r}}) = \sigma_\perp \left(1 - \frac{1}{2}\left[\frac{(\hat{\boldsymbol{r}} \cdot \hat{\boldsymbol{u}}_1 + \hat{\boldsymbol{r}} \cdot \hat{\boldsymbol{u}}_2)^2}{1 + \chi \widehat{\boldsymbol{u}}_1 \cdot \hat{\boldsymbol{u}}_2} + \frac{(\hat{\boldsymbol{r}} \cdot \hat{\boldsymbol{u}}_1 - \hat{\boldsymbol{r}} \cdot \hat{\boldsymbol{u}}_2)^2}{1 - \chi \widehat{\boldsymbol{u}}_1 \cdot \hat{\boldsymbol{u}}_2}\right]\right)^{-1/2} \tag{7.1}$$

where $\hat{\boldsymbol{u}}_1, \hat{\boldsymbol{u}}_2$ are the unit vectors along the long axis of the two interacting ellipsoids, $\hat{\boldsymbol{r}}$ is the unit vector along the line joining the particle centres,

$$\chi = \frac{\sigma_{\parallel}^2 - \sigma_{\perp}^2}{\sigma_{\parallel}^2 + \sigma_{\perp}^2}$$

and $\sigma_{\parallel} = 2(a+h)$, $\sigma_{\perp} = 2(b+h)$ are the length and width of the hard ellipse respectively. Note that for prolate ellipsoids, the Berne-Perchukas model for σ_c is accurate to within 2%.[148]

7.2.2.2 Cappillary Interactions between Core-Shell Ellipsoids

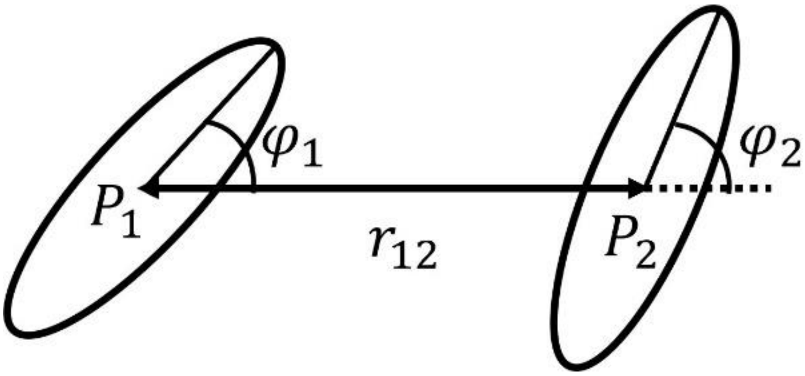

Figure 7.1: The coordinates specifying the configuration of two interacting ellipsoids at a liquid interface. The ellipses represent the projection of the contact line on each ellipsoid on the interfacial plane while P_1, P_2 denote the centres of the two ellipsoids on the interfacial plane.

In this Chapter, we assume that the capillary interactions between the core-shell ellipsoids are due to quadrupolar contact line undulations on the ellipsoidal cores and this interaction is a function of the centre-to-centre separation of the interacting ellipsoids r_{12} and the azimuthal angle that the long axis of each particle makes to the centre-to-centre φ_1, φ_2 as shown in Figure 7.1. In this section, we continue our discussion from Section 2.4 following Lewandowski et al,[50] and calculate the capillary interaction energy between two ellipsoid cores $V(r_{12}, \varphi_1, \varphi_2)$ by treating the contact line undulations on the cores as capillary quadrupoles in elliptical coordinates.

A key parameter in calculating the capillary interaction is the position of the centre of particle 2 (P2) in a coordinate system where the centre of particle 1 (P1) is the origin. If we denote the position of P2 in Cartesian coordinates as (x', y'), from Figure 7.1, we see that $x' = r_{12}\cos\varphi_1$, $y' = -r_{12}\sin\varphi_1$. Substituting this result into equation (2.16) and rearranging, we can write the position of P2 in elliptical coordinates (s^*, t^*) in terms of r_{12} and φ_1 as

$$s^* = \sinh^{-1}\left[\left\{\frac{1}{2}\left(\frac{r_{12}^2}{\alpha^2} - 1\right) + \frac{1}{2}\left[\left(\frac{r_{12}^2}{\alpha^2} - 1\right)^2 + \frac{4r_{12}^2\sin^2\varphi_1}{\alpha^2}\right]^{1/2}\right\}^{1/2}\right] \tag{7.2}$$

$$t^* = \sin^{-1}\left[\frac{-r_{12}\sin\varphi_1}{\alpha}\left\{\frac{1}{2}\left(\frac{r_{12}^2}{\alpha^2}-1\right)+\frac{1}{2}\left[\left(\frac{r_{12}^2}{\alpha^2}-1\right)^2+\frac{4r_{12}^2\sin^2\varphi_1}{\alpha^2}\right]^{1/2}\right\}^{-1/2}\right]$$

Finally, the interaction energy between the two elliptical quadrupoles is given by[50]

$$\begin{aligned} V(r_{12},\varphi_1,\varphi_2) = -2\gamma\pi\alpha^2 H_e \cosh(s_0)\sinh(s_0)\,[C'_{11}\cos(2\varphi_1-2\varphi_2) \\ - C'_{21}\sin(2\varphi_1-2\varphi_2)] \end{aligned} \tag{7.3}$$

where γ is the interfacial tension of the fluid interface, H_e is the amplitude of the elliptical quadrupole and

$$\begin{aligned} C'_{11} = \frac{H_e e^{2s_0} e^{-2s^*}}{r_{12}^2\cos^2\varphi_1\,(\tanh^2 s^* - \tan^2 t^*)^2}\Bigg[& 4\cos(2t^*)(\tanh^2 s^* - \tan^2 t^*) \\ & - 8\sin(2t^*)\tan t^*\tanh s^* \\ & + 2(\tanh^2 s^* + \tan^2 t^*)(\cos(2t^*)\tanh s^* - \sin(2t^*)\tan t^*) \\ & - \frac{2\cos 2t^*\tanh s^*}{\cosh^2 s^*} - \frac{2\sin 2t^*\tan t^*}{\cos^2 t^*} \\ & + \frac{4(\cos(2t^*)\tanh s^* - \sin(2t^*)\tan t^*)}{\tanh^2 s^* + \tan^2 t^*}\left(\frac{\tanh^2 s^*}{\cosh^2 s^*} - \frac{\tan^2 t^*}{\cos^2 t^*}\right)\Bigg] \end{aligned} \tag{7.4}$$

$$\begin{aligned} C'_{21} = \frac{H_e e^{2s_0} e^{-2s^*}}{r_{12}^2\cos^2\varphi_1\,(\tan^2 t^* + \tanh^2 s^*)^2}\Bigg[& 4\sin(2t^*)(\tanh^2 s^* - \tan^2 t^*) \\ & + 8\cos(2t^*)\tan t^*\tanh s^* \\ & + 2(\tanh^2 s^* + \tan^2 t^*)(\sin(2t^*)\tanh s^* + \cos(2t^*)\tan t^*) \\ & - \frac{2\sin 2t^*\tanh s^*}{\cosh^2 s^*} + \frac{2\cos 2t^*\tan t^*}{\cos^2 t^*} \\ & + \frac{4(\sin(2t^*)\tanh s^* + \cos(2t^*)\tan t^*)}{\tanh^2 s^* + \tan^2 t^*}\left(\frac{\tanh^2 s^*}{\cosh^2 s^*} - \frac{\tan^2 t^*}{\cos^2 t^*}\right)\Bigg] \end{aligned} \tag{7.5}$$

where s^*, t^* are given by equation (7.2).

Note that in equations (7.3)-(7.5), we have corrected some typographical errors in the corresponding equations presented by Lewandowski et al.[50] Specifically, in equation (7.3), there is a minus between the two terms inside the square bracket (not a plus),[50] while in equations (7.4), (7.5), the denominator on the right hand side contains an extra factor of $\cos^2\varphi_1$.[50] Note also that, in spite of this extra factor, C'_{11}, C'_{21} do not diverge for $\varphi_1 \longrightarrow \pm\pi/2$ but tend towards finite limiting values. To avoid any numerical instabilities in our calculations, we therefore set C'_{11}, C'_{21} to be equal to these limiting values for φ_1 very close to $\pm\pi/2$.

7.2.3 Statistical Analysis of Clusters

In order to observe and quantify different particle assemblies, the particles were classified as belonging to side-to-side chains or tip-to-tip triangular clusters based on their separation and orientation relative to other particles in the system, with the criteria based on these quantities chosen to ensure that the classification coincides with the classification based on visual inspection. For this analysis, the centre-to-centre separation between two nearest-neighbour core-shell ellipsoids in contact was $d_C = 2b'$ and $d_T = \sqrt{a'^2 + 3b'^2}$ respectively for the side-to-side chains and tip-to-tip triangular lattices,[88] where $a' = a + h$, $b' = b + h$. For the simulation system, a particle was classified as belonging to a side-to-side chain if its centre-to-centre separation to any other particle satisfied the condition $r_{12} < 1.3d_C$ and the relative orientation of the two particles satisfied the condition $|\hat{a}_1 \cdot \hat{a}_2| \geq 0.9$, where $\hat{a}_1$, $\hat{a}_1$ are the unit vectors along the semi-major axes of the two particles. On the other hand, a particle as belonging was classified to a tip-to-tip triangular cluster if its centre-to-centre separation to any other particle satisfied $0.7d_T \leq r_{12} \leq 1.15d_T$ and the relative orientation of the two particles satisfied $|\hat{a}_1 \cdot \hat{a}_2| < 0.9$. If a particle belonged to both a chain and a triangular cluster, we classified it as belonging to a triangular cluster.

For the experimental system, a neural network was used to analyse the experimental micrographs to capture the position of the ellipsoid centres, the long and short axes lengths and the orientation of the long axis relative to one of the lab frame axes. We then filtered the data by eliminating any particles whose long axis length is smaller than 60% of the mean or two standard deviations greater than the mean. Further, by assuming that all ellipsoids have a long and short axes length equal to the mean, all particle pairs whose centre-to-centre separation is smaller than the contact separation predicted by the Berne-Pechukas model[147] were also removed from the analysis (see Section 7.2.2.1). We note that the neural network used by the experimentalists underpredicts the aspect ratio of the ellipsoidal particles compared to values obtained from direct measurements of the experimental micrographs but fortunately this discrepancy does not have a significant impact on our statistical classification. Having filtered the experimental data as described above to remove any artefacts of the ellipsoid identification process, an ellipsoid was classified as being part of a side-to-side chain if its separation and orientation relative to any other particle satisfied the conditions $r_{12} < 1.3d_C$, $|\hat{a}_1 \cdot \hat{a}_2| \geq 0.9$ and $|\hat{a}_1 \cdot \hat{r}_{12}| < 0.5$, where $\hat{r}_{12}$ unit vector along the centre-to-centre line connecting the two particles. On the other hand, an ellipsoid was classified as being part of a tip-to-tip triangular cluster if its separation and orientation relative to any other particle satisfied the conditions $0.5d_T \leq r_{12} \leq 0.8d_T$, $|\hat{a}_1 \cdot \hat{a}_2| < 0.9$ and $|\hat{a}_1 \cdot \hat{r}_{12}| > 0.2$. If an ellipsoid belonged to both a chain and a triangular cluster, we classified it as belonging to a triangular cluster. The statistical classification above was carried out for 4 – 20 experimental micrographs for each aspect ratio and shell thickness.

7.3 Results and Discussion

7.3.1 Summary of Experimental Data

In this Chapter we seek to understand the self-assembly behaviour of core-shell ellipsoids found in experimental results generated by our colleagues at the Friedrich-Alexander University in Germany. To provide context and motivation for our theoretical study, in this Section, we report the key experimental finding produced by our experimental colleagues. However, we did perform statistical analysis of some of the experimental images, to highlight the different assemblies and to provide quantitative analysis (see Section 7.2.3).

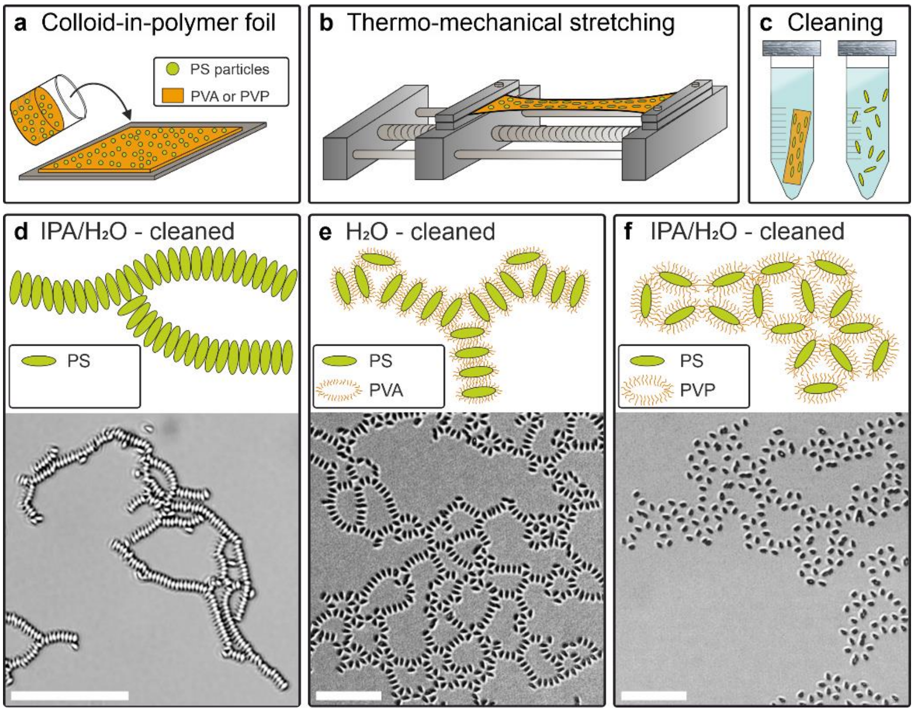

Figure 7.2: The self-assembly behaviour of ellipsoids at the air/water interface depends on their fabrication process. a-c) Schematic illustration of the fabrication process: a) Colloidal polystyrene (PS, radius R_0 = 0.55 µm) particles are embedded in a PVA or PVP foil, followed by (b) thermo-mechanical stretching. c) The ellipsoidal particles are recovered by dissolving the foil in H_2O followed by cleaning using centrifugation and redispersion in either pure H_2O or IPA/H_2O mixtures. d-f) Schematic illustration and optical microscopy images of the interfacial self-assembly at an air/water interface for ellipsoidal particles prepared by different fabrication procedures. d) Ellipsoids prepared in a PVA foil and cleaned in an IPA/H_2O mixture assemble in direct contact in a "chain-like" side-to-side arrangement. e) The same ellipsoids but cleaned solely with H_2O assemble in a mixture of side-to-side and tip-to-tip configurations and retain a non-close packed arrangement. f) Ellipsoids prepared in a PVP foil assemble in a "flower-like" tip-to-tip configuration with non-close packed arrangement, even when cleaned with an IPA/H_2O mixture. Scale bars: 20 µm.

In Figure 7.2, we show experimental data from our colleagues for the self-assembly of polymeric polystyrene (PS) ellipsoids with a similar aspect ratio (AR) of 3 at the air/water interface, produced using the thermo-mechanical stretching technique[145] with different fabrication protocols. In the fabrication process, spherical PS colloidal particles (radius R_0 = 0.55 μm) are embedded in either a poly(vinyl alcohol) (PVA) or poly(vinyl pyrrolidone) (PVP) foil (Figure 7.2a).[145] This composite foil is stretched in an oil bath above the glass transition temperature of the polymeric particles, deforming them into ellipsoids (Figure 7.2b). The resulting anisotropic particles were subsequently retrieved by dissolving the foil in water, followed by cleaning in either an isopropanol (IPA)/water mixture or pure water (Figure 7.2c).

The synthesized ellipsoids were then spread at an air/water interface, and their self-assembly behaviour is observed in situ using optical microscopy. A striking difference was observed depending on the fabrication protocol. Ellipsoidal particles prepared following the original work by Ho et al.,[145] using a PVA foil and cleaning in IPA/water mixtures, self-assemble into a "chain-like" structure, where the ellipsoids are in direct contact in a side-to-side configuration (Figure 7.2d). The same ellipsoids but cleaned using dissolution and subsequent centrifugation/redispersion in water, self-assemble into a non-close-packed structure where the ellipses are visibly separated from each other. They assume both side-to-side and tip-to-tip configurations (Figure 7.2e). Ellipsoids prepared in a PVP foil, on the other hand, assemble into a "flower-like" tip-to-tip configuration (Figure 7.2f), but also visibly separated and non-close-packed.

We attribute the difference in self-assembly behaviour to the presence of polymeric chains adsorbed onto the particle surface during the fabrication process. An IPA/water mixture is required to sufficiently remove PVA from the ellipsoid surfaces.[145,146] In contrast, using pure water for the centrifugation/redispersion leaves a layer of PVA chains on the particle surface with a swollen thickness of roughly 40 nm, as determined by dynamical light scattering.[146] These PVA chains extend at the liquid interface to reduce the surface energy and thereby form a 2D corona around the ellipsoidal particles, which is even visible in situ using cryo-scanning electron microscopy (SEM).[41] This prevents the particles from coming into close contact and, as we will discuss later in Section 7.3.3, affects the energy landscape of the tip-to-tip and side-to-side configurations.

Assembling PVA-coated ellipsoids at liquid interfaces is challenging. To overcome this challenge, the PVA matrix used in the stretching process is replaced with PVP (polyvinylpyrrolidone). In bulk liquid, both PVA and PVP chains produce a similar shell thickness of around 40 nm. However, ellipsoids with a PVP shell appear more separated at the air/water interface compared to those with a PVA shell (cf. Figure 7.2e, Figure 7.2f). We hypothesize that PVP chains extend further at the liquid interface, leading to a more extended corona around the ellipsoids than PVA chains. Although the exact mechanism is not yet fully understood, this data suggest that the physicochemical properties of the polymer shell significantly influence corona formation at liquid interfaces, which, in turn, affects the self-assembly behaviour of the ellipsoidal particles.

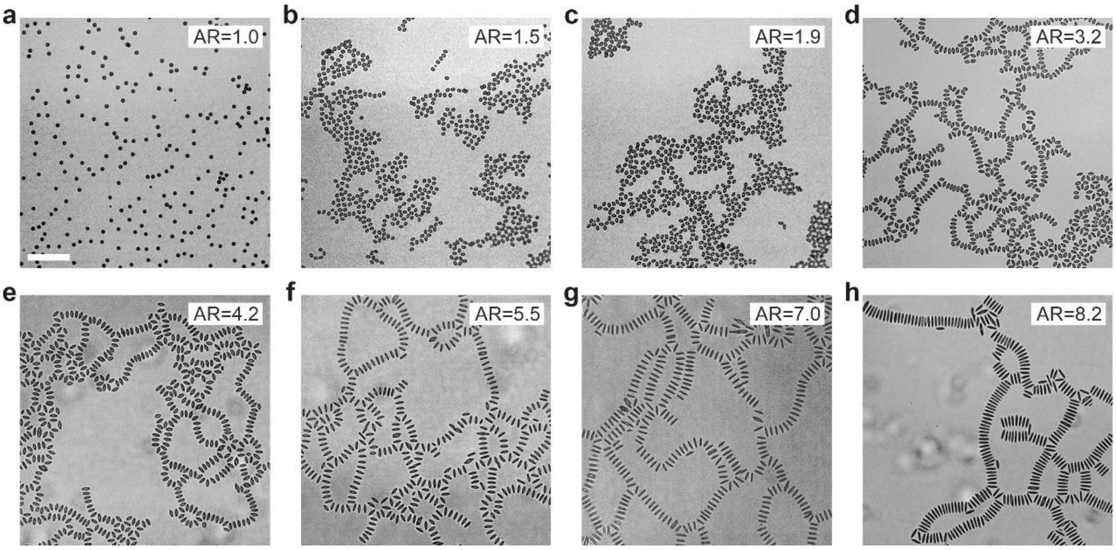

Figure 7.3: Interfacial self-assembly behaviour of core-shell ellipsoids as a function of aspect ratio (AR). Microscopy images of the self-assembly behaviour of (a) spherical particles and (b-h) ellipsoids with increasing aspect ratio. We observe a transition from a "flower-like" tip-to-tip assembly (b-d) to a "chain-like" side-to-side assembly (e-h). Scale bars: 50 µm.

Next, the variation of the self-assembly behaviour of these ellipsoids with aspect ratio was investigated (Figure 7.3). Spherical polymethyl methacrylate (PMMA) particles (radius R_0 = 1.65 µm) remain fully separated (Figure 7.3a), indicating predominant repulsive interactions. In contrast, when stretched into ellipsoidal particles they exhibited attractive interactions at the liquid interface (Figure 7.3b-h). At low aspect ratios, ellipsoids primarily formed a "flower-like" tip-to-tip assembly (Figure 7.3b-d). As the aspect ratio increases, "flower-like" and "chain-like" structures with side-to-side arrangement coexist (Figure 7.3d-f). These ellipsoids form network-like structures where tip-to-tip triangles form branching points of individual side-by-side chains. The length of the chains continuously increases, until, at the highest aspect ratios (AR>6), the predominant assembly is in the form of chains.

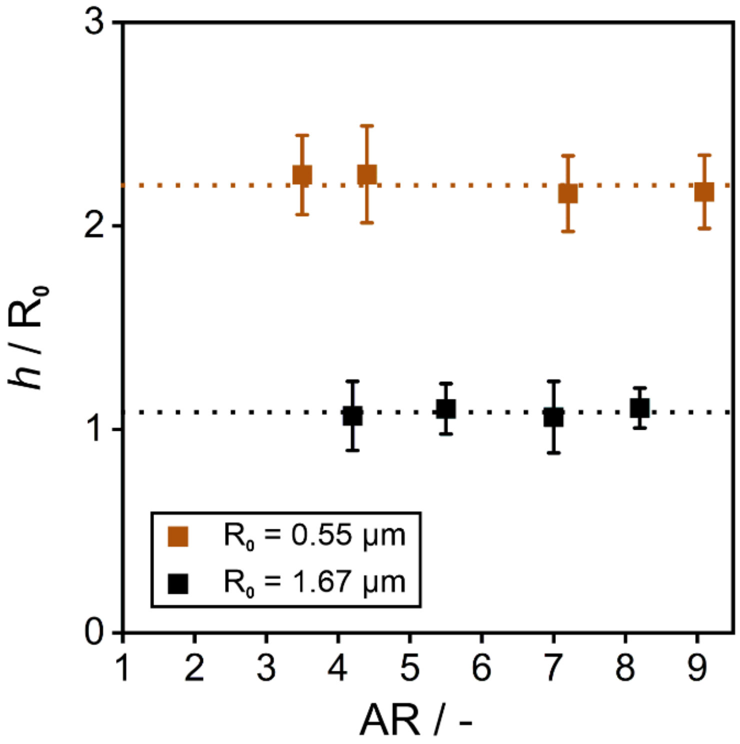

Figure 7.4: Shell thickness h as a function of aspect ratio. The shell thickness h is determined experimentally by measuring the center-to-center distance for ellipsoids in a side-to-side arrangement from optical microscopy images and subtracting the corresponding short-axis measurements obtained from SEM images.

Motivated by the interfacial spreading of the PVP and PVA chains leading to different assemblies, the interfacial self-assembly behaviour of the ellipsoidal particles as a function of their shell-to-core ratio and aspect ratio was quantified. Experimentally, the shell-to-core ratio, h/R_0, was varied by stretching colloidal particles with different initial radii (R_0=0.55 µm and R_0=1.65 µm), while maintaining the same PVP shell polymer. The interfacial shell thickness h formed by the PVP polymer chains stretched at the liquid interface is quantitatively determined by averaging over the distances between ellipsoids in the side-to-side configuration. This model assumes that the ellipsoidal particles in this configuration are in shell contact, which seems reasonable as capillary forces will tend to bring the particles into the closest possible configuration. The thickness of the shell as a function of aspect ratio was also measured to confirm that h/R_0 remains independent of the aspect ratio (see Figure 7.4). It is important to note that the PVP shell thickness in bulk is roughly 40 nm, but once adsorbed to the liquid interface, the PVP polymer chains extend to form a micron-sized 2D shell, also termed a corona, along the interface as they spread out to reduce surface tension.[146]

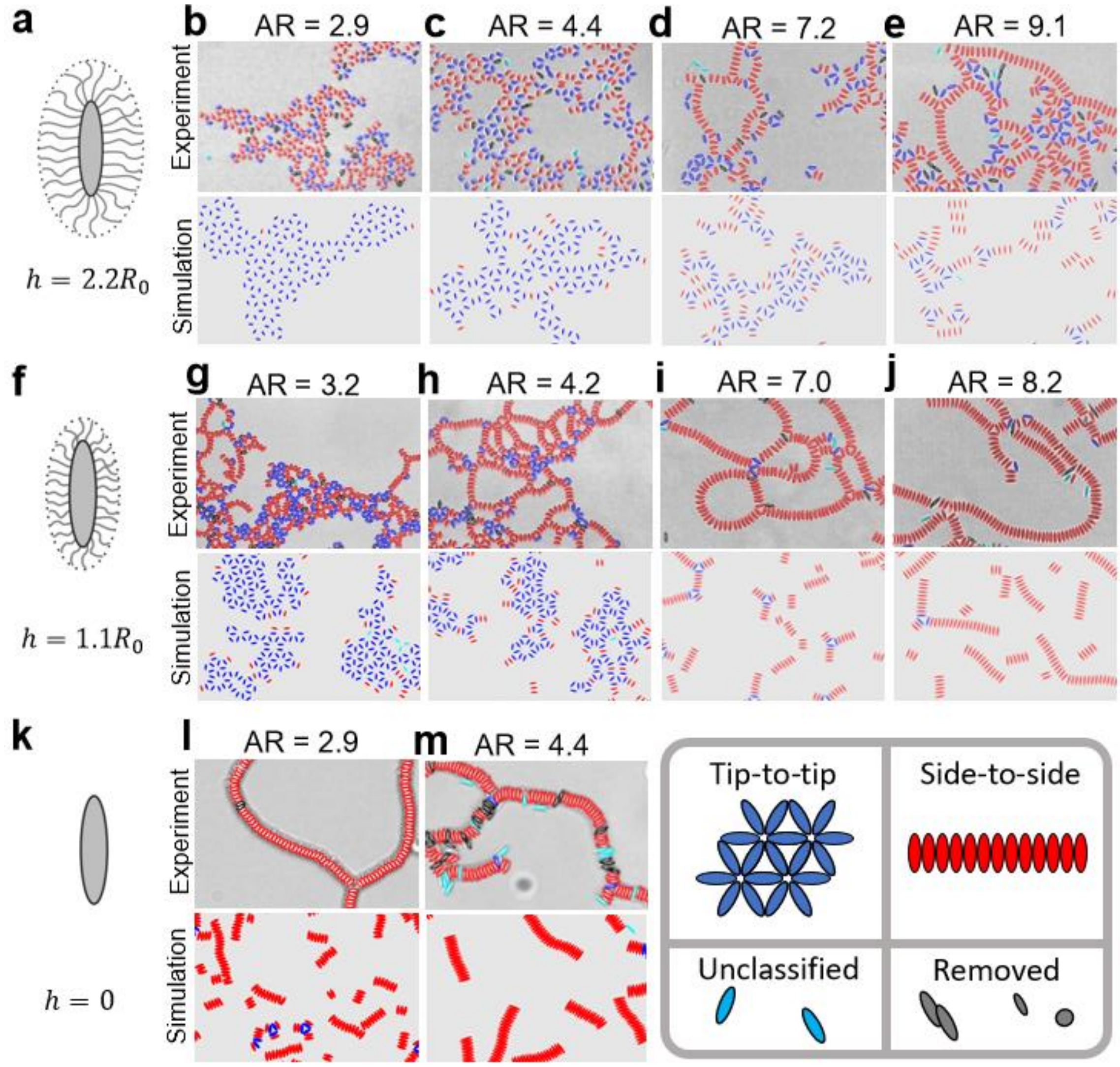

Figure 7.5: Self-assembly of core-shell ellipsoids at the air/water interface as a function of shell thickness *h* and aspect ratio AR. a,f,k) Schematic illustration of the core-shell ellipsoids. b-e, g-j,l-m) Microscopy images (top) with colour-coded overlay and corresponding Monte Carlo simulations (bottom). Ellipsoids in tip-to-tip are colour-coded blue, in side-to-side red, unclassified cyan and ill-defined, removed ellipsoids in black. a-e) Ellipsoids with a shell thickness *h* = 2.2 R_0 predominantly assemble in tip-to-tip configuration at low and intermediate aspect ratios (b,c) and coexistence of tip-to-tip and side-to-side at higher aspect ratio (d,e). f-j) Ellipsoids with a shell thickness *h* = 1.1 R_0 assemble in a tip-to-tip configuration at low aspect ratio (g), a mixture of tip-to-tip and side-to-side at intermediate aspect ratio (h) and side-to-side at high aspect ratio (i,j). k-m) Ellipsoids without a shell (*h* = 0) only assemble side-to-side.

The combined approach reveals that ellipsoids with the higher shell-to-core ratio (*h* = 2.2 R_0), produced using polystyrene particles with an initial radius R_0 = 0.55 µm, predominantly assemble in a "flower-like" tip-to-tip structure at low and intermediate aspect ratios, with a notable coexistence with a "chain-like" side-to-side structure at high aspect ratios (see Figure 7.5a-e). A similar pattern is observed for ellipsoids with a lower shell-to-core ratio (*h* = 1.1 R_0), where tip-to-tip structures are present at low aspect ratios, coexistence is seen at intermediate aspect ratios, and side-to-side configurations dominate at higher aspect ratios (see Figure 7.5f-j). However, the transition to side-to-side configurations occurs at lower aspect ratios for these ellipsoids. For ellipsoids without a shell (*h* = 0), essentially only "chain-like" side-to-side assemblies are observed experimentally, irrespective of aspect ratio (see Figure 7.5k-m).

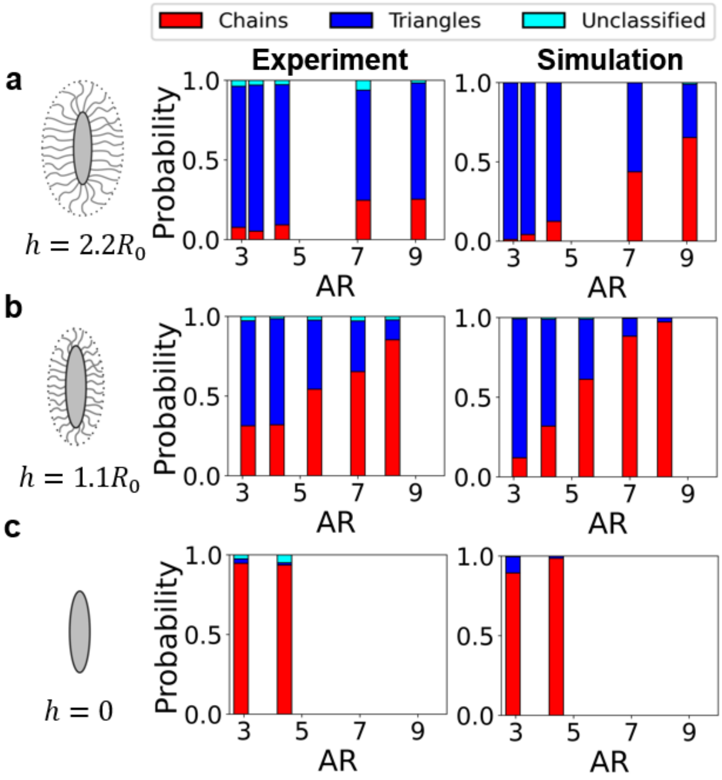

Figure 7.6: Quantitative analysis of the self-assembly behaviour of core-shell ellipsoids. Probability of finding ellipsoids in a tip-to-tip (blue) or side-to-side (red) configuration. For core-shell ellipsoids (a,b), we find a continuous transition from a tip-to-tip assembly to a side-to-side assembly with increasing aspect ratio. c) Ellipsoids without a shell essentially only assemble into side-to-side configurations.

To quantify the experimental system we perform statistical analysis (see Section 7.2.3) to obtain the probability per particle to be in a chain, triangular, or neither configuration (Figure 7.6). Specifically, we see that for a fixed shell thickness increasing the aspect ratio does indeed increase the likelihood of chain formation, and by comparing the two shell thicknesses (Figure 7.6a with Figure 7.6b) we see that the smaller shell thickness leads to increased probability of chain formation.

7.3.2 Monte Carlo Simulations

To gain a deeper understanding of the fundamental forces driving the self-assembly of core-shell ellipsoids at the liquid interface, we perform Monte Carlo (MC) simulations of core-shell ellipsoids with aspect ratios and shell thicknesses *h* corresponding to the experimental system, including both steric and capillary interactions between the particles. For simplicity, we neglect electrostatic repulsions in our model.

As discussed earlier, the PVP chains adsorbed to the ellipsoid particle core are stretched out more significantly along the liquid interface compared to the bulk. The steric interactions between the core-shell ellipsoids are therefore dominated by the 2D shell formed by the interfacial PVP chains rather than the 3D shell formed by the bulk PVP chains. In Chapter 6, we studied the self-assembly of core-shell particles at liquid interfaces that were subjected to an external compression where it is sometimes energetically favourable for the shells of neighbouring particles to locally collapse so that their cores come into contact. In contrast, the core-shell particles we are studying here are not subjected to any external compression and the steric repulsion between the 2D shells is sufficient to prevent particles from coming closer than shell-shell contact, as experimentally evidenced by the formed non-close-packed patterns (Figure 7.2 and Figure 7.3). In the experiments, it was also observed that this shell repulsion occurs at both the sides and the tips of particles and for simplicity, we assume that the shell thickness is the same at the sides and the tips. In our MC simulation, we therefore treat the core-shell ellipsoids as hard ellipses with long and short axis lengths of $a' = a + h$ and $b' = b + h$ respectively, where h is the experimentally measured shell thickness which is independent of the aspect ratio AR (see Section 7.2.2.2).

The capillary interactions between the core-shell ellipsoids come from the quadrupolar deformation of the three-phase contact line on the ellipsoid surface due to the constant contact angle requirement at the contact line.[65] Note that the contact line resides on the PVP coated core rather than the boundary of the shell since we assume that the shell is essentially a 2D object formed by interfacially adsorbed polymer chains. In addition, it is reasonable to assume that the PVP shell renders the core more hydrophilic and we therefore assign a water contact angle of the core as $\theta_w = 40^\circ$ in our model.[137] As discussed in 7.2.2.2, we treat each ellipsoid core as a capillary quadrupole in elliptical coordinates.[50,52] The advantage of working in elliptical coordinates is that it allows us to accurately model the capillary interactions between rod-like particles using a small number of capillary multipoles,[52] in our case one multipole at quadrupolar order.

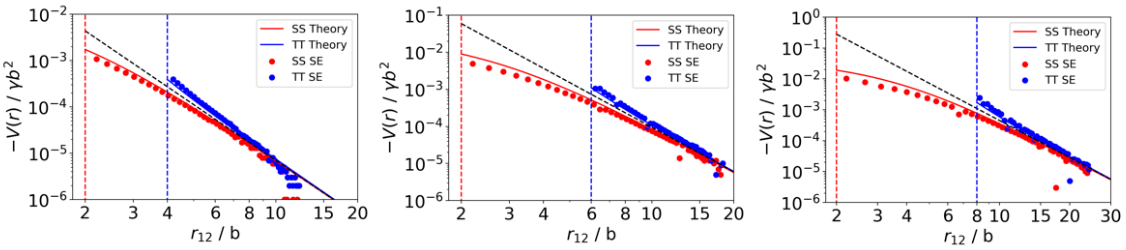

Figure 7.7: Comparison of elliptical quadrupole model with Surface Evolver simulations for the capillary interaction energy as a function of centre-to-centre separation r_{12} for ellipsoids with no shells and contact angle $\theta_w = 40^\circ$ with aspect ratio (a) $\mathrm{AR} = 2$; (b) $\mathrm{AR} = 3$; (c) $\mathrm{AR} = 4$. Note that in all cases we plot $-V$ in the vertical axis. We compare theory (solid lines) to simulations (data points) for ellipsoids in the side-to-side configuration (red) and tip-to-tip configuration (blue). The red and blue vertical dashed lines represent the contact separation for the side-to-side and tip-to-tip configuration respectively while the

dashed black line represents the quadrupolar power law. The values of the fitting parameter H_e used to fit theory to simulation for the different AR are given in Table 7.1.

Aspect Ratio	H_e	H_0	T^*
2	$0.0205b$	$0.0506b$	7.4×10^{-4}
3	$0.0445b$	$0.0878b$	2.1×10^{-4}
4	$0.0690b$	$0.115b$	1.0×10^{-4}

Table 7.1: The amplitude of quadrupolar contact line undulations for ellipsoids with $\theta_w = 40°$ and different aspect ratios AR obtained from fitting the elliptical quadrupole model to the Surface Evolver simulation data in Figure 7.7 (H_e) and calculated directly from Surface Evolver simulations of isolated ellipsoids ($H_0 = (z_{max} - z_{min})/2$, where z_{max}, z_{min} are the maximum and minimum heights respectively of the contact line). We also list the normalized temperature $T^* = k_B T/\gamma H_e^2$ for the ellipsoids assuming $R_0 = 0.55\mu\text{m}$, $T = 300\text{K}$ and $\gamma = 70\text{mN}\cdot\text{m}^{-1}$.

In Figure 7.7a,b,c, we compare our theoretical model, i.e., equations (7.2)-(7.5), with Surface Evolver simulations for the interaction energy as a function of r_{12} for ellipsoids with no shells and contact angle $\theta_w = 40°$ which have aspect ratios $\text{AR} = 2,3,4$ respectively, see Section 7.2.1. Specifically, we compare theory (solid lines) to simulations (data points) for ellipsoids in the side-to-side (red) and tip-to-tip configuration (blue). We use H_e as a fitting parameter to fit the theory to the simulation data and the fitted values of H_e for the different AR are given in Table 7.1. We see that the theoretical model captures the key features of the numerical data almost quantitatively, including the far-field quadrupolar scaling of $V \sim -1/r_{12}^4$ (dashed black lines) and the near-field deviations from this scaling. In particular, the model correctly predicts that the lowest energy configuration for two ellipsoids with no shells is where the ellipsoids are in side-to-side contact rather than tip-to-tip contact (note that we plot $-V$ in the vertical axis of Figure 7.7).

The fitted values of H_e also agree with the amplitude of contact line undulations H_0 calculated directly from Surface Evolver simulations of isolated ellipsoids to within a factor of around 2, where we define the amplitude to be $H_0 = (z_{max} - z_{min})/2$, i.e., half the difference in the maximum height z_{max} and minimum height z_{min} of the contact line (see Table 7.1). The good agreement between theory and simulations in Figure 7.7 and Table 7.1 confirms that modelling the contact line undulations on the ellipsoid cores as elliptical quadrupoles is a good approximation.

The MC simulations were performed at a core area fraction of $\eta = \pi ab/8a'^2$ to ensure that the system is in the dilute regime (i.e., core-shell ellipsoids on a hexagonal lattice can freely rotate about their centres without interfering with each other) like in the experiments. The energy scale for capillary interactions is γH_e^2, where γ is the interfacial tension of the air-water interface. The importance of capillary interactions relative to the thermal energy is characterized by the normalized temperature $T^* = k_B T/\gamma H_e^2$. In Table 7.1, we list the values of T^* for ellipsoids with $\mathrm{AR} = 2,3,4$ where we assume that $R_0 = 0.55\mu\mathrm{m}$, $T = 300\mathrm{K}$ and $\gamma = 70\mathrm{mN} \cdot \mathrm{m}^{-1}$, based off of the experimental system. We see that in all cases $T^* \ll 1$ and that T^* decreases with increasing AR. Since all the experimental ellipsoids have $\mathrm{AR} > 2.5$ and T^* will be lower for ellipsoids with larger R_0 (since H_e is proportional to R_0), we conclude that all experimental systems we are studying in this Chapter are in the low temperature regime where $T^* \ll 1$. To model the experimental system, we therefore quench the system from a high initial temperature to a final temperature of $T^* = 0.2$. The choice of the final temperature represents a good compromise between being low enough for the system to be in the low temperature regime while still being high enough for the MC simulation to equilibrate the system efficiently.

From Figure 7.5, we see that the MC simulation accurately reproduces the experimentally observed trends, namely that increasing aspect ratio favours the formation of "chain-like" side-to-side arrangements, while increasing shell thickness favours "flower-like" tip-to-tip configurations. We colour and quantitatively analyse the snapshots as discussed in Section 7.2.3. In Figure 7.6, we quantitatively compare the statistical classification of the different structures formed in the MC simulations as a function aspect ratio and shell thicknesses with their experimental counterparts. The data confirms that the MC simulation reproduces the experimentally observed trend that increasing aspect ratio favours the formation of "chain-like" side-to-side arrangements, while increasing shell thickness favours "flower-like" tip-to-tip formations.

We note from the snapshots in Figure 7.5 that for each aspect ratio and shell thickness, the MC simulations not only reproduce the proportion of side-to-side chains versus tip-to-tip triangular lattices but also the local microstructure of the particle clusters and networks that are observed experimentally. One feature of the microstructure that is not captured so well by the simulations is that the cluster size of side-to-side chains tend to be smaller than what is observed experimentally, especially for the higher aspect ratio ellipsoids. We attribute this discrepancy to two reasons. Firstly, the interaction potential for side-to-side contacts is lower than for tip-to-tip contacts and this energy difference increases with increasing aspect ratio so that the relaxation time for side-to-side chains is much longer compared to tip-to-tip triangular lattices in the low temperature regime for larger aspect ratio ellipsoids. Secondly, the area fraction we use in the simulations roughly scales as $\sim\mathrm{AR}^{-1}$ and therefore decreases with increasing aspect ratio AR. These factors mean that for the same overall simulation length, the higher aspect ratio systems are not as well equilibrated as the lower aspect systems, resulting in smaller side-to-side chain lengths and cluster sizes for higher aspect ratio systems. However, apart from this discrepancy, the agreement between simulation and experiments for both the statistics and the local microstructure of the self-assembled structures is remarkable, especially considering the simplicity of our theoretical model. The fact that our simulations capture the key features of the experiments suggests that the self-assembly of core-shell ellipsoids is primarily driven by a competition between steric repulsions from the shell and capillary interactions from the core, while electrostatic interactions seem to play a negligible role.

7.3.3 Minimum Energy Calculations

To assess the thermodynamics underpinning the observed self-assembled structures, we first consider how the interaction potential between core-shell ellipsoids varies with aspect ratio and shell thickness. As we increase the aspect ratio of the core-shell ellipsoids, side-to-side contacts become increasingly more favourable energetically compared to tip-to-tip contacts, essentially because the difference in centre-to-centre separation for the two configurations increases. This explains why increasing aspect ratio favours the formation of side-to-side chains compared to tip-to-tip triangular lattices.

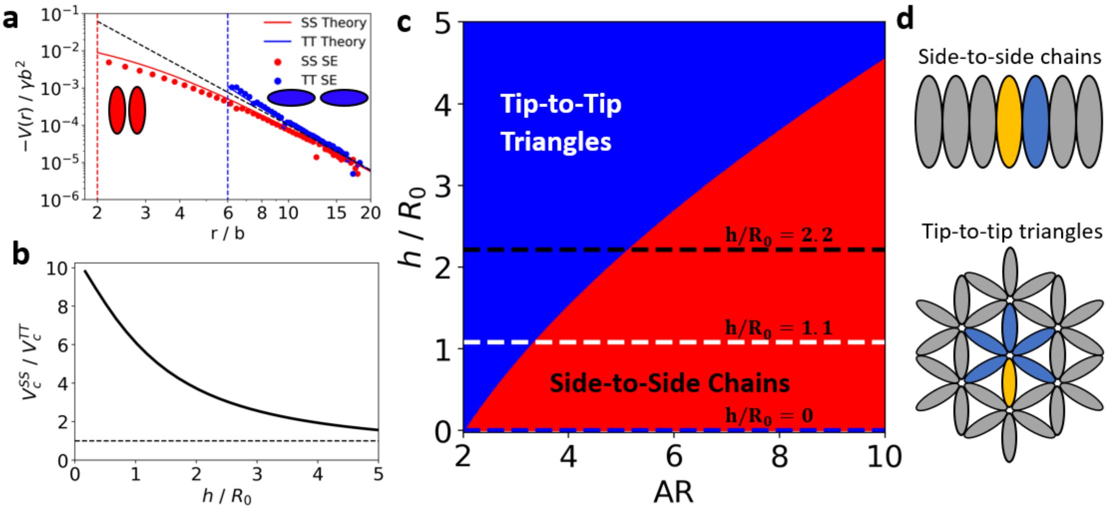

Figure 7.8: Theoretical evaluation of interactions between core-shell ellipsoids at liquid interfaces. a) Capillary interaction energy between two bare ellipsoids (i.e., no shell) with aspect ratio 3 as a function of centre-to-centre separation r_{12} normalized by the length of the short axis of the ellipsoids, b, for ellipsoids oriented side-to-side (red) and tip-to-tip (blue). The solid lines are calculated analytically assuming the ellipsoids are elliptical quadrupoles while the points are calculated numerically using Surface Evolver. The dashed coloured lines represent the contact distance for each configuration, and the black dashed line represents a simple power law r_{12}^{-4}. Note that we are plotting $-V$ in the vertical axis. b) Ratio of capillary energies for core-shell ellipsoids in side-to-side vs. tip-to-tip contact as a function of shell thickness h calculated from analytical theory assuming the cores are elliptical quadrupoles. c) Zero temperature phase diagram for core-shell ellipsoids in the aspect ratio (AR) vs. shell to core ratio h/R_0 plane. The experimental values of h/R_0 are indicated by the blue, white and black dashed lines, respectively. d) Minimum energy configurations of side-to-side chains and tip-to-tip triangular lattice that are used to compute the phase diagram, where the energy per particle is calculated from the interaction between the yellow particle and its neighbouring blue particles.

We now focus on the role of shell thickness on the assembly process, using ellipsoidal particles with an aspect ratio of 3 as a model. We first note that as we increase the shell thickness h, the fractional increase in the centre-to-centre separation r_{12} will be greater for ellipsoids in side-to-side contact compared to those in tip-to-tip contact. Since the capillary interaction between the ellipsoidal cores is to a first approximation an inverse power law in r_{12} (black dotted line in Figure 7.8a), this means that the capillary bond energy (i.e., magnitude of the attractive potential at contact) for core-shell ellipsoids in side-to-side contact should drop more than those in tip-to-tip contact as we increase shell thickness. This point is confirmed in Figure 7.8b where we plot the ratio V_c^{SS}/V_c^{TT} as a function of shell thickness h for core-shell ellipsoids with aspect ratio $\mathrm{AR} = 3$, where V_c^{SS} and V_c^{TT} are the capillary bond energies for side-to-side and tip-to-tip contacts respectively calculated from the elliptical quadrupole model. We see that the capillary bond energy for side-to-side contacts falls relative to that for tip-to-tip contacts as we increase h. Despite this decrease, we note that $V_c^{SS}/V_c^{TT} > 1$ for the shell thicknesses explored in this Chapter, i.e., the capillary bond energy for side-to-side contact is always greater than that for tip-to-tip contact, so that this effect alone is not enough to tip the balance in favour of the formation of tip-to-tip structures.

However, in both the experiments and the simulations, the core-shell ellipsoids with large h do not form tip-to-tip chains but "flower-like" tip-to-tip triangular lattices, where the number of capillary bonds per particle is greater than in the chain state. Specifically, the number of capillary bonds per particle is 1 for side-to-side chains and 5 for tip-to-tip triangular lattices, as schematically shown in Figure 7.8d by the interactions between a central particle (yellow) and its neighbours (blue). In Figure 7.8c, we quantify the total capillary interactions for side-to-side and tip-to-tip arrangements as a function of aspect ratio and shell thickness, taking into account both the evolution of V_c^{SS}/V_c^{TT} with shell thickness, and the increased number of neighbours for triangular tip-to-tip lattices. These calculations are based on the elliptical quadrupole model (see Section 7.2.2.2), where the centre-to-centre separation between contacting nearest neighbours are given in Section 7.2.3.

In our calculations, we assume the structures are infinite, i.e., we neglect defects and edge effects. We also neglect interactions of the yellow particle with particles beyond the blue particles, i.e., we assume an effective cutoff distance of $\approx a' = a + h$ for particle interactions; this is a good approximation since we are considering quadrupolar interactions which fall off rapidly with separation. Finally, we assume that the equilibrium structure for any given geometry is the structure with the minimum energy per particle. This assumption is justified since the experimental system is in the low temperature regime $T^* \ll 1$ where entropic effects are negligible. Figure 7.8c shows the resultant zero-temperature phase diagram for core-shell ellipsoids in the aspect ratio AR-shell thickness h plane.

This phase diagram accurately reproduces the trends observed in both experiments and simulation. Increasing the aspect ratio favours the formation of side-to-side chains, while increasing shell thickness favours the formation of tip-to-tip triangular lattices. In particular, it predicts that as we increase shell thickness from $h/R_0 = 0$, via $h/R_0 = 1.1$ to $h/R_0 = 2.2$ (blue, white and black horizontal lines, respectively), the transition from tip-to-tip triangular lattices to side-to-side chains occurs at higher and higher aspect ratios. Note that we do not see pure phases but a coexistence of different phases in both the experiments and the simulations, indicating that the system is not globally ergodic. However, the fact that the equilibrium structures predicted by the zero-temperature phase diagram correlate well with the dominant structures seen in both experiments and simulations suggests that the structures shown in Figure 7.8d are kinetically accessible, and the experimental core-shell ellipsoid system is at least locally ergodic.

7.4 Conclusions

We use Monte Carlo simulations to investigate the self-assembly of polymeric ellipsoidal particles experimentally fabricated through thermo-mechanical stretching at a liquid interface, with a particular focus on the role of soft shells formed from polymeric residues during fabrication. When these polymers on the ellipsoid surface adsorb at a liquid interface, they spread under the influence of surface tension, forming a 2D shell around the ellipsoid that prevents direct contact between neighbouring ellipsoids. We demonstrate that this alteration in interfacial structure significantly changes the minimum energy landscape and, consequently, the self-assembly behaviour of these ellipsoidal particles.

Using a combined experimental and simulation approach, we systematically explore the resultant self-assembly behaviour and identify two key trends: increasing the aspect ratio of the ellipsoids favours their assembly into a "chain-like" side-to-side configuration, while increasing the shell thickness promotes "flower-like" tip-to-tip configurations. A phase diagram, based on the total capillary interactions as a function of core separation and the number of neighbours, reveals a transition in minimum energy structures from side-to-side to tip-to-tip configurations with increasing shell thickness and decreasing aspect ratio, corroborating both experimental and simulation findings.

Our results may explain contradictory reports on the self-assembly of elliptical particles by accounting for the significant effects of the often-overlooked polymer corona on interactions at a liquid interface. The proposed framework is general and may provide a foundation for the predictive self-assembly of anisotropic particles into predetermined, complex arrangements. This can be achieved through the rational engineering of polymer coronae as two-dimensional spacers separating particles at a liquid interface.

Chapter 8 Capillary Assembly of Polygonal Plates with Undulating Edges at Flat Fluid Interfaces

8.1 Introduction

The aim of this Chapter is to use capillary interactions to create fully programmable two-dimensional (2D) materials. While the studies we covered in Section 2.3 demonstrate the tremendous possibilities for controlling capillary assembly by tuning particle anisotropy, an important limitation in these systems is the fact that the position of the three-phase contact line is not fixed *a priori* but is determined indirectly by the constant contact angle condition. The indirect link between particle anisotropy and contact line position makes it difficult to gain full control over the capillary interactions in these systems. Furthermore, the complex patchy particle morphology used by Whitesides and co-workers covered in Section 2.3 is very challenging to scale down below the millimetre scale, limiting the system sizes that can be produced.[62]

In order to overcome these important challenges, in this Chapter, we consider a novel particle geometry where our colloidal building blocks are polygonal plates with homogeneous surface chemistry and undulating edges. In terms of the aims of our study, this particle geometry possesses a number of game-changing advantages. Firstly, as we show later, provided the plates are thin enough and the amplitude of the undulations is small enough, the three-phase contact line is effectively pinned to the particle edge, giving us direct control over the position of contact line undulations and hence capillary interactions in the system. This control allows us to introduce selective interactions between polygon sides, favouring specific polymorphs over others and thus create 2D structures with much longer-ranged order than was possible with previous systems.

Secondly, since we control capillary interactions through particle shape rather than surface chemistry, this considerably simplifies the fabrication of the colloidal building blocks, allowing us to increase throughput and reduce particle size. For example, relatively low throughput production of the required particle shapes (e.g., ~10s of particles) can be achieved using 3D printing,[30,31] with sub-micron resolution achievable using two-photon polymerization techniques.[32,33] Much higher throughput production (>100 particles) can be achieved by stamping defined surface textures onto a flat sheet and morphing the resultant flat objects into the required 3D shapes, for example through asynchronous swelling.[149]

Thirdly, our novel particle geometry above gives us independent control over both short-ranged and long-ranged interactions using particle shape alone. Specifically, short-ranged hard-core repulsions can be controlled by changing the shape of the polygonal plates in the interfacial plane, while longer-ranged capillary interactions can be controlled by changing edge undulations normal to the interface. For colloidal polyhedra interacting only through hard-core repulsions, Glotzer and co-workers found that changing particle shape allowed them to access an incredibly rich variety of self-assembled structures, including crystals, liquid crystals, plastic crystals and quasicrystals.[150] For our system, where we can use shape to fully control the interplay between short-ranged hard-core repulsions (which determine local packing) and longer-ranged capillary interactions (which determine directional aggregation), the possibilities for self-assembly are even richer.

To illustrate the immense potential provided by our system for programming self-assembly, in this Chapter we use both minimum energy calculations and Monte Carlo simulations to show how we can engineer the shape of the colloidal building blocks to create a variety of 2D structures, including hexagonal, honeycomb, open Kagome and quasi-crystalline lattices. Note that the complex structures we create arise from higher order multipole capillary interactions. These multipolar interactions would be overwhelmed if gravity-induced capillary interactions are present, as the latter are monopolar in nature and therefore have a much longer range (see Chapter 2).[65,66] In our calculations, we assume that gravitational forces are negligible. Our calculations therefore apply to polygonal plates on the micron-scale, which are small enough for gravity to be negligible[87] and Brownian motion to be significant, but large enough for the energy scale for capillary interactions to much greater than thermal energy $k_B T$, so that we are in the low temperature regime where minimum energy calculations are valid.[56,57] However, our calculations are also applicable to larger particles (say on the millimetre-scale) if we 'switch-off' gravity by density-matching the adsorbed particles with the liquid subphase and introduce random motion by using external mechanical vibration.[61,151]

The Surface Evolver simulations in this Chapter build on the preliminary work done by Dr Scott Morgan in his PhD thesis.[152] However, apart from Figure 8.7, which is based on data from Dr Morgan's PhD thesis, all other results in this chapter are original.

8.2 Theoretical Methods

8.2.1 Particle Geometry

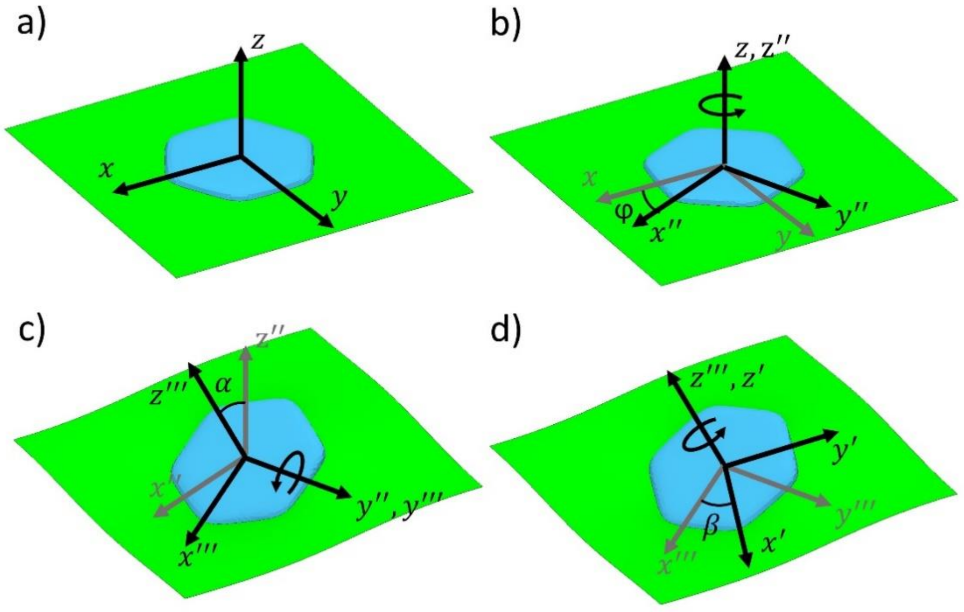

Figure 8.1: Definitions of the azimuthal angle φ, the polar angle α and the rotation angle β for a non-axisymmetric plate. For the sake of clarity, we show a flat plate with no edge-undulations. Here (x, y, z) and (x', y', z') are the lab frame and particle frame coordinates respectively.

We consider a system of polygonal plate-like particles adsorbed at a flat fluid-fluid interface. We define the lab frame coordinates (x, y, z) such that the z axis is perpendicular to the fluid interface when no particles are adsorbed, and the fluid interface is in the $z = 0$ plane. It is also convenient to define particle frame coordinates (x', y', z'), where the z' axis is perpendicular to the average plane of the polygonal plate and, depending on the orientation of the particle, they are related to the particle frame coordinates (x', y', z') via the following rotational coordinate transformations

$$\begin{pmatrix} x' \\ y' \\ z' \end{pmatrix} = \begin{pmatrix} \cos\beta & \sin\beta & 0 \\ -\sin\beta & \cos\beta & 0 \\ 0 & 0 & 1 \end{pmatrix} \begin{pmatrix} \cos\alpha & 0 & -\sin\alpha \\ 0 & 1 & 0 \\ \sin\alpha & 0 & \cos\alpha \end{pmatrix} \begin{pmatrix} \cos\varphi & \sin\varphi & 0 \\ -\sin\varphi & \cos\varphi & 0 \\ 0 & 0 & 1 \end{pmatrix} \begin{pmatrix} x - x_p \\ y - y_p \\ z - z_p \end{pmatrix} \quad (8.1)$$

where (x_p, y_p, z_p) are the coordinates of the particle centre in the lab frame, and α, β, φ are the polar, rotation, and azimuthal angle as defined in Figure 8.1 respectively.

To describe the geometry of the polygonal plate particles with undulating edges, we use the generalised super-ellipsoid equation

$$\left(\frac{x' \cos\psi_1 + y' \sin\psi_1 - \Delta}{a}\right)^{\zeta_1} + \left(\frac{x' \cos\psi_2 + y' \sin\psi_2 - \Delta}{a}\right)^{\zeta_1} + \left(\frac{x' \cos\psi_3 + y' \sin\psi_3 - \Delta}{a}\right)^{\zeta_1} + \left(\frac{z' - z_0(r,\theta)}{b}\right)^{\zeta_2} = 1 \tag{8.2}$$

where the exponents ζ_1, ζ_2 are even integers that determine the sharpness of the corners for the polygon and plate cross section respectively, with higher values leading to sharper corners. In our study, we use $\zeta_1 = 20$ and $\zeta_2 = 2$, i.e., relatively sharp polygon corners and rounded plate cross sections. The undulation of the plate edge is given by the function

$$z_0(r,\theta) = Ar\cos[m(\theta - \theta_0)] \tag{8.3}$$

where (r,θ) are circular polar coordinates in the (x', y') plane, A is a parameter that determines the amplitude of the edge undulations, m is the multipole order of the edge undulations (with $m = 2, 3, \ldots$, corresponding to quadrupolar, hexapolar etc.) and θ_0 controls the phase shift between the edge undulations and polygon shape.

To understand the particle geometry represented by equation (8.2), let us first consider a simplified version of the equation where we only include the first term on the left-hand side, i.e.,

$$\left(\frac{x' \cos\psi_1 + y' \sin\psi_1 - \Delta}{a}\right)^{\zeta_1} = 1 \tag{8.4}$$

Since ζ_1 is an even integer, equation (8.4) is equivalent to two equations

$$x' \cos\psi_1 + y' \sin\psi_1 - \Delta = \pm \mathrm{a} \tag{8.5}$$

The positive case for equation (8.5) represents a straight line in the $x' - y'$ plane with perpendicular distance $a_1 = a + \Delta$ from the origin, where the perpendicular line makes an angle ψ_1 to the positive x' axis, while the negative case represents a straight line with perpendicular distance $a_2 = a - \Delta$ from the origin, where the perpendicular line makes an angle α_1 to the negative x' axis, see Figure 8.2a. Note that $a = (a_1 + a_2)/2$ and $\Delta = (a_1 - a_2)/2$.

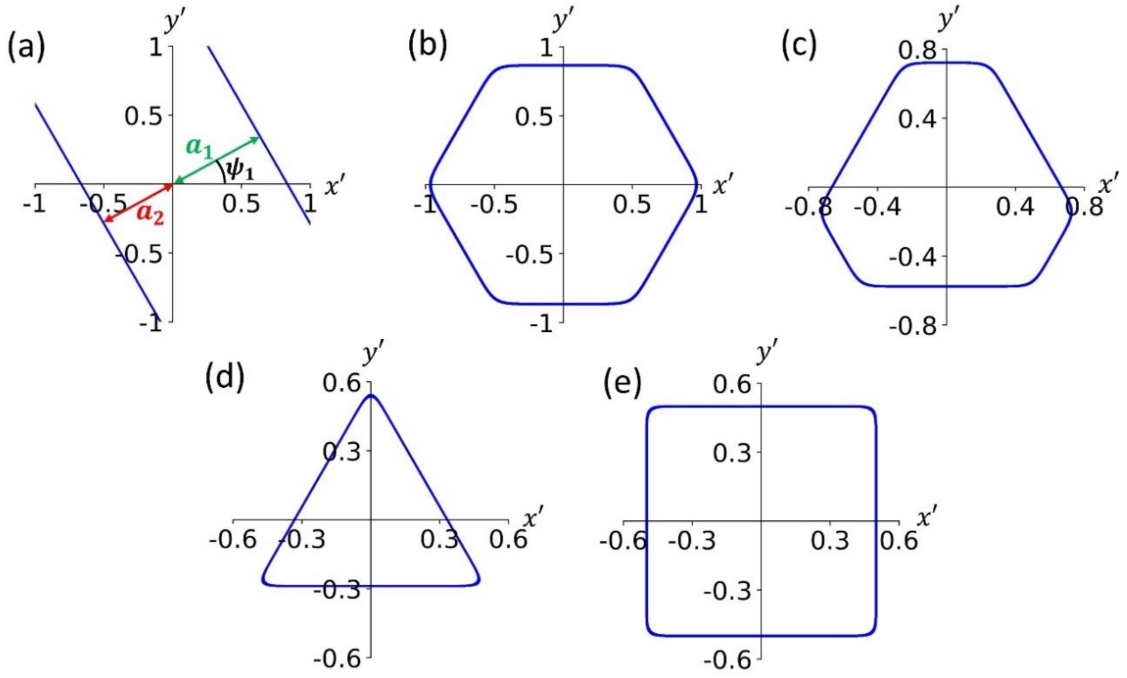

Figure 8.2: (a) Plot of equation (8.5). (b-e) Plots of equation (8.6) to represent (b) a hexagon, (c) a truncated triangle, (d) an equilateral triangle and (e) a square, working in units where $L = 1$.

Generalising the discussion above, we can readily see that the superellipse equation

$$\left(\frac{x'\cos\psi_1 + y'\sin\psi_1 - \Delta}{a}\right)^{\zeta_1} + \left(\frac{x'\cos\psi_2 + y'\sin\psi_2 - \Delta}{a}\right)^{\zeta_1} + \left(\frac{x'\cos\psi_3 + y'\sin\psi_3 - \Delta}{a}\right)^{\zeta_1} = 1 \tag{8.6}$$

represents a smooth curve which approximates a polygon formed by three pairs of parallel lines like those shown in Figure 8.2a, where the orientation for each pair of parallel lines is given by ψ_1, ψ_2, ψ_3 respectively. On the other hand, the superellipsoid equation given by equation (8.2) represents a smooth surface which approximates the surface of a polygonal plate with undulating edges, where a, b represent the average radius and half thickness of the plate, Δ allows us to control the distortion of the polygon away from a regular polygon and $z_0(r, \theta)$ given by equation (8.3) is the curve representing the edge undulations of the plate. In our study, we consider thin plates where $a/b \gg 1$.

To illustrate how equation (8.6) works in practice, let's consider how we can use it to generate the polygonal shapes considered in this Chapter. To obtain the hexagon shown in Figure 8.2b, we set $\psi_1 = \pi/2\,, \psi_2 = 7\pi/6\,, \psi_3 = 11\pi/6$. Since $a_1 = a_2 = a$ in this case, we have $\Delta = 0$. If we denote the side length of the hexagon as L, from simple geometry we have $a = \sqrt{3}L/2$.

In order to obtain the truncated triangle shown in Figure 8.2c, we set $\psi_1 = \pi/2\,, \psi_2 = 7\pi/6\,, \psi_3 = 11\pi/6$ and $a_1 > a_2$. If we denote the long and short side lengths of the truncated triangle as L and S respectively, from calculating the height of the truncated triangle, we find $a_1 + a_2 = \sqrt{3}(L + S)/2$ and from calculating the distance between the centre and the corner of the truncated triangle, we find $a_1^2 + (S/2)^2 = a_2^2 + (L/2)^2$. Solving these two simultaneous equations, we find $\Delta = (L - S)/\left(4\sqrt{3}\right)$ and $a = \sqrt{3}(L + S)/4$.

To obtain the equilateral triangle shown in Figure 8.2d, we set $\psi_1 = \pi/2\,, \psi_2 = 7\pi/6\,, \psi_3 = 11\pi/6$. In this case we have $a_1 = 2a_2$ which gives us $\Delta = a_2/2$, $a = 3a_2/2$. If we denote the side length of the triangle to be L, from simple geometry we have $a_2 = L/\left(2\sqrt{3}\right)$ so that $\Delta = L/\left(4\sqrt{3}\right)$ and $a = \sqrt{3}L/4$.

In order to obtain the square shown in Figure 8.2e, we only need two terms on the left-hand-side of equation (8.6) and we set $\psi_1 = 0, \psi_2 = \pi/2$. Since $a_1 = a_2 = a$ in this case, we have $\Delta = 0$. If we denote the side length of the square as L, we have $a = L/2$.

To describe the shape and multipole undulation of the particles used in this paper, we have named them H0, H30, H30+, TT, Sq, and Tr. Here the letters refer to the specific in plane shape of the particles, I.e., H (Hexagon), TT (truncated triangle), Tr (triangle), and Sq (square) as shown in Figure 8.2. For in plane shapes where we use different out of plane undulations, i.e., H0, H30, and H30+ we use numbers to refer to the phase of the out of plane undulations in degrees with respect to the vertices of the hexagon, i.e., θ_0. For example, H0 and H30 refer to particles with a hexagonal in-plane shape where the out of plane undulation antinodes coincide with the vertices or edges of the hexagon respectively. Additionally, we differentiate between our hexapolar H30 particle and our hexapolar plus dodecapolar particle H30+ by using an addition sign to note it is a combination of multipoles.

8.2.2 Surface Evolver

As discussed in Section 8.1, the focus of our study is on adsorbed particle systems where gravity is negligible, e.g., micron-scale particles or larger particles which are density-matched with the fluid subphase. In this case, the energy of the system is primarily due to interfacial energy and is given by equation (2.5) To highlight the role played by particle shape in controlling self-assembly, in this Chapter, we assume $\theta_w = 90°$, i.e., the adsorbed particles are neutrally wetting. In fact, the specific value of θ_w is not crucial since the fluid interface is pinned to the particle edge for the thin plate geometry we consider in this Chapter (see later). For a given configuration of adsorbed particles, the energy of the system, given by equation (2.5) is calculated using the finite element software Surface Evolver.[74]

In the Surface Evolver simulation, we work with length and energy units where the longest particle side length $L = 1$ and the fluid-fluid interfacial tension $\gamma = 1$ and use a variable triangular mesh with edge length between $0.02L$ to $0.1L$ with quadratic edges to capture the shape of the fluid-fluid interface more accurately. When calculating pair capillary interactions, we use reflecting boundary conditions at the simulation box edge. Since we are considering higher order capillary multipoles whose interactions fall off rapidly with separation, finite size effects are less severe, and we can use relatively small simulation box sizes. Specifically, we use a simulation box with boundaries at $x = \pm 8r_0$, $y = \pm 4r_0$, the interacting particles are at $(\pm 2r_0, 0)$ at maximum separation, and at $(\pm 4r_0, 0)$ at 'infinite' separation, where r_0 is the radius of the circle circumscribing the polygonal plates; in the case of squares and equilateral triangles, we use r_0 for the square, i.e., the larger circumscribing circle.

When calculating many-body capillary interactions to predict the minimum energy configurations we use periodic boundary conditions at the edge of the simulation, with a nearest neighbour separation of $d = 10L$ at 'infinite' separation. When calculating capillary interactions, the smallest surface-to-surface separation we consider is $0.1L$ for many-body interactions, $0.03L$ for pair interactions for binary mixtures of squares and triangles, and $0.03r_0$ for all other pair interactions. These separations are small enough to give a good approximation to the true contact energy, but large enough to avoid numerical problems in our finite element simulations.

8.2.3 Monte Carlo Simulations

NVT Metropolis simulations were performed on 400 polygonal plates interacting via both hard-core and capillary interactions with periodic boundary conditions (see Section 8.2.3.1 and 8.2.3.2 respectively). We used a rectangular simulation box with aspect ratio of $2{:}\sqrt{3}$ starting with particles in a hexagonal lattice with an area fraction of $\eta = 0.3$. In a MC move, particles were either translated or rotated (with equal probability) with adjustable step lengths or rotation angles to achieve an acceptance probability of 30% for each type of move. To ensure efficient equilibration, for hexagons and truncated triangles, the particles were first disordered at a temperature of $T^* = 100$ for 10^3 attempted moves per particle, then brought to the final temperature $T^* = 0.05$ through a slow cool process by successively quenching to $T^* = 0.15, 0.12, 0.1, 0.09, 0.08, 0.07, 0.05$, with 5×10^5 attempted moves per particle at each temperature. For the mixture of squares and equilateral triangles, we used a much slower cooling protocol to minimize the number of defects. Specifically, the system was first disordered at a temperature of $T^* = 100$ for 10^3 attempted moves per particle then quenched to $T^* = 0.25$. The temperature was then reduced by a factor of 0.95 every 3×10^5

attempted moves per particle until we reached $T^* = 0.1$. Finally, the temperature was reduced by a factor of 0.95 every 10^5 attempted moves per particle until we reached a final temperature of $T^* = 0.05$. For each composition of the squares and triangles, 10 simulation runs were carried out to increase the effective sample size from which to identify quasicrystalline structures.

8.2.3.1 Hard-Core Interactions

Hard-core repulsions were included in our MC simulations geometrically by rejecting any MC move that led to an overlap of the hexagonal plates, where the occurrence of overlap was determined using the Gilbert-Johnson-Keerthi (GJK) algorithm.[153] The GJK algorithm is chosen simply for its ease of implementation and logical understanding. On a fundamental level, the GJK algorithm checks for collisions by firstly creating a new shape using the Minkowski difference. The Minkowski difference is the set of all points from one shape subtracted from the other. Computationally this shape is calculated by using opposite and counter rotating vectors at the centre of each shape and subtracting the vertices that are furthest in that direction. Doing so generates a new set of vertices which are the boundaries for the Minkowski difference. Since the Minkowski difference is the set of all points of one shape subtracted from the other, if this new shape contains the origin, at least one point on each shape must share the same co-ordinates, and therefore a collision has occurred. The rest of the GJK algorithm is then a way to efficiently determine whether the Minkowski difference contains the origin.

For equilateral triangles and squares, we do not allow the surface-to-surface distance for triangles or squares in side-to-side contact to be less than $\delta = 0.03L$, i.e., we effectively add a steric barrier of thickness $\delta/2$ around the triangles and squares when applying the GJK algorithm. This procedure ensures that the side-to-side contact distance coincides with the grid point with the smallest distance that we calculate in the look-up table for capillary interactions, allowing us to capture the side-to-side contact energies between the squares and triangles more accurately in the look-up table (see discussion in the Capillary Interaction subsection below).

8.2.3.2 Capillary Interactions

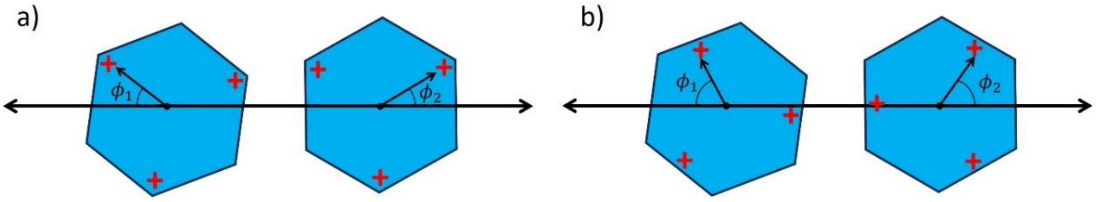

Figure 8.3: Definition of the azimuthal angles ϕ_1, ϕ_2 of two interacting capillary multipoles relative to the centre-to-centre line between the particles for the case of (a) H0 particles and (b) H30 particles.

The capillary pair interaction between particle 1 and particle 2 for different relative orientations of the two particles as a function of their centre-to-centre separation d is defined as

$$V_2(d, \phi_1, \phi_2) = E_2(d, \phi_1, \phi_2) - E_2(\infty) \tag{8.7}$$

where $E_2(d, \phi_1, \phi_2)$, $E_2(\infty)$ are the energies of the two-particle system at separation d with orientation ϕ_1, ϕ_2 and at infinite separation respectively calculated from equation (2.5). Following Danov *et al.*,[66] we define ϕ_1 as the angle between the vector going from the centre of particle 1 to a positive pole and the vector going from the centre of particle 2 to the centre of particle 1, and ϕ_2 to be the angle between the vector going from the centre of particle 2 to a positive pole and the vector going from the centre of particle 1 to the centre of particle 2, see Figure 8.3. From symmetry, the range of ϕ_1, ϕ_2 is $0°$ to $120°$ for H0, H30, H30+, TT and equilateral triangles and $0°$ to $90°$ for squares.

In our MC simulations, we modelled the capillary interaction between two polygonal plates using a look-up table. Specifically, we first used Surface Evolver to calculate the capillary interaction given by equation (8.7) for d, ϕ_1, ϕ_2 values on a grid. For ϕ_1, ϕ_2, the range is given above, and we used an interval of $5°$ for ϕ_1, ϕ_2. Since we are considering high order capillary multipoles whose interactions fall off rapidly with separation, we can use a relatively small cut-off distance of $d_c = 2d_0$ for capillary interactions in our simulations, where d_0 is the diameter of the circle circumscribing the polygonal plates. For example, for hexapolar interactions, the interaction energy at $d = d_c$ is less than 2% of the contact energy, indicating that the truncation error associated with our choice of the cut-off distance is negligible. For H0, H30, H30+, TT, the range of d goes from d_c down to the smallest value of d where the particles do not overlap for any given ϕ_1, ϕ_2, and we used an interval of $0.1d_0$ for d.

For equilateral triangles and squares, the range of d goes from a surface-to-surface distance of $0.03L$ (which we define as criteria for side-to-side contact between squares and triangles, see Section 8.2.3.1 above), to the cut-off distance $d_c = 2d_0$, where d_0 is the diameter of the circle circumscribing the square, and we calculated the capillary interaction for 10 evenly spaced values of d within this range. Although this discretization procedure means that the d intervals are different for square-square, triangle-triangle and square-triangle interactions, it allows us to capture the side-to-side contact energies between the squares and triangles (i.e., the ground state capillary bond energies) more accurately in the look-up table since these energies are now exact as they do not involve either interpolation or extrapolation. As will be discussed later in Section 8.3.4, it is vital that we capture the ground state contact energies between squares and triangles accurately in our MC simulations if we are to obtain quasicrystals, since quasicrystals only exist over a very narrow range of relative contact energies.

The above discretization procedure results in between around 4000 to 7000 grid points for each particle shape pair. We then used linear interpolation and (for d values very close to contact) linear extrapolation to calculate the capillary interactions for d, ϕ_1, ϕ_2 values off-grid.

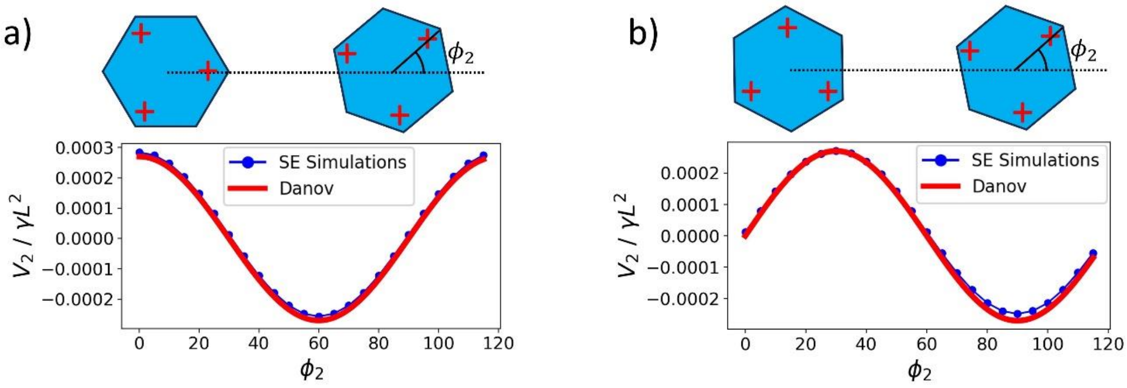

Figure 8.4: Comparison between equation (2.15) (red curves) and the look-up table (blue curves and points) for the capillary pair interaction between H0 particles for (a) $d = d_c$, $\phi_1 = 0°$ and variable ϕ_2 and (b) $d = d_c$, $\phi_1 = 30°$ and variable ϕ_2. The value of H_c in equation (2.15) is set to $H_c = 0.0237L$.

Note that analytical formulas for capillary interactions between capillary multipoles of arbitrary order we covered in Section 2.4 are only valid in the far-field regime. To illustrate the limitation of the analytical formulas, we compare the results of our look-up table for H0 with the analytical formula for two capillary hexapoles which is given by equation (2.15) where H_c is the amplitude of the interfacial deformation around each hexagon at the radial coordinate $r_c = R$, and we set $R = 1.1r_0$, where r_0 is the radius of the circle circumscribing the polygon. Specifically, using H as a fitting parameter, we first fitted equation (2.15) to the look-up table data for $d = d_c$, $\phi_1 = 0°$ and variable ϕ_2 in order to obtain the effective value of H_c for H0. The result of this fitting is shown in Figure 8.4a. Using the same value for H_c, we then compared equation (2.15) with our look-up table for the interaction potential as a function of

ϕ_2 for $d = d_c$, $\phi_1 = 30°$ (Figure 8.4b). We see that in this far-field regime, there is excellent agreement between equation (8.7) and the look-up table in Figure 8.4a and Figure 8.4b, providing independent confirmation that our look-up table has been calculated correctly.

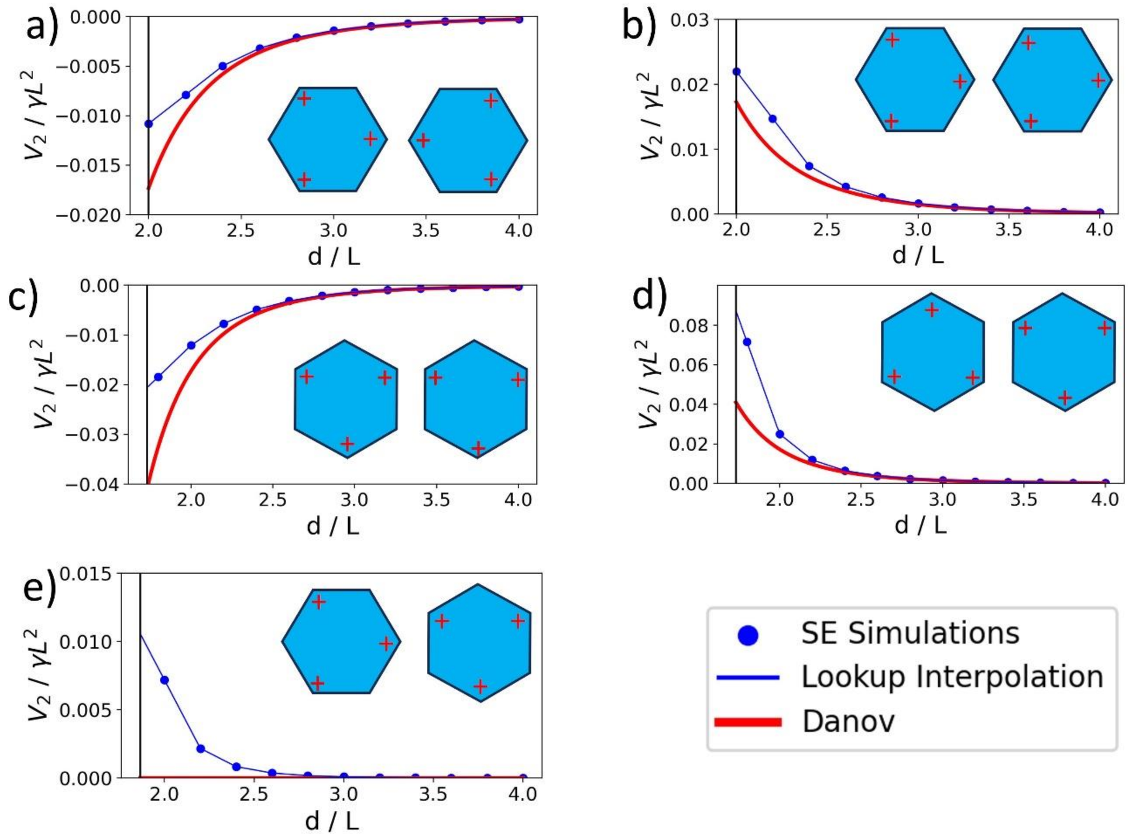

Figure 8.5: (a-e) Comparison between equation (2.15) (red curves) and the look-up table (blue curves and points) for the capillary pair interaction between H0 particles as a function particle separation d for different relative orientations of the interacting particles. The value of H_c in equation (2.15) is set to $H_c = 0.0237L$.

In Figure 8.5, we compare equation (2.15) with our look-up table for the interaction potential as a function of d for different relative orientations of the two particles that equation (2.15) predicts should lead to attraction (Figure 8.5a,c) repulsion (Figure 8.5b,d) or zero interactions (Figure 8.5e). We see that while there is excellent agreement between the two results in the far field regime $d \geq 3L$, quantitative and sometimes even qualitative discrepancies between the two appear in the near-field. This is not surprising since the analytical formula of Danov *et al*. is a far-field formula that is only valid for $d \gtrsim 1.5d_0$. Since capillary assembly is dominated by the near-field interactions, we therefore model capillary interactions in our MC simulations using a look-up table instead of the analytical formulas covered in Section 2.4.

8.2.4 Structural Analysis of Quasicrystals

To quantify if the binary mixture of squares and triangles do indeed for 12-fold quasicrystalline structures, we analyse the largest cluster by calculating the m-fold bond orientational order. To determine the largest cluster in the binary mixture of squares and triangles, we first connect all particles and their nearest neighbours into a tree data structure, where we define nearest neighbours as particles whose centre-to-centre separation is less than 1.2 times the minimum separation between the particles (i.e., when they are in side-to-side contact). We then use a depth first search (DFS) algorithm to group particles and their nearest neighbours into clusters and analyse the structure of the cluster containing the most particles. Specifically, we calculate the m-fold bond orientational order parameter of the largest cluster using

$$\chi_m = \left| \frac{1}{N} \sum_{j=1}^{N} \frac{1}{N_j} \sum_{k=1}^{N_j} e^{im\theta_{jk}} \right| \tag{8.8}$$

where θ_{jk} is the angle between the bond vector from the jth particle to its kth nearest neighbour and the positive x-axis, N_j is the number of nearest neighbors for the jth particle and N is number of particles in the cluster. We also calculate the structure factor of the cluster using

$$S(\boldsymbol{q}) = \frac{1}{N} \left| \sum_{j=1}^{N} e^{-i\boldsymbol{q}\cdot\boldsymbol{r}_j} \right|^2 \tag{8.9}$$

where $\boldsymbol{q} = (q_x, q_y) = \left(\frac{2n\pi}{L_x}, \frac{2m\pi}{L_y}\right)$ is the scattering wave vector in the x-y plane, $n, m = 0, \pm1, \pm2, \cdots$, L_x, L_y are the simulation box lengths in the x and y direction respectively, and $\boldsymbol{r}_j$ is the vector position of the jth particle.

8.3 Results and Discussion

8.3.1 Hexagons – Isolated Particles

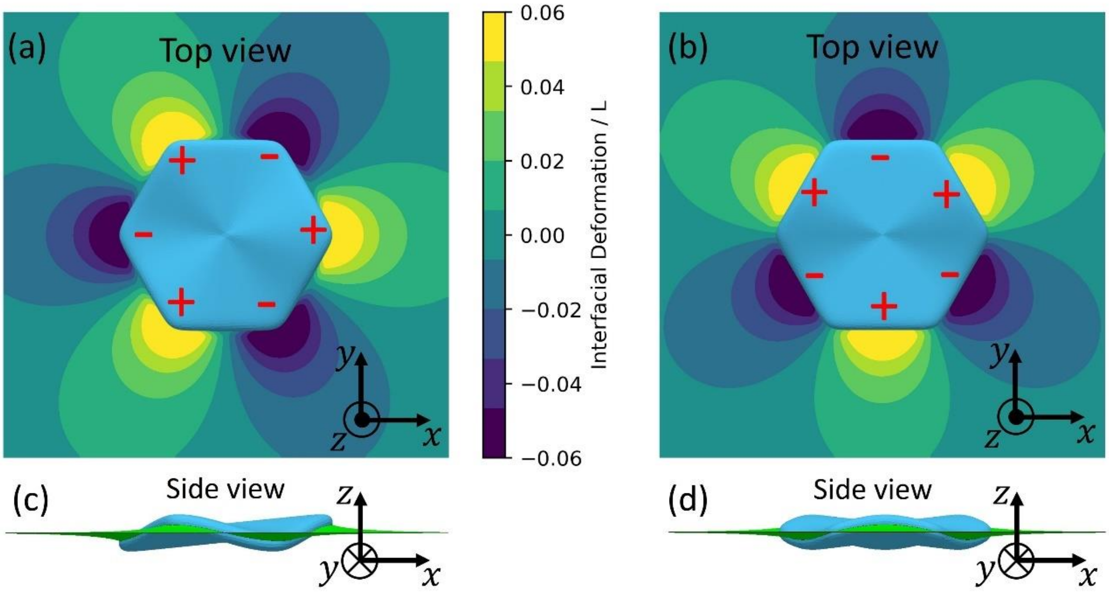

Figure 8.6: (a,b) Top view of particle geometry and contour plot of the liquid interface height (normalized to the hexagon side length L) around (a) H0 and (b) H30 hexagonal plates adsorbed at a liquid interface. The positive and negative signs denote the position of the positive and negative antinodes of the particle edge undulations respectively. (c,d) Side view of the system for (c) H0 and (d) H30 hexagonal plates.

The first particle shape we consider is that of a thin hexagonal plate with hexapolar edge undulations. The shape parameters we use in equations (8.2) and (8.3) for this shape are $\psi_1 = \pi/2$, $\psi_2 = 7\pi/6$, $\psi_3 = 11\pi/6$, $\Delta = 0$, $a/b = 10$, $m = 3$ and we work with length units where the side length of the hexagon $L = 1$ so that $a = \sqrt{3}/2$. We consider two types of hexagonal plates, H0 where the maximum displacement of the undulations coincides with the corners of the hexagon (i.e., $\theta_0 = 0$ in equation (8.3), see Figure 8.6a,c), and H30 where the maximum displacement coincides with the middle of the hexagonal side (i.e., $\theta_0 = \pi/6$ in equation (8.3), see Figure 8.6b,d). As we shall see later, the subtle change in the phase angle between edge undulations and the hexagonal shape for these two types of particles leads to dramatic changes in their self-assembly behaviour.

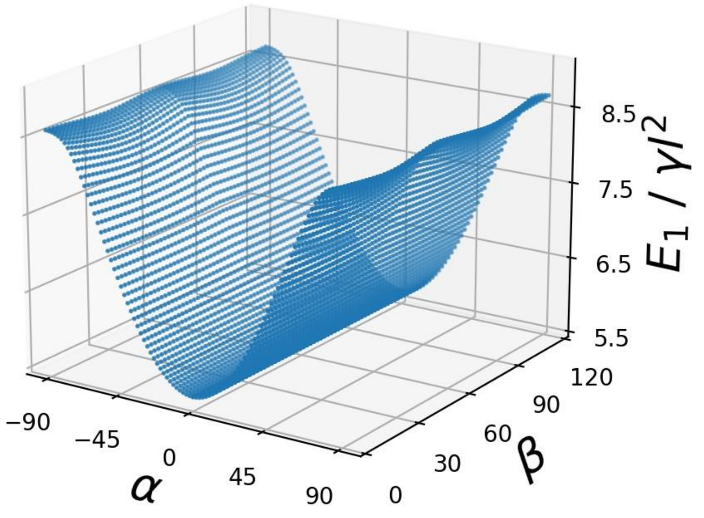

Figure 8.7: Interfacial energy for H0 particles as a function of the angles α and β, with the energy minimized with respect to the height of the particle z_p for each particle orientation. The interfacial energy is normalized with respect to $\gamma\ell^2$, where $\ell = \sqrt{3}L/2$ and L is the side length of the hexagon.

We first consider the properties of isolated adsorbed particles. In general, we require six variables to fully specify the position and orientation of a non-axisymmetric plate,[56,57] namely the centre of mass coordinates x_p, y_p, z_p of the plate in the lab frame, the azimuthal angle φ of the plate about the interface normal (i.e., z axis), the polar angle α between the plate normal and the interface normal and the rotation angle β of the plate about its normal (i.e., z' axis), see Figure 8.1. However, for an isolated adsorbed particle, the energy depends only on z_p, α and β. In Figure 8.7, we plot the energy of a H0 particle as a function of α and β, with the energy minimized with respect to z_p for each particle orientation. We see that the equilibrium orientation of the hexagonal plate is $\alpha = 0°$ (where β becomes irrelevant). This result is in good agreement with our previous results for adsorbed cylindrical particles, where in the limit of thin cylindrical plates, the plate normal is perpendicular to the interface.[53] The result is also in good agreement with the results of Whitesides and coworkers covered in Section 2.3 for patchy hexagonal plates,[151] where plates with centrosymmetric arrangements for their patchy edges have plate normals that are perpendicular to the liquid interface. Since all the polygonal particles we consider in this study are thin and have centrosymmetric edge undulations, in what follows we set $\alpha = \beta = 0°$ in our calculations

Next, we consider the degree to which the edge undulations of the particles control the deformation of the liquid meniscus around the particle. In Figure 8.6a,b we plot the top view of the particle and the height of the liquid meniscus around H0 and H30 respectively for edge undulations with amplitude parameter $A = 0.1L$ in equation (8.3); we use positive and negative signs to denote the positive and negative antinodes of the undulations in each case.

.

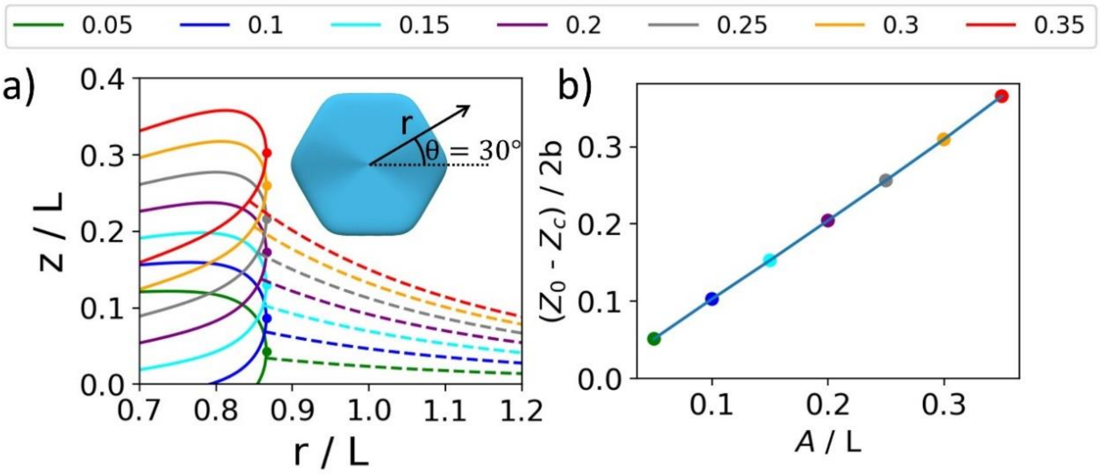

Figure 8.8: (a) The cross-section of an adsorbed H30 particle along the direction $\theta = 30°$ (see inset) for different values of A/L shown in the top legend. The solid and dashed lines represent the cross sections of the solid and liquid interfaces respectively, and the filled circles denote the plate edge with height z_0. (b) Deviation of the height of the contact line (z_c) from the height of the plate edge (z_0), normalized with respect to the plate thickness $2b$, as a function of A.

To study the pinning of the three-phase contact line to the polygonal plate edge in more detail, in Figure 8.8a we plot the cross-section of an adsorbed H30 particle along the direction where the polar angle $\theta = 30°$ (i.e., cutting through the middle of the hexagon side) as a function of A. We see that, the deviation of the contact line from the plate edge (which has height $z_0(r, \theta)$ given by equation (8.3)) is small for small A. Specifically, from Figure 8.8b, the deviation is $\lesssim 10\%$ of the plate thickness for $A \leq 0.1L$. In this Chapter, we therefore set $A = 0.1L$ for all our particles unless otherwise stated. Essentially, for $A = 0.1L$ we see that the liquid meniscus follows closely the deformation of the particle edge, and therefore the three-phase contact line is effectively pinned to the plate edge. In the rest of the Chapter, we therefore simplify our Surface Evolver calculations by eliminating the particle surface and set the z' coordinate of the contact line to satisfy equation (8.3), and the (x', y') coordinates of the contact line to satisfy equation (8.2) but without the term containing z' on the left-hand side.

8.3.2 Hexagons – Many Particles

Having established the equilibrium properties for isolated particles, we now study the pair interaction and self-assembly of many particles. Note that when calculating the energy of two- or many-particle systems, we fix z_p, α and β for each particle to their isolated-particle values since previous studies have shown that the height and polar orientation of adsorbed configuration of a system consisting of N polygonal plates is specified by the set of variables

$\{x_{pi}, y_{pi}, \varphi_i\}$ with $i = 1, \dots, N$, where x_{pi}, y_{pi} are the x, y centre of mass coordinates of the i-th plate and φ_i is the azimuthal angle of the i-th plate (see Figure 8.1).

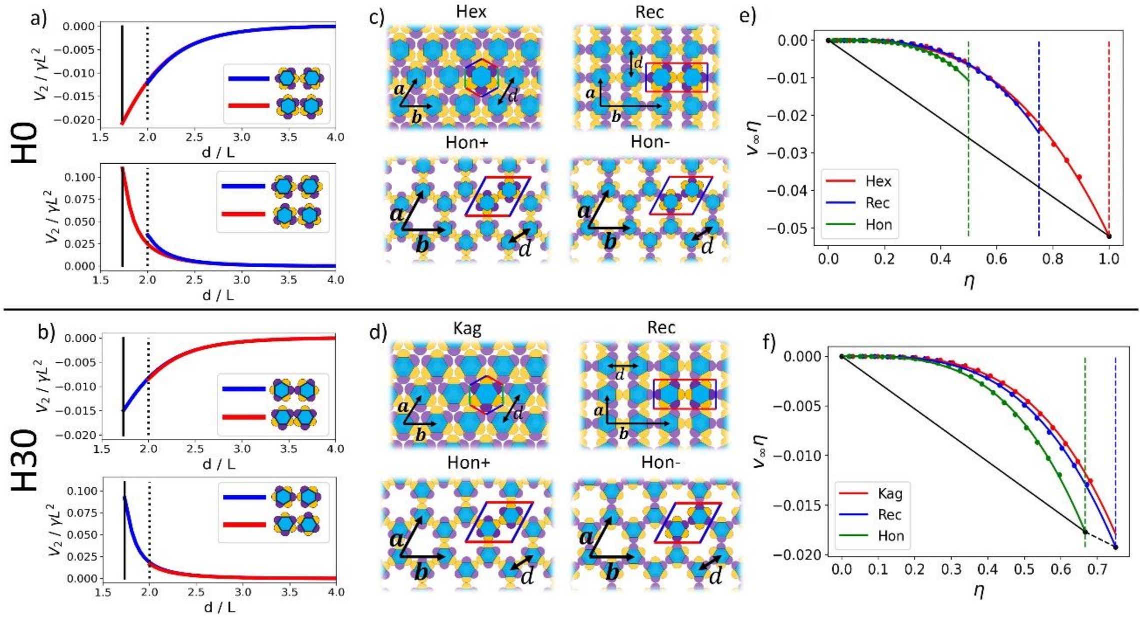

Figure 8.9: (a,b) Attractive (top) and repulsive (bottom) capillary pair interactions as a function of centre-to-centre separation for different relative orientations of interacting particles for (a) H0 and (b) H30 particles. The solid and dotted vertical lines denote the separation for side-to-side and corner-to-corner contact of the hexagons respectively. (c,d) The crystal structures we consider for (c) H0 and (d) H30. For each crystal structure, we show the lattice vectors $\boldsymbol{a}, \boldsymbol{b}$, the nearest neighbour separation d, and the unit cell used in the Surface Evolver calculations, where sides of the unit cell with the same colour have the same interface height. The yellow and purple spots in (a-d) denote positive and negative capillary poles respectively. (e,f) Plot of ηv_∞ vs. η for the different crystals structures shown in (c) and (d), where η is the area fraction and v_∞ is the many-body capillary interaction per particle given by equation (8.10). The data points are numerical results calculated from Surface Evolver and the solid lines are the fits to the numerical data using the form $B\eta^C$, where the fitting parameters B, C for each crystal phase are given in Table 8.1. The vertical dashed lines are the highest area fraction for each crystal phase and the black solid and dashed lines are the equilibrium lever rule lines.

Shape	**Crystal**	**B**	**C**
H0	Hex	-0.0522	2.97
	Rec	-0.0643	3.32
	Hon	-0.134	3.63
H30	Kag	-0.0499	3.56
	Rec	-0.0511	3.40
	Hon	-0.0683	3.33

Table 8.1: Fitting parameters for the lever rule line plots shown in Figure 8.9e,f. Hex = hexagonal lattice, Rec = rectangular lattice, Hon = honeycomb lattice, Kag = Kagome lattice.

In Figure 8.9a,b, we show the capillary interaction for H0 and H30 respectively for different relative azimuthal orientations of the interacting particles. Note that the yellow and purple spots in Figure 8.9 indicate positive and negative interfacial deformations (or capillary poles) respectively. We see that particles attract each other when capillary poles of the same sign overlap (Figure 8.9a,b top), and they repel each other when capillary poles of opposite sign overlap (Figure 8.9a,b bottom). Specifically, following the terminology used by Soligno et al.,[56,57] there are two types of particle orientations that are attractive: (i) dipole-dipole attraction, where one set of two capillary poles from one plate (one positive, one negative) overlap with the same set of two capillary poles from the other plate (red curves); (ii) tripole-tripole attraction, where one set of three capillary poles from one plate (positive-negative-positive or negative-positive-negative) overlap with the same set of three capillary poles from the other plate (blue curves). From Figure 8.9a,b, we see that for both H0 and H30, the interaction energy at the same particle separation is essentially the same for dipole-dipole and tripole-tripole attractions. For a given particle type, the minimum interaction energy is therefore given by the relative orientation that allows the two particles to come closest to each other, i.e., where the hexagons are in side-to-side contact. Since the orientation of the capillary hexapole relative to the hexagonal shape is different for H0 and H30, the lowest energy (i.e., strongest) capillary bond is the dipole-dipole bond for H0 (red curve in Figure 8.9a top) but the tripole-tripole bond for H30 (blue curve in Figure 8.9b top).

The apparently subtle difference between H0 and H30 in the nature of their ground state capillary bonds have profound consequences for their self-assembly as we shall now discuss. When H0 or H30 are bonded to six nearest-neighbours via dipole-dipole bonds, they form a hexagonal lattice (Hex), specifically a hexagonal close-packed lattice for H0 (i.e., hexagons in edge to edge contact Figure 8.9c top left) and a Kagome lattice (Kag) for H30 (i.e., hexagons in vertex to vertex contact Figure 8.9d top left). On the other hand, when these particles are bonded to two opposite nearest-neighbours via dipole-dipole bonds and two other nearest-neighbours via tripole-tripole bonds, they form a rectangular lattice (Rec, Figure 8.9c,d top right). Finally, when these particles are bonded to three nearest-neighbours via tripole-tripole bonds, they form a honeycomb lattice (Hon, Figure 8.9c,d bottom). Note that there are two versions of the honeycomb phase, namely where the primary overlapping capillary pole is positive (Hon+, Figure 8.9c,d bottom left) or negative (Hon-, Figure 8.9c,d bottom right). For the neutrally wetting particles we are considering in this Chapter ($\theta_w = 90°$), Hon+ and Hon- are degenerate in energy. Note also the honeycomb phase is not an incomplete hexagonal phase because the holes in the honeycomb lattice are surrounded by capillary poles of the same sign (either negative for Hon+ or positive for Hon-), so that it is energetically unfavourable to insert hexapolar particles to fill these holes.[56,57]

Since the ground state capillary bond is the dipole-dipole bond for H0 and the tripole-tripole bond for H30, we anticipate that in the low temperature regime that we are considering in this Chapter, the equilibrium phase is the hexagonal close-packed structure for H0 but the honeycomb structure for H30. In order to check this prediction, we calculate the equilibrium state of the two particle shapes by plotting ηv_{∞} vs. η for the different phases discussed above for H0 (Figure 8.9e) and H30 (Figure 8.9f), where η is the area fraction of the hexagonal plates and v_{∞} is the many-body capillary interaction per particle for a given phase which is defined by

$$v_{\infty}(d) = \varepsilon_{\infty}(d) - \varepsilon_{\infty}(\infty) \tag{8.10}$$

Here d is the separation between nearest neighbours (shown in Figure 8.9c,d for the different phases) and $\varepsilon_{\infty}(d)$, $\varepsilon_{\infty}(\infty)$ is the energy per particle in a given phase at separation d and at infinite separation respectively. These energies are obtained by using Surface Evolver to calculate the energy of a unit cell (shown in Figure 8.9c,d for the different phases) and applying periodic boundary conditions to the sides of the unit cell as indicated in Figure 8.9c,d.

For H0 we consider 3 different periodic lattice geometries. The hexagonal close-packed lattice (Hex), the unit cell is a hexagon with vertex coordinates $(0, d/\sqrt{3})$, $(d/2\,, d/2\sqrt{3})$, $(d/2\,, -d/2\sqrt{3})$, $(0, -d/\sqrt{3})$, $(-d/2\,, -d/2\sqrt{3})$ and $(-d/2\,, d/2\sqrt{3})$; the unit cell contains one particle with configuration $(0,0,\pi/6)$. The rectangular lattice (Rec), the unit cell is a rectangle with vertex coordinates $(0,0)$, $(0, 4d/\sqrt{3})$, $(d, 4d/\sqrt{3})$ and $(d, 0)$; the unit cell contains two particles with configurations $(d/2\,, d/\sqrt{3}\,, \pi/6)$ and $(d/2\,, 3d/\sqrt{3}\,, 7\pi/6)$. The honeycomb lattice (Hon), the unit cell is a rhombus with vertex coordinates $(0,0)$, $(\sqrt{3}d/2\,, 3d/2)$, $(3\sqrt{3}d/2\,, 3d/2)$ and $(\sqrt{3}d, 0)$; the unit cell contains two particles with configurations $(\sqrt{3}d/2\,, d/2\,, \pi/6)$ and $(\sqrt{3}d, d, 7\pi/6)$.

For H30 we also consider 3 different periodic lattice geometries. The Kagome lattice (Kag), the unit cell is a hexagon with vertex coordinates $(0, d/\sqrt{3})$, $(d/2\,, d/2\sqrt{3})$, $(d/2\,, -d/2\sqrt{3})$, $(0, -d/\sqrt{3})$, $(-d/2\,, -d/2\sqrt{3})$ and $(-d/2\,, d/2\sqrt{3})$; the unit cell contains one particle with configuration $(0,0,0)$. The rectangular lattice (Rec), the unit cell is a rectangle with vertex coordinates $(0,0)$, $(0,2d)$, $(2d/\sqrt{3}\,, 2d)$, $(2d/\sqrt{3}\,, 0)$; the unit cell contains two particles with configurations $(d/\sqrt{3}\,, d/2\,, 0)$ and $(d/\sqrt{3}\,, 3d/2\,, \pi)$. The honeycomb lattice (Hon), the unit cell is a rhombus with vertex coordinates

$(0,0)$, $(\sqrt{3}d/2\,, 3d/2)$, $(3\sqrt{3}d/2\,, 3d/2)$, $(\sqrt{3}d, 0)$; the unit cell contains two particles with configurations $(\sqrt{3}d/2\,, d/2\,, 0)$ and $(\sqrt{3}d, d, \pi)$.

Shape	**Crys.**	$\boldsymbol{a}$	$\boldsymbol{b}$	$\boldsymbol{\eta}$	$\boldsymbol{d_c}$	$\boldsymbol{\eta_c}$
H0	Hex	$d(1,0)$	$d\left(\frac{1}{2},\frac{\sqrt{3}}{2}\right)$	$\frac{3L^2}{d^2}$	$\sqrt{3}L$	1
	Rec	$d(1,0)$	$\frac{4}{\sqrt{3}}d(0,1)$	$\frac{9L^2}{4d^2}$	$\sqrt{3}L$	$\frac{3}{4}$
	Hon	$\sqrt{3}d(1,0)$	$\sqrt{3}d\left(\frac{1}{2},\frac{\sqrt{3}}{2}\right)$	$\frac{2L^2}{d^2}$	$2L$	$\frac{1}{2}$
H30	Kag	$d(1,0)$	$d\left(\frac{1}{2},\frac{\sqrt{3}}{2}\right)$	$\frac{3L^2}{d^2}$	$2L$	$\frac{3}{4}$
	Rec	$\frac{2}{\sqrt{3}}d(1,0)$	$2d(0,1)$	$\frac{9L^2}{4d^2}$	$\sqrt{3}L$	$\frac{3}{4}$
	Hon	$\sqrt{3}d(1,0)$	$\sqrt{3}d\left(\frac{1}{2},\frac{\sqrt{3}}{2}\right)$	$\frac{2L^2}{d^2}$	$\sqrt{3}L$	$\frac{2}{3}$

Table 8.2: The lattice vectors $\boldsymbol{a}, \boldsymbol{b}$ and the area fraction η as a function of the nearest neighbor separation d, the nearest neighbor separation at contact d_c and the area fraction at contact η_c for the crystals structures shown in Figure 8.9c, Figure 8.9d for H0, H30 respectively. For H0, H30, L is the side length of the hexagon. Hex = hexagonal lattice, Rec = rectangular lattice, Hon = honeycomb lattice, Kag = Kagome lattice.

Note that the Hex and Kag phases contain one particle per unit cell, while the Rec and Hon phases contain two particles per unit cell, with one of the particles rotated azimuthally by $180°$ relative to the other. Note also that since Hon+ and Hon- are degenerate, we only plot a single curve for the honeycomb phase in Figure 8.9e,f. In addition, the maximum area fraction for each phase η_c (i.e., when nearest neighbours are in contact $d = d_c$) is represented by vertical dashed lines in Figure 8.9e,f. The exact values of the lattice vectors, area fraction η, contact separation d_c and maximum area fraction η_c are given in Table 8.2 for all crystal structures considered.

In fact, since the total number of particles in the system are conserved, when the system crystalises we effectively have two phase co-existence between a close packed crystal and vacuum. The total energy per unit area of such a two-phase system is therefore a weighted average of the energy per unit area of the vacuum phase and the crystal phase, where the contribution of each phase to the average is weighted by the fraction of the total area occupied by each phase. A simple graphical method for calculating this weighted average is called the lever rule.[154] Specifically, since Figure 8.9e,f are essentially plots of energy per unit area versus density, the lever rule says that the energy per unit area for a specific crystal structure at a given area fraction can be calculated by joining the point corresponding to the empty phase $\eta = 0$ and the highest density state of that crystal $\eta = \eta_c$ with a straight line; and evaluating the straight line at the original area fraction.[56,57] The equilibrium state of the system for any given value of η is then given by the lowest lever rule line at that value of η, and these lines are denoted by black solid or dashed lines in Figure 8.9e,f. From the lever rule analysis of Figure 8.9e, we see that (for small enough η) the equilibrium state for H0 is where the empty phase coexists with the hexagonal close-packed structure, while from Figure 8.9f, the equilibrium state for H30 is where the empty phase coexists with the honeycomb structure. These results confirm our earlier prediction that the ground state crystal structure for H0 and H30 are the hexagonal close-packed structure and the honeycomb structure respectively. Thus, by a subtle change in the orientation of the capillary hexapole relative to the hexagonal shape, we have changed the equilibrium crystal structure of the hexagonal plates dramatically.

Shapes	$\boldsymbol{U_0/\gamma L^2}$
H0-H0	0.0248
H30-H30	0.0179
H30+-H30+	0.0195
TT-TT ($L/S = 2$)	0.0078
Square-Square	0.0402

Table 8.3: Ground state capillary bond energies between different particle shape pairs.

To check whether the ground state crystal structures for H0 and H30 are accessible kinetically, we performed finite temperature Monte Carlo (MC) simulations for these particle shapes, including both hard-core and capillary interactions between the particles in our simulations. The MC simulations were performed at an area fraction of $\eta = 0.3$. This area fraction was chosen since it is low enough for the system to be in the dilute regime (i.e., polygons on a hexagonal lattice can freely rotate about their centres without interfering with each other) but high enough for extended structures to be formed in reasonable simulation time. In Supplementary Information, we show that for particles on the micron-scale or larger, the system is in the low temperature regime $T^* = k_B T/U_0 \ll 1$, where $k_B T$ is the thermal energy and U_0 is the energy of the ground state capillary bond; values for U_0 for the different particle shape pairs are given in Table 8.3. We see that the smallest value of $U_0/\gamma L^2$ above is 0.0078 for the case of TT-TT interactions. For micron-scale particles at an air-water interface (i.e., $L \approx 10^{-6}$ m, $\gamma = 70 \times 10^{-3}\ \mathrm{N \cdot m^{-1}}$), this translates to $U_0 \approx 10^5\ k_B T$, confirming that particles on the micron-scale or larger are in the low temperature regime $T^* = k_B T/U_0 \ll 1$.

For larger than micron-scale particles whose random motion is induced by external mechanical vibrations rather than thermal energy, motivated by the equipartition theorem, we can define an effective temperature for the system T_{eff} from the relation $k_B T_{\mathrm{eff}} \approx \gamma \langle u^2 \rangle$, where γ is the interfacial tension and $\langle u^2 \rangle$ is the mean-squared vertical displacement of the fluid-fluid interface relative to its equilibrium height.[155] The low temperature regime in this case therefore corresponds to the condition $T^* = \gamma \langle u^2 \rangle / U_0 \ll 1$. To ensure efficient equilibration of the system in our MC simulation, the system is slowly cooled from a high initial temperature to a final normalised temperature of $T^* = 0.05$ (see Section 8.2.3). The choice of the final temperature represents a good compromise between being low enough for the system to be in the low temperature regime while still being high enough for the MC simulation to equilibrate the system efficiently.

In our simulations, we assume that the capillary interactions are pair-wise additive and quasistatic. We therefore model capillary interactions by calculating V_2 given by equation (8.7) for d, ϕ_1, ϕ_2 values on a grid and use this data to generate a look-up table. Note that the quasistatic approximation is accurate for $T^* \ll 1$, as evidenced by the fact that it is possible to accurately model the trajectory of micron-sized particles moving under the action of capillary forces by using this approximation.[17,50] Note also that V_2 represents the capillary interaction at zero temperature. At finite temperature, thermal fluctuations of the liquid interface induce additional interactions due to the Casimir effect.[156–158] However, since such thermal Casimir interactions are proportional to $k_B T$,[156,157] we can safely neglect them in the low temperature regime $k_B T \ll U_0$ that are we considering here.

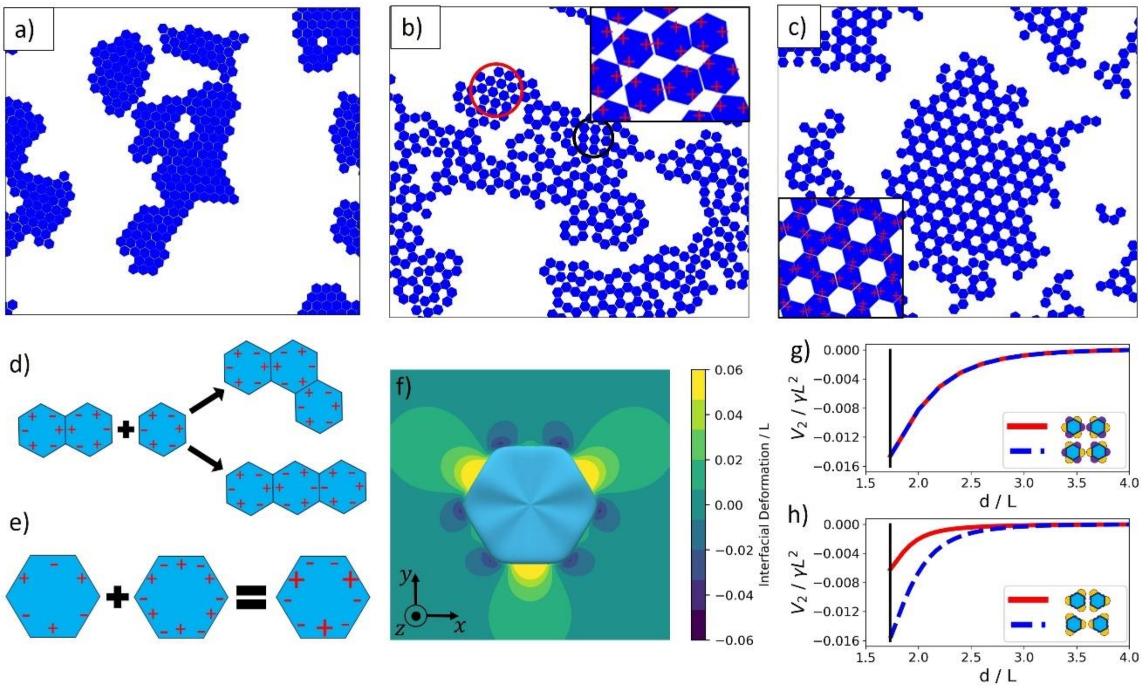

Figure 8.10: (a-c) Final snapshots for Monte Carlo simulations of (a) H0, (b) H30 and (c) H30+ particles. In (b), we highlight small domains of Kagome (red) and Rectangular (black) structures and in the inset we show the linear structures that poison the formation of extended honeycombs. In the inset of (c), we

confirm that the honeycomb structures are Hon+. (d) Two options for adding a third H30 particle to an existing dimer of H30 particles. (e) Superposition of hexapole and dodecapole edge undulations to create H30+. (f) Top view of the particle geometry and contour plot of the liquid interface height (normalized to the hexagon side length L) around H30+. (g,h) The negative and positive tripole-tripole interaction potentials as a function of particle separation for (g) H30 and (h) H30+. The solid vertical lines denote the separation for side-to-side contact of the hexagons. The yellow and purple spots in (g,h) denote positive and negative capillary poles respectively.

In Figure 8.10a and Figure 8.10b, we show the final snapshots from our MC simulations for H0 and H30 respectively. We see that H0 forms hexagonal close packed structures, in good agreement with the thermodynamic analysis in Figure 8.9e. However, rather surprisingly, H30 forms a mixture of different structures, with only small domains of honeycomb order, even though the latter is predicted by Figure 8.9f to be the ground state structure. One reason for this surprising result is the fact that from Figure 8.9f, H30 has several competing metastable structures which are very close in energy to the honeycomb structure, i.e., the lever rule lines for the rectangular (Rec) and Kagome (Kag) structures in Figure 8.9f are very close to the ground state lever rule line. Indeed, as highlighted in Figure 8.10b, we do see small domains of Rec and Kag structures in the final snapshot.

However, the absence of extended honeycomb structures in Figure 8.10b also arises from a deeper kinetic problem where the formation of the two degenerate honeycomb phases Hon+ and Hon- are antagonistic to each other. This point is illustrated in Figure 8.10d (Figure 8.10c will be discussed later in this section). Consider a dimer consisting of two H30 particles which are attached to each other via a positive tripole-tripole bond. When a third H30 particle is introduced, this particle can either attach itself to the dimer via a tripole-tripole bond of the same sign to form a bent trimer which is compatible with the subsequent formation of a honeycomb structure (in this case Hon+), or it can attach itself to the dimer via a tripole-tripole bond of the opposite sign to form a linear trimer which blocks the further formation of the honeycomb structure. However, since positive and negative tripole-tripole bonds are degenerate in energy, both pathways are equally likely. This means that as successive H30 particles are added to a growing cluster, the probability that all particles in the cluster are bonded to each other via tripole-tripole bonds of the same sign becomes vanishingly small. Thus, although Hon+ and Hon- are the thermodynamic ground states for H30, neither structure is accessible kinetically. The prevalence of the linear structures discussed above in Figure 8.10b (see for example the inset), confirms that the self-assembly process is indeed 'poisoned' by the bottom pathway in Figure 8.10d, preventing H30 from forming extended honeycomb structures.

To overcome this problem, we can make one set of alternate sides in H30 more 'sticky' than the other by adding a $m = 6$ multipole (dodecapole) to the contact line undulations of the hexapolar particle. This is illustrated in Figure 8.10e, where the dodecapole is oriented such that, it reinforces the positive poles and suppresses the negative poles of the hexapole. Specifically, we modify the edge undulation given by including both $m = 3$ and $m = 6$ multipoles in equation (8.3), with $A_3, A_6 = 0.05L$ and $\theta_{03}, \theta_{06} = \pi/6$, where A_m, θ_{0m} are the amplitude and phase angle of the mth multipole, and we call this particle shape H30+. In Figure 8.10f, we plot the height of the liquid meniscus around an isolated H30+ particle and we see that the addition of the $m = 6$ multipole amplifies the magnitude and range of the positive deformations of the liquid interface and suppresses the same for the negative deformations. In Figure 8.10g and 3h, we plot the positive and negative tripole-tripole interaction potential as a function of particle separation for H30 and H30+ respectively. We see that adding the $m = 6$ multipole indeed makes the positive tripole-tripole bonds much stronger than the negative tripole-tripole bonds for H30+. These results suggest that adding the $m = 6$ multipole breaks the degeneracy between Hon+ and Hon-, causing Hon+ to be the thermodynamic ground state for H30+.

The fact that the Hon+ structure is the kinetically accessible ground state structure for H30+ is confirmed in Figure 8.10c where we show the final snapshots from MC simulations for H30+. We see that, in contrast to H30, the H30+ particles are able to self-assemble into extended honeycomb structures, and the inset confirms that the honeycomb structures are Hon+ rather than Hon-. The good agreement in the ground state crystal structure between the Surface Evolver calculations in Figure 8.9 (which include all many-body interactions through the periodic boundary conditions) and the Monte Carlo simulations in Figure 8.10 (which include two-body interactions only) suggests that many-body interactions are negligible in this system. This fact is not surprising since the capillary interactions between high order multipoles are very short-ranged, and we therefore expect two-body interactions to be dominant over many-body interactions in this case.

8.3.3 Truncated Triangles

In the previous section, we saw that the Kagome lattice in Figure 8.9d (top left) is a metastable crystal structure for H30. However, we can also form a Kagome lattice using equilateral triangular plates instead of hexagonal plates by interchanging the role of particle and free space in the figure. Since the polygonal plates in all the lattice structures considered in this Chapter are bonded to each other by soft, flexible capillary bonds, the resultant open Kagome lattice is isostatic, i.e., it has marginal mechanical stability, and there has been growing interest in such lattices in recent years because of the unique mechanical properties they possess.[159,160]

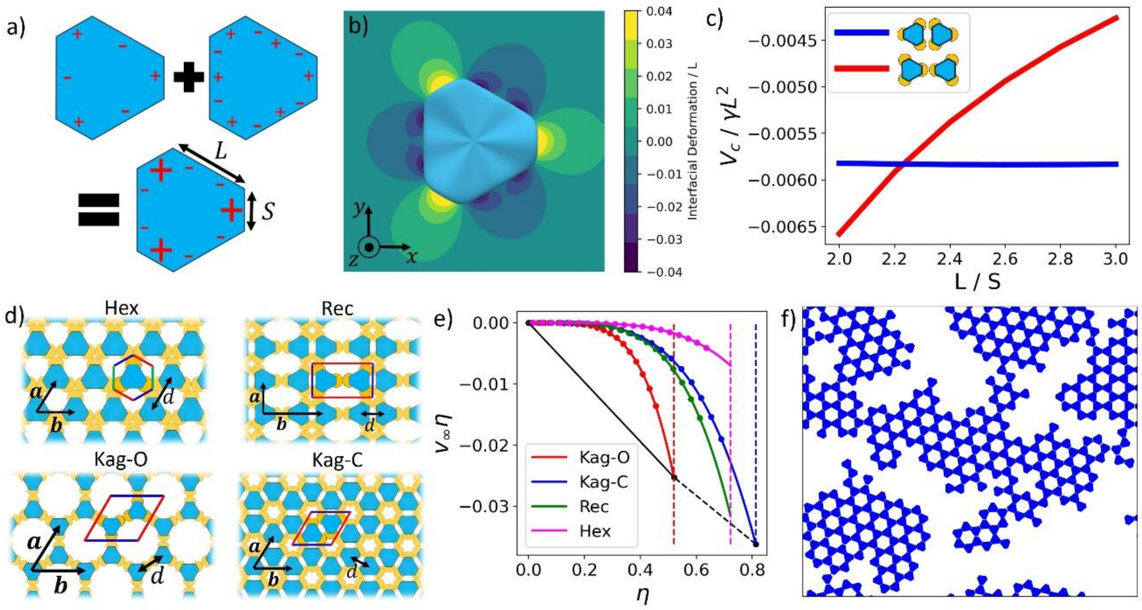

Figure 8.11: (a) Superposition of hexapole and dodecapole edge undulations in the truncated triangle (TT) particles. (b) Top view of the particle geometry and contour plot of the liquid interface height (normalized to the long side length L) around the TT particles. (c) Capillary bond energy at contact V_c as a function of L/S for short side-short side and long side-long side contact of the TT particles. (d) The crystal structures we consider for the TT particles. For each crystal structure, we show the lattice vectors $\boldsymbol{a}$, $\boldsymbol{b}$, the nearest neighbour separation d, and the unit cell used in the Surface Evolver calculations, where sides of the unit cell with the same colour have the same interface height. The yellow spots in (c,d) denote positive capillary poles. (e) Plot of ηv_∞ vs. η for the different crystals structures shown in (d), where η is the area fraction and v_∞ is the many-body capillary interaction per particle given by equation (8.10). The data points are numerical results calculated from Surface Evolver and the solid lines are the fits to the numerical data using the form $B\eta^C$, where the fitting parameters B, C for each crystal phase are given in Table 8.4. The vertical dashed lines are the highest area fraction for each crystal phase and the black solid and dashed lines are the equilibrium lever rule lines. (f) Final snapshots for Monte Carlo simulations of the TT particles.

Shape	**Crystal**	**B**	**C**
TT ($L/S = 2$)	Kag-O	-0.512	4.60
	Kag-C	-0.0816	3.91
	Rec	-0.126	4.26
	Hex	-0.0277	4.22

Table 8.4: Fitting parameters for the lever rule line plots shown in Figure 8.11e. Hex = hexagonal lattice, Rec = rectangular lattice, Kag-O = open Kagome lattice, Kag-C = compact Kagome lattice.

To create the open Kagome lattice, in principle we could use equilateral triangular plates with appropriate edge undulations to promote capillary bonding between the corners of the triangles. However, the relatively large separation between triangular plates when they are in corner-to-corner contact reduces the capillary bond strength significantly, making it challenging to stabilize the open lattice structure against collapse into compact lattice structures where the plates are in side-to-side contact. To address this problem, we reduce the particle separation for corner-to-corner contact by considering triangles with slightly truncated corners (see Figure 8.11a). Denoting the long and short side lengths of the truncated triangle as L and S respectively, the shape parameters in equation (8.2) for this particle shape are $\psi_1 = \pi/2\,, \psi_2 = 7\pi/6\,, \psi_3 = 11\pi/6\,, \Delta = (L - S)/(4\sqrt{3})\,, a = \sqrt{3}(L + S)/4$ and we work with length units where $L = 1$. In order to encourage the truncated triangles to associate with each other along their short sides rather than their long sides, we use the same strategy that was used to create honeycombs in the previous section, namely we include both hexapoles ($m = 3$) and dodecapoles ($m = 6$) in the edge undulations, orienting the hexapole so that it's poles coincide with the middle of the short or long sides, and orienting the dodecapole so that it reinforces the poles on short sides and suppresses the poles on the long sides, see Figure 8.11a. Specifically, we include both $m = 3$ and $m = 6$ multipoles in equation (8.3), with $A_3, A_6 = 0.05L$ and $\theta_{03}, \theta_{06} = \pi/2$, where A_m, θ_{0m} are the amplitude and phase angle of the mth multipole.

Shape	**Crys.**	$\boldsymbol{a}$	$\boldsymbol{b}$	$\boldsymbol{\eta}$	$\boldsymbol{d_c}$	$\boldsymbol{\eta_c}$
TT	Kag-O	$\sqrt{3}d(1,0)$	$\sqrt{3}d\left(\frac{1}{2},\frac{\sqrt{3}}{2}\right)$	$\frac{L^2 + 4LS + S^2}{3d^2}$	$\frac{2L + S}{\sqrt{3}}$	$\frac{L^2 + 4LS + S^2}{(2L + S)^2}$
	Kag-C	$\sqrt{3}d(1,0)$	$\sqrt{3}d\left(\frac{1}{2},\frac{\sqrt{3}}{2}\right)$	$\frac{L^2 + 4LS + S^2}{3d^2}$	$\frac{L + 2S}{\sqrt{3}}$	$\frac{L^2 + 4LS + S^2}{(L + 2S)^2}$
	Rec	$\frac{\sqrt{3}(L + S)d}{L + 2S}(1,0)$	$\frac{3(L + S)d}{L + 2S}(0,1)$	$\frac{(L^2 + 4LS + S^2)}{6d^2\frac{(L + S)^2}{(L + 2S)^2}}$	$\frac{L + 2S}{\sqrt{3}}$	$\frac{L^2 + 4LS + S^2}{2(L + S)^2}$
	Hex	$d(1,0)$	$d\left(\frac{1}{2},\frac{\sqrt{3}}{2}\right)$	$\frac{L^2 + 4LS + S^2}{2d^2}$	$L + S$	$\frac{L^2 + 4LS + S^2}{2(L + S)^2}$

Table 8.5: The lattice vectors $\boldsymbol{a}, \boldsymbol{b}$ and the area fraction η as a function of the nearest neighbor separation d, the nearest neighbor separation at contact d_c and the area fraction at contact η_c for the crystals structures shown in Figure 8.11d for truncated triangles (TT). L, S are the long and short side lengths respectively of the truncated triangle. Hex = hexagonal lattice, Rec = rectangular lattice, Kag-O = open Kagome lattice, Kag-C = compact Kagome lattice.

In Figure 8.11b, we plot the height of the liquid meniscus around an isolated truncated triangle (TT) with $L/S = 2$ and we see that the addition of the $m = 6$ multipole indeed amplifies the magnitude and range of interfacial deformations near the short sides and suppresses interfacial deformations near the long sides. In Figure 8.11c, we plot the capillary bond energy at contact V_c as a function of L/S for short side-short side (SS) contact (V_C^{SS}, red curve) and long side-long side (LL) contact (V_C^{LL}, blue curve). These results show that we can change the ground state capillary bond of the system by tuning the ratio L/S. Specifically, the ground state capillary bond is SS for L/S values below the crossover point $L/S = 2.23$, and it is LL for L/S values above the crossover point.

Figure 8.11c suggests that the ground state crystal structure for TT particles with $L/S < 2.23$ is the open Kagome lattice (Kag-O, Figure 8.11d, bottom left) while for $L/S > 2.23$, it is the compact Kagome lattice (Kag-C, Figure 8.11d, bottom right). In order to check this prediction, in Figure 8.11e, we perform a lever rule analysis for TT particles with $L/S = 2$ by plotting ηv_∞ against η for all the crystal structures shown in Figure 8.11d. We consider 4 different crystal structures for the truncated triangle TT shown in Figure 8.11d. For the open Kagome lattice (Kag-O), the unit cell is a rhombus with vertex coordinates $(0,0)$, $\left(\sqrt{3}d/2\,, 3d/2\right)$, $\left(3\sqrt{3}d/2\,, 3d/2\right)$, $\left(\sqrt{3}d, 0\right)$; the unit cell contains two particles with configurations $\left(\sqrt{3}d/2\,, d/2\,, \pi\right)$ and $\left(\sqrt{3}d, d, 0\right)$. For the compact Kagome lattice (Kag-C), the unit cell is a rhombus with vertex coordinates $(0,0)$, $\left(\sqrt{3}d/2\,, 3d/2\right)$, $\left(3\sqrt{3}d/2\,, 3d/2\right)$, $\left(\sqrt{3}d, 0\right)$; the unit cell contains two particles with configurations $\left(\sqrt{3}d/2\,, d/2\,, 0\right)$ and $\left(\sqrt{3}d, d, \pi\right)$. For the rectangular lattice (Rec), the unit cell is a rectangle with vertex coordinates $(0,0)$, $\left(0, \frac{3(L+S)d}{L+2S}\right)$, $\left(\frac{\sqrt{3}(L+S)d}{L+2S}, \frac{3(L+S)d}{L+2S}\right)$ and $\left(\frac{\sqrt{3}(L+S)d}{L+2S}, 0\right)$; the unit cell contains two particles with configurations $\left(\frac{\sqrt{3}(L+S)d}{2(L+2S)}, \frac{d}{2}, 0\right)$ and $\left(\frac{\sqrt{3}(L+S)d}{2(L+2S)}, \frac{(5L+4S)d}{2(L+2S)}, \pi\right)$. For the hexagonal lattice (Hex), the unit cell is a hexagon with vertex coordinates $\left(0, d/\sqrt{3}\right)$, $\left(d/2\,, d/2\sqrt{3}\right)$, $\left(d/2\,, -d/2\sqrt{3}\right)$,$\left(0, -d/\sqrt{3}\right)$, $\left(-d/2\,, -d/2\sqrt{3}\right)$ and $\left(-d/2\,, d/2\sqrt{3}\right)$; the unit cell contains one particle with configuration $(0,0,0)$.

Note that in Figure 8.11d, we show the nearest neighbour separation d and the unit cell for each crystal structure, while in Figure 8.11e, the vertical dashed lines represent the maximum area fraction η_c for each crystal phase and the black solid and dashed lines are the equilibrium lever rule lines of the system. The exact values of the lattice vectors, area fraction η, contact separation d_c and maximum area fraction η_c are given in Table 8.5 for all crystal structures considered. The results in Figure 8.11e confirm that Kag-O is indeed the ground state crystal structure for $L/S = 2$. In Figure 8.11f, we show the final snapshot from MC simulations of TT particles with $L/S = 2$ with area fraction $\eta = 0.3$, where the system is slowly cooled from a high initial temperature to a final temperature of $T^* = 0.05$. We see that the TT particles indeed self-assemble into open Kagome lattice structures, confirming that this structure is kinetically accessible to the system.

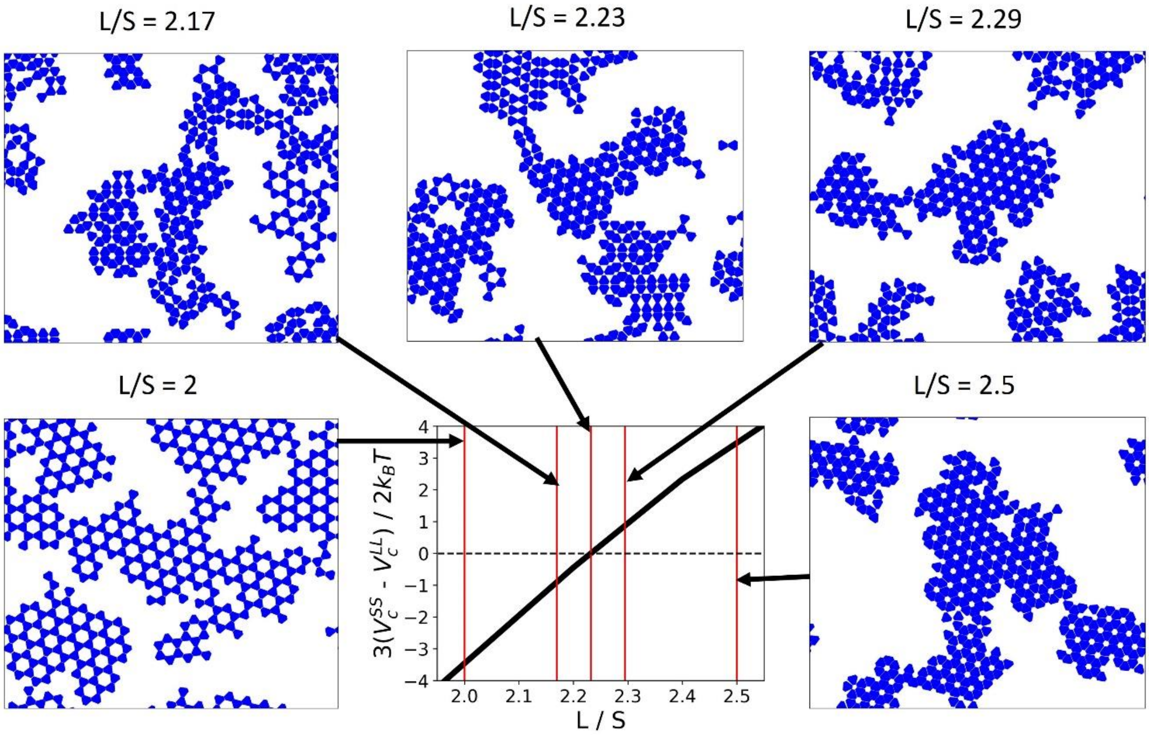

Figure 8.12: Difference in the capillary bond energy per particle between Kag-O and Kag-C, i.e., $\Delta v_c = 3(V_C^{SS} - V_C^{LL})/2$, as a function of L/S for the TT particles (bottom middle panel) and final snapshots for Monte Carlo simulations for different L/S values (surrounding panels).

To study how the self-assembly of TT particles depends on the value of L/S in more detail, in Figure 8.12, we show the final snapshot from MC simulations of TT particles with area fraction $\eta = 0.3$ and a range of different L/S values around the crossover point, where the system is slowly cooled from a high initial temperature to a final temperature of $T^* = 0.05$. We also plot the difference in the capillary bond energy per particle between Kag-O and Kag-C, i.e., $\Delta v_C = 3\left(V_C^{SS} - V_C^{LL}\right)/2$, as a function of L/S, where the factor $3/2$ comes from the fact that there are $3/2$ capillary bonds per particle in the Kagome structures. As expected, the system forms Kag-O for $L/S = 2$ where $\Delta v_C \approx -3k_BT$, while it forms Kag-C for $L/S = 2.5$ where $\Delta v_C \approx +3k_BT$. Interestingly, for L/S values very close to the crossover point, i.e., where $|\Delta v_C| \lesssim k_BT$, the system forms a mixture of Kag-O, Kag-C, Rec (Figure 8.11d top right) and intricate hybrid structures involving both SS and LL bonds, with a bias towards Kag-O below the crossover point, and towards Kag-C above the crossover point. The results in Figure 8.12 demonstrate that the ground state structure is the one with the lowest capillary interaction energy per particle, and that we can exclusively select one polymorph over another by ensuring that the difference in this energy for the different polymorphs is significantly greater than k_BT. This result provides a simple but powerful design principle for programming self-assembly in our system.

8.3.4 Binary Mixtures of Squares and Triangles

So far, we have studied the self-assembly of one-component systems consisting of a single particle shape. However, we can access an even richer range of self-assembled structures if we consider mixtures of different particle shapes. In this section, we illustrate this point by using a binary mixture of squares and equilateral triangles to form randomly tiled 12-fold quasicrystals (46,47).[161,162] Specifically, we consider squares and equilateral triangle plates with side length L where the shape parameters in equation (8.2) are $\psi_1 = \pi/2\,, \psi_2 = 7\pi/6\,, \psi_3 = 11\pi/6\,, \Delta = L/(4\sqrt{3})\,, a = \sqrt{3}L/4$ for the triangles and $\psi_1 = 0$, $\psi_2 = \pi/2$, $\Delta = 0$, $a = L/2$ for the squares (we only need two sets of parallel sides to form squares) and we work in units of length where $L = 1$.

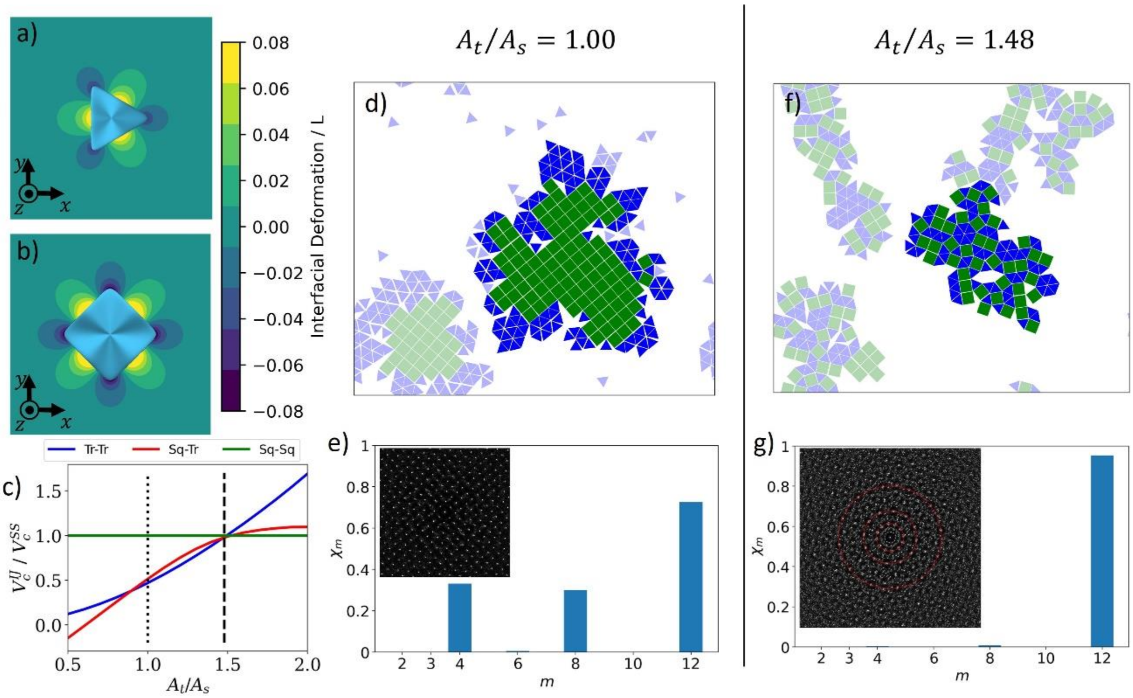

Figure 8.13: (a,b) Top view of the particle geometry and contour plot of liquid interface height (normalized to the side length L) around (a) triangular and (b) square particles. (c) Contact energies for the different shape pairs V_c^{IJ} (normalized to the square-square contact energy) as a function of A_t/A_s, where A_s, A_t are the A values in equation (8.3) for squares and triangles respectively. The vertical dotted and dashed lines correspond to the cases $A_t/A_s = 1.00$ and $A_t/A_s = 1.48$ respectively. (d) Final snapshots for Monte Carlo simulations of a mixture of squares and triangles for $A_t/A_s = 1.00$. The largest cluster is highlighted. (e) The m-fold bond orientational order parameter χ_m as a function of m for the largest cluster in (d). The inset shows the structure factor for the largest cluster. (f), (g) show the plots corresponding to (d), (e) for $A_t/A_s = 1.48$.

To promote random tiling, the edge undulations along the square and triangle sides need be commensurate with each other so that the capillary bond energies for square-square, triangle-triangle and square-triangle side-to-side contact are equal to each other.[49] Having the same contact energies between the different species is important for two reasons. Firstly, the contact energy for triangle-square contacts needs to be at least as large as that for triangle-

triangle and square-square contacts to suppress phase separation between the two species.[162,163] Secondly, the triangle-triangle and square-square contact energies need to be the same to prevent the two species from crystallizing at different points as we cool the system which would lead to kinetic de-mixing (see later). In order to obtain commensurate edge undulations for squares and triangles, we use hexapolar edge undulations for the triangles and octopolar edge undulations for squares, with the multipoles oriented so that the positive poles coincide with the middle of each side, i.e., $m = 3$, $\theta_0 = \pi/6$ for triangles and $m = 4$, $\theta_0 = 0$ for squares in equation (8.3). In Figure 8.13a and Figure 8.13b respectively, we plot the interfacial deformations around an isolated square with $A_s = 0.200L$ and around a triangle with $A_t/A_s = 1.48$, where A_s, A_t are the A values in equation (8.3) for squares and triangles respectively, and we see that the interfacial deformations conform well to the edge undulations in both cases. Note that we use slightly larger A values for both squares and triangles compared to the other shapes we have studied in this Chapter to increase the signal-to-noise ratio in our Surface Evolver simulations as the centre-to-side distances (relative to L) are smaller for triangles and squares compared hexagons and truncated triangles.

Note that since the centre-to-side distance is different for squares and triangles, we need to use different A_t and A_s values to match the amplitude of interfacial undulations for the two shapes and hence match the contact energy between the different species. This point is illustrated in Figure 8.13c where we plot the contact energies for the different shape pairs V_c^{IJ} (normalized to the square-square contact energy) as a function of A_t/A_s for $A_s = 0.200L$, where $I, J = s$ (square) or t (triangle). We see that for $A_t/A_s = 1.00$ (vertical dotted line), there is a large discrepancy in contact energies for the different shape pairs, while for $A_t/A_s = 1.48$ (vertical dashed line), the contact energies for the different shape pairs are essentially equal.

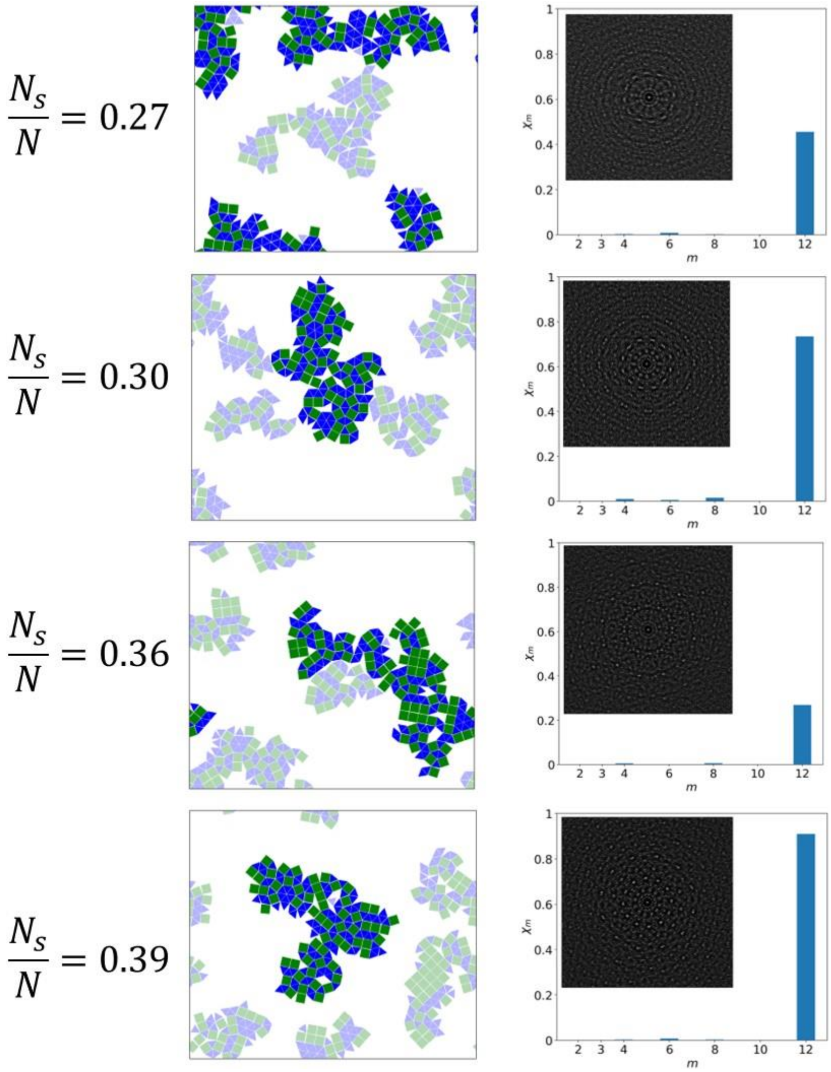

Figure 8.14: Results of Monte Carlo simulations of a mixture of squares and triangles with $A_t/A_s = 1.48$ and square number fractions of (a) 0.27, (b) 0.30, (c) 0.36 and (d) 0.39. For each number fraction, on the left, we show the final snapshot of Monte Carlo simulation with the largest cluster highlighted. On the right, we show the m-fold bond orientational order parameter χ_m as a function of m for the largest cluster. In the inset, we also show the structure factor of the largest cluster.

To illustrate the importance of tuning A_t/A_s in order to obtain 12-fold quasicrystals, we performed MC simulations of mixtures of squares and triangles with a total area fraction of $\eta = 0.3$, $A_s = 0.200L$ and different A_t/A_s values. Theoretically, the optimum number ratio of squares to triangles to form randomly tiled 12-fold quasicrystals is $\sqrt{3}/4$, i.e., a square number fraction of $\sqrt{3}/\left(4+\sqrt{3}\right) \approx 0.30$.[162,164] In fact, we found that the highest quality quasicrystals were obtained for a slightly higher square number fraction of 0.33, and we therefore report results for this composition in Figure 8.13d-g below. However, in Figure 8.14 we show that quasicrystals (albeit of poorer quality) are also formed for the compositions 0.27, 0.30, 0.36 and 0.39, indicating that the formation of quasicrystals is relatively insensitive to composition for the composition range we have studied. Quasicrystals are very delicate structures that are easily destroyed by the presence of too many defects.[162] We therefore cooled the mixture much more slowly compared to the other systems studied in this Chapter (see Section 8.2.3), with a final temperature of $T^* = 0.05$, allowing us to minimize defects and grow large enough crystal domains to produce clear diffraction patterns.

In Figure 8.13d, we show the final snapshot from MC simulations of a mixture of squares and triangles with $A_t/A_s = 1.00$ (i.e., dotted vertical line in Figure 8.13c). We see that no 12-fold quasicrystals are formed in this case as there is a clear phase separation between squares and triangles within the clusters, with the square crystals forming the core and the triangle crystals forming the corona. The observed core-corona cluster morphology is a consequence of the square-square capillary bond energy being significantly higher than the square-triangle and triangle-triangle bond energies. This means that as the system is slowly cooled during the MC simulation, the squares crystallize out of solution first, and act as the nuclei for the subsequent crystallization of the triangles. The dominance of square crystalline order, and absence of 12-fold quasicrystalline order, is confirmed in Figure 8.13e where we plot the m-fold bond orientational order parameter χ_m for different values of m for the largest cluster (highlighted in Figure 8.13d). The order parameter $\chi_m \in [0,1]$ characterizes the degree of m-fold orientational order of the system (see Section 8.2.4), and we see that there is significant orientational order for $m = 4, 8, 12$, consistent with the presence of 4-fold orientational order in the cluster. In the inset, we show the scattering structure factor for the largest cluster, which clearly shows strong square crystalline order in the sample.

In Figure 8.13f, we show the final snapshot from MC simulations of a mixture of squares and triangles with $A_t/A_s = 1.48$ (i.e., dashed vertical line in Figure 8.13c). In contrast to Figure 8.13d, there is now very good mixing between squares and triangles within the clusters. However, because the clusters consist of close-packed polygons, rearrangements are very restricted after structures are formed, making it very difficult to heal any defects in the interior or boundary of the cluster. The very slow structural relaxation limits the maximum crystalline domain size to just over 100 particles, even with the very slow cooling protocol we use. Notwithstanding this limitation, we can clearly see characteristic features of 12-fold quasicrystalline order in the largest cluster (highlighted in Figure 8.13f), for example the presence of complete or partially complete dodecagons consisting of 6 triangles in the core surrounded by 6 squares and 6 triangles.[161,162]

The presence of 12-fold quasicrystalline order for the system with $A_t/A_s = 1.48$ is more strikingly demonstrated in Figure 8.13g, where we plot the bond orientational order parameter χ_m for different m for the largest cluster. We see that the cluster has significant 12-fold orientational order ($\chi_{12} \approx 0.95$), but negligible orientational order for all lower m, in particular for $m = 3, 4, 6$, the factors of 12. In the inset we show the scattering structure factor of the cluster, and we clearly see 12 scattering peaks around each of the circles that have been highlighted. Furthermore, the wavenumber ratio between successive circles is 1.93, consistent with the presence of 12-fold quasicrystalline order in the system.[165]

8.4 Conclusions

We have used minimum energy calculations and Monte Carlo simulations to study the capillary assembly of a novel class of colloidal particles at a liquid interface, namely polygonal plates with homogeneous surface chemistry and undulating edges. This particle geometry gives us precise and independent control over both short-ranged hard-core repulsions (through the polygonal shape) and longer-range capillary interactions (through the edge undulations), allowing us to select specific polymorphs over others and providing essentially limitless possibilities for programming self-assembly in 2D. In addition, the fact that particle interactions are controlled by particle shape rather than surface chemistry considerably simplifies the task of fabricating the colloidal building blocks, allowing us to synthesise the required particle shapes down to the micron scale using currently available fabrication technologies.[32,33,149]

To illustrate the immense potential provided by our system for programming self-assembly, we used polygonal plates with different in-plane shapes and edge undulations to create a rich variety of complex 2D structures. Specifically, for hexagonal plates, we showed that a subtle change in the phase angle between the hexapolar edge undulations and the hexagon shape led to a dramatic change in the thermodynamic ground state from a hexagonal close packed structure to an open honeycomb structure. We also showed that by using a suitable superposition of hexapolar and dodecapolar edge undulations, we could selectively make some edges of a hexagon or truncated triangle more 'sticky' than others, allowing us to effectively create 2D patchy particles using shape alone. Using such particles allowed us to control both the thermodynamics and kinetics of self-assembly to create open structures such as honeycomb and Kagome lattices. Finally, by carefully tuning the multipole order and amplitude of edge undulations in triangles and squares, we were able to accurately tune the contact energies between the two shapes and create 12-fold quasicrystals.

Since the particle shapes above can be readily fabricated experimentally, we can use our novel colloidal system to control the entire process chain for materials design, from initial design and fabrication of the building blocks to final self-assembled structure and emergent properties of the material. As such, our novel colloidal system could revolutionise colloidal self-assembly in two dimensions, in the same way that DNA linker technology has revolutionised colloidal self-assembly in three dimensions.[166]

Chapter 9 Conclusions and Future Work

Given that specific conclusions for each topic are at the end of the relevant chapters, in this chapter, we want to summarise the thesis as a whole, to draw out the broader implications and outline fruitful directions for future research.

In the introductory chapter, we set out the aims and goals of the thesis. We aimed to examine the ways in which the interaction between interfacial forces and the anisotropic characteristics and morphologies of particles can be harnessed to influence the self-assembly of colloids at liquid interfaces, resulting in a wide range of complex two-dimensional structures. We believe that throughout this thesis we have largely succeeded in this ambitious aim.

In the first part of the content chapters (Chapter 4 and Chapter 5), we demonstrated that it is possible to use interfacial curvature as a powerful external field to direct the assembly of anisotropic particles. In particular, the simple cylindrical drop geometry that we considered is amenable to experimental realisation for several reasons. Firstly, we showed that it is possible to direct the configuration and assembly of anisotropic particles using cylindrical drops whose width is much larger than the length of the particles, which allows the use of photolithography to create the necessary substrates to control particles on the nanoscale. This is a major advancement compared to the best current methods available, where controlling the configuration of nanoscale particles requires us to create topographic features on the substrate with length scales comparable to width of the particles which requires nanofabrication.[84–86] Secondly, by varying drop height, we can work in either the flotation or immersion regime, where we have good control over particle orientation or good control over particle position and assembly respectively. We hope that our theoretical study will encourage future experiments in this direction. Specifically, it would be interesting to assemble micron to nanometre sized ellipsoidal or cylindrical particles at a cylindrical interface created by depositing water drops onto a long rectangular hydrophilic patch created using photolithography. By tuning the surface chemistry of the rods, it should be possible to cause the single rods to orient either parallel or perpendicular to the cylindrical drops, and if more than one particle is adsorbed to the same patch in near proximity, obtain a tip-to-tip or side-to-side assembly of the rods.

In the second part of the content chapters (Chapter 6, Chapter 7 and Chapter 8), we showed that the unique nature of particle interactions at liquid interfaces provide powerful handles with which to design and control self-assembly of colloidal particles. In Chapter 6, where we studied the self-assembly of core-shell spheres, we showed that the presence of the interface created extremely flat coronae for the core-shell particles. We believe that this flat corona morphology is essential to cause soft-shell interaction potentials with a flat enough profile for achieving core-collapse morphologies such as cluster phases and braided chains. These core-collapse phases were predicted theoretically to exist for over two decades[98,102] but were only observed experimentally for the first time in our study. In Chapter 7 and Chapter 8, we exploited capillary interactions to control self-assembly. Capillary forces are mediated by interfacial deformations and therefore do not have an analogue for colloids in the bulk. Specifically, in Chapter 7, we studied the self-assembly of core-shell ellipsoids and showed that, by tuning the interplay between capillary forces arising from the core, and steric forces caused by the flat corona, it was possible to achieve rational control over whether the ellipsoids assembled side-to-side or tip-to-tip. Prior to our study, both tip-to-tip and side-to-side arrangements for seemingly similar ellipsoidal particles were observed experimentally.[137–141] However, the origin of the preference for either structure was not yet fully understood. For both core-shell spheres and core-shell ellipsoids, we achieved remarkably good agreement between our simulation results and experiments, demonstrating that we can use our simulations to guide experiments to achieve deterministic control of the self-assembly of these systems.

In Chapter 8, we studied the self-assembly of polygonal plates with undulating edges and showed that we could use this geometry to create a rich variety of 2D structures. Similar structures were observed in the work of Whitesides and coworkers using flat polygonal plates with patchy edges.[60,61] However, the patchy particle geometry made it difficult to scale down particle synthesis below the mm-scale.[62] For our polygonal plate system, self-assembly is controlled by geometry rather than surface chemistry, which greatly simplifies the creation of particles that produce complex menisci. With modern advances in 3D printing and laser technology, the required 3D particle shapes can be achieved to sub mm resolution, and we hope that our theoretical study will stimulate future experiments to fabricate these particles and create the final 2D materials through self-assembly.

In addition to the future experimental work discussed above, our thesis also suggests several directions for future theoretical work that would be fruitful to pursue.

Firstly, the work presented in Chapter 4 and Chapter 5 suggests a way to assemble rod-like particles into side-to-side or tip-to-tip structures using cylindrical drops whose width is much larger than the length of the particles. In our calculations we assumed that the cylindrical drops had infinite length so that there is no rod migration owing to gradients in the deviatoric curvature,[17] which is a good assumption for very long cylindrical drops where assembly occurs near the middle of the drop. However, in practice, the deposition of rod-like particles on the cylindrical drop is a random process and particles could therefore adsorb and assemble near the ends of the drop where there may be strong gradients in deviatoric curvature. For future work, we therefore suggest studying the assembly of rod-like particles on a finite length sessile cylindrical drop. Additionally, it would be interesting to investigate other easy-to-fabricate patch geometries (in addition to the rectangular geometry) to supress or promote migration. These geometries could include ellipses and a 2D equivalent of the spherocylinder called a stadium.

Secondly, the results in Chapter 6 suggest that the interaction potential between the experimentally fabricated uncrosslinked core-shell particles were close to a linear Jagla potential with pairwise-additive behaviour. However, the determination of the interaction potential profile was indirect. For future work, it would be interesting to perform monomer-resolved simulations of the polymer 'hairs' in the soft-shell to calculate the soft-shell interactions between the particles directly.

Finally, the work presented in Chapter 8 serves as a proof of principle and highlights the tremendous number of possibilities of self-assembled structures that could be created following these polygonal plates with undulating edges. The natural next step would be to use edge undulations to impose matching rules, i.e., rules that dictate which polygon sides may or may not be next to each other,[49] allowing us to assemble deterministic quasicrystals which should form much larger clusters.[164] The application of such matching rules may also allow us to utilise self-assembly to create the recently discovered quasicrystals made from a single tile shape.[167] Without such matching rules, the concave shape of these tiles would greatly restrict structural rearrangements during self-assembly, potentially causing the system to be kinetically trapped in metastable states with many defects, therefore preventing the system from reaching its ground state. Additionally, because our system consists of polygonal plates connected to their neighbours via directional capillary bonds, we can exploit these bonds to act as soft 'hinges' and introduce 'floppy modes' into the system (i.e., low energy deformations that only involve rotations of the polygons about the hinges). These floppy modes can be used to create auxetic materials with negative Poisson ratio[40] or thermal expansivities[168] and mechanical metamaterials with transformable mechanical properties.[159,160]

To conclude, the results of this thesis have the potential to impact and shape the future of material synthesis, allowing for the self-assembly of complex functional 2D materials with applications in fields such as photonics, phononics, and plasmonics.

Reference list / Bibliography

1. McGee, H. *On Food and Cooking*. (Scribner, 1984).

2. Kralchevsky, P. A. & Nagayama, K. *Particles at Fluid Interfaces and Membranes Attachment of Colloid Particles and Proteins to Interfaces and Formation of Two-Dimensional Arrays*. (Elsevier B.V., 2001).

3. Aulton, M. E. & Taylor, K. M. G. *Aulton's Pharmaceutics: The Design and Manufacture of Medicines*. (Elsevier, 2018).

4. Aveyard, R., Binks, B. P. & Clint, J. H. Emulsions stabilised solely by colloidal particles. *Adv. Colloid Interface Sci.* **100**–**102**, 503–546 (2003).

5. Yang, Y. *et al.* An overview of pickering emulsions: Solid-particle materials, classification, morphology, and applications. *Frontiers in Pharmacology* vol. 8 287 (2017).

6. Binks, B. P. & Horozov, T. S. *Colloidal Particles at Liquid Interfaces*. (Cambridge University Press, 2006). doi:10.1017/CBO9780511536670.

7. Gonzenbach, U. T., Studart, A. R., Tervoort, E. & Gauckler, L. J. Stabilization of foams with inorganic colloidal particles. *Langmuir* **22**, 10983–10988 (2006).

8. Herzig, E. M., White, K. A., Schofield, A. B., Poon, W. C. K. & Clegg, P. S. Bicontinuous emulsions stabilized solely by colloidal particles. *Nat. Mater.* **6**, 966–971 (2007).

9. Stratford, K., Adhikari, R., Pagonabarraga, I., Desplat, J. C. & Cates, M. E. Chemistry: Colloidal jamming at interfaces: A route to fluid-bicontinuous gels. *Science (80-.).* **309**, 2198–2201 (2005).

10. Mishra, B., Patel, B. B. & Tiwari, S. Colloidal nanocarriers: a review on formulation technology, types and applications toward targeted drug delivery. *Nanomedicine Nanotechnology, Biol. Med.* **6**, 9–24 (2010).

11. Pieranski, P. Two-dimensional interfacial colloidal crystals. *Phys. Rev. Lett.* **45**, 569–572 (1980).

12. Ruths, M. Surface Forces, Surface Tension, and Adhesion. in *Encyclopedia of Tribology* 3435–3443 (Springer US, 2013). doi:10.1007/978-0-387-92897-5_463.

13. Israelachvili, J. *Intermolecular and Surface Forces*. (Elsevier, 2011). doi:10.1016/C2009-0-21560-1.

14. Kralchevsky, P. A. & Nagayama, K. Capillary interactions between particles bound to interfaces, liquid films and biomembranes. *Adv. Colloid Interface Sci.* **85**, 145–192 (2000).

15. Loudet, J. C., Alsayed, A. M., Zhang, J. & Yodh, A. G. Capillary interactions between anisotropic colloidal particles. *Phys. Rev. Lett.* **94**, 2–5 (2005).

16. Ferrar, J. A., Pavlovsky, L., Viges, E., Liu, Y. & Solomon, M. J. Two-step continuous production of monodisperse colloidal ellipsoids at rates of one gram per day. *AIChE J.* **64**, 697–707 (2018).

17. Cavallaro, M., Botto, L., Lewandowski, E. P., Wang, M. & Stebe, K. J. Curvature-driven capillary migration and assembly of rod-like particles. *Proc. Natl. Acad. Sci. U. S. A.* **108**, 20923–20928 (2011).

18. Park, B. J. *et al.* Geometrically and chemically anisotropic particles at an oil-water interface. *Soft Matter* **9**, 3383–3388 (2013).

19. Song, Q., Steuber, M., Druzhinin, S. I. & Schönherr, H. Tailored Combinatorial Microcompartments through the Self-Organization of Microobjects: Assembly, Characterization, and Cell Studies. *Angew. Chemie* **131**, 5300–5304 (2019).

20. Song, Q. & Schönherr, H. Control of Orientation, Formation of Ordered Structures, and Self-Sorting of Surface-Functionalized Microcubes at the Air-Water Interface. *Langmuir* (2019) doi:10.1021/acs.langmuir.9b00792.

21. Anzivino, C. *et al.* Equilibrium configurations and capillary interactions of Janus dumbbells and spherocylinders at fluid-fluid interfaces. *Soft Matter* **15**, 2638–2647 (2019).

22. Johnson, P. M., van Kats, C. M. & van Blaaderen, A. Synthesis of Colloidal Silica Dumbbells. *Langmuir* **21**, 11510–11517 (2005).

23. Park, B. J. & Lee, D. Equilibrium Orientation of Nonspherical Janus Particles at Fluid–Fluid Interfaces. *ACS Nano* **6**, 782–790 (2012).

24. Qian, J. Y., Pearson, R. A., Dimonie, V. L. & El-Aasser, M. S. Synthesis and application of

core–shell particles as toughening agents for epoxies. *J. Appl. Polym. Sci.* **58**, 439–448 (1995).

25. Rey, M. *et al.* Isostructural solid-solid phase transition in monolayers of soft core-shell particles at fluid interfaces: Structure and mechanics. *Soft Matter* **12**, 3545–3557 (2016).

26. Rauh, A. *et al.* Compression of hard core-soft shell nanoparticles at liquid-liquid interfaces: influence of the shell thickness. *Soft Matter* **13**, 158–169 (2017).

27. Chen, Q., Yan, J., Zhang, J., Bae, S. C. & Granick, S. Janus and multiblock colloidal particles. *Langmuir* **28**, 13555–13561 (2012).

28. Park, B. J. *et al.* Double hydrophilic janus cylinders at an air-water interface. *Langmuir* **29**, 1841–1849 (2013).

29. Hong, L., Cacciuto, A., Luijten, E. & Granick, S. Clusters of amphiphilic colloidal spheres. *Langmuir* **24**, 621–625 (2008).

30. Gardi, G., Ceron, S., Wang, W., Petersen, K. & Sitti, M. Microrobot collectives with reconfigurable morphologies, behaviors, and functions. *Nat. Commun.* **13**, 2239 (2022).

31. Wang, W., Giltinan, J., Zakharchenko, S. & Sitti, M. Dynamic and programmable self-assembly of micro-rafts at the air-water interface. *Sci. Adv.* **3**, 446–458 (2017).

32. Kawata, S., Sun, H.-B., Tanaka, T. & Takada, K. Finer features for functional microdevices. *Nature* **412**, 697–698 (2001).

33. Lin, Y. & Xu, J. Microstructures Fabricated by Two-Photon Polymerization and Their Remote Manipulation Techniques: Toward 3D Printing of Micromachines. *Adv. Opt. Mater.* **6**, 446–458 (2018).

34. Kolle, M. *et al.* Mimicking the colourful wing scale structure of the Papilio blumei butterfly. *Nat. Nanotechnol.* **5**, 511–515 (2010).

35. Bley, K. *et al.* Hierarchical Design of Metal Micro/Nanohole Array Films Optimizes Transparency and Haze Factor. *Adv. Funct. Mater.* **28**, 1–11 (2018).

36. Boechler, N. *et al.* Interaction of a contact resonance of microspheres with surface acoustic waves. *Phys. Rev. Lett.* **111**, 1–5 (2013).

37. Graczykowski, B., Vogel, N., Bley, K., Butt, H. J. & Fytas, G. Multiband Hypersound Filtering in Two-Dimensional Colloidal Crystals: Adhesion, Resonances, and Periodicity. *Nano Lett.* **20**, 1883–1889 (2020).

38. Nemiroski, A. *et al.* Engineering shadows to fabricate optical metasurfaces. *ACS Nano* **8**, 11061–11070 (2014).

39. Volk, K., Fitzgerald, J. P. S., Retsch, M. & Karg, M. Time-Controlled Colloidal Superstructures: Long-Range Plasmon Resonance Coupling in Particle Monolayers. *Adv. Mater.* **27**, 7332–7337 (2015).

40. Gatt, R. *et al.* Hierarchical Auxetic Mechanical Metamaterials. *Sci. Rep.* **5**, 8395 (2015).

41. Coertjens, S., Moldenaers, P., Vermant, J. & Isa, L. Contact angles of microellipsoids at fluid interfaces. *Langmuir* **30**, 4289–4300 (2014).

42. Faraudo, J. & Bresme, F. Stability of particles adsorbed at liquid/fluid interfaces: Shape effects induced by line tension. *J. Chem. Phys.* **118**, 6518–6528 (2003).

43. Davies, G. B., Krüger, T., Coveney, P. V. & Harting, J. Detachment energies of spheroidal particles from fluid-fluid interfaces. *J. Chem. Phys.* **141**, (2014).

44. Vella, D. & Mahadevan, L. The “Cheerios effect”. *Am. J. Phys.* **73**, 817–825 (2005).

45. Dushkin, C. D., Kralchevsky, P. A., Paunov, V. N., Yoshimura, H. & Nagayama, K. Torsion balance for measurement of capillary immersion forces. *Langmuir* **12**, 641–651 (1996).

46. Maenosono, S., Dushkin, C. D. & Yamaguchi, Y. Direct measurement of the viscous force between two spherical particles trapped in a thin wetting film. *Colloid Polym. Sci.* **277**, 993–996 (1999).

47. Shi, Y. *et al.* Spontaneous Particle Ordering, Sorting, and Assembly on Soap Films. *Nano Lett.* (2024) doi:10.1021/acs.nanolett.4c01840.

48. Dasgupta, S., Auth, T. & Gompper, G. Nano- and microparticles at fluid and biological interfaces. *J. Phys. Condens. Matter* **29**, (2017).

49. Botto, L., Yao, L., Leheny, R. L. & Stebe, K. J. Capillary bond between rod-like particles and the micromechanics of particle-laden interfaces. *Soft Matter* **8**, 4971–4979 (2012).

50. Lewandowski, E. P. *et al.* Orientation and self-assembly of cylindrical particles by

anisotropic capillary interactions. *Langmuir* **26**, 15142–15154 (2010).

51. Loudet, J. C., Yodh, A. G. & Pouligny, B. Wetting and contact lines of micrometer-sized ellipsoids. *Phys. Rev. Lett.* **97**, 1–4 (2006).

52. Lehle, H., Noruzifar, E. & Oettel, M. Ellipsoidal particles at fluid interfaces. *Eur. Phys. J. E* **26**, 151–160 (2008).

53. Newton, B. J. & Buzza, D. M. A. Magnetic cylindrical colloids at liquid interfaces exhibit non-volatile switching of their orientation in an external field. *Soft Matter* **12**, 5285–5296 (2016).

54. Lewandowski, E. P., Searson, P. C. & Stebe, K. J. Orientation of a nanocylinder at a fluid interface. *J. Phys. Chem. B* **110**, 4283–4290 (2006).

55. Anzivino, C., Soligno, G., van Roij, R. & Dijkstra, M. Chains of cubic colloids at fluid-fluid interfaces. *Soft Matter* **17**, 965–975 (2021).

56. Soligno, G., Dijkstra, M. & Van Roij, R. Self-Assembly of Cubes into 2D Hexagonal and Honeycomb Lattices by Hexapolar Capillary Interactions. *Phys. Rev. Lett.* **116**, 1–6 (2016).

57. Soligno, G., Dijkstra, M. & Van Roij, R. Self-assembly of cubic colloidal particles at fluid-fluid interfaces by hexapolar capillary interactions. *Soft Matter* **14**, 42–60 (2017).

58. Boneschanscher, M. P. *et al.* Long-range orientation and atomic attachment of nanocrystals in 2D honeycomb superlattices. *Science (80-.).* **344**, 1377–1380 (2014).

59. Evers, W. H. *et al.* Low-dimensional semiconductor superlattices formed by geometric control over nanocrystal attachment. *Nano Lett.* **13**, 2317–2323 (2013).

60. Bowden, N., Oliver, S. R. J. & Whitesides, G. M. Mesoscale self-assembly: Capillary bonds and negative menisci. *J. Phys. Chem. B* **104**, 2714–2724 (2000).

61. Bowden, N., Terfort, A., Carbeck, J. & Whitesides, G. M. Assembly of mesoscale objects into ordered two-dimensional arrays. *Science (80-.).* **276**, 233–235 (1997).

62. Bowden, N., Arias, F., Deng, T. & Whitesides, G. M. Self-assembly of microscale objects at a liquid/liquid interface through lateral capillary forces. *Langmuir* **17**, 1757–1765 (2001).

63. Mugele, F. & Heikenfeld, J. *Electrowetting: Fundamental Principles and Practical Applications*. (Wiley-VCH, 2019).

64. Stamou, D., Duschl, C. & Johannsmann, D. Long-range attraction between colloidal spheres at the air-water interface: The consequence of an irregular meniscus. *Phys. Rev. E - Stat. Physics, Plasmas, Fluids, Relat. Interdiscip. Top.* **62**, 5263–5272 (2000).

65. Botto, L., Lewandowski, E. P., Cavallaro, M. & Stebe, K. J. Capillary interactions between anisotropic particles. *Soft Matter* **8**, 9957–9971 (2012).

66. Danov, K. D., Kralchevsky, P. A., Naydenov, B. N. & Brenn, G. Interactions between particles with an undulated contact line at a fluid interface: Capillary multipoles of arbitrary order. *J. Colloid Interface Sci.* **287**, 121–134 (2005).

67. Garcia-Botella, A., Fernandez-Balbuena, A. A., Vázquez-Moliní, D., Bernabeu, E. & Gonzalez-Cano, A. Field method for concentrator design. *Nonimaging Opt. Effic. Des. Illum. Sol. Conc. VI* **7423**, 742307 (2009).

68. Forstneric, F. *Minimal surfaces for undergraduates*. (2021).

69. Gauss, K. F. *General Investigations of Curved Surfaces of 1827 and 1825*. *Nature* vol. 66 (1902).

70. Zeng, C., Brau, F., Davidovitch, B. & Dinsmore, A. D. Capillary interactions among spherical particles at curved liquid interfaces. *Soft Matter* **8**, 8582–8594 (2012).

71. Fisher, J. W., Miller, S. W., Bartolai, J. & Yukish, M. A. Using Mean Curvature of Implicitly Defined Minimal Surface Approximations to Generate New Unit Cells for Lattice Design. in *33rd Annual International Solid Freeform Fabrication Symposium 2022* 2233–2243 (2022).

72. Ershov, D., Sprakel, J., Appel, J., Stuart, M. A. C. & Van Der Gucht, J. Capillarity-induced ordering of spherical colloids on an interface with anisotropic curvature. *Proc. Natl. Acad. Sci. U. S. A.* **110**, 9220–9224 (2013).

73. Lewandowski, E. P., Bernate, J. A., Searson, P. C. & Stebe, K. J. Rotation and alignment of anisotropic particles on nonplanar interfaces. *Langmuir* **24**, 9302–9307 (2008).

74. Brakke, K. A. The surface evolver. *Exp. Math.* **1**, 141–165 (1992).

75. Frenkel, D. & Smit, B. *Understanding Molecular Simulation: From Algorithms to*

Applications Volume 1 of Computational science. (Elsevier, 2001).

76. Leach, A. R. *Molecular Modelling: Principles and Applications*. (Pearson Education, 2001).

77. Allen, M. P. & Tildesley, D. J. *Computer Simulation of Liquids*. vol. 1 (Oxford University Press, 2017).

78. Fichthorn, K. A. & Weinberg, W. H. Theoretical foundations of dynamical Monte Carlo simulations. *J. Chem. Phys.* **95**, 1090–1096 (1991).

79. Kang, H. & Weinberg, W. Dynamic Monte Carlo Simulations of Surface-Rate Processes. *Acc. Chem. Res.* **25**, 253–259 (1992).

80. Sanz, E. & Marenduzzo, D. Dynamic Monte Carlo versus Brownian dynamics: A comparison for self-diffusion and crystallization in colloidal fluids. *J. Chem. Phys.* **132**, (2010).

81. Kikuchi, K., Yoshida, M., Maekawa, T. & Watanabe, H. Metropolis Monte Carlo method as a numerical technique to solve the Fokker—Planck equation. *Chem. Phys. Lett.* **185**, 335–338 (1991).

82. Guzowski, J., Tasinkevych, M. & Dietrich, S. Free energy of colloidal particles at the surface of sessile drops. *Eur. Phys. J. E* **33**, 219–242 (2010).

83. Guzowski, J., Tasinkevych, M. & Dietrich, S. Effective interactions and equilibrium configurations of colloidal particles on a sessile droplet. *Soft Matter* **7**, 4189–4197 (2011).

84. Kuemin, C., Nowack, L., Bozano, L., Spencer, N. D. & Wolf, H. Oriented assembly of gold nanorods on the single-particle level. *Adv. Funct. Mater.* **22**, 702–708 (2012).

85. Greybush, N. J. *et al.* Plasmon-enhanced upconversion luminescence in single nanophosphor-nanorod heterodimers formed through template-assisted self-assembly. *ACS Nano* **8**, 9482–9491 (2014).

86. Flauraud, V. *et al.* Nanoscale topographical control of capillary assembly of nanoparticles. *Nat. Nanotechnol.* **12**, 73–80 (2017).

87. Kralchevsky, P. A. & Nagayama, K. Capillary Forces between Colloidal Particles. *Langmuir* **10**, 23–36 (1994).

88. Newton, B. J., Mohammed, R., Davies, G. B., Botto, L. & Buzza, D. M. A. Capillary Interaction and Self-Assembly of Tilted Magnetic Ellipsoidal Particles at Liquid Interfaces. *ACS Omega* **3**, 14962–14972 (2018).

89. Newton, B. J., Brakke, K. A. & Buzza, D. M. A. Influence of magnetic field on the orientation of anisotropic magnetic particles at liquid interfaces. *Phys. Chem. Chem. Phys.* **16**, 26051–26058 (2014).

90. Loudet, J. C. & Pouligny, B. How do mosquito eggs self-assemble on the water surface? *Eur. Phys. J. E* **34**, (2011).

91. Morgan, S. O. *et al.* Adsorption trajectories of nonspherical particles at liquid interfaces. *Phys. Rev. E* **103**, 42604 (2021).

92. Morgan, S. O. *et al.* Using adsorption kinetics to assemble vertically aligned nanorods at liquid interfaces for metamaterial applications. *Phys. Chem. Chem. Phys.* 11000–11013 (2022) doi:10.1039/d1cp05484h.

93. Collins, P. *Differential and Integral Equations*. (Oxford University Press, 2006).

94. Rezvantalab, H. & Shojaei-Zadeh, S. Role of geometry and amphiphilicity on capillary-induced interactions between anisotropic janus particles. *Langmuir* **29**, 14962–14970 (2013).

95. Newton, B. J., Brakke, K. A. & Buzza, D. M. A. Influence of magnetic field on the orientation of anisotropic magnetic particles at liquid interfaces. *Phys. Chem. Chem. Phys.* **16**, 26051–26058 (2014).

96. Domínguez, A., Oettel, M. & Dietrich, S. Force balance of particles trapped at fluid interfaces. *J. Chem. Phys.* **128**, (2008).

97. Savitzky, A. & Golay, M. J. E. Smoothing and Differentiation of Data by Simplified Least Squares Procedures. *Anal. Chem.* **36**, 1627–1639 (1964).

98. Jagla, E. A. Phase behavior of a system of particles with core collapse. *Phys. Rev. E - Stat. Physics, Plasmas, Fluids, Relat. Interdiscip. Top.* **58**, 1478–1486 (1998).

99. Glaser, M. A. *et al.* Soft spheres make more mesophases. *Epl* **78**, (2007).

100. Rey, M., Law, A. D., Buzza, D. M. A. & Vogel, N. Anisotropic Self-Assembly from Isotropic Colloidal Building Blocks. *J. Am. Chem. Soc.* **139**, 17464–17473 (2017).

101. Somerville, W. R. C. *et al.* Pattern formation in two-dimensional hard-core/soft-shell systems with variable soft shell profiles. *Soft Matter* **16**, 3564–3573 (2020).

102. Jagla, E. A. Minimum energy configurations of repelling particles in two dimensions. *J. Chem. Phys.* **110**, 451–456 (1999).

103. Pattabhiraman, H. & Dijkstra, M. On the formation of stripe, sigma, and honeycomb phases in a core-corona system. *Soft Matter* **13**, 4418–4432 (2017).

104. Dotera, T., Oshiro, T. & Ziherl, P. Mosaic two-lengthscale quasicrystals. *Nature* **506**, 208–211 (2014).

105. Malescio, G. & Pellicane, G. Stripe patterns in two-dimensional systems with core-corona molecular architecture. *Phys. Rev. E - Stat. Physics, Plasmas, Fluids, Relat. Interdiscip. Top.* **70**, 6 (2004).

106. Malescio, G. & Pellicane, G. Stripe phases from isotropic repulsive interactions. *Nat. Mater.* **2**, 97–100 (2003).

107. Lafitte, T., Kumar, S. K. & Panagiotopoulos, A. Z. Self-assembly of polymer-grafted nanoparticles in thin films. *Soft Matter* **10**, 786–794 (2014).

108. Fornleitner, J. & Kahl, G. Pattern formation in two-dimensional square-shoulder systems. *J. Phys. Condens. Matter* **22**, (2010).

109. Karg, M. *et al.* Nanogels and Microgels: From Model Colloids to Applications, Recent Developments, and Future Trends. *Langmuir* **35**, 6231–6255 (2019).

110. Deshmukh, O. S. *et al.* Equation of state and adsorption dynamics of soft microgel particles at an air-water interface. *Soft Matter* **10**, 7045–7050 (2014).

111. Camerin, F. *et al.* Microgels Adsorbed at Liquid-Liquid Interfaces: A Joint Numerical and Experimental Study. *ACS Nano* **13**, 4548–4559 (2019).

112. Style, R. W., Isa, L. & Dufresne, E. R. Adsorption of soft particles at fluid interfaces. *Soft Matter* **11**, 7412–7419 (2015).

113. Rey, M., Fernandez-Rodriguez, M. A., Karg, M., Isa, L. & Vogel, N. Poly-N-isopropylacrylamide Nanogels and Microgels at Fluid Interfaces. *Acc. Chem. Res.* **53**, 414–424 (2020).

114. Zielińska, K., Sun, H., Campbell, R. A., Zarbakhsh, A. & Resmini, M. Smart nanogels at the air/water interface: Structural studies by neutron reflectivity. *Nanoscale* **8**, 4951–4960 (2016).

115. Stieger, M., Richtering, W., Pedersen, J. S. & Lindner, P. Small-angle neutron scattering study of structural changes in temperature sensitive microgel colloids. *J. Chem. Phys.* **120**, 6197–6206 (2004).

116. Harrer, J. *et al.* Stimuli-Responsive Behavior of PNiPAm Microgels under Interfacial Confinement. *Langmuir* **35**, 10512–10521 (2019).

117. Bochenek, S., Scotti, A. & Richtering, W. Temperature-sensitive soft microgels at interfaces: air-waterversusoil-water. *Soft Matter* **17**, 976–988 (2021).

118. Geisel, K., Isa, L. & Richtering, W. Unraveling the 3D localization and deformation of responsive microgels at oil/water interfaces: A step forward in understanding soft emulsion stabilizers. *Langmuir* **28**, 15770–15776 (2012).

119. Rey, M., Hou, X., Tang, J. S. J. & Vogel, N. Interfacial arrangement and phase transitions of PNiPAm microgels with different crosslinking densities. *Soft Matter* **13**, 8717–8727 (2017).

120. Tang, J. S. J. *et al.* Surface Patterning with SiO2@PNiPAm Core-Shell Particles. *ACS Omega* **3**, 12089–12098 (2018).

121. Vogel, N. *et al.* Ordered arrays of gold nanostructures from interfacially assembled Au@PNIPAM hybrid nanoparticles. *Langmuir* **28**, 8985–8993 (2012).

122. Ciarella, S. *et al.* Soft Particles at Liquid Interfaces: From Molecular Particle Architecture to Collective Phase Behavior. *Langmuir* **37**, 5364–5375 (2021).

123. Rahane, S. B., Kilbey, S. M. & Metters, A. T. Kinetics of Surface-Initiated Photoiniferter-Mediated Photopolymerization. 8202–8210 (2005).

124. Tom, J., Brilmayer, R., Schmidt, J. & Andrieu-Brunsen, A. Optimisation of Surface-Initiated Photoiniferter-Mediated Polymerisation under Confinement, and the Formation of Block Copolymers in Mesoporous Films. *Polymers (Basel).* **9**, 539 (2017).

125. Vogel, N., Retsch, M., Fustin, C. A., Del Campo, A. & Jonas, U. Advances in Colloidal Assembly: The Design of Structure and Hierarchy in Two and Three Dimensions. *Chem.*

Rev. **115**, 6265–6311 (2015).

126. Pusey, P. N. & van Megen, W. Phase behaviour of concentrated suspensions of nearly hard colloidal spheres. *Nature* **320**, 340–342 (1986).

127. Rey, B. M. *et al.* Fully Tunable Silicon Nanowire Arrays Fabricated by Soft Nanoparticle Templating. *Nano Lett.* **16**, 157–163 (2016).

128. Fornleitner, J. & Kahl, G. Lane formation vs. cluster formation in two-dimensional square-shoulder systems —A genetic algorithm approach. *EPL (Europhysics Lett.* **82**, 18001 (2008).

129. Rey, M., Yu, T., Guenther, R., Bley, K. & Vogel, N. A Dirty Story: Improving Colloidal Monolayer Formation by Understanding the Effect of Impurities at the Air/Water Interface. *Langmuir* **35**, 95–103 (2019).

130. Schwenke, K., Isa, L., Cheung, D. L. & Del Gado, E. Conformations and Effective Interactions of Polymer-Coated Nanoparticles at Liquid Interfaces. *Langmuir* **30**, 12578–12586 (2014).

131. Camerin, F. *et al.* Microgels at Interfaces Behave as 2D Elastic Particles Featuring Reentrant Dynamics. *Phys. Rev. X* **10**, 031012 (2020).

132. Flory, P. J. & Krigbaum, W. R. Statistical Mechanics of Dilute Polymer Solutions. II. *J. Chem. Phys.* **18**, 1086–1094 (1950).

133. Bolhuis, P. G., Louis, A. A., Hansen, J. P. & Meijer, E. J. Accurate effective pair potentials for polymer solutions. *J. Chem. Phys.* **114**, 4296–4311 (2001).

134. Louis, A. A., Bolhuis, P. G., Hansen, J. P. & Meijer, E. J. Can Polymer Coils Be Modeled as “Soft Colloids”? *Phys. Rev. Lett.* **85**, 2522–2525 (2000).

135. Luo, A. M., Vermant, J., Ilg, P., Zhang, Z. & Sagis, L. M. C. Self-assembly of ellipsoidal particles at fluid-fluid interfaces with an empirical pair potential. *J. Colloid Interface Sci.* **534**, 205–214 (2019).

136. Zhang, Z., Pfleiderer, P., Schofield, A. B., Clasen, C. & Vermant, J. Synthesis and Directed Self-Assembly of Patterned Anisometric Polymeric Particles. *J. Am. Chem. Soc.* **133**, 392–395 (2011).

137. Coertjens, S., Moldenaers, P., Vermant, J. & Isa, L. Contact Angles of Microellipsoids at

Fluid Interfaces. *Langmuir* **30**, 4289–4300 (2014).

138. Coertjens, S., De Dier, R., Moldenaers, P., Isa, L. & Vermant, J. Adsorption of Ellipsoidal Particles at Liquid–Liquid Interfaces. *Langmuir* **33**, 2689–2697 (2017).

139. Basavaraj, M. G., Fuller, G. G., Fransaer, J. & Vermant, J. Packing, Flipping, and Buckling Transitions in Compressed Monolayers of Ellipsoidal Latex Particles. *Langmuir* **22**, 6605–6612 (2006).

140. Flores-Tandy, L. M. *et al.* Fractal aggregates formed by ellipsoidal colloidal particles at the air/water interface. *Colloids Surfaces A Physicochem. Eng. Asp.* **590**, 124477 (2020).

141. Madivala, B., Fransaer, J. & Vermant, J. Self-Assembly and Rheology of Ellipsoidal Particles at Interfaces. *Langmuir* **25**, 2718–2728 (2009).

142. Honda, K. *et al.* Hydrogel Microellipsoids that Form Robust String-Like Assemblies at the Air/Water Interface. *Angew. Chemie* **131**, 7372–7376 (2019).

143. Nickel, A. C. *et al.* Anisotropic Microgels Show Their Soft Side. *Langmuir* **38**, 5063–5080 (2022).

144. Benke, D. *et al.* Prolate spheroidal polystyrene nanoparticles: matrix assisted synthesis, interface properties, and scattering analysis. *Soft Matter* **19**, 9006–9016 (2023).

145. Ho, C. C., Keller, A., Odell, J. A. & Ottewill, R. H. Preparation of monodisperse ellipsoidal polystyrene particles. *Colloid Polym. Sci.* **271**, 469–479 (1993).

146. Rey, M. *et al.* Versatile strategy for homogeneous drying patterns of dispersed particles. *Nat. Commun.* **13**, 2840 (2022).

147. Berne, B. J. & Pechukas, P. Gaussian model potentials for molecular interactions. *J. Chem. Phys.* **56**, 4195–4205 (1972).

148. Guevara-Rodríguez, F. D. J. & Odriozola, G. Hard ellipsoids: Analytically approaching the exact overlap distance. *J. Chem. Phys.* **135**, (2011).

149. Tao, Y. *et al.* Morphing pasta and beyond. *Sci. Adv.* **7**, 446–458 (2021).

150. Damasceno, P. F., Engel, M. & Glotzer, S. C. Predictive Self-Assembly of Polyhedra into Complex Structures. *Science (80-.).* **337**, 453–457 (2012).

151. Bowden, N., Choi, I. S., Grzybowski, B. A. & Whitesides, G. M. Mesoscale self-assembly

of hexagonal plates using lateral capillary force: Synthesis using the ‘capillary bond’. *J. Am. Chem. Soc.* **121**, 5373–5391 (1999).

152. Morgan, S. O. Anisotropic Particles at Liquid Interfaces. (University of Hull, 2022).

153. Gilbert, E. G., Johnson, D. W. & Keerthi, S. S. A fast procedure for computing the distance between complex objects in three-dimensional space. *IEEE J. Robot. Autom.* **4**, 193–203 (1988).

154. Dill, K. A., Bromberg, S. & Stigter, D. *Molecular Driving Forces*. (Garland Science, 2010). doi:10.4324/9780203809075.

155. Brochard, F. & Lennon, J. F. Frequency spectrum of the flicker phenomenon in erythrocytes. *J. Phys.* **36**, 1035–1047 (1975).

156. Goulian, M., Bruinsma, R. & Pincus, P. Long-Range Forces in Heterogeneous Fluid Membranes. *Europhys. Lett.* **23**, 155–155 (1993).

157. Park, J.-M. & Lubensky, T. C. Interactions between membrane Inclusions on Fluctuating Membranes. *J. Phys. I* **6**, 1217–1235 (1996).

158. Lee, A. A., Vella, D. & Wettlaufer, J. S. Fluctuation spectra and force generation in nonequilibrium systems. *Proc. Natl. Acad. Sci.* **114**, 9255–9260 (2017).

159. Kane, C. L. & Lubensky, T. C. Topological boundary modes in isostatic lattices. *Nat. Phys.* **10**, 39–45 (2014).

160. Rocklin, D. Z., Zhou, S., Sun, K. & Mao, X. Transformable topological mechanical metamaterials. *Nat. Commun.* **8**, 14201 (2017).

161. Oxborrow, M. & Henley, C. L. Random square-triangle tilings: A model for twelvefold-symmetric quasicrystals. *Phys. Rev. B* **48**, 6966–6998 (1993).

162. Leung, P. W., Henley, C. L. & Chester, G. V. Dodecagonal order in a two-dimensional Lennard-Jones system. *Phys. Rev. B* **39**, 446–458 (1989).

163. Widom, M., Strandburg, K. J. & Swendsen, R. H. Quasicrystal equilibrium state. *Phys. Rev. Lett.* **58**, 706–709 (1987).

164. Henley, C. L. Random tilings with quasicrystal order: transfer-matrix approach. *J. Phys. A. Math. Gen.* **21**, 1649–1677 (1988).

165. Rucklidge, A. M., Silber, M. & Skeldon, A. C. Three-Wave Interactions and Spatiotemporal Chaos. *Phys. Rev. Lett.* **108**, 074504 (2012).

166. Rogers, W. B. & Manoharan, V. N. Programming colloidal phase transitions with DNA strand displacement. *Science (80-.).* **347**, 639–642 (2015).

167. Smith, D., Myers, J. S., Kaplan, C. S. & Goodman-Strauss, C. An aperiodic monotile. *Comb. Theory* **4**, 1–91 (2024).

168. Hammonds, K. D., Dove, M. T., Giddy, A. P., Heine, V. & Winkler, B. Rigid-unit phonon modes and structural phase transitions in framework silicates. *Am. Mineral.* **81**, 1057–1079 (1996).

Appendix 1: Sphere at a Flat Interface Surface Evolver Script

```
//Define the half span of the interface
parameter x_len = 4
parameter y_len = 4

parameter rad = 1 //Radius of sphere
parameter Contact_angle = 70

parameter gamma = -cos(Contact_Angle*pi/180) //Surface tension in simulation units

constraint Sphere convex
formula: x^2 + y^2 + z^2 = rad^2

constraint Sphere_Contact_Line convex //Separate constraint only applied to the contact line
formula: x^2 + y^2 + z^2 = rad^2

//Constraints to make sure the interface edges are fixed in the x, y directions
constraint x_min
formula: x = -x_len

constraint x_max
formula: x = x_len

constraint y_min
formula: y = -y_len

constraint y_max
formula: y = y_len

vertex
//interface Perimeter
//      X                  Y                    Z            Constraints
1   x_len               y_len                0     constraints x_max, y_max
2   0                   y_len                0     constraints y_max
3  -x_len               y_len                0     constraints x_min, y_max
4  -x_len               0                    0     constraints x_min
5  -x_len              -y_len                0     constraints x_min, y_min
6   0                  -y_len                0     constraints y_min
7   x_len              -y_len                0     constraints x_max, y_min
8   x_len               0                    0     constraints x_max

//particle perimeter set in generic hexagon which allows surface to easily morph to complex
geometries
9   rad*cos(0*pi/3)     rad*sin(0*pi/3)      0     constraints Sphere_Contact_Line
10  rad*cos(1*pi/3)     rad*sin(1*pi/3)      0     constraints Sphere_Contact_Line
11  rad*cos(2*pi/3)     rad*sin(2*pi/3)      0     constraints Sphere_Contact_Line
12  rad*cos(3*pi/3)     rad*sin(3*pi/3)      0     constraints Sphere_Contact_Line
13  rad*cos(4*pi/3)     rad*sin(4*pi/3)      0     constraints Sphere_Contact_Line
14  rad*cos(5*pi/3)     rad*sin(5*pi/3)      0     constraints Sphere_Contact_Line

//particle top
```

```
15  0                   0                       rad      constraints Sphere

edges
//interface perimeter
1  1  2  constraints y_max
2  2  3  constraints y_max
3  3  4  constraints x_min
4  4  5  constraints x_min
5  5  6  constraints y_min
6  6  7  constraints y_min
7  7  8  constraints x_max
8  8  1  constraints x_max

//interconnecting lines (connects surface perimeter to particle)
9  1  10
10 2  10
11 2  11
12 3  11
13 4  12
14 5  13
15 6  13
16 6  14
17 7  14
18 8  9

//particle perimeter
19 9  10  constraints Sphere_Contact_Line
20 10 11  constraints Sphere_Contact_Line
21 11 12  constraints Sphere_Contact_Line
22 12 13  constraints Sphere_Contact_Line
23 13 14  constraints Sphere_Contact_Line
24 14 9   constraints Sphere_Contact_Line

//particle top
25 9  15  constraints Sphere
26 10 15  constraints Sphere
27 11 15  constraints Sphere
28 12 15  constraints Sphere
29 13 15  constraints Sphere
30 14 15  constraints Sphere

faces
//fluid-fluid interface
1  1   10 -9  color green
2  11 -20 -10 color green
3  2   12 -11 color green
4  3   13 -21 -12 color green
5  4   14 -22 -13 color green
6  5   15 -14 color green
7  16 -23 -15 color green
8  6   17 -16 color green
9  7   18 -24 -17 color green
```

```
10 8   9  -19 -18 color green

//particle fluid interface
11 19  26 -25 color yellow tension gamma constraints Sphere
12 20  27 -26 color yellow tension gamma constraints Sphere
13 21  28 -27 color yellow tension gamma constraints Sphere
14 22  29 -28 color yellow tension gamma constraints Sphere
15 23  30 -29 color yellow tension gamma constraints Sphere
16 24  25 -30 color yellow tension gamma constraints Sphere


read

//try to even out the mesh
groom_length := 0.2;
groom := {
        refine edge where length > groom_length;
        u;V;
        delete edge where length < groom_length/5;
}

hess_loop := {
        k 0;
        fix vertex where on_constraint Sphere;
        hessian_seek; hessian_seek;
        unfix vertex where on_constraint Sphere;
        k 1;
}

//Writes all vertices of surface around particle to a CSV
Interface_Data :={recalc;
        File_Name := sprintf "D:/Evolver/Myfiles/Sphere_Interface.csv";
        printf "x-posn,y-posn,z-posn,\n" >> File_Name;
        foreach vertex where x < 2 and x > -2 and y > -2 and y < 2 and not on_constraint
Sphere do {printf "%f,%f,%f,\n",x,y,z} >> File_Name
}

//Writes all vertices of the contact line around the particle to a CSV
Sphere_Contact_Line_Line_Data :={recalc;
        File_Name:= sprintf "D:/Evolver/Myfiles/Sphere_Sphere_Contact_Line Line.csv";
        printf "x-posn,y-posn,z-posn,\n" >> File_Name;
        foreach vertex where x < 2 and x > -2 and y > -2 and y < 2 and on_constraint
Sphere_Contact_Line do {printf "%f,%f,%f,\n",x,y,z} >> File_Name
}

//Allows the simulation to be reset easily
reset := {
        LOAD "D:/Evolver/Myfiles/Sphere at a flat interface.txt"
}

//Meshing, tessellation parameters and procedure
gogo := {
```

```
  groom 8;
  {g 5; groom; update_txt} 20;
  hess_loop;
  { g 5; groom; } 5;
}

// standard tessellation and minimisation procedure (step 1)
go_more := {
  { recalc; M 1;
    {g 5; groom } 10;
     hess_loop;
    {g 5; groom } 10;
    M 2; {g 5; u; V;} 10;
    refine edge where on_constraint Sphere;
    u; V;
    {g 5; u; V;} 50;
     }
}

//Simulation function
run:= {gogo 8;update_txt; go_more; update_txt; Interface_Data; Contact_Line_Data}
```

Appendix 2: Volume Overlap Between Two Core-Shell Particles

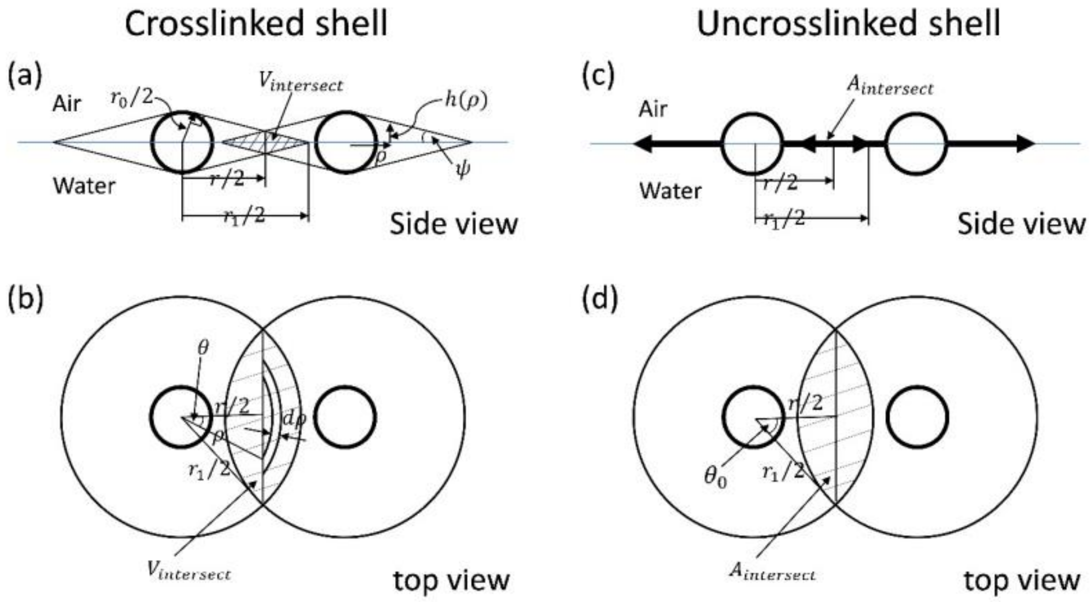

Figure 9.1: Simplified geometry used to calculate the soft-shell repulsion for crosslinked shells (a,b) and uncrosslinked shells (c,d). The thick and thin circles represent the core and shell respectively. A 3D view of both cases is shown in Figure 6.1a,b.

To simplify our calculations for the potential profile of crosslinked microgel core-shell particles in Chapter 6, we approximate the quasi three dimensional shape of the soft shell as two wide-based cones (base radius $r_1 / 2$) with their bases stuck together and their axis of symmetry perpendicular to the liquid interface (Figure 6.1a,b and Figure 9.1a,b). From simple geometry, the angle ψ is given by $\sin\psi = r_0 / r_1$ while the height of the shell as a function of the radial distance ρ is $h(\rho) = \tan\psi\left(\frac{r_1}{2} - \rho\right)$. We can approximate the interaction potential between two core-shell particles with separation r as[100]

$$V(r) \approx P_{corona} V_{intersect}(r) \tag{9.1}$$

where P_{corona} is the pressure exerted by the soft shell for typical microgel concentrations found in the interacting soft shells and $V_{intersect}(r)$ is the intersection volume between the two soft shells at separation r (see Figure 9.1a,b). The volume of the volume element dV corresponding the partial anulus shown in Figure 9.1b is given by

$$dV = 8\rho\theta h(\rho) d\rho \tag{9.2}$$

where $\theta = \cos^{-1}(r / 2\rho)$ so that the intersection volume is given by

$$V_{intersect}(r) = 2\tan(\psi) \int_{r/2}^{r_1/2} \cos^{-1}\left(\frac{r}{2\rho}\right) \rho \left(\frac{r_1}{2} - \rho\right) d\rho \tag{9.3}$$

Inserting equation (9.3) into equation (9.1) and defining ε as the interaction potential at core contact, we finally have

$$V(r) = \varepsilon \frac{V_{intersect}(r)}{V_{intersect}(r_0)} \tag{9.4}$$

which is plotted in Figure 6.1c for the case of $r_1/r_0 = 4$ (red curve).

However, for our calculations for the potential profile of the uncrosslinked core-shell particles in Chapter 6, we approximate the soft shells as circular disks with radius r_1 / 2 (Figure 6.1b and Figure 9.1c,d). In this case, we can approximate the interaction potential between two core-shell particles with separation r as[100]

$$V(r) \approx P_{corona} A_{intersect}(r) \tag{9.5}$$

whereP_{corona} is the surface pressure exerted by the soft shell for typical polymeric concentrations found in the interacting soft shells and $A_{intersect}(r)$ is the intersection area between the two soft shells at separation r (see Figure 9.1c,d). From simple geometry, the intersection area is given by

$$A_{intersect}(r) = \frac{r_1^2}{4}(2\theta - \sin 2\theta) \tag{9.6}$$

where $\theta = \cos^{-1}\frac{r}{r_1}$. Inserting equation (9.6) into equation (9.5) we finally have

$$V(r) = \varepsilon \frac{A_{intersect}(r)}{A_{intersect}(r_0)} \tag{9.7}$$

which is plotted in Figure 6.1c for the case of $r_1/r_0 = 4$ (blue curve).

Appendix 3: Estimation of ε for experimental Core-Shell System

This work was completed by my supervisor Dr D. Martin A. Buzza but is crucial for the assumptions we make within Chapter 6 to validate our approximations for our simulation.

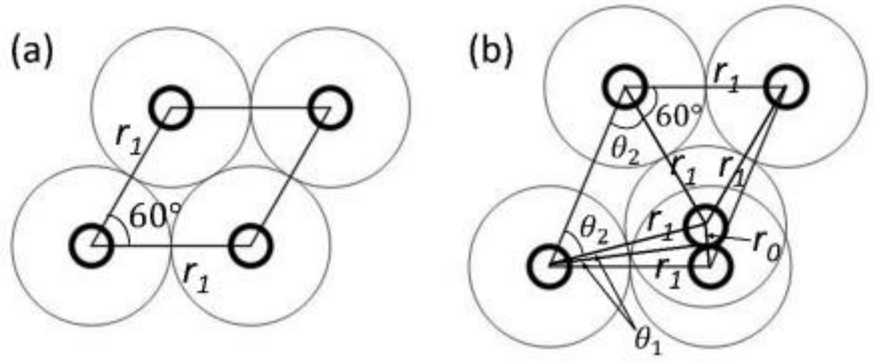

Figure 9.2: Unit cell and geometrical parameters for (a) HEXL phase; (b) DIM1 phase. The thick and thin circles represent the core and shell respectively.

The height of the repulsive shoulder ε can readily be calculated by noting that at the phase boundary between the low-density hexagonal phase HEXL and the dimer phase (specifically DIM1, see Figure 6.13) the enthalpy per particle of both phases are equal, i.e.,

$$\frac{\varepsilon}{2} + P_{coex}A_{DIM1} = P_{coex}A_{HEXL} \tag{9.8}$$

where P_{coex} is the coexistence surface pressure and A_{HEXL} and A_{DIM1} are the area per particle in the low-density hexagonal phase and DIM1 phase respectively. The left-hand side of equation (9.8) is the enthalpy per particle of the chain phase and the $\frac{\varepsilon}{2}$ term comes from the fact that there is one soft shell overlap for every two particles in this phase. The right-hand side of equation (9.8) represents the enthalpy per particle in the low-density hexagonal phase and there is no energy term as there are no soft-shell overlaps in this phase. Rearranging equation (9.8) we obtain

$$\varepsilon = 2P_{coex}(A_{HEXL} - A_{DIM1}) \tag{9.9}$$

From Figure 9.2a, we see that the area per particle for the HEXL phase is $A_{HEXL} = \frac{\sqrt{3}}{2}r_1^2$. From Figure 9.2b, we see that $\theta_1 = \sin^{-1}(r_0 / 2r_1)$, $\theta_2 = (\pi - 2\theta_1 - \pi/3)/2 = \pi/3 - \theta_1$, the unit cell angle is $\phi = 2\theta_1 + \theta_2 = \pi/3 + \theta_1$, the unit cell aspect ratio is $\gamma = 2r_1 \cos\theta_2 / r_1 = 2\cos(\pi/3 - \theta_1)$ and the area per particle for the DIM1 phase is $A_{DIM1} = r_1^2\gamma\sin\phi/2 = r_1^2\cos(\pi/3 - \theta_1)\sin(\pi/3 + \theta_1)$. From Figure 6.6h, we determine the coexistence pressure to be $P_{coex} \approx 25$mN/m. Inserting this and $r_1/r_0 = 4$, $r_0 = 170$nm into equation (9.9), we find $\varepsilon = 7 \times 10^{-15}$J, i.e., $\varepsilon/k_BT = 2 \times 10^6$, thus justifying our assumption in Chapter 6 that $\varepsilon \gg k_BT$. In order to check that this estimate for ε is reasonable, we can also independently calculate ε from the work done in compressing two polymeric corona to full overlap which from equation (9.5) is given by

$$\varepsilon \approx P_{corona}A_{overlap} \tag{9.10}$$

where $A_{overlap} = A_{intersect}(r_0) = \frac{r_1^2}{2}\left(\theta_c - \frac{r_0}{r_1}\sin\theta_c\right)$ is the overlap area of two circular disk-like coronas when their corresponding cores are in contact and $\theta_c = \cos^{-1}\left(\frac{r_0}{r_1}\right)$. From the plateau pressure in the surface pressure-area isotherm in Figure 6.5k, we estimate $P_{corona} \approx 28$mN/m. Inserting this into equation (9.10) yields $\varepsilon = 7 \times 10^{-15}$J, in excellent agreement with our estimate above based on the coexistence pressure. The agreement between the two results confirms that the soft repulsive shoulder in experimental the core-shell particles indeed arise from the elastic compression of the polymer corona around the microspheres.